UNIVERSITÀ
DI SIENA
1240

Dipartimento di Scienze fisiche, della Terra e dell'ambiente

Ph.D. Thesis in Experimental Physics

Development of a Time Of Flight diamond detector and readout system for the TOTEM experiment at CERN

Supervisor

Dr. Nicola Turini

Candidate

Edoardo Bossini

XXVI Cycle - 18 July 2016

Contents

Introduction **13**

1 Diffractive physics **17**
1.1 Introduction to diffractive physics 17
1.2 S-matrix formalism and fundamental theorems 21
1.2.1 Optical theorem 22
1.2.2 Crossing postulate 23
1.2.3 Asymptotical theorems 24
1.3 Regge Theory 24
1.3.1 Soft pomeron 27
1.4 The QCD pomeron 34
1.5 Hard diffraction 38

2 The TOTEM Upgrade **43**
2.1 Introduction to the upgrade program 43
2.2 Physics program 48
2.3 The experimental apparatus 52
2.3.1 The RP and the tracking detectors 54
2.3.1.1 High-$\beta^\star$ scenario : optics and tracker performance . . 59
2.3.2 The T2 telescope 61
2.3.3 The T1 telescope 63
2.3.4 Low central masses in CMS 65
2.4 A milestone: the trigger upgrade 66
2.5 High-$\beta^\star$ upgrade program 71
2.5.1 Overview of the TOTEM diamond TOF system 75
2.6 CT-PPS 78

3 The SiPM trigger detectors **83**
3.1 SiPM structure and operation 83

3.1.1 SiPM output characteristics . . . 87
3.2 Sensors characterization . . . 90
3.2.1 Sensor and electronics . . . 90
3.2.2 Breakdown voltage . . . 93
3.2.3 Sensor performances . . . 93
3.2.4 Afterpulsing and dark counts . . . 98
3.2.5 Laser test . . . 99
3.3 Detector assembly . . . 103

4 Diamond Detectors 107
4.1 Introduction to diamond detectors . . . 107
4.1.1 The Diamond structure . . . 107
4.1.2 Energy band structure . . . 110
4.1.3 Crystal defects . . . 113
4.1.4 CVD Diamond . . . 115
4.2 Diamond for MIP detection . . . 117
4.2.1 Principle and signal shape . . . 117
4.2.2 Expected output . . . 119
4.3 Tests with commercial diamond detectors . . . 124
4.3.1 Beam lines and experimental setup . . . 124
4.3.2 Results . . . 130

5 The TOTEM TOF detector: development and performances 139
5.1 Detector development . . . 139
5.1.1 The HADES telescope . . . 140
5.1.2 TOTEM amplification chain . . . 142
5.2 Prototype validation . . . 147
5.2.1 Experimental setup . . . 150
5.2.2 Optimization and performances . . . 155
5.2.3 Efficiency . . . 158
5.3 The TOTEM TOF detector . . . 162

6 Signal digitization 167
6.1 The fast sampler . . . 167
6.1.1 SAMPIC performance . . . 170
6.2 Discriminator and Time to Digital Converter . . . 172
6.2.1 Development of TOTEM NINO board . . . 174

6.2.2 Tests with waveform generator 177
6.2.3 NINO performances with the TOTEM diamond detector . . . 179

7 Detector readout and control **187**
7.1 The readout board 187
7.2 The firmware 190

Conclusions **195**

Acknowledgments **199**

Bibliography **200**

List of Figures

1.1 Visualization of diffractive processes in the $\eta - \phi$ plane 20
1.2 Graphical representation of the unitary equation 22
1.3 Regge trajectories for ρ, $f2$, $a2$ and ω mesons 27
1.4 Elastic differential cross-section measurements by TOTEM 30
1.5 Elastic slope B as a function of the energy $\sqrt{s}$ 30
1.6 $\mathrm{d}\sigma_{el}/\mathrm{d}t$ in the Coulomb-Nuclear interference region and energy dependence of the ρ parameter 31
1.7 Compilation of the total, inelastic and elastic cross-section measurements 32
1.8 A 2^{++} glueball candidate on pomeron trajectory 33
1.9 Pomeron evolution from Regge to QCD framework 34
1.10 Sample of two-loop diagrams for the qq scattering 35
1.11 Lipatov vertex and the reggezeid gluon 37
1.12 BFKL pomeron diagram 37
1.13 DIS and DDIS diagrams 39
1.14 Kinematical regions for the dPDF evolution equations 42

2.1 Central diffractive three jet event recorded by TOTEM and CMS . . 45
2.2 Pile-up w.r.t bunches population for $\beta^\star = 90$ m 47
2.3 Leading order diagrams for some process investigated 50
2.4 Example of BSM search 52
2.5 LHC scheme 53
2.6 Drawing of the TOTEM-CMS close to IP5 54
2.7 Picture of the RP station and individual units 55
2.8 Strip detector actually installed in the RP 56
2.9 Scheme of the RP station with a tilted unit 57
2.10 RP inner box and and sensor placements around the beam 57
2.11 Concept of the proton kinematic reconstruction with the RP 58

2.12 The effective length $L_{x,y}$ and the magnification $v_{x,y}$ 59
2.13 Angular resolution on scattered protons at $\sqrt{s} = 8$ TeV 60
2.14 Simulation of the protons acceptance in the RP 61
2.15 The T2 telescope 62
2.16 Structure of the T2 GEM 63
2.17 The T1 telescope 64
2.18 CMS tracker efficiency for low momentum particle and PID 66
2.19 Conceptual scheme of the TOTEM trigger structure 67
2.20 Scheme of the LOneG trigger 68
2.21 Tracks multiplicity in the RP 73
2.22 Hit distribution for $\beta^\star = 90$ and detector segmentation 74
2.23 Scheme the complete timing detector for the high$-\beta^\star$ upgrade 78
2.24 Hit distribution with standard optics and detector segmentation . . . 80
2.25 Scheme of our detector in the CT-PPS configuration 81
2.26 Layout of the Roman Pot system after the LS1 82

3.1 Picture of Hamamatsu S12571-100P SiPM and internal architecture . 84
3.2 Example of APDs internal structure 85
3.3 APD charge distribution and electric field 85
3.4 GM-APD equivalent circuit and signal example 86
3.5 Superimposition of multiple SiPM waveforms 88
3.6 SiPM prototype board and polarization circuit 91
3.7 Electronic boards for SiPM operation 92
3.8 SiPM I-V curve and V_{break} determination 94
3.9 Examples of SiPM waveform with multiple peaks 95
3.10 Amplitude distribution for DC signals 96
3.11 Gain, resolution, SNR and crosstalk probability w.r.t. V_{ov} 97
3.12 Time difference distribution between consecutive peaks 98
3.13 Laser setup for SiPM timing studies 100
3.14 Single photon timing resolutions 102
3.15 Picture of the scintillators manufacturing 104
3.16 Trigger detector assembly picture 105
3.17 Picture of the trigger detectors completed and in operation 105

4.1 Example of unit cell for a bidimensional lattice. 108
4.2 fcc lattice conventional cell and diamond structure 109
4.3 First brillouin zone for fcc lattice 110

4.4 Band structure for diamond . . . 111
4.5 Example of crystal defect . . . 114
4.6 Energy levels crated by Boron and Lithium in diamond crystal . . . 115
4.7 Detector scheme for diamond detector . . . 117
4.8 Current generated from a MIP in a diamond detector . . . 119
4.9 Energy release for e-h pair in different material . . . 120
4.10 Simulated Field and charge release from a MIP in a diamond detector 123
4.11 Simulated current from a MIP in a diamond detector . . . 123
4.12 Pion and electron fluxes at PSI . . . 125
4.13 Picture of PSI setup and experimental hall . . . 126
4.14 Detector scheme at PSI . . . 127
4.15 Particle TOF distribution measured in πM1 . . . 128
4.16 Detector photo at PSI . . . 129
4.17 Detector scheme at PS . . . 129
4.18 Picture of the reduced capacitance detector . . . 130
4.19 Diamond detector event display . . . 131
4.20 V_{am} distribution for D2 with reduced capacitance . . . 131
4.21 ΔT_{12} with method 6 at PS . . . 133
4.22 Comparison between D1 and D2 with low capacitance . . . 135
4.23 Detector parameter dependence with Capacitance . . . 136

5.1 Picture of the HADES telescope during the test . . . 141
5.2 Distribution of the time difference between the two HADES sensors . 142
5.3 Distributions of the HADES signal amplitude, t_r^{20-80} and SNR. . . . 143
5.4 Scheme of the first TOTEM hybrid prototype . . . 144
5.5 Scheme of the setup used for the TOF electronics test at SPS . . . 145
5.6 Resolution of the TOTEM sensor w.r.t the second stage configuration 146
5.7 The amplification chain developed at SPS . . . 147
5.8 Best timing result obtained with the TOTEM hybrid at SPS . . . 147
5.9 Comparison between HADES and TOTEM sensor parameters at SPS 148
5.10 Picture of the second version of the hybrid board prototype . . . 149
5.11 Scheme of the amplifier and shaper integrated by TOTEM . . . 150
5.12 Setup of the DATURA telescope . . . 151
5.13 Signal amplitude from electrons at 4 GeV and 5.6 GeV . . . 152
5.14 Scheme of DESY test beam setup . . . 153
5.15 Pictures of the DESY setup . . . 154
5.16 Scheme of the TLU/oscilloscope trigger handshake . . . 155

5.17 Timing resolutions with different electronic configurations 156
5.18 Time resolution as a function of the detector area 157
5.19 Distribution of the time difference between 2 pF and 0.29 pF sensor . 158
5.20 Comparison between 2 pF and 0.29 pF sensors parameters 159
5.21 Distributions of the track hits in the DUT plane 160
5.22 Efficiency scan in the diamond bulk area 161
5.23 Efficiency measure in the inter-strip area 161
5.24 Pictures of the Totem TOF hybrid boards 162
5.25 The totem TOF detector during the final tests 163
5.26 Time resolution of the TOTEM TOF detector 164

6.1 Picture of the SAMPIC module 168
6.2 Scheme of the SAMPIC chip 169
6.3 Screenshot of the SAMPIC GUI during data taking 171
6.4 ΔT_{12} distribution for pixel #3 with LHC showers 172
6.5 Block scheme of the NINO chip 173
6.6 Concept of the input charge encoded in the NINO output width . . . 174
6.7 Connection of a single-ended signal to a NINO input channel 175
6.8 Picture of the ALICE and TOTEM boards with the NINO chip . . . 177
6.9 Output leading edge and width resolution w.r.t. V_{ampl} 178
6.10 NINO W as a function of signal V_{ampl} 179
6.11 ΔT_{12} distribution between the generator and the NINO output 180
6.12 Scheme used to test the TOTEM NINO board 180
6.13 Scatter plot of input signal amplitude and NINO output width 181
6.14 Raw ΔT_{12} distribution between the two NINO output 182
6.15 Scatter plot of ΔW Vs raw ΔT_{12} 183
6.16 Profile distribution for the $\Delta W - \Delta T_{12}$ scatter plot 183
6.17 Corrected ΔT_{12} distribution between the two NINO output 184
6.18 Scatter plot and profile of W_2 vs raw ΔT_{12} 185
6.19 Raw and corrected ΔT_{12} distribution between the N_2 and D_2 signals . 185

7.1 Scheme of the diamond sensors readout and control 188
7.2 Scheme of the firmware control path 191
7.3 Scheme of the firmware readout path 193

List of Tables

2.1 Expected running scenarios at $\sqrt{s} = 13$ TeV 46

3.1 Summary of the afterpulse and DC measurements 99
3.2 Parameter comparison with different amplifiers 103

4.1 Comparison chart between carbon and silicon properties 122
4.2 πM1 beam line characteristics 125
4.3 Analysis methods comparison 133
4.4 Commercial Diamond result summary 134

5.1 Summary of the diamond sensors employed at DESY 152
5.2 Summary of the results obtained with different area sensors 159

Introduction

In this work I will describe the development of a Time of Flight (TOF) detector and its readout system for the TOTEM[1] experiment. The detector, based on diamond sensors, will have a key role in the study of hadronic diffractive processes at the LHC[2].

Diffractive physics has been an active field of research since the first particle accelerators were built in the 60's. There the discovery of hadronic processes with similarities with the optical diffraction (i.e diffractive minima) gave a first pulse to the development of a theory which could give an interpretation to the experimental data. The Regge theory emerged as a successful theory for this context. In the Regge theory the diffractive processes are modeled through an exchange of one or more *trajectories*, called *Reggeons*. The dominant trajectory, which determines the hadron-hadron cross section behaviour at high energy, keeps the name of *Pomeron*. The Pomeron, as we will later see, is still a phenomenological object used to successfully parameterize the data, but a connection between the Pomeron and the *glueball* search has been established. The importance of diffractive physics, that was thought to be relevant only for processes involving low momentum transferred, grew significantly when diffractive characteristics were identified also in processes with high momentum transferred. In this framework the translation of the phenomenological Pomeron in terms of QCD language opened a series of questions that modern physics must address. Nowadays the study of diffractive physics can open new scenarios in the understanding of the proton structure. In chapter 1 I will give an introduction to the world of diffractive physics, highlighting the open questions that the TOTEM experiment can investigate. In this field the experiment as already produced important results that greatly enhance our knowledge of diffractive processes at high energy scale.

TOTEM has developed a wide and important new physics program to investi-

[1] TOTal cross section, Elastic scattering and diffraction dissociation Measurements at the LHC.
[2] Large Hadron Collider, CERN laboratory, Geneva, Swiss.

gate diffractive processes together with the CMS[3] experiment. The joint detector will give an exceptional pseudo-rapidity coverage, making possible the study of central diffractive processes in an almost background free environment. The physics channels that will be investigated include the low mass spectroscopy, connected to the glueball search, diffractive charmonium state production and central diffractive Jet production. The main TOTEM detectors involved in the measurements will be the Roman Pot (RP), vacuum vessels located symmetrically more than 200 meters from the beam interaction point, that can bring the equipped detector to few millimeters from the beam axis. In this way is possible to tag and track the protons that escape intact from the central diffractive interactions. This measurements will be done in the so called high-$\beta^\star$ machine optics, specially designed for this measurements. However the high luminosity, needed to collect all the required data, leads to the pile-up problem, represented by simultaneous events from multiple *pp* interactions. Due to their position the detectors installed in the RPs are not able to reconstruct the point of origin of the tagged protons with enough precision to assign them to the right *pp* interaction vertex. To disentangle the detected protons and perform a precise event reconstruction the RPs need to be equipped with very precise timing detectors (resolution < 50 ps) to measure the proton TOF. This will make possible to reconstruct the longitudinal coordinate from where the protons were originated by making the difference of the proton arrival times in the two detector arms. In chapter 2 I will describe the physics program and the scenarios that the TOTEM detector will face. After the description of the actual setup, the strategy for the upgrade will be outlined. There the diamond technology will be addressed as our best choice and an overview of the final TOF detector structure will be given. Simultaneously to the high-$\beta^\star$ upgrade, another joint project of CMS and TOTEM, called CT-PPS[4] is being carried out. Its physics program will be complementary to the high-$\beta^\star$ program, running with the standard machine optics. In view of the good results obtained and here reported the TOTEM diamond detector will be employed also in this project as described in chapter 2. This is particularly exiting, since it will be involved in the investigation of some recent hints of physics beyond the standard model.

The thesis is focused in the description of my work on the timing detector development, describing also the alternative solutions, both for sensor technology and readout strategy, which I studied. Already in chapter 3 I will indeed introduce

[3]Central Muon Solenoid.

[4]CMS-TOTEM Proton Precision Spectrometer

the Silicon Photomultiplier (SiPM) sensors and some preliminary studies to use the SiPM to build our TOF detector will be presented. The characteristics of such devices did not convinced us to go further with them. However I used the acquired knowledge to build some auxiliary detectors, which proved really useful during the diamond test beams.

The diamond will be instead the main actor of chapter 4, where a description of its structure and of its usage as a MIP detector will be studied. In the same chapter I will also report about the first tests performed with commercial detectors. Even if the results on timing were poor, important hints on how to use and optimize this technology will emerge. All the analysis techniques employed in this work to extract the timing information are also described. Moving from such results we decide to build a custom board, integrating the sensor and the front-end electronics (from which the name of *hybrid* board).

The development of the TOTEM hybrid board is reported in chapter 5. I will describe the steps that brought us to define the best amplification scheme for the diamond signal and the first promising results obtained. Based in this first attempt we developed a four channel hybrid prototype. The validation of the hybrid prototype and its performances will be reported. The final board, ready for the installation, will be presented and I will briefly report about the final tests performed on it.

To have a complete detector, a suitable readout must be used, so that degradation of the sensor performances is avoided. Two signal digitization techniques have been taken in consideration. The first is the use of a fast sampler, which allows for sophisticate offline reconstruction algorithms. The second foreseen the usage of a discriminator, especially designed for TOF systems, coupled to an high performance time to digital converter. Both solutions will be investigated, since both of them will be finally used, one for the high-$\beta^\star$ and the other for the CT-PPS project. The reasons of this dual readout and the differences in the final performance of the system will became clear through chapter 6.

Finally in chapter 7 an overview of the the entire readout and slow control for the TOF system will be given. The system is designed to be operated both in the LHC tunnel, integrated with the existing TOTEM DAQ and control structures, or in a stand-alone configuration for test beams. The setup is based on an high-end FPGA from Microsemi, the SmartFusion 2. I will provide a description of the firmware blocks, which I am actually developing, highlighting the main features.

Chapter 1

Diffractive physics

The goal of this chapter is to give a general background and address the main questions of modern diffractive physics that the TOTEM-CMS joint detector, outlined in chapter 2, will deeply investigate. The characteristics of diffractive processes and the Regge theory of soft interactions will be discussed. The phenomenological soft pomeron will be compared with the hard pomeron obtained from the translation of the Regge theory in the QCD framework. We will finally point out the importance of hard diffractive processes in the understanding of the proton structure. The results obtained by the TOTEM collaboration during the first LHC run, here presented and discussed, even if not being the main subject of the thesis, represent an important result of my work.

1.1 Introduction to diffractive physics

A *diffractive* process can be identified with two equivalent definitions:

1. a process with final states characterized by one or more large *rapidity gaps*[1] $\Delta\eta$, non exponentially suppressed.

[1]The rapidity, referred to the beam axis z, of a particle with energy E and momentum component p_z along the z-axis is defined as

$$y = \frac{1}{2} \ln \frac{E + p_z}{E + p_z}. \tag{1.1}$$

It transforms additively under longitudinal boost, so that *rapidity* variations are invariant in any collinear frame. Rapidity gaps are regions without final state particles. Another observable often used is the *pseudorapidity* η defined as $\eta = -\ln \tan \frac{\theta}{2}$ where θ is the angle between the particle trajectory and the z-axis. For high energy particles $y \approx \eta$.

2. an high energy process where no quantum numbers are exchanged between the colliding particles.

In the former definition we should stress that large rapidity gap are possible also in a non-diffractive process, but with a $\mathrm{d}N/\mathrm{d}\Delta\eta$ ratio almost constant. The latter will be useful when we will describe diffractive processes in the QCD framework; for the moment is enough to notice that it defines the diffraction as an asymptotic process, that take place at high energy.

In hadron-hadron diffractive reactions one or both hadrons can dissociate into a bunch of particles X_n. We speak of *single diffraction* when only one of the hadrons dissociate, while the other, called *leading*, stay intact and just loose part of its momentum:

$$1 + 2 \to 1' \oplus X_2. \tag{1.2}$$

When both hadrons dissociate we have instead a *double diffraction*

$$1 + 2 \to X_1 \oplus X_2. \tag{1.3}$$

In both case there are no final state particles in the central region (low η value); the corresponding rapidity gap is identified with the $\oplus$ symbol. On the other side, when a rapidity-isolated system X is generated in the central region we speak of *Central diffractive* (CD) events. CD processes where both hadrons stay intact

$$1 + 2 \to 1' \oplus X \oplus 2' \tag{1.4}$$

are of particular interest, being one of the main fields that can be deeply investigated only with a joint TOTEM-CMS detector.

Finally even elastic scattering

$$1 + 2 \to 1' + 2', \tag{1.5}$$

where both colliding particles survive the interaction and no other particles are generated, can be included in the list of diffractive processes. Exactly elastic scattering, as we will see in section 1.2.1, is a relevant interaction being related with the total cross section measurement.

The large majority of diffractive processes fall in the category of the so called *soft* hadronic interactions. Such reactions are characterized by an energy scale of the

other of the hadron radius (∼1 fm) and a low momentum transfer squared[2] $|t|$, of the order of few hundreds MeV^2. At such scales perturbative Quantum Chromodynamic (pQCD) is not applicable.

The study of soft diffractive physics start at early 60's, with the development of particle accelerators, when hadronic processes with diffractive characteristics were first discovered. The name is not accidental, and it is due to the similarities between such events and optical diffraction (i.e. diffraction minima in the angular distribution). However the relativistic approach also predicts some behaviour with no equivalent in optics and experimentally confirmed. In this context in 1960 Good and Walker[1] predicted "processes with final diffractive-produced systems with a characteristic extremely narrow distribution in transverse momentum and the same quantum numbers as the initial particle". Their models were confirmed few years later.

Almost simultaneously the Regge theory of strong interactions[2] was developed. In the model the diffraction at high energy is described through the exchange of an universal trajectory with vacuum quantum number, called the *pomeron* ($\mathbb{P}$). Since Regge theory has a main role in the description of diffractive phenomena an extended description will be given in section 1.3, after an introduction to the strong interaction S-matrix formalism in section 1.2. At present all theoretical modelizations of soft interaction contain parameters that are not predicted by the theory and must be inferred from experimental data through phenomenological considerations. The results obtained from the TOTEM collaboration show a strong power in the discrimination of different models and are therefore reported in section 1.3.1, were the soft pomeron characteristics will also be discussed.

In figure 1.1 are reported the diffractive process described in terms of pomeron exchange together with an example of final state particle distribution in the $\eta - \phi$ plane (ϕ is the azimuthal angle related to the beam axis). Central diffractive reactions described in equation (1.4) can happen through many different processes. For our scope the two main processes are the *double pomeron exchange* (DPE) and

[2]In a two body scattering $1 + 2 \to 3 + 4$, where p_i is the 4−momentum of the i−th particle, three Lorentz invariant variable are defined (Mandelstam variables):

$$s = (p_1 + p2)^2 = (p_3 + p4)^2 \tag{1.6}$$

$$t = (p_1 - p3)^2 = (p_2 - p4)^2 \tag{1.7}$$

$$u = (p_1 - p4)^2 = (p_2 - p3)^2 \tag{1.8}$$

In a s−channel reaction as the one above $\sqrt{s}$ represent the center of mass energy while t is the square of the 4−momentum transferred.

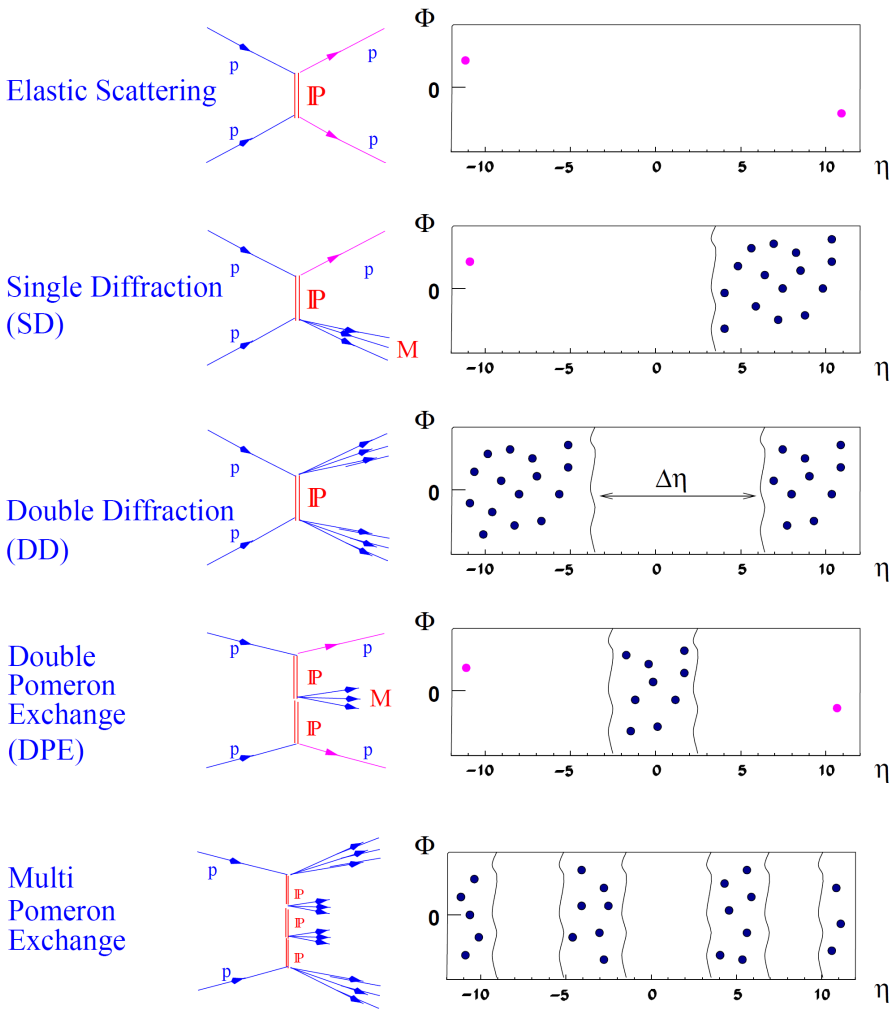

Figure 1.1: Visualization of diffractive processes in the $\eta - \phi$ plane.

the *photoproduction*. In the first the system X is generated from the interaction among the two pomerons emitted by the protons (see fig.1.1), while in the second the interaction is between one virtual photon and one pomeron.

The attempt of translate the pomeron of the Regge theory in term of QCD is very interesting, allowing to investigate the pomeron in the QCD framework. This attempt will be described in section 1.4, where the *hard pomeron* will emerge in the high energy limit as a gluon ladder. The interest in the QCD pomeron structure and thus in diffractive physics spread further when diffractive characteristics were identified among *hard* processes. In hard interactions the high value of momentum transfer (≥ 1 GeV^2) allows the use of pQCD, but part of the process remain of non-perturbative origins. The factorization theorem allows to separate the contributions,

embodying the non-perturbative contribution in the quark and gluon distribution functions, that can be studied with the methodologies introduced in section 1.5.

1.2 S-matrix formalism and fundamental theorems

Relativistic description of the strong interaction can be given in terms of the S-matrix, defined as the linear operator which transform the initial state $|i\rangle$ into the final state $|f\rangle$

$$S\,|i\rangle = |f\rangle\,. \tag{1.9}$$

In such formalism the transition probability from the initial state to the final state $P_{i\to f}$ reads

$$P_{i\to f} = |\,\langle f|S|i\rangle|^2 = S_{if}. \tag{1.10}$$

We can introduce a *transition matrix* T and the relativistic *scattering amplitude* A_{if} as

$$S_{if} = \delta_{if} + i\,\langle f|T|i\rangle = \delta_{if} + i(2\pi)^4\delta^4(p_f - p_i)A_{if}. \tag{1.11}$$

The scattering amplitude is thus derived from the T matrix by extracting the $4-$momentum conservation and is usually expressed as a function of the Mandelstam variables s and t[3], $A(s,t)$. The differential cross section is given by

$$\mathrm{d}\sigma = \frac{1}{\Phi}|A_{if}|^2\mathrm{d}\Pi_n, \tag{1.12}$$

where $\mathrm{d}\Pi_n$ is the Lorentz invariant phase space for n final state particles and ϕ is the total incident flux. If we consider an high-energy elastic scattering process with azimuthal symmetry (as for pp elastic scattering at LHC energy scale), is possible to derive the explicit form of equation (1.12) as

$$\frac{\mathrm{d}\sigma_{el}}{\mathrm{d}t} \simeq \frac{1}{16\pi s^2}|A(s,t)|^2 \tag{1.13}$$

The total cross section σ_{tot} is obtained integrating equation (1.12) and summing over all the possible number of particles in the final state:

$$\sigma_{tot} = \frac{1}{\Phi}\sum_n \int |A_{if_n}|^2\mathrm{d}\Pi_n. \tag{1.14}$$

[3] u can be derived from the other through the identity relation $s + t + u = \sum_{i=1}^{4} m_i^2$.

1.2.1 Optical theorem

One of the main results of the S-matrix approach is the *optical theorem*, which follows directly from the request of unitarity of S

$$S^\dagger S = S S^\dagger = \mathbb{1}. \tag{1.15}$$

The unitarity condition is a direct consequence of the conservation of probability, requiring that the sum of the transition probabilities to all the possible final states must be the unity. In terms of the Transition matrix the unitarity condition leads to the following relation

$$2\,\mathrm{Im}\{T_{if}\} = \sum_{\{n\}} T^*_{fn} T_{in}, \tag{1.16}$$

where $\{n\}$ denote the integration over all final state momenta and the sum over all the possible quantum numbers. If we extract the δ function of the $4-$momentum conservation we get a similar equation for the scattering amplitude

$$2\,\mathrm{Im}\{A_{if}\} = \sum_{n} \int \mathrm{d}\Pi_n A^*_{fn} A^*_{in}. \tag{1.17}$$

A graphical representation of relation (1.17) can be seen in figure 1.2. Almost the

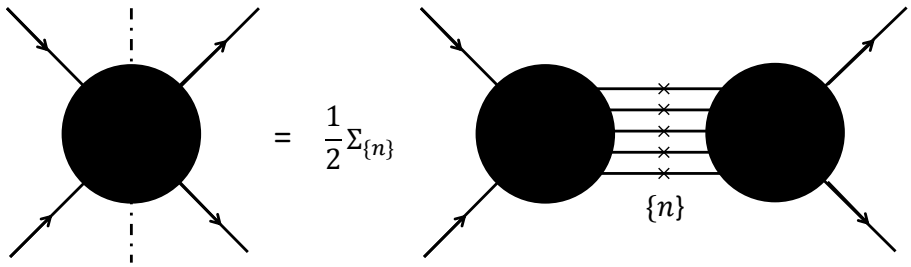

Figure 1.2: Graphical representation of the unitary equation. The imaginary part is denoted with the dot-dashed line. The crosses on the right represent on-shell particles.

same diagram can be used to calculate loop diagrams in QCD (Cutkosky rules), were the loop can be cut in a similar way in order to compute the process cross section. We will use it later in section 1.4.

If we consider the elastic scattering in the forward direction, since no momentum is transferred (forward direction $\rightarrow t = 0$), the final state is identical to the initial ($|f\rangle = |i\rangle$). With this constraint equation (1.17) can be rewritten as

$$2\,\mathrm{Im}\{A_{el}(s, t = 0)\} = \sum_n \int \mathrm{d}\Pi_n |A_{in}|^2. \tag{1.18}$$

Comparing equations (1.18) and (1.14) we get the relation between the total cross section and the forward elastic scattering amplitude, known as the optical theorem

$$\sigma_{tot} = \frac{2}{\Phi}\,\mathrm{Im}\{A_{el}(s, t = 0)\}. \tag{1.19}$$

1.2.2 Crossing postulate

Another useful property that will come to hand shortly is the *crossing postulate*. In the two-body scattering $1+2 \rightarrow 3+4$ the center of mass energy is represented by $\sqrt{s}$ while the $4-$momentum transferred squared by t, the reaction is called $s-$channel. Is possible to define the crossed reaction ($t-$channel and $u-$channel) as

$$1 + 2 \rightarrow 3 + 4 \qquad (s - channel), \tag{1.20}$$

$$1 + \bar{3} \rightarrow \bar{2} + 4 \qquad (u - channel), \tag{1.21}$$

$$1 + \bar{4} \rightarrow 3 + \bar{2} \qquad (t - channel), \tag{1.22}$$

where the momenta of antiparticles in t and u channels are reverted. The physical meaning of the Mandelstam variable are thus changed: for example in the $t-$channel the center of mass energy is $\sqrt{t}$. With simple kinematical calculation is possible to set some constraints on the physical domains of the three channels (equal-mass scattering)

$$s \geq 4m^2, \quad t \leq 0, \quad u \leq 0 \qquad (s - channel) \tag{1.23}$$

$$t \geq 4m^2, \quad s \leq 0, \quad u \leq 0 \qquad (t - channel) \tag{1.24}$$

$$u \geq 4m^2, \quad s \leq 0, \quad t \leq 0 \qquad (u - channel) \tag{1.25}$$

The crossing postulate of the S-Matrix states that the same scattering amplitude describes three different processes. Applying the CPT (charge conjugation + time reversal + parity reversal) invariance the set of processes described by the same amplitude further increases. This possibility, only postulated in the S-matrix, is known to be true in field theory.

1.2.3 Asymptotical theorems

Before introducing Regge theory is worth mentioning two theorems which put some important constraints on the cross section behaviour at high energy.

The Froissart-Martin theorem predicts that the total cross section in hadron-hadron collisions cannot grow faster than $\ln^2 s$, more exactly

$$\sigma_{tot} \leq C \ln^2 s \qquad \text{when} \qquad s \to \infty. \tag{1.26}$$

A general derivation of theorem, based on axiomatic field theory can be found in [3]. The theorem does not predict the value of the C constant, but a lower bound on it can be found

$$C \geq \frac{\pi}{m_\pi^2}, \tag{1.27}$$

where m_π^2 is the pion mass. The result is a quite large C value, at least 60 mb.

Another fundamental result is the *Pomeranchuk* theorem[4], which states that the total cross section for particle-particle and particle-antiparticle reaction became equal at high energy

$$\sigma_{tot}(ab) \underset{s\to\infty}{\simeq} \sigma_{tot}(a\bar{b}). \tag{1.28}$$

The results of Pomeranchuck is derived from the *Okun-Pomeranchuk* relation[5], stating that all nucleon-antinucleon ($N\bar{N}$) total cross section are asymptotically equals.

1.3 Regge Theory

Regge theory has been first developed for non-relativistic fields and then exported to high energy particle physics. While in its original form it is based on solid assumption, when extended to relativistic processes it relies on a series of assumptions. However its success in the prediction of soft physics phenomena, where no alternative framework is available, cannot be denied. The phenomenological success of the Regge theory in the description soft processes, where pQCD is not applicable, has determined its glory. In the present work only the main concepts and results of Regge theory in the case of a two body scattering with equal-mass, spinless particles will be given. A non-zero spin treatment of the Regge theory can be found in [2].

For central potential, as the one involved in our case, the scattering amplitude

in the $t-$channel can be expanded in partial waves:

$$A(t, z_t) = \sum_{l=0}^{\infty} (2l+1) a_l(t) P_l(z_t), \tag{1.29}$$

$$a_l(t) = \frac{1}{2} \int_{-1}^{+1} dz_t P_l(z_t) A(t, s(z_t, t)), \tag{1.30}$$

where $P_l(z_t)$ are Lagrange polynomials, $a_l(s)$ are the partial wave coefficients and z_t is defined as

$$z_t \equiv \cos\theta_t = 1 + \frac{2s}{t - 4m^2}. \tag{1.31}$$

Regge derived his theory from quantum-mechanic, where symmetric potentials lead to bound states that appear as pole of the partial wave amplitude A_l for a given l. The idea of Regge was to extend the partial wave coefficients for the $t-$channel process to complex value of the angular momentum l ($A_l(t) \to A(l,t)$). His bet was that, under some hypothesis, the resulting function would show simple poles located at

$$l = \alpha(t), \tag{1.32}$$

where $\alpha(t)$ took the name of *Regge trajectory*. The final goal was to obtain a relation between the scattering amplitude and the Regge trajectories. Moreover in principle it is possible to find real bound states (resonances) for integer real values of l. The extension to complex angular momenta can rise some doubt. However the crossing postulate of the S-Matrix imply that the scattering amplitude is the same in all cross channels and the extension of $a_l(t)$ must be valid for all the channel domains of equation (1.23-1.25): this is achievable only moving to complex $l-$value. The result of the expansion became rather hard to read, but in the limit $z_t \to \infty$ (that from eq.(1.31) can be done with $s \to \infty$) we get for the scattering amplitude:

$$A(t, z_t) \underset{|z_t|\to\infty}{\simeq} -\sum_{\xi=\pm 1} \sum_i \beta_{i_\xi}(t) \frac{1 + \xi e^{-i\pi\alpha_{i_\xi}(t)}}{\sin \pi\alpha_{i_\xi}(t)} (-z_t)^{\alpha_{i_\xi}(t)}, \tag{1.33}$$

where $\alpha_i(t)$ is the location in the complex $l-$plane of the $i-$th pole and $\beta_i(t)$ is the residual at that pole. The ξ factor, a newly introduced quantum number called *signature*, which take the value $\xi = \pm 1$, arise from the request that the scattering amplitude vanishes for large value of l. Is clear that in the high s-limit (remember that we are working in the $t-$channel) the pole $\alpha_i(t)$ with the largest real part dominates the series and we get the asymptotic form of the expansion

$$A(s, t) \underset{|s|\to\infty}{\sim} -\beta(t) \frac{1 + \xi e^{-i\pi\alpha(t)}}{\sin \pi\alpha(t)} s^{\alpha(t)}. \tag{1.34}$$

Since the scattering amplitude is equal for all channel we can read the above equation as the scattering amplitude in $s-$channel in the high energy limit, that turns out to be determined by the leading singularity in the crossed $t-$channel, a remarkable result.

From (1.34) is immediate to extrapolate the Regge prediction for total cross section in case of a single leading pole through the optical theorem:

$$\sigma_{tot} \underset{s\to\infty}{\simeq} \frac{1}{s} \operatorname{Im} A(s, t=0) \underset{s\to\infty}{\propto} s^{\alpha(0)-1}. \tag{1.35}$$

When multiple poles contribute we will have the weighted sum of many terms:

$$\sigma_{tot} \sim \sum_i c_i s^{\alpha_i(0)-1}. \tag{1.36}$$

The process in the $s-$channel can thus be described through the exchange of Regge trajectories, called *Reggeons* ($\mathbb{R}$), and in the high energy limit the exchange is reduced to the leading trajectory. In section 1.1 we said that high energy diffractive processes can be modeled through a pomeron (single or multiple) exchange. Is seem obvious to identify the pomeron with the leading Regge trajectory, but we will see in next section that the situation is not straightforward.

It is interesting to investigate if, when we restrict to integer value of l, Regge trajectories interpolate real particles. Experimentally has been confirmed that all resonances of the same family (resonance with same quantum number) lie on the same trajectory, which take is name from the lower mass particle. The reggeon, even if it is not a particle, can thus be conceived as a family of resonances exchanged in the process. In figure 1.3 we can see the ρ, $f2$, $a2$ and ω mesons trajectories. They are almost overlapped and can be fit with a straight line. We can thus reasonably expand $\alpha(t)$ linearly as

$$\alpha(t) \simeq \alpha(0) + \alpha' t. \tag{1.37}$$

It must be noted that each trajectories contains only particles with even (odd) angular momentum, this is a consequence of $\xi = +1$ ($\xi = -1$) signature of the trajectory. Moreover all the resonances on the same trajectories have the same quantum numbers. Trajectories reported in figure 1.3 are the one with the higher intercept known and so they should represent the leading singularity at high energy. Therefore the cross section should decrease with energy.

If we translate the elastic scattering differential cross section (1.13) into Regge language and we use (1.37) we get (single pole case):

$$\frac{\mathrm{d}\sigma_{el}}{\mathrm{d}t} = K(t) s^{2(\alpha(0)-\alpha' t)-2} = K(t) s^{2\alpha(0)-2} e^{-2\alpha'|t| \ln s}, \tag{1.38}$$

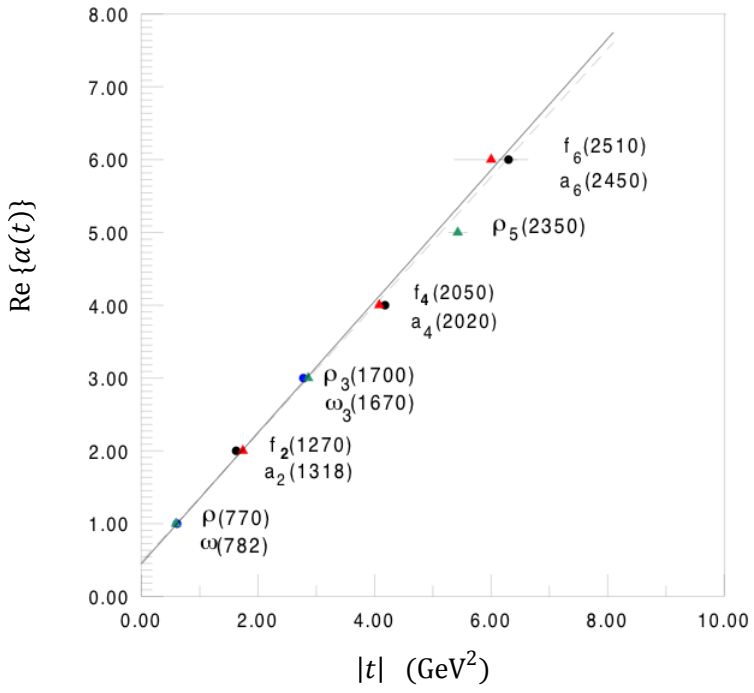

Figure 1.3: Regge trajectories for ρ, $f2$, $a2$ and ω mesons. A Regge trajectory is named by the lower l particle on it.

where $K(t)$ incorporates signature and residual factors. If we assume that also the residual function shows an exponential $t-$dependence, we get that asymptotically the differential cross section should behave like $\frac{\mathrm{d}\sigma_{el}}{\mathrm{d}t} \propto e^{-B|t|}$. The exponential term puts in evidence that the width of the forward peak decrease as energy increase. This result, with have no optical equivalent, is often seen as a growth of the proton interaction radius $R_{int} \sim \sqrt{\alpha' \ln s}$ with energy. This important results of the Regge theory have been proved experimentally.

1.3.1 Soft pomeron

We have introduced the pomeron as the main actor of the Regge theory. To understand what it is and what are its characteristics is necessary to discuss more in details some phenomenological aspects of high energy soft processes, in particular the experimental results on the total cross section.

Before LHC era, total cross section measurements have been performed up to $\sqrt{s} = 1.8$ TeV. The ISR[4] performed studies in the range $\sqrt{s} = 20 - 62$ GeV, both

[4] *Intersecting Storage Ring*, CERN.

on pp and $p\bar{p}$. The results show the asymptotic equality between pp and $p\bar{p}$ total cross section as predicted from the Pomeranchuck theorem. Later experiments at SPS[5] ($\sqrt{s} = 0.546$ TeV and $\sqrt{s} = 0.90$ TeV) and at Tevatron[6]($\sqrt{s} = 1.8$ TeV) on $p\bar{p}$ demonstrate that the cross section grows with energy, in contrast with the expectation previously discussed. At higher energies only cosmic ray data, with large uncertainties, were available. The issue on the exact growth of the total cross section with energy was delicate and unresolved. Was indeed impossible to discriminate among different theoretical models, since basically every form could fit the data. Moreover no data on pp were available above ISR energy. One of the goal of the TOTEM experiments was to perform very precise total cross section studies at the LHC energies, clarifying the asymptotical behaviour of the cross section.

At symmetric colliders[7] the measure of the forward elastic scattering is the most precise procedure to measure the total cross section through the optical theorem. In fixed target experiments the total cross section can be computed measuring the beam survival probability after the target and the machine luminosity $\mathcal{L}$[8]. Unfortunately fixed target accelerators cannot provide sufficient energy to explore the asymptotic behaviour of the cross section ($\sqrt{s} \propto \sqrt{E}$, where E is the particle energy). On the contrary, pp and $p\bar{p}$ cross section measurements have been carried out up to $\sqrt{s} = 1.8$ TeV in symmetric colliders ($\sqrt{s} = 2E$). The colliders drawback is that a direct measure of the beam after the target is not possible since the detectors can not be placed on the beam axis. The solution is the development of some special detectors, called *Roman Pot* (RP), placed far away from the interaction point (even hundreds of meters!) and moved as close as possible to the beam to measure the low$-t$ distribution of the elastic scattering and then perform an extrapolation to zero. However, for the same reason, a precise measurement of the luminosity is challenging. A work around can be used with a simultaneous measurement of both elastic (N_{el}) and inelastic (N_{ine}) events. Is indeed possible to relate N_{el} to the total cross section

$$\mathrm{d}N_{el}/\mathrm{d}t \Big|_{t=0} = \mathcal{L}\ \mathrm{d}\sigma_{el}/\mathrm{d}t \Big|_{t=0} = \mathcal{L}\frac{1+\rho^2}{16\pi}\sigma_{tot}^2, \tag{1.40}$$

[5] *Super Proton Synchrotron*, CERN.

[6] *Tevatron*, Fermi National Accelerator Laboratories, Chicago, USA.

[7] We will refer to *symmetric colliders* as *colliders* only, but they must not be confused with fixed target experiments.

[8] The machine luminosity is ratio of the interaction rate to the interaction cross-section

$$\mathcal{L} = \frac{1}{\sigma}\frac{\mathrm{d}N}{\mathrm{d}t}. \tag{1.39}$$

where in the second equality we use equation (1.13) and the optical theorem (1.19). The ρ parameter, defined as the ratio between imaginary and real part of the scattering amplitude

$$\rho = \frac{\mathrm{Re}\, A(s,t)}{\mathrm{Im}\, A(s,t)} \tag{1.41}$$

is a fundamental parameter but is not predicted by the theory. We will se later how ρ can be measured, while if not known a priori it can be only extrapolated from previous measurements. With the measure of N_{ine} is possible to get rid of the luminosity term ($\mathcal{L} = (N_{el} + N_{ine})/\sigma_{tot}$) and the relation (1.40) can be rewritten as

$$\sigma_{tot} = \frac{16\pi}{1+\rho^2} \frac{\mathrm{d}N_{el}/\mathrm{d}t \,\big|_{t=0}}{N_{el} + N_{in}}, \tag{1.42}$$

which represent the *Luminosity independent* cross section measurement method.

In figure 1.4 the $\mathrm{d}\sigma_{el}/\mathrm{d}t$ distribution obtained by the TOTEM collaboration at $\sqrt{s} = 7$ TeV is reported. Thanks to the experimental apparatus described in the next chapter we were able to measure elastic scattering down to $|t| = 5 \cdot 10^{-3}$ GeV^2 together with the inelastic cross section. The distribution is composed of three different data sets. The first diffraction minima is clearly visible from at $|t| \sim 0.5$ GeV^2. The measured differential cross-section can be well described with the parametrization

$$\mathrm{d}\sigma_{el}/\mathrm{d}t \;=\; \mathrm{d}\sigma_{el}/\mathrm{d}t \,\Big|_{t=0} \; e^{-B|t|} \tag{1.43}$$

in the highlighted $|t|-$ range. The parametrization is in accordance with the prediction of the Regge theory, with $B = 19.89 \pm 0.03^{stat} \pm 0.27^{syst}$ GeV^{-2} and $\mathrm{d}\sigma_{el}/\mathrm{d}t\big|_{t=0} = 506.4 \pm 0.9^{stat} \pm 23^{syst}$ mb. Moreover, compared to previous collider experiments at lower energies (fig.1.5), B rises steadily with the collision energy $\sqrt{s}$ as expected. No evidence for Coulomb-hadronic interference (which dominates at small $|t|$) is found in the analyzed $|t|-$ range and thus the fit can be used in the optical theorem and, with the inelastic rate measure, is possible to compute the total cross-section. For details about the inelastic events measurement we prompt the reader to [9]. For the ρ parameter the COMPETE[11] preferred-model extrapolation of $\rho = 0.141 \pm 0.007$ was chosen. The ρ parameter has been measured indirectly inverting equation (1.40) and using the luminosity measured from the CMS experiment. The result, even if affected by large uncertainties was compatible with the COMPETE prediction.

Almost the same procedure has been adopted for the measurements at $\sqrt{s} = 8$ TeV. In this case a direct measure of ρ has been carried out[12]. The measure has been done analyzing the very low$-|t|$ region below $5 \cdot 10^{-3}$GeV^2, where the Coulomb-hadronic interference region is found. In the interference region we can indeed model

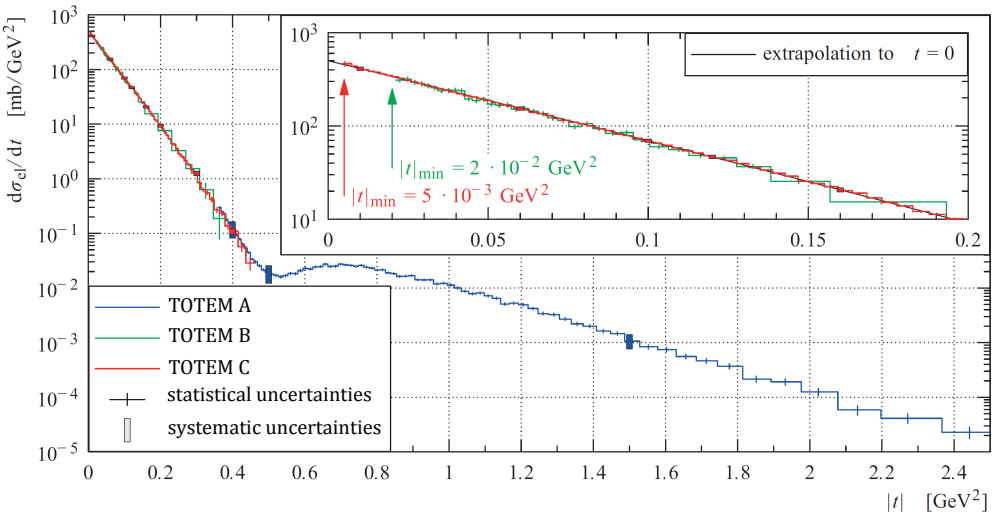

Figure 1.4: The elastic differential cross-section measurement by TOTEM. Three different data sets are showed. TOTEM A[7] spans $|t|-$values in the range 0.3-2.5 GeV^2 and shows the dip in the diffraction figure. The embedded figure provides a zoom of the region used for extrapolation (black line) to $t = 0$, showing the lowest $|t|-$values accessible in the analysis from [8](TOTEM B) and [6] (TOTEM C). Figure from [6].

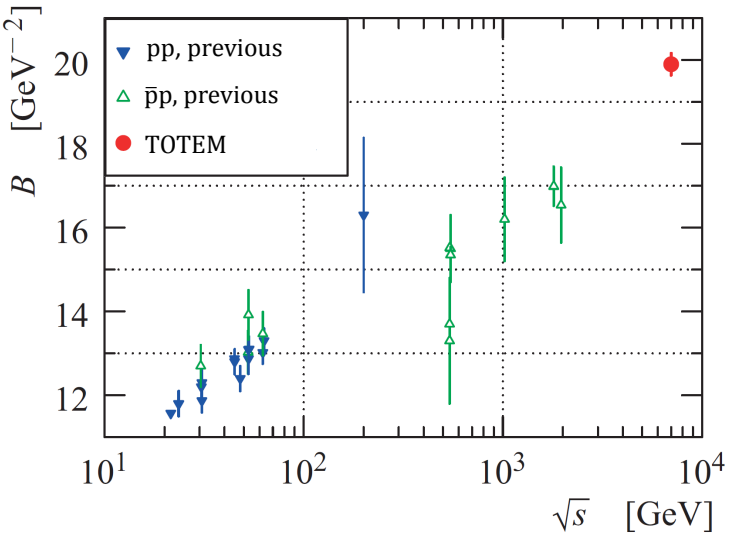

Figure 1.5: The elastic slope B as a function of the energy $\sqrt{s}$. For details on the previous measurements refer to [10]. Figure from [6].

the differential cross section as

$$\frac{\mathrm{d}\sigma_{el}}{\mathrm{d}t} = \frac{1}{16\pi s^2}\left|A_h + A_c e^{\pm i\alpha_{em}\Phi}\right|^2, \tag{1.44}$$

where A_c is the Coulomb amplitude, $\alpha_{em}\Phi$ is the relative Coulomb-hadronic phase and A_h is the hadronic amplitude parametrized as

$$A_h = s(i+\rho)\sigma_{tot}e^{Bt/2}. \tag{1.45}$$

In the low$-t$ region the terms $|A_h|^2$ can be neglected and the interference term became proportional to $(\rho+\alpha_{em}\Phi)$. The value obtained by TOTEM is in accordance with the prediction and represent the first direct measure at the LHC energy scale (fig. 1.6).

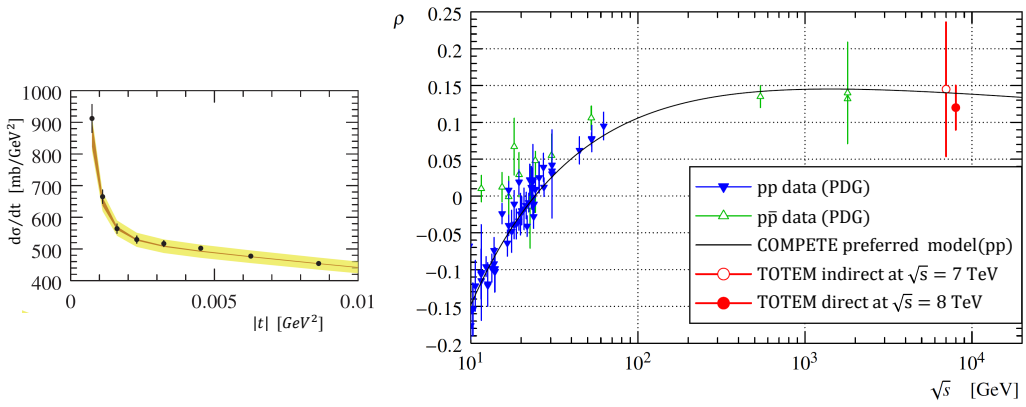

Figure 1.6: $\mathrm{d}\sigma_{el}/\mathrm{d}t$ in the Coulomb-Nuclear interference region (left) and energy dependence of the ρ parameter (right). ρ measures at lower energies are from[13]. The black curve gives the preferred pp model by COMPETE, obtained without using LHC data.

The TOTEM and other LHC experiments results, together with the previous measurements for total, elastic and inelastic cross sections are summarized in figure 1.7. The best fit proposed by the COMPETE collaboration shows a logarithmic dependence of the total cross section from the energy. To interpret the results in terms of the Regge theory we must refer to the work of Donnachie and Landshof[15]. In their paper they showed that the available data can be fitted with a power dependence

$$\sigma_{tot} = Xs^{0.0808} + Ys^{-0.4525}, \tag{1.46}$$

where X and Y are reaction independent free parameters. This is still valid with the LHC data. If we recall equation (1.36) we can claim that the pp total cross section

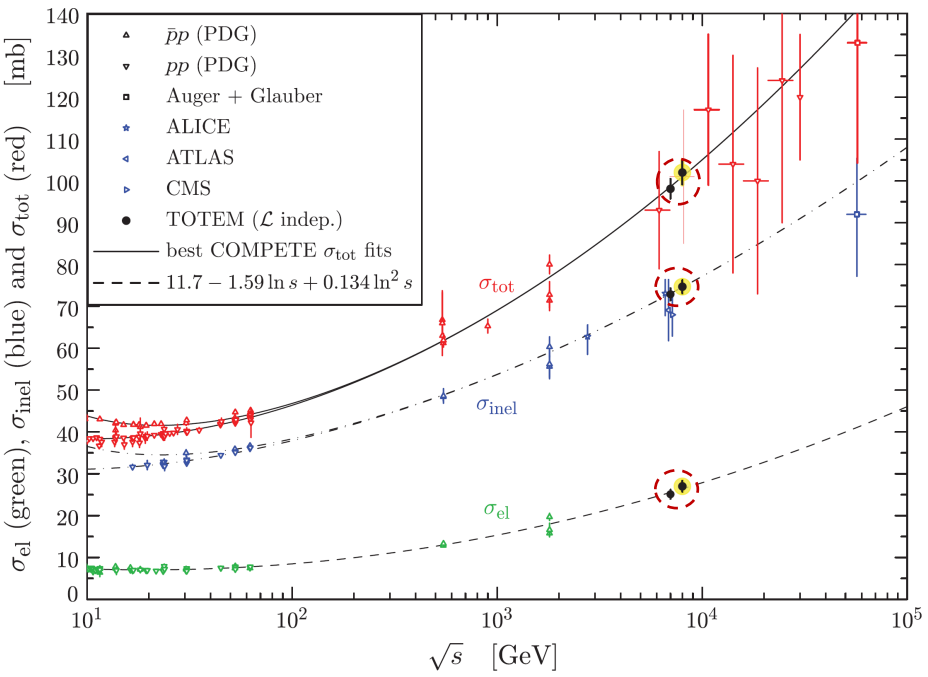

Figure 1.7: Compilation of the total, inelastic and elastic cross-section measurements: the TOTEM measurements are highlighted (dashed circles). The continuous black lines (lower for pp, upper for $p\bar{p}$) represent the best fits of the total cross-section data by the COMPETE collaboration [11]. The dashed line results from a fit of the elastic scattering data. The dash-dotted lines refer to the inelastic cross section and are obtained as the difference between the continuous and dashed fits. Figure from [14] and references therein.

get contribution from two Regge trajectories. The second term of equation (1.46) correspond to a trajectory with intercept $\alpha_{\mathbb{R}}(0) \simeq 0.55$ and is therefore compatible with a contribution of the mesonic trajectories reported in figure 1.3. The first term instead does not correspond to any known reggeon. This new special trajectory took the name of *soft pomeron* and presents an intercept $\alpha_{\mathbb{P}}(0) \simeq 1.08$. The pomeron is thus the dominant contribution to diffractive processes and, since diffractive processes are characterized by the exchange of vacuum quantum numbers, its quantum numbers are the same of the vacuum ($P = +1,\ C = +1,\ G = +1,\ I = 0,\ \xi = +1$). The value of the pomeron trajectory slope $\alpha'_{\mathbb{P}}$ was determined by fitting to the shape of the low$-t$ data at some fixed energy[16], determining $\alpha'_{\mathbb{P}} \simeq 0.25\ \text{GeV}^{-2}$. The linear pomeron trajectory is therefore

$$\alpha_{\mathbb{P}}(t) = 1.08 + 0.25t. \tag{1.47}$$

The pomeron incompatibility with the resonance trajectories leads to the conjecture that the pomeron corresponds to a Regge trajectory for gluonic states (bound state of gluons[9]), and most likely one describing the J^{++} glueballs. Glueballs are predicted by QCD as bound state with no valence quark content. QCD lattice calculation foresee a $J_z^{PC} = 0^{++}$ ground state and a 2^{++} state followed by a spectrum of exited states [17, 18]. Many articles (i.e. [19, 20, 21]) put in evidence that 2^{++} glueball predictions performed with lattice computation are compatible with the pomeron (fig. 1.8). In this picture diffractive physics processes will be domi-

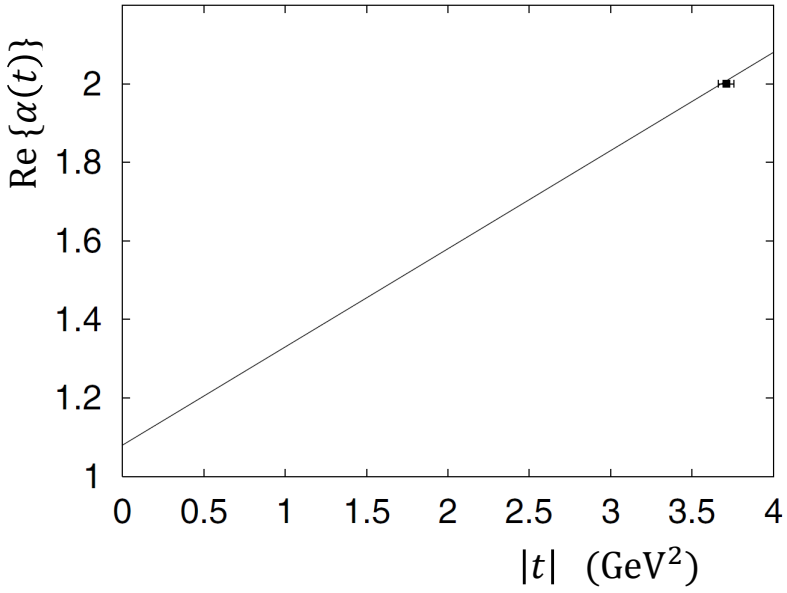

Figure 1.8: A 2^{++} glueball candidate[21], with the pomeron trajectory $\alpha_{\mathbb{P}}(t) = 1.08 + 0.25t$[16].

nated by glueballs exchange, making of diffractive physics an appealing candidate to search for them and some glueball candidates ($f_0(1500)$ and $f_0(1710)$) are indeed already been found at LHC. However the picture is far from being complete. For example the logarithmic growth of the total cross section will eventually violate the Froissart-Martin theorem (1.26). The limit is still far from being reached and is possible that the pomeron intercept can lower with the energy, giving a steady cross section. However further studies are needed to understand the true nature of the

[9]Gluons are elementary particles that act as the exchange particles (or gauge bosons) for the strong force between quarks, analogous to the exchange of photons in the electromagnetic force between two charged particles.

pomeron, and more question will arise in the next section.

Another hypothetical Regge trajectory is the *odderon*, thought to be the $C = P = -1$ partner of the pomeron. It existence has been postulated to explain the difference between the differential cross sections of pp and $p\bar{p}$ scattering. Up to now there is no compelling experimental evidence of the existence of the odderon.

1.4 The QCD pomeron

The fundamental theory of strong interaction is QCD and is thus natural the attempt to translate the soft pomeron in the QCD language. We have seen that the pomeron is supposed to be a glueball trajectory and shall not surprise if the first QCD model described the pomeron as a simple exchange of two gluons computed at the *leading order* (LO) in the strong coupling constant α_s (fig. 1.9). The $t-$channel two gluon exchange cross section is sometimes called the Low–Nussinov pomeron. The minimum number of gluons involved in the diffractive reaction is two, since scat-

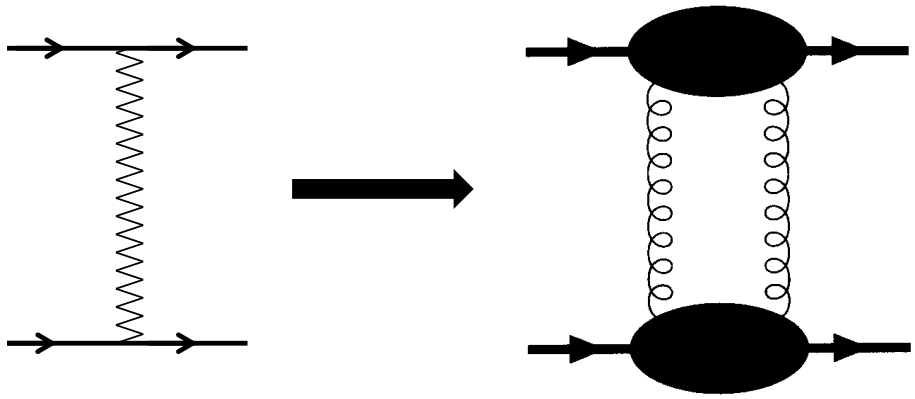

Figure 1.9: Pomeron evolution from Regge to QCD framework: the Low–Nussinov pomeron.

tering through single gluon exchange can not contribute to the pomeron structure. The gluon is indeed a colored[10] object whereas a diffractive event does not involves any color charge exchange by definition and so at least two gluons are needed to have a colorless object.

[10]According to QCD and the Standard Model (SM) of particle physics, quarks carry an SU(3) "color charge" which can be "red", "blue" or "green". The gluons carry a color-anticolor charge and can thus participate in the strong interaction in addition to mediating it. For this reason they can form bound system without valence quark, the glueball.

In pQCD the properties of the two-gluon exchange depends on the process energy, and does not have a universal character like the soft pomeron. Such properties are described in the high energy limit with the *Balitski-Fadin-Kuraev-Lipatov* (*BFKL*) equation[22, 23, 24] and the resulting exchange is called the *hard pomeron*. Hard pomeron can be described with the BFKL equation by fixing t and taking the pp center of mass energy to be large. In this limit the BFKL approach prescribes to compute the corrections to the two gluons exchange model at all orders in α_s. Since we work the large$-s$ limit, for each order we can retain only the leading logarithmic term in $\ln \frac{s}{|t|}$ and then sum up all contributions. This approach is called *leading logarithmic approximation* (LLA). The building blocks of the theory emerge already at the *next to leading oreder* (NLO), involving two-loop corrections: some example can be found in figure 1.10. If we cut the diagrams in the figure we can distinguish

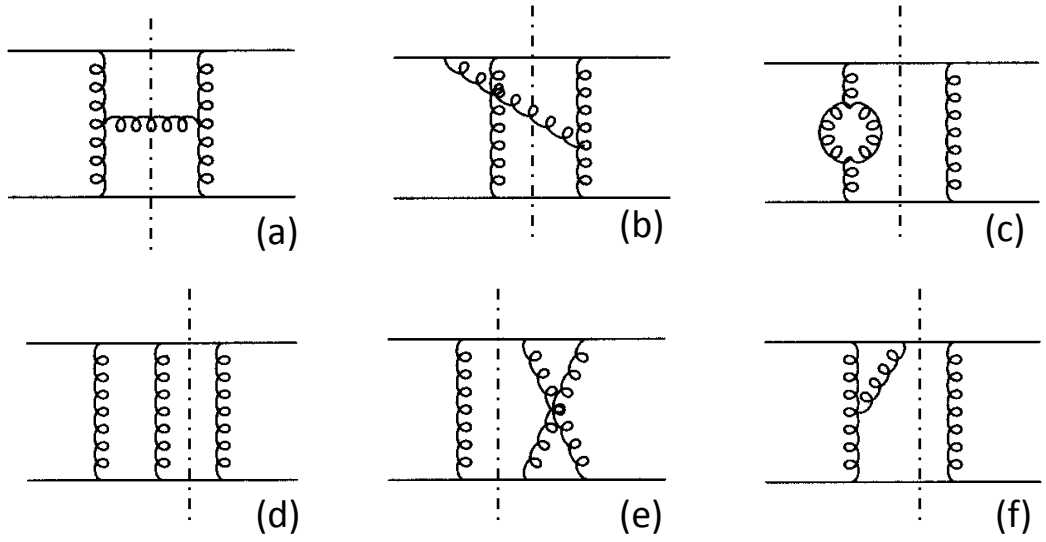

Figure 1.10: Sample of two-loop diagrams for the qq scattering. The dash-dotted lines represent the diagram cuts.

three different type of contributions:

- *self-energy* or *vertex* (i.e. graph (c),(f) in fig. 1.10),
- *real-gluon emission* (i.e. graph (a),(b) in fig. 1.10),
- *virtual radiative* (i.e. graph (d),(e) in fig. 1.10).

Luckily we have a simplification since self-energy or vertex corrections are not dominant in the LLA approximation and we can neglect them. Relevant corrections are instead provided by the real-gluon emission diagrams, that show a real gluon in the final state after the cut. Al this diagram contributions can be handled with the introduction of the *Lipatov effective vertex* $\Gamma^{\rho}_{\mu\nu}$, defined as

$$\Gamma^{\rho}_{\mu\nu}(k_1,k_2)=\frac{2p_{2\mu}p_{1\nu}}{s}\Big[\Big(\alpha_1+\frac{2\mathbf{k}_1^2}{\beta_2 s}\Big)p_1^{\rho}+\Big(\beta_2+\frac{2\mathbf{k}_2^2}{\alpha_1 s}\Big)p_2^{\rho}-(k_{1\perp}^{\rho}-k_{2\perp}^{\rho})\Big], \tag{1.48}$$

where for the gluon momenta we adopted the Sudakov parametrization

$$k_i=\alpha_i p_1+\beta_i p_2+k_{i\perp}. \tag{1.49}$$

The other relevant correction derives from the virtual radiative diagrams. Their effect can be modeled taking into account all the higher order contribution and it can be accounted replacing the gluon propagator with a new propagator $D_{\mu\nu}$ expressed as

$$D_{\mu\nu}(s,k^2)=\frac{-ig_{\mu\nu}}{k^2}\big(\frac{s}{\mathbf{k}^2}\big)^{\epsilon(t)}. \tag{1.50}$$

The Propagator show a Regge exponential dependence with trajectory $\epsilon(t)$ and is thus called *reggeized* gluon. The Lipatov vertex (big black dot) and the reggeized gluon (bold gluon) concepts are represented in figure 1.11.

By performing the calculation at order α^3 (NLO) of the two-gluon scattering amplitude we obtain the two main ingredients that describe high energy scattering in the leading $\ln(s)$ approximation: the reggeized gluon and and the new effective (Lipatov) vertex. Fadin, Kuraev, and Lipatov proved that the general diagram contributing to the high energy amplitude at the leading $\ln(s)$ level can be written as a sum over the produced gluons of the simple ladder-type diagram shown in figure 1.12*a*. In this diagram, each vertex is of the type (1.48), and each $t-$channel gluon is a reggeized gluon with propagator (1.50), while all the produced ($s-$channel) gluons are the regular gluons of the QCD Lagrangian.

The BFKL ladder put some constraints on the process kinematics, known as *Multi-Regge kinematics*. Adopting the Sudakov parametrization the multi-Regge regime corresponds to all transverse momenta being of the same order and much smaller than s

$$k_{1\perp}\simeq k_{2\perp}\simeq\cdots\simeq k_{n\perp}\ll s \tag{1.51}$$

and to a strong ordering of the longitudinal momenta which can be translated into a strong ordering in rapidity

$$Y_1\gg y_1\gg y_2\gg\cdots\gg y_n\gg Y_2, \tag{1.52}$$

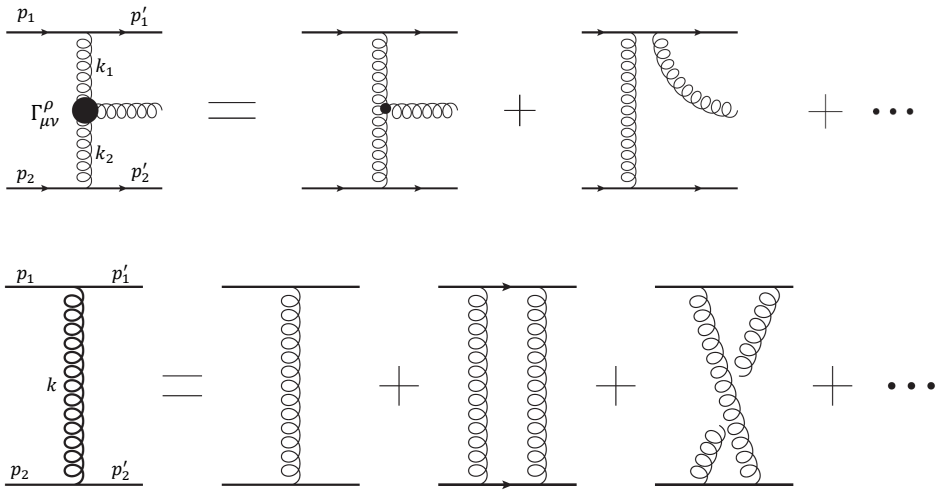

Figure 1.11: Main actors of BFKL approach. On top the Lipatov vertex, defined as the sum of all gluon emission diagrams. The triple gluon vertex is denoted by the smaller solid circle while the Lipatov vertex is shown by the larger solid circle. On bottom the reggezeid gluon (bold), representing the sum of all leading $\ln(s)$ corrections to the single-gluon exchange amplitude.

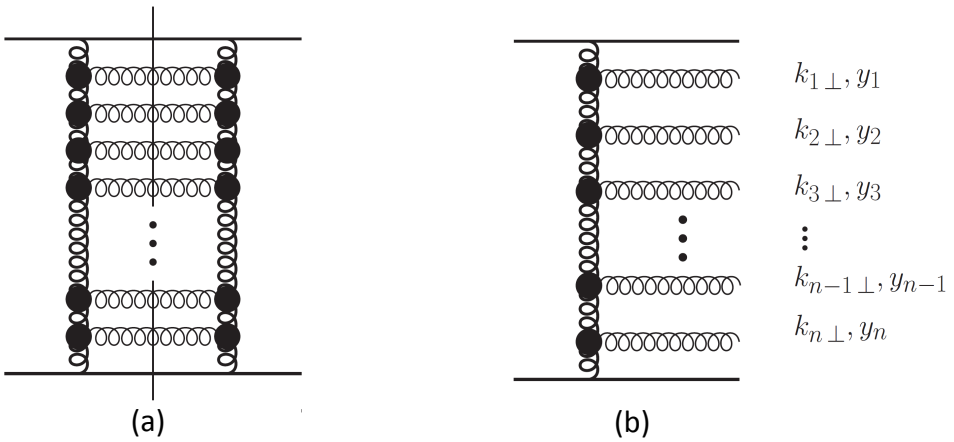

Figure 1.12: (a) Representation of BFKL pomeron as a ladder diagram with effective Lipatov vertices and reggeized gluons. (b) Scattering amplitude forming the gluon ladder. The produced gluons have multi-Regge kinematics.

where y_i is the rapidity of the $i-$th reggezeid gluon and $Y_{1,2}$ are the rapidity of the colliding particles. As a result the multi-Regge kinematics corresponds to the production of gluons uniformly covering the whole available rapidity interval. With such property, is thus possible to calculate the exclusive production cross sections for any given number of gluons in the multi-Regge kinematics using the BFKL approach.

Seems that we successfully translate the Regge pomeron in the QCD language, but a big issue arise when we try to compare the hard pomeron intercept, derived from the theory, to the soft, phenomenological intercept $\alpha_{\mathbb{P}}(0)$. It turns out indeed that the hard pomeron has an intercept $\epsilon_{\mathbb{P}}(0) \simeq 1.5$, not compatible with the soft trajectory of equation (1.47). That should not be surprising if we think to the different nature of the two objects. On one side we have a ladder of interacting reggezeid gluons, while in the other the pomeron is not a physical object, but something inferred from a successful parametrization of a large variety of data. It is still under discussion if the soft and hard pomeron are the same object or not. If they are the same object the actual difference may be due to a $t-$dependence of its intercept. The difference can resides in the non-perturbative structure of the pomeron that dominates at small $|t|$, which although being at present only vaguely known can be better understood through the studies of hard diffractive processes at LHC.

1.5 Hard diffraction

The study of hard diffractive processes, which combine high transverse momentum scattering characteristics with the typical features of diffraction (i.e. the presence of rapidity gaps) has become an hot topic of particle physics since they can be used to understand the structure of the proton and of the pomeron. The first model of hard diffractive physics by Ingelman and Shlein[25], was confirmed by the first observation (1988) of hard diffractive processes by the UA8 experiment at ISR[26]. One of the major contributions to the field was provided by the HERA elctron-positron collider at DESY[11], which investigated the feature of the *Deep Inelastic Scattering*[27] (DIS). DIS is the scattering of a lepton with an hadron at high momentum transfer, where the scattering angle of the outgoing lepton is measured:

$$l(\ell) + p(P) \to l'(\ell') + X(P_X), \tag{1.53}$$

where X is an undetected hadronic system (fig. 1.13a). HERA measurements show

[11] Deutsches Elektronen-Synchrotron, Hamburg, Germany.

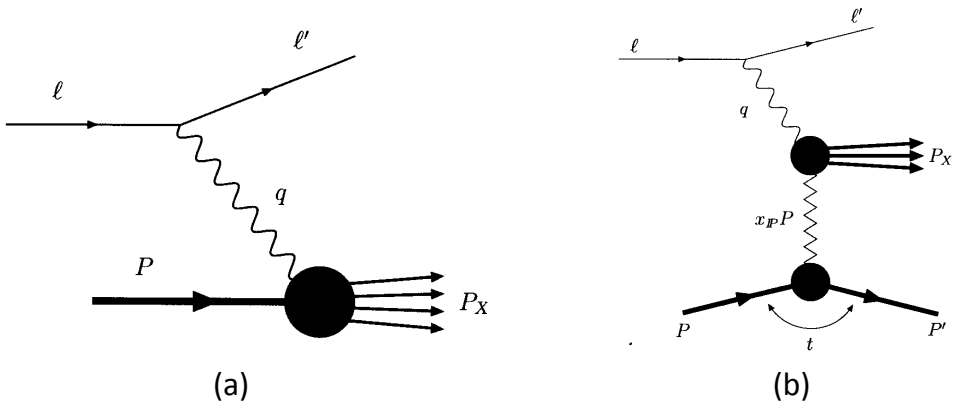

Figure 1.13: Deep inelastic scattering (a) and diffractive deep inelastic scattering (b) diagrams.

that in approximately 10% of DIS events the proton stay intact in the process

$$l(\ell) + p(P) \rightarrow l'(\ell') + p'(P') + X(P_X) \tag{1.54}$$

and the final state configuration shows the presence of large rapidity gaps between the scattered proton and the hadronic system X. This clear signal of no quantum number exchange between the virtual photon and the proton justifies the name of *Diffractive Deep Inelastic Scattering* (DDIS). In terms of Regge theory DDIS is described as the scattering between the virtual photon and a pomeron emitted by the proton (fig. 1.13*b*).

DDIS can be described introducing a set of kinematics variables:

$$x_B = \frac{Q^2}{2P \cdot Q}, \tag{1.55}$$

$$Q^2 = -q = -(\ell - \ell')^2, \tag{1.56}$$

$$y = \frac{P \cdot q}{P \cdot \ell} \simeq \frac{Q^2}{x_B s}, \tag{1.57}$$

$$\xi = \frac{(P - P') \cdot q}{P \cdot q} \simeq 1 - x_F, \tag{1.58}$$

where x_B is called the Bjorken x and x_F is the Feymann variable. x_B represents the fraction of the longitudinal proton momentum carried by the quark involved in the process. The variable ξ (often found in literature as $x_{I\!P}$) is instead the fraction of the proton longitudinal momentum carried by the pomeron. Cross section computation can be done in analogy with the DIS calculation[28, 29] leading to a differential cross section for the $\gamma^* p$ process described by

$$\frac{\mathrm{d}\sigma^D_{\gamma^* p}}{\mathrm{d}x_B \mathrm{d}Q^2 \mathrm{d}\xi \mathrm{d}t} = \frac{4\pi\alpha^2_{em}}{x_B Q^4}\left(1 - y - \frac{y^2}{2}\right) F_2^{D(4)}(x_B, Q^2, \xi, t), \tag{1.59}$$

where the quantity $F_2^{D(4)}$ is called *diffractive structure function* (the superscript 4 indicates the 4 parameters dependence). The key to investigate DDIS (and DIS) resides in the *factorization theorem*[30], which makes part of the dynamics accessible to perturbative QCD. The remaining non-perturbative quantity are embodied in the so-called *diffractive Parton Distribution Function* (dPDF), that can not be predicted by the theory, but can be extracted from measurements. It contains information about partons with small momentum fraction x of the proton that can only be obtained in diffractive processes. For DDIS the factorization theorem can be expressed as

$$\frac{\mathrm{d}F_2^D(x_B, Q^2, \xi, t)}{\mathrm{d}\xi \mathrm{d}t} = \sum_i \int_{x_B}^{\xi} \frac{\mathrm{d}f_i(x, \mu^2, \xi, t)}{\mathrm{d}\xi \mathrm{d}t} \hat{F}_2^i\big(\frac{x_B}{x}, Q^2, \mu^2\big), \tag{1.60}$$

where $\mathrm{d}f_i/\mathrm{d}\xi\mathrm{d}t$ is the dPDF of parton i, that is the probability to find in the proton a parton i carrying momentum fraction x, with the constraint that the proton survives the collision. QCD factorization prescribe that the dPDFs are the same for all diffractive processes. $\hat{F}_2^i$ can be perturbatively computed and it is proportional to the cross section $\sigma_{\gamma^* q}$ between the virtual photon and a free parton with momentum fraction x. The parameter μ is the factorization scale. Is important to point out that the coefficients $\hat{F}_2^i$ are model independent and are therefore the same of DIS. The only difference between DIS and DDIS lies in the parton distributions.

If we move to the Regge framework we can express the factorization theorem as

$$F_2^{D(4)}(x_B, Q^2, \xi, t) = f_{\mathbb{P}}(\xi, t) F_2^{\mathbb{P}}(\frac{x_B}{\xi}, Q^2), \tag{1.61}$$

where $f_{\mathbb{P}}$ is the *pomeron flux*, that is correlated to the probability of pomeron emission, and $F_2^{\mathbb{P}}$ is the *pomeron structure function*, proportional to the gamma-pomeron cross section $\sigma_{\gamma^* \mathbb{P}}$. Equation (1.59) can be rewritten as

$$\frac{\mathrm{d}\sigma^D_{\gamma^* \mathbb{P}}(\frac{x_B}{\xi}, Q^2)}{\mathrm{d}\xi \mathrm{d}t} = f_{\mathbb{P}}(\xi, t) \sigma_{\gamma^* \mathbb{P}}(\frac{x_B}{\xi}, Q^2). \tag{1.62}$$

The factorization theorem can be understood referring to the Feynman's parton model[31]. In the parton model hadrons are described as composite objects made of partons (quarks and gluons), held together by their mutual interaction, that can be described in terms of their virtual states. The factorization theorem embody the fact that if on one hand we are unable to calculate the structure of these states, on the other hand we assume that we do know how to compute the scattering of a *free* parton with, in our case, the virtual photon. This dichotomy of ignorance

and knowledge corresponds to our inability to compute perturbatively at long distances in QCD, while having asymptotic freedom at short distances. To justify this assumption let us think of how DIS (or DDIS) looks in the center of mass frame. The hadron is Lorentz contracted in the direction of the collision, and its internal interactions are time dilated. So increasing the energy leads to an increase in the lifetime of any virtual partonic states, while the time it takes the virtual photon to traverse the hadron get shorter. When the traversing time is much shorter than the hadron state lifetime the hadron will be in definite virtual state with a definite number of partons. Since partons does not interact during this time, each one will bring a definite fraction x (which probability is described by the dPDFs) of the proton momentum in the center of mass frame. In addition, when the momentum transfer is very high, the virtual photon cannot travel far. Then, if the density of partons is not too high, the photon will be able to interact with only one parton, making natural to consider the interaction of the virtual photon with the parton alone instead of the whole hadron.

One of the main goal of the QCD analysis of DDIS data is the extraction of the dPDFs. This is usually done by parametrizing the dPDF at some input scale Q_0^2 and then evolving it to other values. Usually two main evolution equations are used: the Dokshitzer-Gribov-Lipatop-Altarelli-Parisi (DGLAP)[32, 33, 34] and the already introduced BFKL. DGLAP is used for a wide range of Q^2 if the momentum fraction x carried by the parton is not too small. When indeed x became small and Q^2 is fixed the evolution is regulated by logarithms of the type $\ln(1/x)$ and the BFKL evolution equation is used instead. In figure 1.14 are reported the regions of validity for both evolution equations. Two regions are particularly interesting. For small photon virtuality we fall in the Regge area where we can test the factorization formula (1.61). The other important kinematical region is the *saturation* region. The structure function predicted by BFKL presents a steep rise that must eventually stop in order to preserve unitarity. This happens because when the momentum fraction carried by the partons decrease their number grows, and so the cross section. The *gluon recombination effect*, which is supposed to happen in the saturation region, foreseen that the interaction of partons became so large at small$-x$ that they start to recombine, leading to the modification of the BFKL evolution with a negative non-linear term that preserves the unitarity condition.

The generalization of DDIS results to hadron-hadron process is straightforward, resulting in the factorization of both vertices. The study of the dPDFs has thus been extended to the Tevatron energy range and now to the LHC. One of the hard

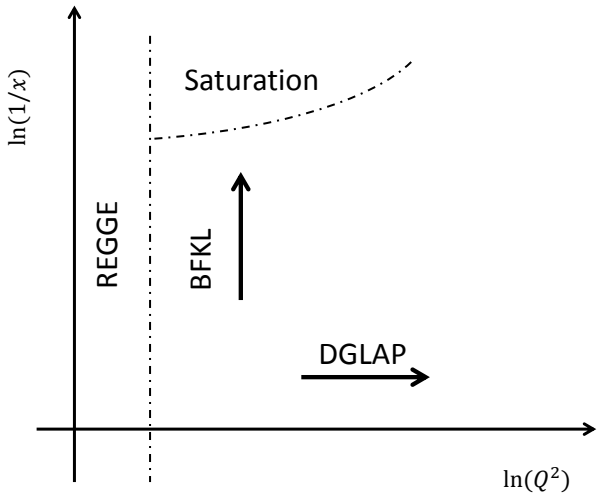

Figure 1.14: Kinematical region of validity for the dPDF evolution equations.

diffraction aspect still under investigation emerged exactly at Tevatron, related to the universality of the dPDFs for all diffractive processes. The measures preformed at Tevatron on single diffractive processes showed rates ten times lower then expected from the calculation based on the dPDFs determined at HERA. An explanation of this breakdown is based on the different initial states of HERA DDIS and Tevatron $p\bar{p}$ diffraction. In the hadron-hadron interaction the description is more challenging for the rescattering between spectator partons, where additional soft scattering between the two interacting hadrons can fill the rapidity gap and/or destroy the hadrons. The diffractive cross section is thus suppressed. The effect is quantified introducing the *gap survival probability* S^2[35, 36]. The dynamics of rescattering is still not completely understood. The data collected so far can be interpreted as an effect derived from multi-pomeron exchange[37] or can be explained using an affective non-linear pomeron trajectory[38], but also other models have been proposed (see [39] and references therein).

All the topics introduced in this chapter will be investigated in details with CMS-TOTEM detector, through the rich physics programs that we are going to describe in the next chapter. The main role will be played by CD processes (expecially DPE and photoproduction), where both soft and hard scales can be studied.

Chapter 2

The TOTEM Upgrade

The TOTEM upgrade for the special high-$\beta^\star$ run will be here described and the physics program, based on the TOTEM-CMS joint detector, outlined. The feasibility of the physics program has been tested on common data acquired by CMS and TOTEM during 2012. The TOTEM trigger upgrade, which make possible the common data taking and were I had an important role, is reported. The general description of the actual experimental apparatus and the analysis of the running scenarios that the TOTEM experiment will face will clearly put in evidence the need for the development of precise timing detectors, to be installed in the Roman Pot region ($\sim$ 200 m from the IP). Multiple technologies have been investigated, among which the diamond resulted as the best choice. The complete detector, from the sensors geometry to the readout strategy, is here introduced and represent the subject of my work. The detector, originally conceived only for the high-$\beta^\star$ upgrade, will be also employed on early stage of the CT-PPS upgrade project, as here discussed.

2.1 Introduction to the upgrade program

The TOTEM upgrade program is focused on the improvement of the study capabilities of the CD events described by (1.4), with common data taking with the CMS experiment. Both detectors share the same beam *interaction point* (IP) and common data taking has been already successfully tested at $\sqrt{s} = 7$ TeV during 2012, where a preliminary analysis for many relevant processes showed the feasibility of the physics program outlined in section 2.2. The data were collected and successfully merged, thanks to the upgrade of the TOTEM trigger, briefly reported in section 2.4.

The combination of the TOTEM and CMS detectors provides an exceptionally

large pseudorapidity coverage for tracking and calorimetry. The reconstruction of the central system X in the CMS detector give access to the study of *exclusive* CD reactions, where X is a well defined state, with a determined number and type of final state particles. The experimental apparatus actually installed is able to measure the four-momentum of X in the CMS detector (if all particles fall in the CMS acceptance region $|\eta| < 5.3$) and at the same time to track the two leading protons in the TOTEM Roman Pots (RP) stations. In such way is possible to overcome the problem of hadron-hadron colliders, where the initial state of the partons is not known since the leading protons escape undetected.

Multiple RP stations, vacuum vessels that can be equipped with a different types of detectors (sec. 2.3), are symmetrically placed at distance range $200 - 220$ meters from the IP, downstream LHC bending magnets. They are placed so far since the momentum loss of a leading proton is so small that it remains in the beam until the first bending magnet. The RPs can be inserted in the machine primary vacuum so that the hosted detectors are placed very close (few millimeters) from the beam axis. The detectors actually installed, better described in section 2.3, are silicon strip detectors that can tag and track the protons. The mass of X can be computed from the RP measurements as

$$M_X \sim \sqrt{\xi_1 \xi_2 s}, \tag{2.1}$$

where $\xi_{1,2}$ are the fractions of the proton longitudinal momenta lost in the interaction. Since $\xi_{1,2}$ are reconstructed from the proton tracks the LHC is effectively used as a proton spectrometer.

The central mass can be simultaneously computed from the particle flow in the CMS region and compared with M_X, resulting in a strong background rejection. Moreover is also possible to compare the transverse (p_T) and longitudinal (p_z) momentum between the central state and the scattered protons. All this crossed information can be used to study events with missing mass/momentum as well as check the rapidity gaps predicted by the $\xi_{1,2}$ measurements. The experimental apparatus is completed by the TOTEM T2 telescope, a tracking detector extending the acceptance to the forward region of pseudo-rapidity $5.4 < \eta < 6.5$. For that area no information from CMS is available, and the T2 coverage is crucial to study rapidity gaps and search for missing momentum or masses. In figure 2.1 is displayed an example of central diffractive three jet event recorded by TOTEM and CMS.

To conduct its wide physics program the TOTEM detector must be able to operate in multiple running scenarios characterized by different settings of the machine

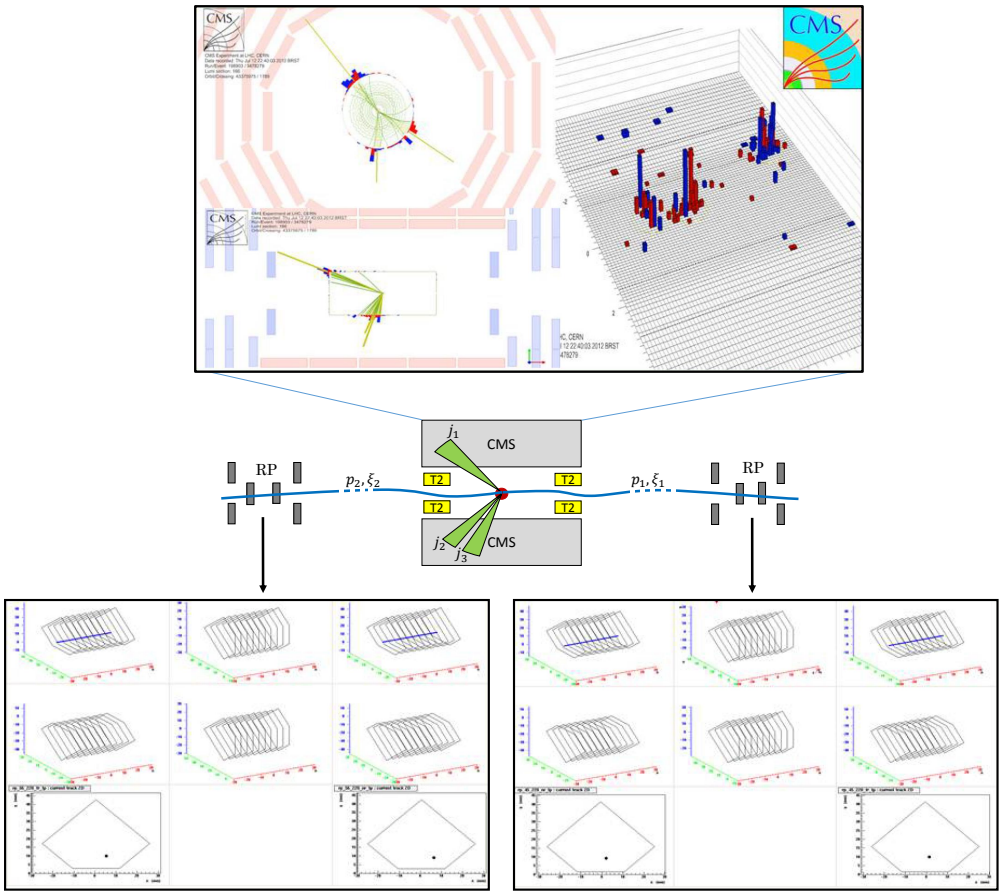

Figure 2.1: Central diffractive three jet event recorded by TOTEM and CMS in a $\beta^\star = 90$ m run at $\sqrt{s} = 8$ TeV. The upper part of the figure displays the central part of the event seen by CMS. The lower part displays the proton tracks in the TOTEM RPs.

magnets (that we will call hereafter *optics*). The acceptance and thus the physics that can be performed with the RP detectors is indeed deeply affected by the optics used (sec. 2.3.1.1).

The main running scenarios are summarized in table 2.1. The first scenario ($\beta^\star = 2500$ m) will make possible to perform TOTEM stand-alone measurements, measuring the total cross section at $\sqrt{s}$ =13 TeV and investigating the very low$-t$ spectrum of the differential elastic cross section. Apart from the measure of the ρ parameter at higher energy it will be possible to observe any anomalous $t-$distribution, that may lead to important discoveries about the odderon. However with this op-

$\beta^\star$ [m]	Emittance ϵ_N [μm rad]	Population [10^{11} p/b]	Bunches	μ	Lumi [$\mathrm{cm^{-2}s^{-1}}$]	Int.Lumi/day
2500	2	0.7-1.5	2	0.004-0.02	$(1.2-5.6)\cdot 10^{27}$	$(0.1-0.5)$ $\mathrm{nb^{-1}}$
90	2	0.5-1.5	156	0.06-0.5	$(1.3-12)\cdot 10^{30}$	$(0.1-1)$ $\mathrm{pb^{-1}}$
90	2	0.5-1.5	1000	0.06-0.5	$(0.9-7.7)\cdot 10^{31}$	$(0.8-7)$ $\mathrm{pb^{-1}}$
0.5	$1.9-3.75$	1.15	~ 2600	$19-34$	$(0.8-1.3)\cdot 10^{34}$	$(0.7-1.1)$ $\mathrm{fb^{-1}}$

Table 2.1: Expected running scenarios at $\sqrt{s} = 13$ TeV, with their respective ranges of pile-up μ and daily integrated luminosity. The normalized emittance ϵ_N is a measure of the beam divergence in the IP.

tics, characterized by an extreme value of the *amplitude function*[1] $\beta^\star$, the LHC will provide a very low luminosity. For this optics no upgrades are needed to the current setup and we will not discuss it further in this work.

To perform detailed studies of hard and/or exclusive diffractive processes (sec. 2.2), with cross sections down to O(pb), higher luminosity is needed. The measurements will be carried out in special runs with $\beta^\star = 90$ m, that we will call *high-*$\beta^\star$ runs, where protons with any ξ can be measured in the RPs (and so any M_X) as long as their $|t|$ value is ≥ 0.04 GeV^2. Processes characterized by even lower cross section O(fb), like high mass central diffraction, will instead be studied by operating continuously with the standard LHC optics ($\beta^\star = 0.5$ m). In this condition the common CMS-TOTEM detector will have access to very rare processes but the RPs acceptance for both protons will be limited to central masses $M_X > 300$ GeV. The high$-\beta^\star$ and the standard optics can thus be regarded as complementary.

The special high$-\beta^\star$ optics can be provided by the machine for only few days each year, and it is mandatory to push the luminosity to the maximum achievable value since some studies will require to collect an integrated luminosity[2] of 100 $\mathrm{pb^{-1}}$. In the LHC the protons are collected in packets (generally called *bunches*) of $\sim 10^{11}$ particles. Higher number of events can be collected by rising the number of bunches

[1]The amplitude function at the interaction point ($\beta^\star$) is often referred as the distance from the focus point where the beam width is twice as wide as at the focus point. Lower values of $\beta^\star$ leads to a less focused beam and thus to lower luminosity, but also to lower uncertainty on the proton trajectories prior the collision.

[2]The integrated luminosity $\mathcal{L}_{int}$ is related to the luminosity $\mathcal{L}$ though the relation

$$\mathcal{L}_{int} = \int \mathcal{L} \mathrm{d}t \tag{2.2}$$

and is used to quantify the amount of events generated by the accelerator.

or the population of each bunch. From table 2.1 we see that a maximum luminosity of ~ 7 pb^{-1}/24h is reached with 1k bunches with a mean population of $\sim 1.5 \cdot 10^{11}$ protons.

Although this value is enough for our scope, in this scenario we will have to deal with a large *pile-up*. During the collision of two bunches multiple independent *pp* interactions may indeed occur. The mean number of interactions for bunch crossing μ rise almost exponentially with the bunch population, as showed in figure 2.2 (left). While CMS can reconstruct the *primary vertex*[3] of each *pp* interaction (as long as

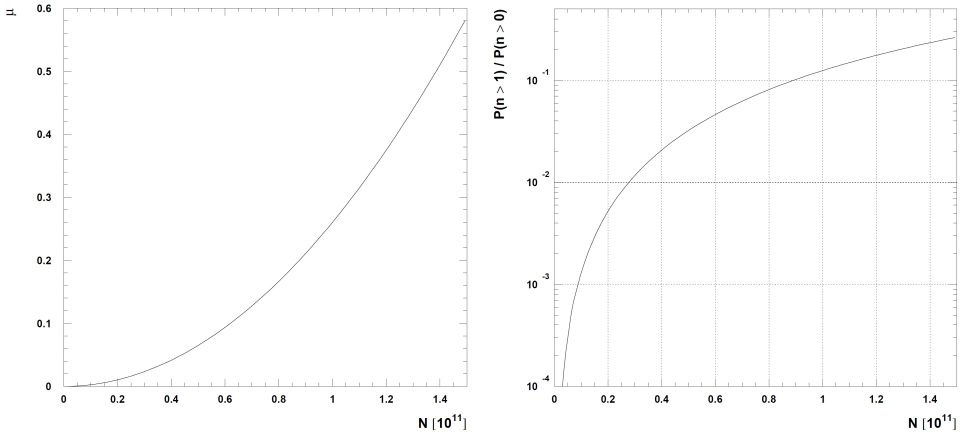

Figure 2.2: Pile-up w.r.t the bunch population for $\beta^\star = 90$ m. On the left the mean number of interactions μ per bunch crossing. On the right the conditional probability, $P(n > 1)/P(n > 0)$.

particles are generated in its acceptance region) and assign each detected particle to the right vertex (with the limitation reported in sec. 2.3.4), the same is not possible with the RPs, due to their position. In this case when more than one event happens in the same bunch collision (events pile-up) we will not able to disentangle the interesting process from the background. The contamination of the data can be computed with the conditional probability to have more than one event when at least one is happened $P(n > 1)/P(n > 0)$, reported in figure 2.2 (right). The data collected in 2012 showed that already $\mu \sim 0.05$ leads to difficulties in selecting a clean sample of central diffractive events. With the actual experimental apparatus a maximum integrated luminosity of ~ 1 pb^{-1}/24h can thus be supported, not enough.

To overcame this limitation an upgrade program is ongoing[40] (sec. 2.5), which

[3]the point where the *pp* interaction took place.

foreseen the installation of additional RP stations equipped with high precision timing detectors. Measuring the TOF of the leading protons will make possible the reconstruction of the $z-$coordinate of the primary vertex and assign the protons to the right vertex. The resolution needed for the high $\beta^\star$ upgrade is $\sim$ 50 ps. Even if the data taking will involve both TOTEM and CMS, this upgrade program is carried out only by the TOTEM collaboration. We will often refer to it as the high-$\beta^\star$ upgrade or, for reasons that will became clear later on, *vertical upgrade*. Different solutions for the timing have been considered, among which the diamond technology has been the preferred one. The vertical upgrade is the motivation of the development of the diamond detector described in this work, and we will focus on it in the next sessions.

The pile-up issue is even more dramatic in the standard runs, where $\mu > 20$ will be reached. For this purpose a joint TOTEM-CMS upgrade project has been developed, that will lead to the construction of the CT-PPS[41]. The upgrade involves both timing and tracking. The timing resolution required from the project is at least $\sim$ 30 ps, but the optimal value is $\sim$ 10 ps. Even if not conceived for the CT-PPS, given the good results obtained and the advanced development stage, our diamond detector will be used in an early stage of the CT-PPS upgrade, with the goal to investigate some recently hints for new physics seen by the LHC experiments. The physics motivation and the upgrade strategy for CT-PPS will be discussed in section 2.6.

2.2 Physics program

The physics topics covered by the high$-\beta^\star$ runs will span multiple fields, here summarized:

- spectroscopy of CD low mass resonances and glueball states.
- exclusive production of $c\bar{c}$ states.
- *Beyond Standard Model* (BSM) physics searches, via missing mass or momentum signature.
- studies of exclusive ultra-pure gluon-gluon jets and hard diffractive physics.

As discussed in the previous chapter diffractive processes are regarded as a golden channel to search for glueballs. In particular the selection rules on J^{PC} and the absence of valence quarks, make of CD the best candidate to investigate. Scalar

and tensorial f_0 states in the mass range $1.5 - 2.5$ GeV, where glueball candidates have been identified, have cross sections and masses that can be exploited with the special high-$\beta^\star$ runs. To check the hypothesis of a glueball, is possible to study the exclusive cross sections as well as its branching ratios and decay modes [17, 42].

Mass distributions for low mass resonances have been measured for exclusive CD $\pi^+\pi^-$ events up to few GeV in fixed target experiments[43] and, at lower center of mass energy, at colliders[44, 45, 46]. In all this experiments deconvolution techniques had to be applied during the data analysis due to the limited mass resolution or, when proton tagging was not possible, to the large background. In the CMS-TOTEM experiment, the possibility to tag the proton and the excellent mass resolution of $\sim 20 - 30$ MeV for the final charged particles will clearly identify the resonance characteristics without further steps. Events with two protons in the RPs and only two or four final state charged particles with zero net charge will be selected for the analysis. Then a selection based on p_T compatibility among the central system and pp system will be performed and enforced with the request of $\xi_{1,2} \sim 0$, as expected in the case of low mass production $M_X < 10$ GeV. In the sample already analyzed about 1000 $\pi^+\pi^-$ were identified, together with few tens of $\rho\rho$ and $\eta\eta$ candidates, requesting that the two $\pi^+\pi^-$ combinations to be compatible with the ρ or η masses. Increasing the statistics we expect to extend the analysis also to six and eight charged particles final states. The distribution of the final state particles and the relative scattering angle between the two protons can provide information about the spin of the resonance. Our sensibility as been confirmed in the analyzed data sample.

Based on the available data set we expect that with an integrated luminosity of ~ 1 pb^{-1} we will be able to determine the spin of the resonance and to perform a first estimation of cross-sections and branching ratios. For more precise measurements, as required in the case of glueball studies, the integrated luminosity must be extended to ~ 10 pb^{-1}. The results will give a relevant contribution in the understanding of gluon systems at low$-x$ and the nature of the soft pomeron.

The mass of $c\bar{c}$ states (i.e. χ_c) is high enough to allow the use of pQCD [47, 48] and are therefore considered an excellent playground to study QCD and the role of the hard pomeron.

In figure 2.3.*a* the leading order description of the χ_c central production as modeled in the previous chapter is reported. The process is already been studied at

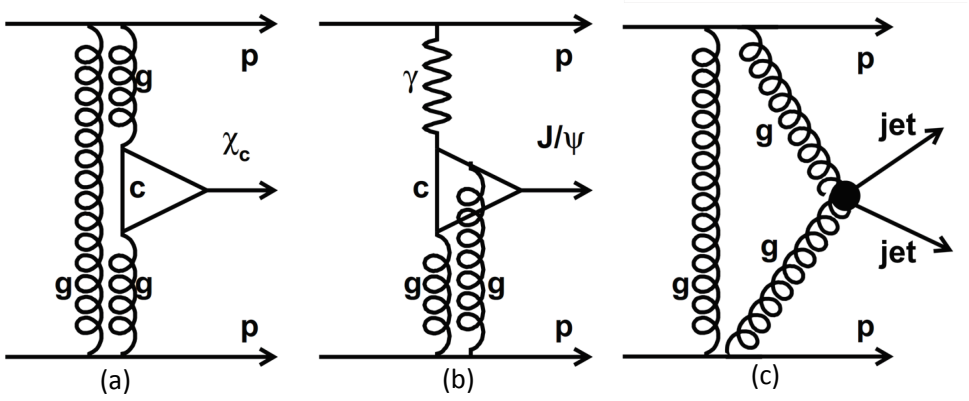

Figure 2.3: Leading order diagrams for exclusive CD production of χ_c (a), J/Ψ (b) and dijet (c).

CDF[4][49] and at LHCb[5][50], and a few candidates are present in our data sample. In both previous studies the observation was made through the decay channel $\chi_c \to J/\Psi\gamma$. The distinction among different χ_c states was made difficult for the low energy resolution on the photon (CDF) and for the proton dissociation background (both).

Other charmed processes of high relevance are the exclusive J/Ψ and $\Psi(2s)$ productions, already observed at LHC in the $\mu^+\mu^-$ channel[51, 52]. This states are mainly created through photo-production (fig. 2.3.*b*) and they allow a direct comparison with the measurements of DDIS made at HERA at lower center of mass energy. Moreover the proton tagging allows to determine the 4−momentum spectrum of the J/Ψ meson, that is predicted to be modified by the odderon[53]. The CMS-TOTEM detector will have the opportunity to test this model and maybe identify the odderon.

Based on the collected data sample and the measure of LHCb we can estimate that $\sim$ 10 pb^{-1} will be sufficient to significantly enhance the precision on the cross sections and branching ratios of the χ_c in the decay channels with charged particles only. This will allow to improve the experimental data and test model predictions[54]. For the photo-production processes an higher statistics of about $\sim$ 100 pb^{-1} is needed.

[4] *Collider Detector at Fermilab*, Chicago, USA
[5] *LHC Beauty experiment, CERN*

Exclusive CD jet production $pp \to p \oplus jj, jjj \oplus p$ is a field that the detector can investigate as well, in order to shade some light on the proton and pomeron structures. Those hard diffractive events can be used to measure the PDF of the proton and, at the same time, the experimental study of the rapidity gap survival probability S^2 will open a new modality on the study of multiple soft parton interactions (like hard diffraction re-scattering). The jet production through diffractive channel is of great interest because they will be pure gluon jets $\sim 99\%$ of time[112], without quark jets contamination. At leading order in QCD, they can be modeled as a two gluon exchange (fig. 2.3.*c*).

The first observation of exclusive jet production was made at Tevatron[55], and triple jet candidate discovered in the CMS-TOTEM data has already been anticipated in figure 2.1. In the special high-$\beta^\star$ runs we will be able to study dijet with transverse energy[6] $E_T > 20$ GeV at any M_X. With 100 pb$^-$1 a sample of $\sim$100K events with $M_X > 60$ GeV is expected. The data will make possible the study of the azimuthal difference $\Delta\phi$ between the colliding protons, the cross section dependence from M_X and the $t-$distribution of the protons, providing a strong test for different models[56, 57].

In the hypothesis that new physics BSM couples mainly or exclusively to gluons, the TOTEM detector can extend the study to processes that may be escaped the detection from general purpose experiments. The missing momentum $\not{P}$ can be computed from the difference between the sum of the proton momenta and the sum of of the momenta of the particles in the central detector. Moreover the rapidity gaps $\Delta\eta_{1,2} = -\ln \xi_{1,2}$ predicted by the protons $\xi_{1,2}$ measurement in the RPs can be verified with the T2 telescope.

In this framework two main topologies of analysis can be exploited. The first is the search for events characterized by particles in T2 violating the predicted rapidity gaps. At present no candidates have been found in the available data set and the large SD pile-up and beam halo[7] background make this search particularly challenging. Stronger BSM signals can be extracted analyzing events where the missing momentum points to a region covered by the CMS+T2 detectors but no charged particles or energy deposit are observed. In this case a cut on the rapidity gaps must be used, to ensure that particles with $|\eta| < 6.5$ are not allowed by the rapidity

[6]The transverse energy is defined as $E_T = \sqrt{m^2 + p_T^2}$, where p_T is the transverse momentum.

[7]Beam halo events are events generated by peripheral particles in the bunch that hit against machine elements, usually collimators.

gaps predicted with the proton measurements (fig. 2.4). Candidate events with

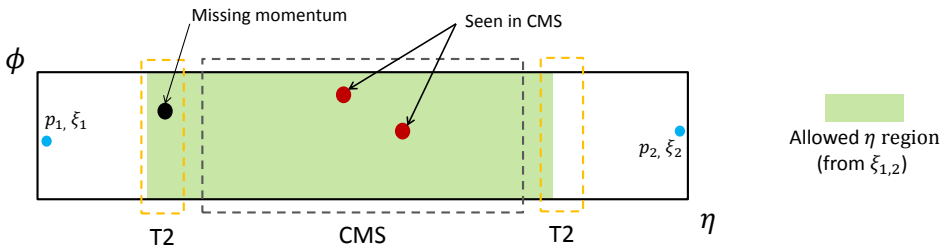

Figure 2.4: Example of BSM search. The allowed η region for the central particles is reconstructed from the $\xi_{1,2}$ measured on the RPs, and a cut is applyed to ensure that region is fully instrumented. In the example the missing momentum points to an area of the T2 detector where no particles have been observed.

missing mass have been identified but their number is compatible with the background estimation, that needs a better modelization. If we want to search for new physics with O(pb) cross sections an integrated luminosity of ~ 100 pb^{-1} is required.

2.3 The experimental apparatus

The LHC[62] is a synchrotron where protons or Pb ions can be accelerated. This synchrotron consists of two rings where a deep vaccum ($\sim 10^{-11}$ mbar) is made. The rings have a circumference of 27 km and are located 175 m underground in the Swiss-France border near Geneva. Inside the rings two counter-circulating particle beams are accelerated by radio frequency cavities and controlled by means of over 1500 superconductive magnets[63]. The LHC magnet coils are made of niobium-titanium cables which are cooled down to 1.9 K with superfluid helium.

The particles inside the beam are grouped in packets or bunches. Each beam circulating in the LHC contains up to ~ 2808 bunches of protons, with a maximum of $1.5 \cdot 10^{11}$ protons/bunch. The bunches are squeezed and brought to collision in four *Intraction Points* (IP). The minimum interval between two collisions is 25 ns (40 MHz) and the revolution frequency of the beam is ~ 11.3 KHz, with a machine peak luminosity of $\sim 10^{34}$ cm^{-2}s^{-1}. All the LHC experiments are located in the proximity of an IP (fig. 2.5): TOTEM and CMS share the IP5, on the opposite side of the ring w.r.t the CERN main complex.

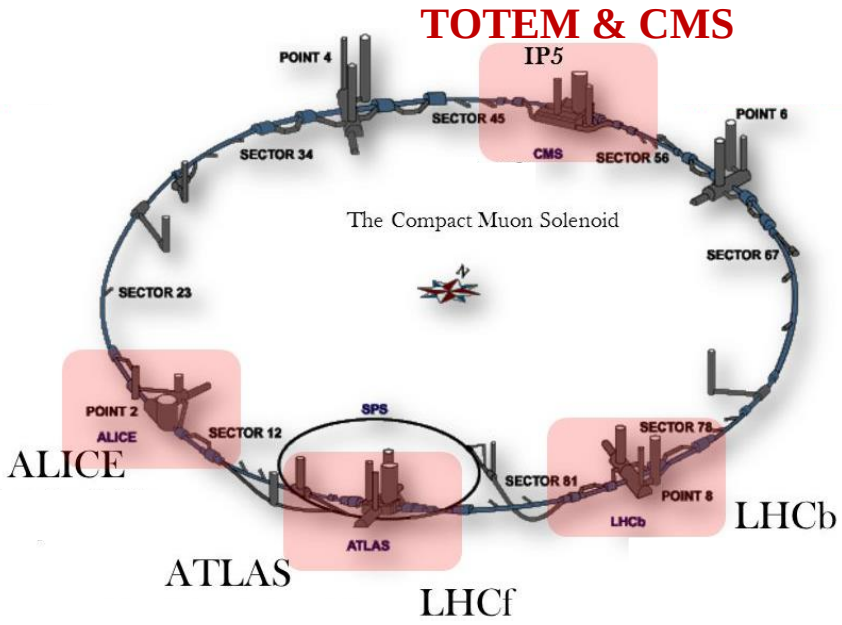

Figure 2.5: Scheme of the Large Hadron Collider. The IP5, shared by TOTEM and CMS experiments, is on top.

The first collision took place in March 2010, with a pp center of mass energy of $\sqrt{s} = 7$ TeV, later raised to 8 TeV in 2012. After a long shutdown for planned repairs and machine upgrades the LHC was restarted in 2015 with $\sqrt{s} = 13$ TeV, with the aim of reaching the original goal of 14 TeV.

This energy is reached thanks to a chain of accelerators, each one boosting the energy of the particles before injecting the beam into the next machine in the chain. Protons, obtained by ionizing hydrogen gas and extracted with an electric field, are first accelerated by the linear accelerator (LINAC2) up to 50 MeV. They are then injected in the PSB+PS system (*Proton Synchrotron Booster + Proton Synchrotron*), where they reach an energy of 26 GeV. The last pre-acceleration stage is performed in the SPS (*Super Proton Synchrotron*) that brings the particles to the LHC injection energy of 450 GeV. When the LHC is filled it can (hopefully) operate for more than 10 hours before it needs to be refill. All this pre-accelerators are not used only for the LHC but provide beam for a huge number of experiments requiring lower energy and luminosity, and are also employed by the CERN test-beam facilities. In my work I made extensive use of the PS and SPS beams indeed.

The TOTEM[64, 65] experiment is designed to detect with high efficiency the very forward particles generated in pp collisions. TOTEM is composed of three

different types of detectors located symmetrically on both side of the IP5. Figure 2.6 shows a drawing of one section of the CMS detector where one arm of the TOTEM T1 and T2 detectors are located. They are called the *inelastic detectors*,

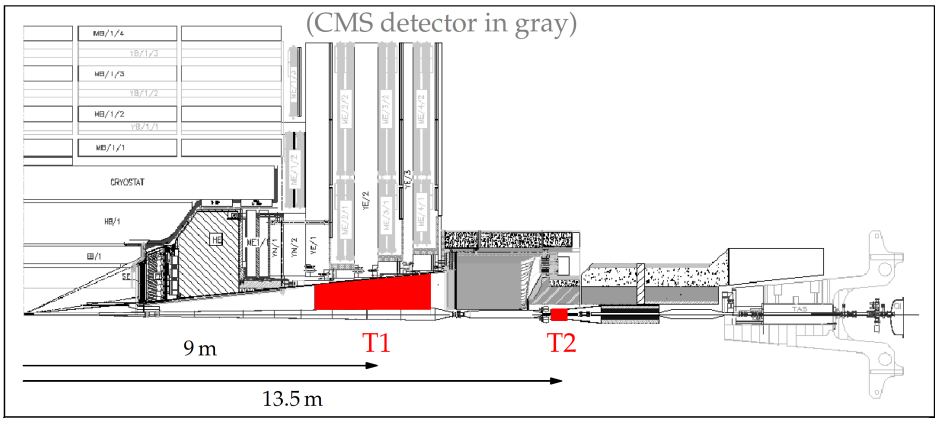

Figure 2.6: Drawing of the TOTEM-CMS detectors in the region close to the IP. The T1 and T2 detectors are highlighted. The TOTEM Roman Pots are not displayed being located at more than 200 m from the IP.

since their scope is the detection and tracking of the forward particles produced in inelastic processes. The detectors devoted to the measures on the leading protons, placed in the Roman Pots, are located much further from the IP5, in the region around $200 - 220$ meters.

2.3.1 The RP and the tracking detectors

The detection of very forward protons is performed in movable beam insertions, called *Roman Pots* (RP). RPs have been first employed at the ISR[66] in 1970 and in later colliders like SPS, TEVATRON, and DESY. The RP is basically a secondary vacuum vessel, hosting some type of detector, that can be moved into the primary vacuum of the machine through vacuum bellows. In this way the inner detector is physically separated from the primary vacuum, preserving any uncontrolled out-gassing from the detector to contaminate the primary vacuum. The RPs are usually retracted during the machine filling and stay in *garage* position, where the collimators protect them from accidental beam lost. When a stable beam condition is reached they can be moved out from the garage and the detector can thus approach the beam down to few millimeters, which allows to detect protons scattered at very low angles. To avoid unessential material near the beam (we don't

want to use the RP as a collimator!) a thin window is created in the RP in proximity of the beam. A liquid Helium cooling is needed for the detector since it will operate in vacuum. Multiple RP stations are installed in the region $\sim 200-220$ m from the IP, on both sides. The exact location will be presented at the end of the chapter, when the configuration will be much more clear.

The standard RP station is composed by two units, called *near* and *far*, about 4 m distant. Each unit is formed by three RPs, two of them approaching the beam vertically from above (*top vertical*) and below (*bottom vertical*) the beam axis, while the third one approach the beam horizontally (fig. 2.7). Each unit is completed with

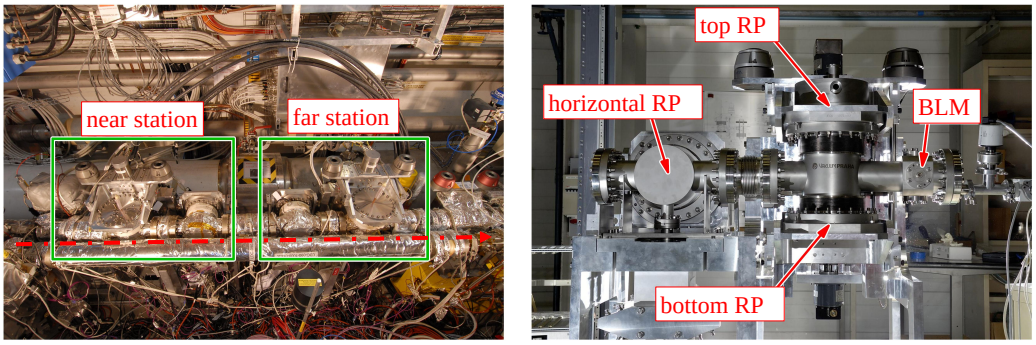

Figure 2.7: On the left a picture of one RP station inserted at 220 m from the IP5. The two units are highlighted. On the right one unit before the installation, where the three RPs are marked. The Beam Loss Monitor (BLM), downstream the RP unit, is essential during the alignment procedure.

a *Beam Loss Monitor* (BLM), that is used to detect the number of protons that exit from the beam (mainly scattered from the RP, when inserted). When a new optics is used for the first time an alignment procedure is needed to search the exact location of the beam. The alignment is performed approaching the RP until an high flux of particles is seen in the BLM, meaning that the RP is "touching" the beam. The distance of the RP from the beam is often expressed in units of the beam transverse size σ_{beam}. Usual working condition are in the range $10-15$ σ_{beam} (few millimeters).

Up to now all RP stations involved in real data taking has been equipped with a set of 10 planes of edgeless planar silicon strip detectors mounted in back to back configuration (fig. 2.8.*a*). The resolution of the sensor is 10 µm. The detectors are special silicon detectors characterized by an edgeless technology, where the physical edge of the detector is terminated with a *Current Terminating Structure*. With this technology the potential applied to bias the device is applied to the cut edges through a guardring surrounding the whole sensor. This external guardring collects the

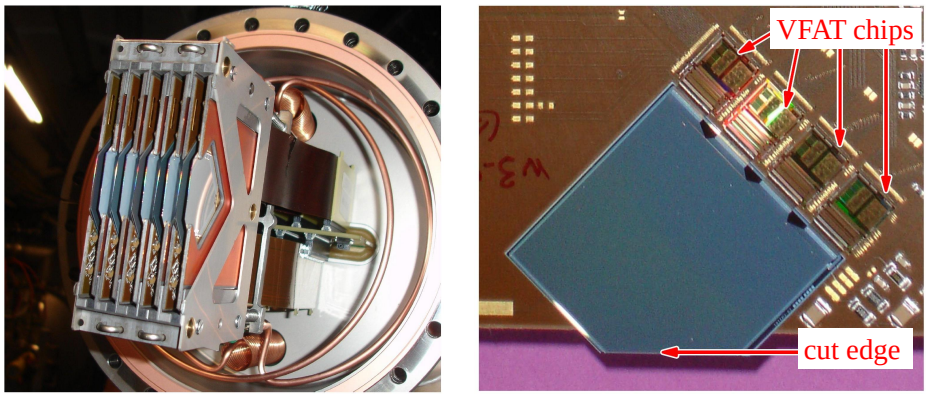

Figure 2.8: (a) The ten planes of strip edgless detector actually installed in the RP. (b) Front picture of one sensor, surrounded by the VFAT[67] chips used for the readout.

leakage current generated from the imperfections of the cut, preventing its diffusion in the surrounding areas of the detector. This expedient is necessary to extend the sensitive area as close as possible to the beam. In TOTEM strip detectors the unsensitive area is limited to the first 50 µm from the cut edge. The detector is readout by 512 strips with a 66 µm pith, oriented at 45° with respect to the edge close to the beam (fig.2.8.*b*).

Due to the back to back configuration the strips of each couple of sensors are perpendicular, allowing a total of maximum five position measurements from a passing particle. However, in case of simultaneous passage of two particles, *ghost* signals (fake signals introduced by the combinatorial) appear. This problem, not important in previous TOTEM measurements, performed at lower luminosity with a very low track multiplicity in the RPs, will became a real issue in the next future. The solution adopted is to tilt one of the RP units in the station located at 210 m from the IP (fig. 2.9). In this way is possible to discriminate the ghosts from the real tracks, since the strips of the two units are no more aligned. Already with an angle of 8°, the multi-track events can be resolved, given a multiplicity below 5 tracks. As I will show later in section 2.5 events with more than 5 tracks are extremely rare. The tilted RP unit are already installed and ready for operation.

In figure 2.10.*a* we can see the inner RP box, going inside the beam pipe, with the thin window to reduce the beam scattering. The size of the stainless steel box is $50 \cdot 124 \cdot 105$ mm^3, with 2 mm thickness wall except in window region where the thickness is reduced to only 150 µm. Those dimensions define the size of the

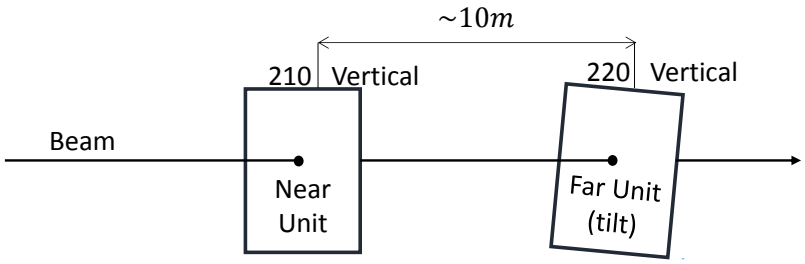

Figure 2.9: Scheme of the RP station with a tilted unit located at 210 meters from the IP.

detectors that can be hosted. When all three detectors of one unit are inserted they wrap around the beam as shown in figure 2.10.*b*, with an overlap region. For each detector the axis u and v are defined, parallel to the strip orientation.

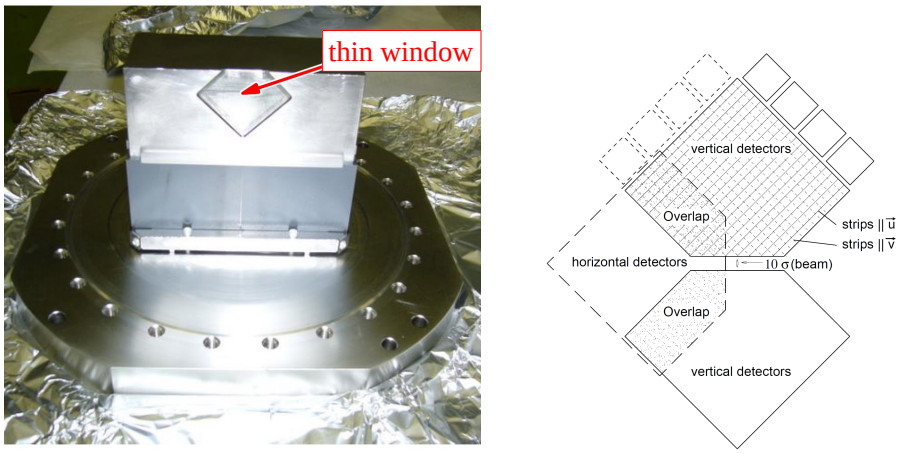

Figure 2.10: (a) RP inner box with the thin window. (b) The three RPs when inserted in the beam pipe. The crossed strips are drawn in the top vertical sensor.

The reconstruction of the proton parameters at the interaction point can be performed only if the beams optics configuration is well known. The *Optical function* determines the explicit evolution of the proton motion in any point s of the machine as a function of the magnet settings and the particle parameters at IP5. Protons that have lost part of their energy in the interaction will emerge from the beam and be detected in the RPs. The transverse coordinates x, y and the projections of the particle trajectory polar angle in the XZ and YZ plane θ_x, θ_y can be measured

using the information of both the near and far units (see fig.2.11). Inverting the

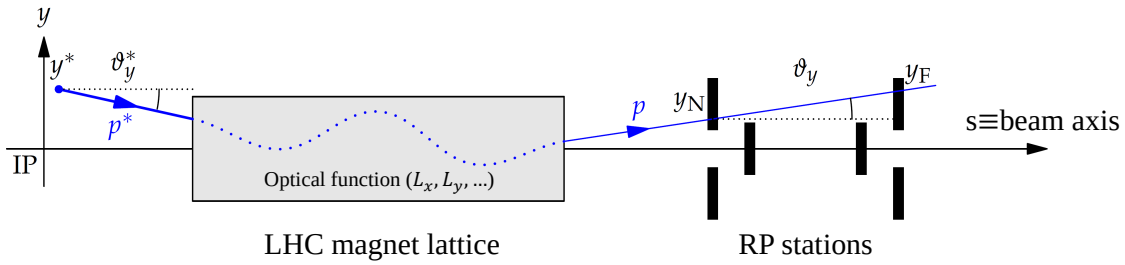

Figure 2.11: Concept of the proton kinematic reconstruction with the RP. y_N and y_F are the hit points in the near and far units of the station.

optical function is possible to determine the same parameters (denote by the '$\star$' superscript) at the IP. To perform the calculation a linearization of the optical function is performed. The equations which relate the proton kinematical quantities measured at the RP position to the values in IP5 are given by:

$$\begin{pmatrix} x \\ \theta_x \\ y \\ \theta_y \\ \xi \end{pmatrix} = \begin{pmatrix} v_x & L_x & 0 & 0 & D_x \\ \frac{\mathrm{d}v_x}{\mathrm{d}s} & \frac{\mathrm{d}L_x}{\mathrm{d}s} & 0 & 0 & \frac{\mathrm{d}D_x}{\mathrm{d}s} \\ 0 & 0 & v_y & L_y & D_y \\ 0 & 0 & \frac{\mathrm{d}v_y}{\mathrm{d}s} & \frac{\mathrm{d}L_y}{\mathrm{d}s} & \frac{\mathrm{d}D_y}{\mathrm{d}s} \\ 0 & 0 & 0 & 0 & 1 \end{pmatrix} \begin{pmatrix} x^\star \\ \theta_x^\star \\ y^\star \\ \theta_y^\star \\ \xi \end{pmatrix} \tag{2.3}$$

The magnification $v_{x,y} = \sqrt{\beta_{x,y}/\beta^\star}\cos\Delta\phi_{x,y}$ and the effective length $v_{x,y} = \sqrt{\beta_{x,y}/\beta^\star}\sin\Delta\phi_{x,y}$ are function of the betatron amplitude $\beta_{x,y}$ and the relative phase advance up to the RP location $\Delta\phi_{x,y} = \int_{IP}^{RP} \frac{\mathrm{d}s}{\beta(s)_{x,y}}$. Together with the dispersion $D_{x,y}$, where nominally $D_y \sim 0$, they are of particular importance in the reconstruction of the proton kinematics. Note that the elements of T depend on the proton longitudinal momentum loss ξ, that in turn can be computed from a combination of the measured quantities. An important parameter of the machine is the *emittance* ϵ, that can be be considered as a measurement of the parallelism of the beam. The emittance changes as a function of the energy, increasing the energy of the beam reduces the emittance. Often the *normalised emittance* ϵ_N is used, which is proportional to the squared root of the energy (so the physical size of the beam will vary inversely to the square root of the energy). The normalized emittance is thus used as a measure of the intrinsic uncertainty on the proton direction before the collision. For the TOTEM measurements this value has to be as little as possible because it degrades the measurements on the scattering angle.

2.3.1.1 High-$\beta^\star$ scenario : optics and tracker performance

The high-$\beta^\star$ physics program is based on the special $\beta^\star = 90$ m optics, and a closer look at its characteristics will later help to understand the scenario that the detectors placed in the RPs will face. The 90 m optics has been chosen in order to maximize the sensitivity of the position measurements on the scattering angle and minimize its dependence on the vertex position. In figure 2.12 the effective length and the magnification functions are reported for the $\beta^\star = 90$ m and $\beta^\star = 1540$ m.

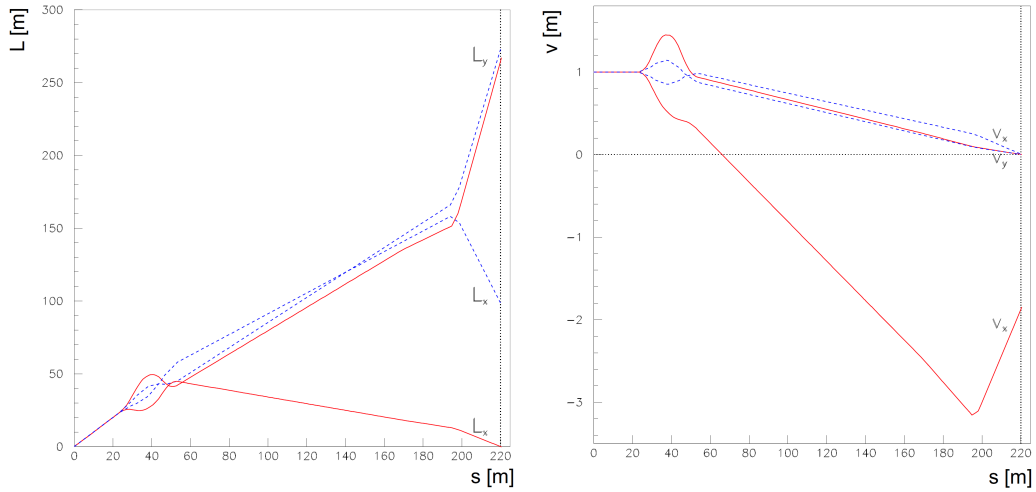

Figure 2.12: The effective length $L_{x,y}$ (left) and the magnification $v_{x,y}$ (right) for $\beta^\star = 90$ m (solid curve) and $\beta^\star = 1540$ m (dashed curve).

If we get their value at RP location for the 90 m optics and we use them in equation (2.3) we get that the scattering angles of the protons in IP5 can be approximated as:

$$\theta_y^\star = \frac{y}{L_y}, \qquad \theta_x^\star = \frac{1}{\frac{\mathrm{d}L_x}{\mathrm{d}s}}(\theta_x - \frac{\mathrm{d}v_x}{\mathrm{d}s}x^\star). \tag{2.4}$$

We see that since $v_y = 0$ (and $D_y \sim 0$) the scattering angle $\theta_y^\star$ does not depend at all from the vertex coordinate. The large value of $L_y \sim 260$ m helps to enhance the sensitivity of the detector to the scattering angle. Moreover the vertical displacement does not depend on the momentum fraction loss ξ. This condition is called *parallel-to-point focusing*, and for the 90 m is reached only in the vertical plane. Thanks to the high resolution of the strip detectors the resolution on $\theta_y^\star$ will be limited only from the beam emittance, that for the high$-\beta^\star$ optics is $\epsilon_N = 2$ µm·rad. The resolution obtained with protons at $\sqrt{s} = 8$ TeV was 2.6 µrad (fig. 2.13, left). Since the D_y term is not exactly zero the resolution will get a little worse with protons

with large ξ. The result can be scaled to $\sqrt{s} = 13$ TeV and $\epsilon_N = 2$, and converted into a momentum resolution: for low ξ particles we get a vertical p_T resolution of 12 MeV.

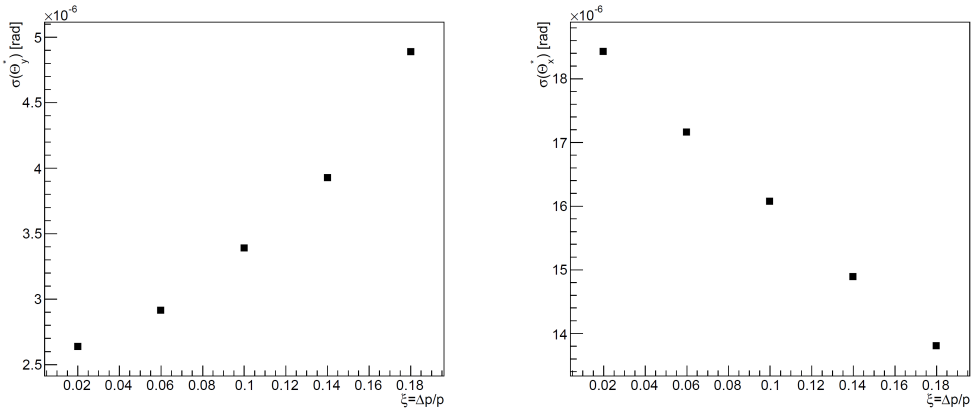

Figure 2.13: Angular resolution on scattered protons at $\sqrt{s} = 8$ TeV in the vertical plane (left) and in the horizontal (right). The values were obtained with a sample of single diffractive events.

The same result is not achieved on the horizontal plane, where $L_x = 0$, and the scattering angle $\theta_x^\star$ must be reconstructed from the track angle θ_x measured with two RP units. The $x^\star$ terms produce a smearing factor since the vertex is reconstructed from CMS with the limitations discussed later in section 2.3.4. This smearing is quite important since in this optics the transverse dimension of the beam is 113 μm. The resolution obtained on $\theta_x^\star$ at $\sqrt{s} = 8$ TeV was 20 μrad (fig. 2.13, right). In this case large ξ lead to better resolution since the vertex contribution get lower. The extrapolation to $\sqrt{s} = 13$ TeV and $\epsilon_N = 2$ leads to horizontal p_T resolution of 91 MeV for the low ξ protons.

The measured horizontal displacement x of the hit will be related to the ξ of the protons (through the magnification factor D_x) and to the vertex position. As for $\theta_x^\star$, also the ξ measurements will be thus limited by the large transverse dimension of the colliding beams. The absolute resolution on ξ is estimated ~ 0.6 %. A fundamental kinematical variable that is used for the spin analysis is the azimuthal angle difference $\Delta\phi_{1,2}$ between the detected protons. The azimuthal angle can be precisely reconstructed through the position measurements, with resolution typically in the range $0.09 - 0.4$ rad, depending on the 4−momentum transferred t[68].

Concerning the acceptance, the large value of the vertical magnification L_y leads to about 40% acceptance of low CD masses for a RP distance from the beam center

of 10 σ_{beam} (fig. 2.14) and the entire $\xi-$range is detected.

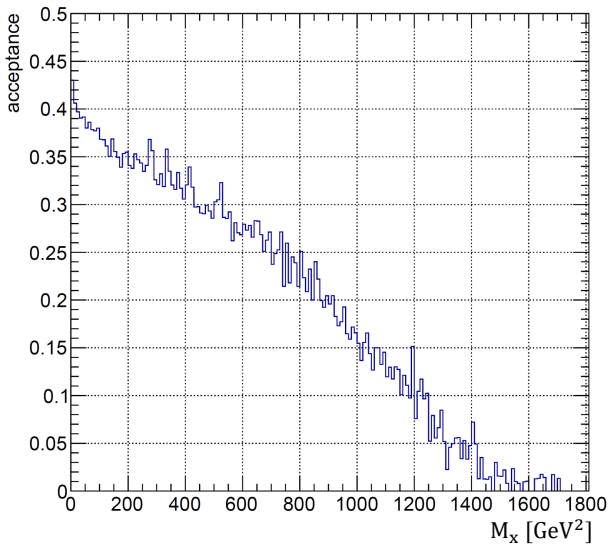

Figure 2.14: Acceptance for detecting both proton in the high-$\beta^\star$ runs in CD events as a function of M_X. The RPs are simulated at 10 σ_{beam} from the beam axis. The events are generated with the PHOJET[69] simulator.

2.3.2 The T2 telescope

The T2 telescope[70] is symmetrically placed at about 14 m from the IP inside the CMS Hadron Forward (HF) calorimeter. It is designed to detect and track charged particles produced in the pseudorapidity range $5.3 < \eta < 6.5$. The role of the detector is to provide a fully inclusive trigger to minimize the loss of events in the inelastic rate measurements and to provide a precise vertex reconstruction to study diffractive event topology. The detector has been used to perform precise measurements of the forward charged particle pseudorapidity density at $\sqrt{s}$ =7 TeV[71] and $\sqrt{s}$ =8 TeV[72], that have a major impact on the tuning of montecarlo both for LHC and for cosmic ray simulations. The detector is designed to work with a luminosity up to $\sim 10^{33}$ cm^{-2}s^{-1} and is therefore possible to use it in the combined CMS-TOTEM measurements at high$-\beta^\star$. The information provided by T2 will be fundamental to perform BSM searches, as already discussed.

The T2 telescope is divided in two arms, one on each side of the IP. Each arm is divided in two semi-cylindrical quarters (fig. 2.15) that are closed on the beam pipe. On each quarter five couples of *triple Gas Electron Multiplier* (GEM) detectors are

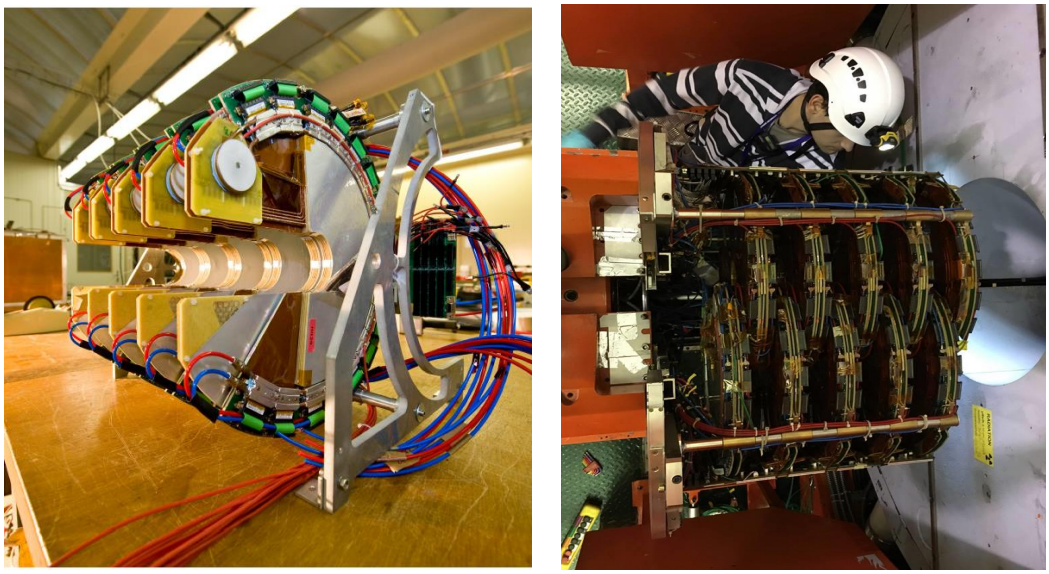

Figure 2.15: The T2 Telescope. On the left a picture of one quarter with the five couples of GEMs. On the right a picture of the opening of one detector arm after the extraction from the CMS calorimeter.

mounted in a back to back configuration, equally spaced of ~ 40 cm. The sensitive volume of the GEM covers an area of $\Delta\phi = 192°$, so that an overlap region is granted, with a radial extension from 42.5 mm to 144 mm from the beam axis. Each particle coming from the interaction vertex in the T2 acceptance region will pass through a minimum of ten GEMs. This redundancy is required in order to achieve the desired detector efficiency of $\sim 100\%$.

The triple GEM is a gaseous detector filled with a mixture of Argon (70%) and CO_2 (30%). The active volume of the detector is divided in four small gaps of few millimeters with special foils, called *GEM foils*(fig. 2.16.*a*). A GEM foil is a polyamide foil of 50 µm thickness with 5 µm copper cladding on both sides. Holes equally spaced by 140 µm are created on the foil by etching (fig. 2.16.*b*). The shape of the holes, that we can observed in figure 2.16.*c*, has been decided so that if a suitable voltage is applied on both copper cladding a very intense electrical field is generated in the hole. When a particle passes through the detector gas ionization occurs and the electrons created in the drift zone start to move towards the readout. When they reach the proximity of the first GEM foil they are attracted and accelerated by one of the hole and amplification of the signal occurs while traversing the hole. The same effect happens in the other two foils, after the passage through the two transfer zones. The amplified signal reaches finally the induction zone where

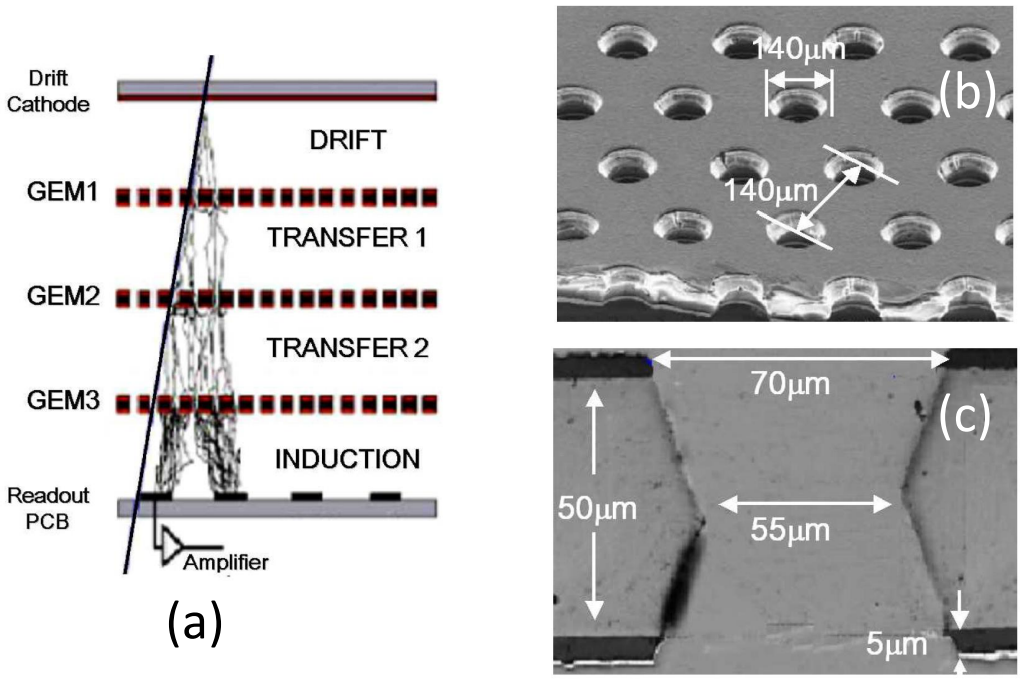

Figure 2.16: Structure of the T2 GEM. Sketch of the amplification processes of a ionizing particle through the three GEM foils. The foil surface and a transverse section of the holes are showed in pictures (b) and (c) respectively.

an electrical signal in induced on the readout. The use of three foils permits to apply a lower voltage on each foil without lowering the overall amplification factor, so that the detector is characterized by less noise and lower discharge probability than a standard single GEM sensor.

The readout is realized with a multi-layer *Printed Circuit Board* (PCB) , with both patterns of strips and pads. The pattern of pads is composed by 1560 trapezoidal pads, which dimensions increase from the inner side (~ 4 mm^2) of the detector to the outer edge (~ 49 mm^2). This segmentation ensures an almost constant coverage of each pad in the $\phi - \eta$ plane. The strip pattern is made with 256 concentric strips, 80 μm wide with a pitch of 400 μm, which provide the radial coordinate of the particles with ∼100 μm resolution.

2.3.3 The T1 telescope

The actual TOTEM experimental setup is completed by the T1 inelastic telescope. The main purpose of T1 is to contribute to the measures of the inelastic and total *pp* cross sections, giving correction to the T2 data. It can not operate with a

luminosity above $\sim 10^{30}$ cm^{-2}s^{-1} and will therefore not contribute to the CD studies in program. The acceptance region $3.2 < |\eta| < 4.7$ covered by T1 region is already instrumented with the CMS end-cap calorimeter, and no information will thus be lost for our purpose.

The detector is installed in two cone-shaped regions centered on the beam and symmetrically placed at a distance of ± 7.5 m from the IP5. Similarly to T2 each arm of the detector is divided in two quarters, composed by five planes equally spaced in z to form a ~ 2.7 m half-cone (fig. 2.17). Each plane of the quarter consists of

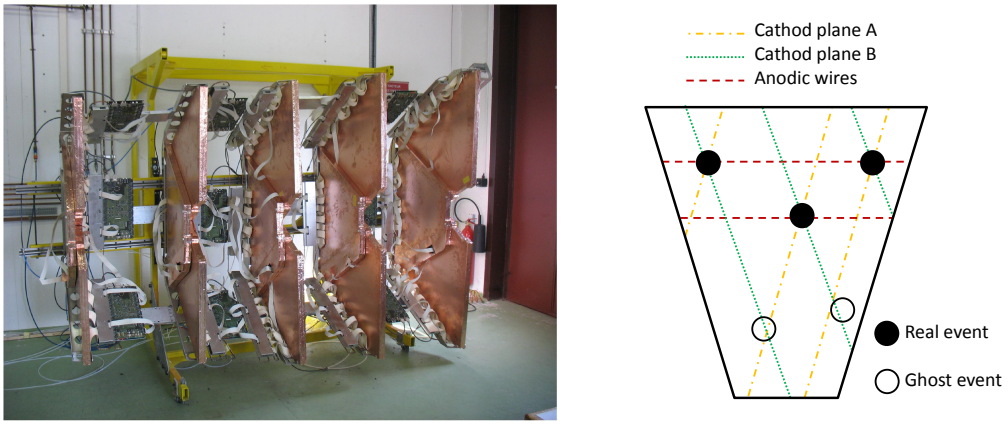

Figure 2.17: The T1 Telescope. On the left a picture of one quarter. On the right an example of three particles passing through one chamber. The requirements of three measurements allow to distinguish the hits from the ghosts.

three *Cathode Strip Chambers*[73] (CSC) roughly covering a region of $\simeq 60°$ in ϕ, with an overlap region. Each detector plane is rotated with respect to the others of 3°, in order to have better track reconstruction efficiency and to reduce the non uniformity of the material in front of the CMS HF calorimeter, placed behind T1.

The CSC is a multi-wire proportional chamber whose cathode planes are segmented into parallel strips. When the high voltage is applied to the internal gold-plated tungsten wires the ions produced by the charged particles are attracted and an avalanche starts in proximity of the wire, where the electric field is higher. Charges are collected by the wires but at the same time a signal is induced on the cathode strips. Finding the centroid of this charge distribution allows a precise determination of the position where the avalanche developed. The strips are placed on both sides of the chamber, with different angle of $\pm 60°$ with respect to the orientation of the anodic wires, as seen in figure 2.17. The orientations of the cathode strips

and of the anode wires allow three measurements for each particle track, which significantly help to reduce the number of ghosts in case of multiple particles. This feature is mandatary for T1, where the mean number of tracks per event already at a luminosity of $\sim 10^{30}$ cm^{-2}s^{-1} is ~ 40. Measurements performed on the LHC data show that a spatial resolution of about 1 mm in the three coordinates can be obtained, with an overall detection and reconstruction efficiency of $\sim 98\%$.

2.3.4 Low central masses in CMS

A detailed description of the CMS detector can be found in [74] while for recent results on its subsystem performances one can refer to [75, 76, 77]. The tracker efficiency and performance are usually quoted only for charged particles with transverse momentum p_T above 1 GeV/c. For such particles the tracker allow for a precise reconstruction of the trajectory in the pseudorapidity range $|\eta| < 2.5$. As described in section 2.2 the study of low mass resonances and the search for glueballs are among of the main topics of the physics program. In this case we have small central masses ($M_X <$ a few GeV) so that the final state hadrons will be characterized by small transverse momenta, below the 1 GeV/c threshold. Few comments on the tracker performance for such particles are therefore needed, particularly on the reconstruction efficiency, particle identification (PID) and vertex reconstruction.

Special tracking algorithms (i.e. [78]) are employed to extend the tracking capabilities down to $p_T \sim 0.1$ GeV/c. The reconstruction efficiency is reported in figure 2.18 (left) for pions, kaons and protons. Such algorithms has already been successfully tested with excellent results in the low mass spectrum acquired in pp collisions[78]. A p_T resolution of ~ 0.02 GeV/c in the range $0.1 < p_T < 2$ GeV/c is provided. Such resolution leads to a precise measure of the central diffractive system with a resolution $\sigma_{M_X} \sim 20 - 30$ MeV/c^2. This must be considered a good result since typically the 0^{++} and 2^{++} resonances in the mass range $0.5 \leq M_X \leq 4$ GeV have widths of the order of hundreds MeV.

The possibility to perform PID on the detected particles helps in the studies of the branching ratios. PID can be preformed with the tracker exploiting the relation between energy loss rate ϵ and total momentum[79]. The CMS tracker is composed of both strip (outer layer) and pixel sensors (inner layer). The standard CMS PID employ the information of the strips only, limiting the discrimination to particles with $p_T > 0.5$ GeV. To extent the PID down to $p_T \sim 0.1$ GeV/c, pixel sensors must be used together with the strips. In figure 2.18 the most probable energy loss rate w.r.t the particle momentum is reported for pions, kaons, protons and electrons. We

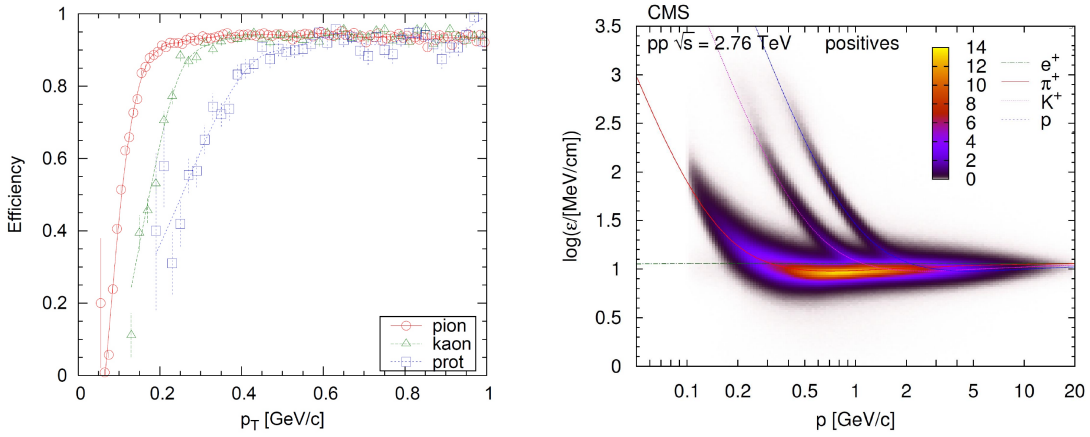

Figure 2.18: On the left the CMS tracker reconstruction efficiency as a function of p_T for tracks in the range $|\eta| < 1$[78]. On the right the distribution of the most probable energy loss rate as a function of the total momentum p used for the PID[79].

see that at high p_T the populations overlap and PID is no more possible. This puts un upper limit on the momentum of the identifiable particle (0.15 GeV/c for e, 1.20 GeV/c for π, 1.50 GeV/c for k, 1.70 GeV/c for p).

The CMS vertex reconstruction is fundamental in high pile-up environment, when all particles must be assigned to the correct vertex of interaction. In soft processes, where only low p_T tracks are produced, the resolution of the primary vertex is limited. The precision on vertex transverse position is indeed of few hundreds of μm, grater than the beam transverse size (113 μm for $\beta^\star = 90$ m). Fortunately the longitudinal vertex position can be reconstructed with a precision of few millimeters (while the longitudinal bunch extension is ~ 7 cm), enough to disentangle the pile-up events when combined with the timing information of the RP.

2.4 A milestone: the trigger upgrade

Before going into the details of the upgrade program I would like to point out that the common data taking, which represent the proof of the feasibility of our physics program for both physics and technical aspects, has been possible only through the TOTEM trigger upgrade. The TOTEM trigger must indeed be able to exchange information with the CMS trigger so that decisions based on both detectors can be taken. Moreover, as we will shortly see, the possibility to merge the data is crucially linked to the TOTEM trigger, that will continue to play a central role also

in the future. Details of the trigger structure can be found in [80, 81]. Here I will focus on the firmware of the LOneG (*Level One Generator*) board, where I have a key role in the development, giving only a short description of the general trigger infrastructure.

The TOTEM trigger system has a multi-level structure, with all data converging to the LOneG board (fig. 2.19). On each level a data reduction is performed.

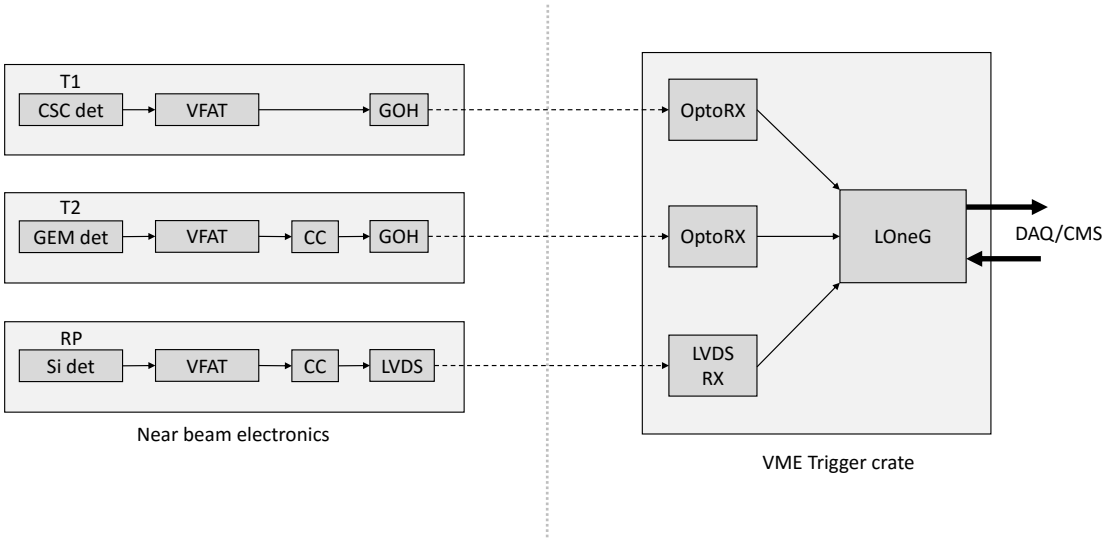

Figure 2.19: Conceptual scheme of the TOTEM trigger structure.

The VFAT[67] front-ends chips used in all the present subdetectors represent the first layer of the structure. They perform the detector signal discrimination and digitization. The data are stored in a buffer for a possible consecutive readout. In parallel they generate trigger signal performing a logic OR of a cluster of strips or pads. For the T2 and for the RP silicon detectors such cluster information are sent to the CC (*Coincidence chips*[82]). Signals coming from aligned sectors on different detector planes are collected in the CCs. A *trigger track* is identified when a coincidence between a programmable number of the sensors is found and the coincidence bit is transmitted. This strategy is possible because the trajectory of the primary particles are almost perpendicular to the sensors. With this requirements we can discriminate the primary particles from the one generated by secondary showers. The trigger tracks information are then sent to the trigger crate through optical (with the GOH chips[83]) or electrical (LVDS) transmission. The electrical transmission represents an important step in the trigger upgrade. It has been introduced for the

RP, since it can lower the latency of the trigger data being faster than the optical transmission. A gain of $\sim$ 600 ns was measured w.r.t optical transmission for the RPs placed at 220 meters from the IP, and hence from the trigger crate. This reduction was essential to be compliant with the CMS trigger latency requirements and make the CMS-TOTEM trigger handshake feasible. All the subdetector trigger information are finally collected in the central trigger where for each subdetector a discrimination based on the trigger track multiplicity is made and the results are sent to the trigger final stage, the LOneG.

The LOneG firmware has been upgraded in the last two years to handle the handshake with the CMS L1 trigger and allow offline data merging. Compatibility with the CMS DAQ must also be granted in view of the CT-PPS project. A scheme of the firmware after the upgrade is reported in figure 2.20. The LOneG firmware

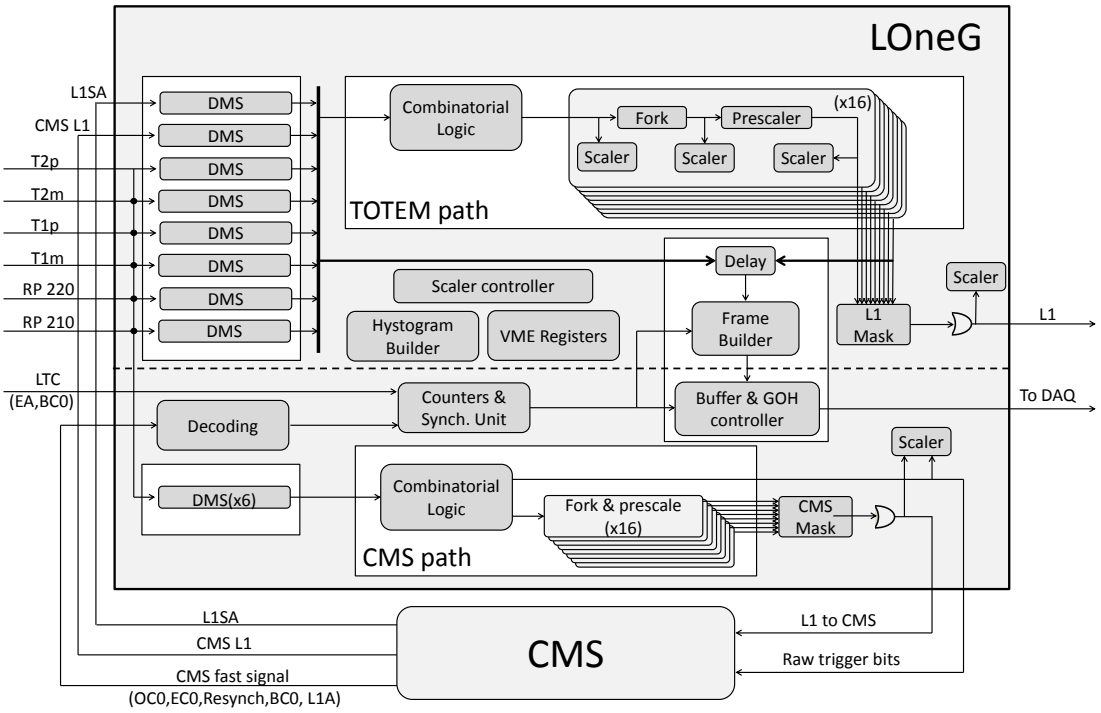

Figure 2.20: Scheme of the LOneG trigger. The dashed line is used to conceptually divide the old firmware (top) from the new modules (bottom).

performs multiple tasks, some of which has been added/upgraded with my major contribution:

- performs the trigger algorithm and generates the TOTEM L1 trigger.
- handles the CMS-TOTEM trigger handshake, so that trigger decision based on both experiment detectors can be taken (added).
- generates an event timestamp for the offline data merge, essential for common data analysis (added).
- builds the trigger data frame for the DAQ .
- handles the frame readout from both TOTEM and CMS DAQs (added).
- performs trigger rates and status monitoring (upgraded).

The totem L1 trigger is generated with a combination of all the three TOTEM subdetectors and two signals from CMS: the CMS L1 and the L1SA signal (*L1 Special algorithm*), described below. All the input signals goes first through the DMS units (*Delay-Mask-Stretch*). The individually programmable delay blocks are used for synchronization, since each subsystem has different response time and different distance from the IP5. Then a mask can be applied. The final stage of the DMS is a monostable used to stretch the input signals. This stage is needed for the T1 and T2 detectors, that suffer of 2-3 clock cycle jitter on the output signal (this is not an issue since they will not work in runs with bunch spacing ≤ 3 clock cycles). For them the stretch value is usually set to 4, while for the RPs no stretch is applied. After the DMS units the signals enter into a combinatorial logic, where a total of 16 physics triggers are generated. The combinatorial logic is not fixed and a certain degree of programmability, especially for the RPs, is provided. Those 16 bits are the *trigger bits*, a crucial information for the data analysis. Many information (there was at least one track in a certain T2 quarter? was the L1SA present?) are encoded in the bits. Data selection criteria can be applied with the trigger information without even look at the data. Moreover, when the number of bunches and their population grow, the huge amount of data from T2 can saturate the DAQ bandwidth. Is thus possible to exclude it (if track information are not essential for the physics under study) from the acquisition but keep it's multiplicity information through the trigger bits. After the generation each trigger bit enters in one dedicated *fork and prescale* unit. For each LHC fill a filling scheme, which contains the structure and location of the bunches in the machine, is provided. With this information is thus possible to select the colliding bunches in IP5. The fork is basically a FIFO, where a list of bunches can be loaded. The fork module keep tracks of which bunch has generated the trigger signal and, if the number is not on the list, block it. In such way it allows to trigger only on bunches that are written in the programmable list, reducing the

final trigger rate without prescaling. This feature is essential to collect data on the same bunch for better background estimation and greatly helps when prescale are not wanted. Signals surviving the fork and the eventual prescalers pass through a final selection mask and a global OR. The resulting output is the TOTEM L1 trigger signal.

The handshake with CMS is shown in the lower par of the figure 2.20. The input signals follow almost the same path as before but of course only TOTEM subdetectors are used. A L1 for CMS is produced and sent to the CMS trigger in the same way as it is done for the TOTEM L1. The information to CMS is completed with three additional raw bits, that bring additional important information on the detector status. CMS integrates our information with its subdetectors and generates the CMS L1. The L1SA signal, a special programmable TOTEM-CMS combination is also generated (for example protons in the RPs and two jets in the central region can be required). L1SA is used to allow TOTEM to acquire only events with common physics and not all the CMS triggered events, leaving bandwidth for TOTEM independent data acquisition.

The offline data merge is possible only if some sort of data synchronization is provided. Such synchronism can not rely directly on the event number since the two DAQ systems are not synchronous. It is instead performed in the LOneG, by intercepting the fast signals of CMS, broadcasted to all its subsystems in a encoded transmission. Among them there is the OC0 (*Orbit Counter Reset*), that is used to reset the counter of the number of orbits (beam revolutions in the machine) elapsed. The LOneG can thus synchronize its orbit counter with the CMS one. Adding the bunch number to orbit number a timestamp is created and saved together with the event number. This information can be considered a *Rosetta stone*, connecting the TOTEM event number (present in all subdetector data frames) to the common timestamp.

The trigger data frame is built every time an *Event Accepted* signal (EA) is generated from the DAQ. The LOneG frame consists of 5 word of 64 bits each, where, among other information, the trigger bits and the timestamp are present. Historically, TOTEM readout was performed through VME and the frame was read directly from the *frame builder* unit. In order to be readout in a transparent way both from TOTEM and CMS DAQs, we had to abandon the VME and to move towards optical transmission. Apart from the data format there is only one golden rule to respect: for each EA one and only one frame must be sent to the DAQ. If not, the detector is excluded from the acquisition. The optical transmission through the

GOH allows a 16 bit transfer in one clock cycle, so that the complete frame readout will last 20 clock cycles (500 ns), plus a few clock cycles of overhead to prepare the frame. Since multiple EA can be generated in this time I also added some buffers. The average EA rate is $\sim$ 100 KHz, compatible with our transmission time. The firmware is completed by a set of scalers and the VME controller. The *histogram builder* unit is also present, a powerful module to automatically generate an histogram (inside the FPGA) to check the trigger distribution w.r.t the bunch number, free of any prescale/fork.

All the new firmware features, except the frame buffers, as already been tested successfully with multiple common data taking from 2012, with published results[84]. This was the first milestone for all the future upgrades.

2.5 High-$\beta^\star$ upgrade program

As discussed in section 2.1 the goal of ~ 100 pb^{-1} integrated luminosity, needed for the high-$\beta^\star$ physics program, requires to operate at the maximum luminosity that the LHC can provide with the special 90 m optics. This rises the pile-up probability up to $\mu = 0.5$. The vertex reconstruction of the forward protons is limited and is not possible to assign the detected protons to the correct interaction vertex. Without the pile-up rejection our program is not feasible. To overcame this limitation the challenging upgrade program subject of my thesis as been carried out, based on the development of a very precise timing detector to be housed in additional RPs.

The timing detector can measure the TOF of the leading protons as the sum of the vertex generation time[8] t_v and the travelling time to the detector. Tracks detected on opposite arms will be paired and the sum and the difference of the arrival time will be computed. The sum can be used to check the compatibility with the bunch collision time, while the time difference Δt, free of the uncertainty on t_v, will be used to compute the longitudinal position of the collision vertex $z_{pp} = c\Delta t/2$. The resolution needed can be extrapolated from the RMS of the vertex longitudinal position that, for the high-$\beta^\star$ optics, is $\sim$ 7 cm. A resolution of at leat 1 cm is required, that translates into a time resolution better than 50 ps. The detector will be housed in the actual RP box (fig. 2.10). Depending on the detector width multiple detection planes can be hosted in a single RP so that the timing constraint

[8]The colliding bunches have a longitudinal RMS size of $\sim$ 10 cm. The reference LHC clock is synchronous with the time at which they have the maximum overlap but the interaction can happen before or after that time.

on the detector can be slightly relaxed. The high timing precision must be coped with an efficiency of $\sim 100\%$, since events without timing information can not be used in the analysis.

To perform a precise timing difference measurement between the two detector arms a very precise reference clock must be provided to the stations on both sides. The clock must stable over time and with a jitter lower that few ps. We readapted the clock distribution system based on the commercial *Universal Picosecond Timing System*[85] (UPTS) developed for FAIR[9]. The concept of the system is to transmit the clock signal to the stations through optical fibers. There it is partially reflected back to the source for a phase measurement w.r.t the initial clock with a network analyzer. This feedback is used to keep the frequency accurate and stable. Preliminary measurements show a clock jitter below 1 ps.

To understand the scenario that the detector placed in the RPs will face a simulation has been performed[86], based on the cross sections measured from the TOTEM collaboration at $\sqrt{s} = 7$ TeV[6, 9] and already presented in chapter 1. Since the average number of interactions for bunch crossing is given by the pile-up probability μ, only the relative cross section ratios are meaningful. In the simulation those ratios are assumed to not change when $\sqrt{s} = 14$ TeV. The elastic distribution, which is the dominant contribution, has been assumed with an exponential $t-$distribution, as measured by TOTEM[7]. The beam induced background, mainly generated from beam halo, has been modeled from a data sample acquired in a well defined condition ($\beta^\star = 90$ m, $\sqrt{s} = 8$ TeV, $\mu = 0.05$, RP inserted at 9.5 σ_{beam}). The data sample for the background estimation was acquired using a random trigger and the background tracks were defined requiring no signal in T2 and no elastic signature in the event. The measured background rates has been extrapolated to $\mu = 0.5$. The track multiplicity (number of tracks in the detector per bunch cross) measured at low pile-up on a data sample triggered with the RP, and our extrapolation to $\mu = 0.5$ are reported in figure 2.21. The simulation has been checked simulating the low pile-up data to ensure its consistency.

At $\mu = 0.5$ the probability of multiple tracks in the detector is not negligible, with >10% of events having at least two tracks on one side. If two particles (either primary or secondary) hit the detector almost simultaneously ($\Delta T < 20$ ns) no timing information can be extracted (the two output signals are summed up), leading to a detector inefficiency. To reduce the inefficiency a proper detector segmentation must be done, a request that tights the constraints on the detector choice.

[9]Facility for Antiproton and Ion Research, GSI laboratory, Germany.

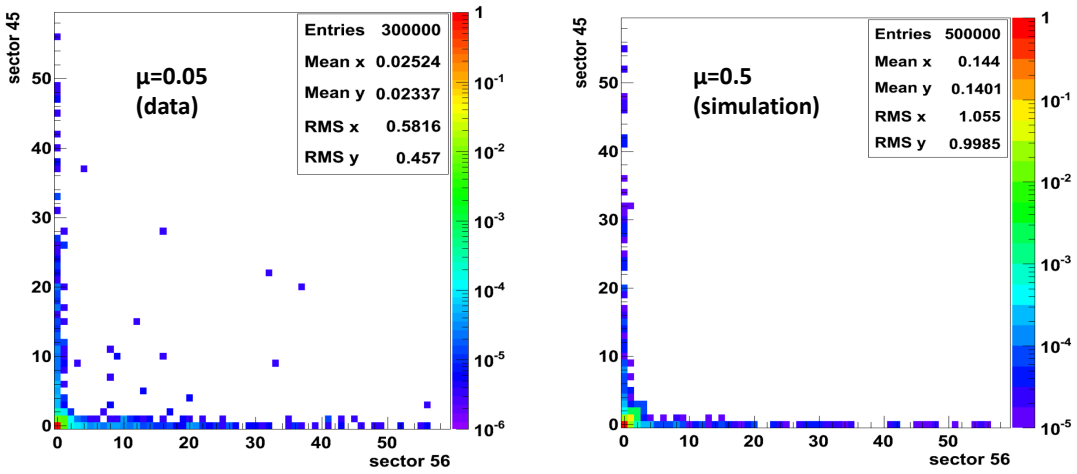

Figure 2.21: On the left the track multiplicity measured in the 8 TeV data at $\mu = 0.05$. On the right the track multiplicity simulated for 13 TeV and $\mu = 0.5$. Only the vertical RP are considered (top and bottom RPs are summed). The sector codes identify the arm of the detector.

To reduce to ~ 0 the detector inefficiency due to multiple hits the desired track multiplicity on each cell was set to a maximum of ~ 0.01 per bunch crossing. An increase of the detector granularity to match the multiplicity specification is not practical since it leads to a large number of channels to be readout, while for practical reasons, a maximum number of 12 channels per plane were desired. The adopted solution is to make pixels of different sizes, all with almost the same occupancy. Of course setting both the number of channels and the maximum allowed multiplicity leads to a compromise with the area coverage of the detector.

To choose the proper segmentation we referred to the same simulation used to study the track multiplicity, but the hit distribution can already be inferred from the general optics characteristics introduced in section 2.3.1.1. Since the events with low ξ dominate we expect that the majority of the protons will hit the vertical RPs and only a small fraction will be measured in the horizontal. Our expectation is confirmed from the simulation in figure 2.22, where the hit distribution on the actual tracking detector is reported. The simulation shows that only the vertical RPs play an important role in the high-$\beta^\star$ physics, and therefore the high-$\beta^\star$ upgrade will regard only the vertical RPs (therefore we often refer to this upgrade as the *vertical timing* upgrade). After the choice of the diamond as the primary option a final fine tuning of the pad dimensions has been done since diamonds are easily found on the market with surface area of $\sim 4.5 \cdot 4.5$ mm^2. The final geometry (optimized

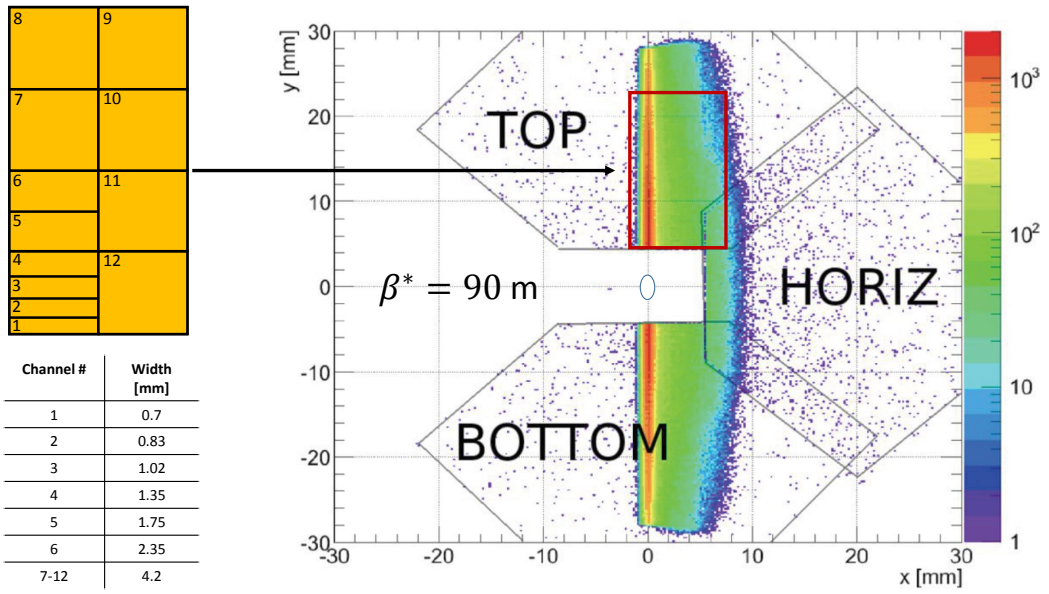

Channel #	Width [mm]
1	0.7
2	0.83
3	1.02
4	1.35
5	1.75
6	2.35
7-12	4.2

Figure 2.22: Hit distribution in one RP unit for the special $\beta^\star = 90$ m. The area covered from the timing detector is highlighted. The segmentation of the detector is shown on the left. Same segmentation is used in the bottom RP.

for diamond) for the sensor is shown on the left of figure 2.22. The timing detector will not cover all the tracker area, but the interesting part of the physics lies in the central near-beam area of the vertical RP, where our timing detector will provide optimal coverage. The surface is covered with 12 pixels of different sizes, with the smaller located in central near-beam area. The pixel size goes from $4.2 \cdot 0.7$ mm^2 to $4.2 \cdot 4.2$ mm^2.

Other requirements on the timing detector come from the environment in which they operate. First of all high radiation hardness is necessary, being the foreseen irradiation estimated in $\sim 5 \cdot 10^{10}$ protons/mm^2 to collect the 100 pb^{-1} needed. Than, the technology had to be chosen taking also into account the material density (more material we put near the beam, more showers will form in our detector and hit the down-stream RPs) and the thickness of the detector, that must fit in the existing RP. Moreover we already said that multiple planes can be inserted in the RP box depending on the single layer thickness.
Before explaining why the diamond represents the best choice and describe our detector final design, let's summarize the requirements on the detector technology:

- time resolution better than 50 ps (scale if multiple planes can fit in the RP).
- detector segmentation with different pad dimensions.

- high radiation hardness.
- efficiency $\sim 100\%$.
- low density/thickness detector.

2.5.1 Overview of the TOTEM diamond TOF system

To find the best solution for the timing detector different technologies have been investigated and R/D have been performed on the ones fitting all the above requirements. The most promising technologies were represented by the Silicon Photomultipliers (SiPM), the Ultra Fast Silicon (UFSi) detectors and, of course, the diamonds.

The Quartic project[91] is based on quartz bars used as Cherenkov radiators, read out by a SiPM array. For the vertical upgrade the Quartic presented some difficulties due to the length of the quartz bar, that could not fit the vertical RP (but some adjustment could be done). The project was instead regarded as the primary option for CT-PPS, since the horizontal RPs (used for CT-PPS) have been redesigned with reduced beam impedance and the internal box has more space. After some very promising tests performed with laser, poor results were obtained in test beam and actually the CT-PPS collaboration is looking for other solutions (among which our diamonds). The SiPM technology will be better discussed in chapter 3. I indeed performed and here reported some preliminary studies on this technology. I used my acquired experience to build some auxiliary detectors, needed for the test-beams performed with diamonds.

The actual first candidate for CT-PPS is represented by the UFSi[92, 93]. The UFSi has an architecture close to the one of the SiPM but with lower dopant concentration and thus lower depletion depth. The idea is to obtain a controlled low gain avalanche, by inducing the multiplication only on the electrons. In this way amplification of the primary charge can still be performed but with an internal gain of 10-100. In contrast typical gain of 10^5 or more are obtained in SiPMs, but the avalanche is uncontrolled until cell saturation and subsequently dump occur. The output signal from the UFSi will be proportional to the charge release and the long recovery time of the SiPM cell is avoided. Moreover the dark count problem of the SiPMs (see section 3.1) is mitigated and the sensor can thus be exposed directly to the beam without the need of cherenkov or scintillator radiators. This technology is still under development but promising results are coming. However from the beginning was clear that a complete detector will not be ready before 2017, too late

for our timescale.

The best technology for our project is represented by the diamond sensors. My work covered all the components of the detector: the sensor, the front-end electronics, the digitization of the signal, the readout and control system. The diamond sensor will be extensively described in chapter 4 together with our preliminary tests with commercial devices, where my experience with the diamonds started. Diamonds or, better, ultra pure synthetic diamonds have all the characteristics discussed. The segmentation of the sensor can be easily done during the metallization of the diamond, and patterns with different pixel areas can be obtained without problem. The material (carbon) is a low density material and typical sensors have 500 μm thickness. When placed on the support board the global thickness of one plane is < 1 mm. This allows to put up to 4 planes in each RP, so that the required resolution on the single sensor is 100 ps. It also shows one of the higher radiation hardness among the available solid state detectors. The efficiency in the detection of a *Minimum Ionizing Particle*[10] (MIP) particle, measured in this work, is almost 100%. The sensor has exceptional intrinsic signal to noise ratio (SNR), that is mandatory to achieve the desired time resolution. The main drawback of diamond detector is related to the low output signal (~ 1 fC/MIP), which is almost the same order of magnitude of the input noise of the commercially available amplifiers. This leads to a very low SNR after the amplification stage, lowering the timing resolution.

To overcame this limitation we developed a 3 stage custom amplification chain, tuned on the diamond signal, and characterized by an extremely low-noise first stage. Due to low number of channels, discrete components are used. To reduce the capacitance seen by the amplifier, which have a negative impact on the time performance, a controlled impedance custom hybrid board was made (chapter 5). The board hosts the diamonds, glued on the board near the edge closer to the beam, and the full amplification chain, reducing to the minimum the parasitic capacitance. To obtain the desired segmentation a total of 8 synthetic diamonds with surface area of $4.2 \cdot 4.2$ mm^2 and 500 μm thickness are needed on each hybrid board, with three different patterns of metallization and distributed on two columns. In this field I participate in a long series of test-beam in order to develop and optimize all the stages of the amplification chain. Important results on the detector efficiency and performances have been obtained.

Usually fast discriminators followed by a precise Time to Digital Converters

[10] A MIP is a particle whose mean energy loss rate through matter is close to the minimum (~ 2 MeV/gcm^2). Details on the particles energy loss in matter can be found in [13].

(TDC) are used for time measurement. The TDC information is concentrated into a single digital integer timestamp, reducing drastically the dataflow. This is optimal when the number of channels is large or when the rates are very high (tens of MHz). However such solution do not provide information on the waveform, except sometimes the Time Over Threshold[11] (TOT) when the discriminator can provide such measure and the TDC is able to measure both edges of the signal. Also when the TOT is available the precision on the amplitude or charge of the signal remains poor. Instead of using a TDC, in our architecture the output signals from the hybrid board are extracted from the RP and sent to a fast sampler: the SAMPIC[87, 88], developed in Saclay. The Sampic has 16 input channels with a sampling rate up to 10 Gs/s. Each channel will work in a independent self-triggered mode and up to 64 sample will be acquired on each trigger. Our solution permits to sample the whole leading edge of the signal ($\sim$ 2 ns), allowing the offline reconstruction algorithms that I will describe through this thesis. The resulting time resolution greatly benefits from the usage of a sampler. The digitization stage will be described in chapter 6, where I will also investigate the performance of the diamond when coped to a fast discriminator and a TDC. As expected the TDC performance are not competitive with the SAMPIC in terms of timing, but nevertheless the results are of great interest in view of other applications of our diamond detector, when large number of channels and/or very high input rate are foreseen, as the one described in the next section. Both my early studies and the latest test-beam results will be reported.

The SAMPIC chip is mounted on a SAMPIC mezzanine board developed in Saclay. Two SAMPIC mezzanine can be plugged in the *Readout MotherBoard* (RMB), a joint project of TOTEM and CMS that will be used also in CT-PPS. The board is based on the Microsemi SmartFusion2 (SF2) FPGA, an high performance FPGA protected against SEU (*Single Event Upset*) events. The SF2 collects the data from the SAMPICs, performs the event building and sends the data to the DAQ. Moreover it handles the control interface of the chip. The RMB can host also a mezzanine with four high precision Time to Digital Converters (HPTDC), used by CT-PPS (see next section). A simple change of firmware will allow to use the SAMPIC or the HPTDC mezzanine. A better description of the board is provided in chapter 7, where I will also give details on the SF2 firmware for the SAMPIC configuration, which I am in charge of.

The complete timing system is composed of two timing units, one on each side

[11] The *Time Over Threshold* is a measure of the time that a pulsed signal stay above a selected threshold.

of the IP, consisting of diamond detectors in the vertical RPs. Since each RP can host 4 diamond planes, a total of 96 channels/arm are foreseen. The readout of one arm will thus require 6 SAMPIC mezzanines, mounted on 3 RMBs. The scheme of one arm of the system is presented in figure 2.23.

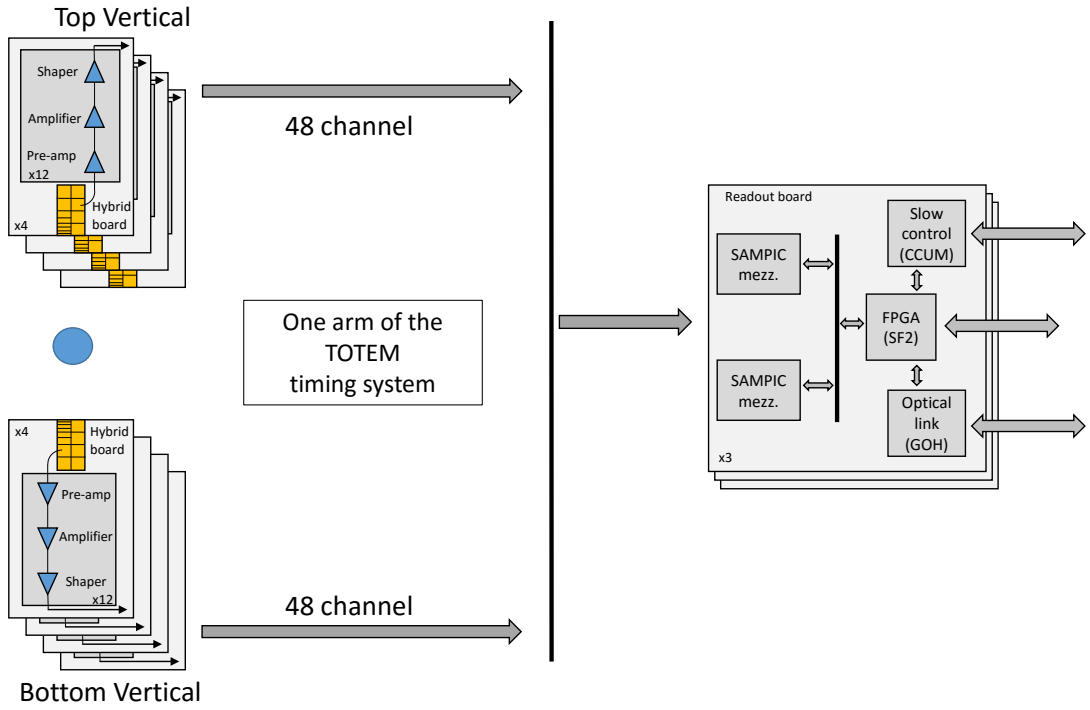

Figure 2.23: Scheme the complete timing detector for the high$-\beta^{\star}$ upgrade (one arm). Only one amplification channel is drawn on the Hybrid Board (instead of 12). The RMB board will be located few meters away from the beam, reducing the radiations.

2.6 CT-PPS

The CT-PPS physics program will push the TOTEM-CMS physics program down O(fb) cross sections, even if with the already mentioned limitation on of $M_X > 300$ GeV. It will cover studies on processes where high transverse energy jets and high central masses are produced, whose importance we have already discussed, and open new windows on the BSM physics based on CD *two-photon collision*. The LHC can be indeed seen as a $\gamma\gamma$ collider where the two interacting γ are generated by the colliding protons.

Of particular interest is the search for BSM physics through the study of the exclusive diffractive process $p + p \rightarrow p + \gamma + \gamma + p$. Has indeed been recently reported by ATLAS and CMS about an excess in the di-photon channel[58, 59]. For both experiments the excess is located at ~ 750 GeV and this hint for a new resonance, not predicted by the SM, has excited the scientific community. If this hypothetical new particle is produced through CD the two-photon production is theorized to be the dominant production channel (being the other the two-gluon exchange) and CT-PPS will be in the perfect position to identify it in an almost background free environment[60, 61].

To study this exiting excess the timing information is not mandatory, since the signature of the event is quite clear in the central region (2 γ pointing to the same vertex), but still usefull. What is really needed is the tracking, so that measuring the ξ of the two protons the central mass M_X can be reconstructed with relation (2.1) and confronted with the invariant mass of the two protons. Additional cuts can be done on the γ energy, γ/P_T balance and on the difference in the azimuthal angle $\Delta\phi$ between the two photons. Calculations from the TOTEM collaboration show that with our tracking detectors and an integrated luminosity of ~ 30 fb^{-1}, that can be reached already in 2016, there is the chance to claim the discovery (if the excess really exist and is produced through CD).

Everything seem fine except that our tracking sensors are not designed to operate at maximum LHC luminosity. The upgrade of the tracking sensors with pixel radiation hard detector was indeed foreseen by the CT-PPS program, but their installation is scheduled for 2017. Our strip detectors are expected to survive only two months with a luminosity above 10^{34} cm^{-2}s^{-1}. Even using our spares we will loose the tracking capability in late summer, without collect the desired amount of data.

The only feasible solution to be pursued in this limited time is to readapt our TOF system and use them as tracker (the radiation hardness of the diamond will be discussed in chapter 4.2). The idea is to use the same hybrid board developed for the vertical upgrade, but with a different diamond distribution and segmentation. The same simulation of the hit distribution discussed in section 2.5 has been performed for standard optics and can be found in figure 2.24, where the area covered by the diamond sensor has been highlighted. In the same figure the diamond pattern is reported. Again a total of 12 channels are used, but distributed on 4 diamond in a single column. With this segmentation the maximum track multiplicity per bunch crossing on one channel is 0.14. To be noted that with the standard LHC optics

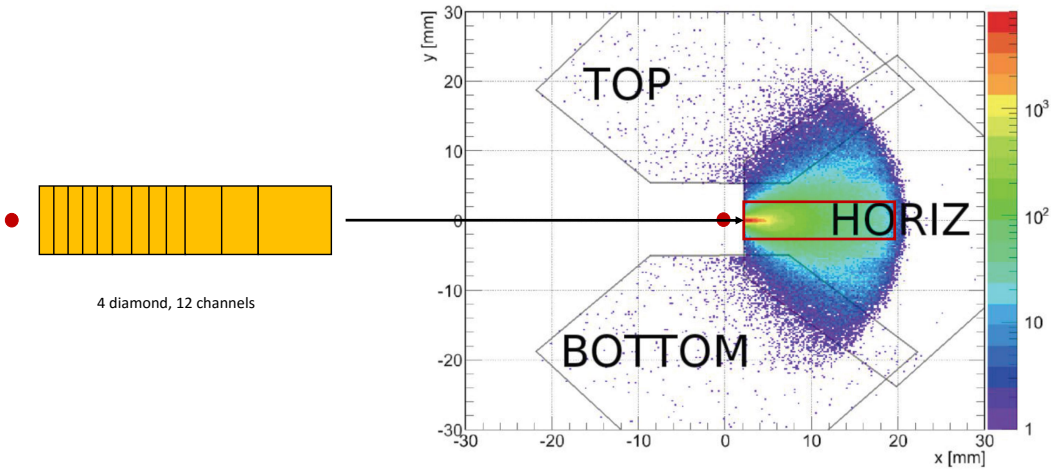

Figure 2.24: Hit distribution of one RP units for the standards optics (CT-PPS). The area covered from the timing detector is highlighted. The segmentation of the detector is shown on the left.

all the particles will hit the horizontal RP, while the vertical will not contribute. The CT-PPS upgrade will indeed regard only the horizontal RPs. This pixelization, even if very raw with respect to what is achievable with a detector developed for tracking, can ensure a resolution on the central mass of ~ 50 GeV, sufficient for the background rejection when coped with the others cuts.

The foreseen track rate in the detector is estimated $\sim$ 2 MHz/channel, that translate in a SAMPIC input rate ~ 32 MHz. The actual revision of the SAMPIC chip can not be used with this input rate, due to the rate limitation discussed later in section 6.1.1. In short is not possible to provide an external trigger to the SAMPIC acquisition (can be provided with few ns latency, too few for our application) and all the hits must be readout. The time employed to readout a sampled waveform is not compatible with a 30 MHz particle rate. Is thus not possible to apply the same readout chain developed for the vertical upgrade. The solution, since timing is not essential in this framework, is to employ a fast discriminator (the NINO chip[89]) and a TDC (the HPTDC[90]), as previously discussed. The NINO chip is a 8 channel fast discriminator where the input charge measure is encoded in the output signal width. Each NINO is coped to the input of one HPTDC, that can measure the rising and the falling edges of the signal with a precision better than 25 ps. A TOTEM NINO board with 4 on board NINO chips has been developed. Since I had already experience[94] with the NINO chip and the HPTDC, I was involved in the board design and in the characterization and optimization of the system performance. The

project foreseen to build two NINO boards for each detector arm, which settings will be controllable through an I^2C interface. In this way all the 48 channels from the horizontal RP will be read with the two NINO boards (leaving 24 spare channels) and two RMBs. The scheme used for the horizontal detector is reported in figure 2.25.

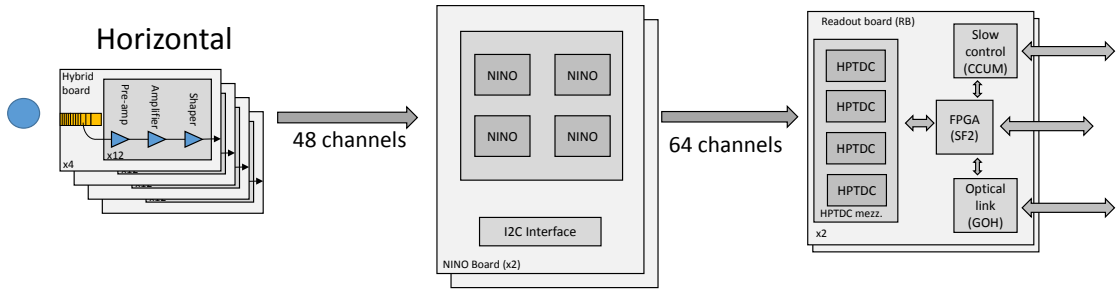

Figure 2.25: Scheme of our detector in the CT-PPS configuration (one arm). Only one amplification channel is drawn on the Hybrid Board (instead of 12). The NINO board will be located in the same protected area as the RMBs.

Although not being CT-PPS the main subject of my thesis in chapter 6 I will show the performance of the TOTEM diamond sensors using the NINO for the digitization stage, representing the entry point to the project. The integration in the CT-PPS framework can indeed be considered a key step to use our detector also for the timing of CT-PPS. To be compliant with CT-PPS timing requirements we will have to push the performance of the diamond, but we already have some ideas...

Before the end of the chapter I want to show (fig. 2.26) the complete layout of one arm of the Roman Pot system. In the layout a description of the composition of each unit is reported. The installation of the additional RPs has been performed during the *Long Shutdown 1* (LS1), and can now be equipped with our detectors.

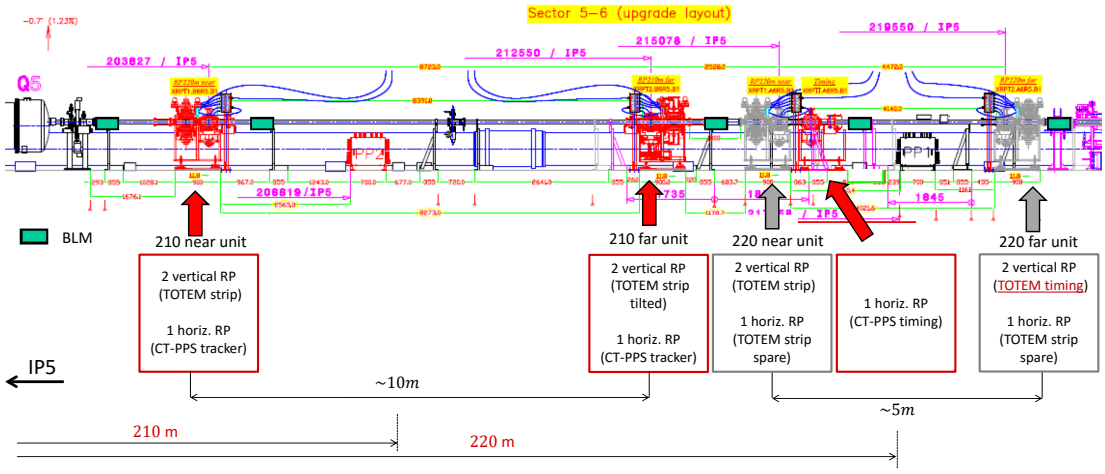

Figure 2.26: Layout of the Roman Pot system after the LS1 (one arm). The installation of our timing detectors is foreseen in the 220 far unit.

Chapter 3

The SiPM trigger detectors

My studies on the SiPM technology started as an R/D for the final TOF system, but the results obtained did not convince us that it was the best strategy for the upgrade. However I used the acquired knowledge to develop the trigger detectors used for the test beams on the TOTEM diamond detector. The devices are based on SiPM sensors coupled to very thin fingers of plastic scintillator. In section 3.1 I will give a brief introduction to the SiPM structure and principle of operation, highlighting the main parameters that are used for the characterization of the sensor. Later, in section 3.2, I will present the measurement campaign which I performed on the sensor and the electronics employed in my work. The choice of the polarization scheme and the amplification stage will be discussed. On top of the standard studies usually performed on the SiPM (gain, energy resolution, SNR, noise) I will also present in section 3.2.5 some measurements on the intrinsic time resolution of the system. The requirements on the final detectors and the assembly procedure which I followed are finally reported in section 3.3. The detectors here described have been successfully employed during almost all the later measurements reported in this work, always performing as requested.

3.1 SiPM structure and operation

A Silicon Photomultiplier (SiPM) consists of a matrix of small-sized pixels all connected in parallel. From the outside the device presents only two pins. Each pixel is composed by Geiger-Mode avalanche photo-diodes (GM-APDs), integrating a resistor for passive quenching, and can be represented with a reverse biased diode in series with a quenching resistor R_q (fig. 3.1).

An APD is a multiple junction diode working with a reverse bias voltage: a

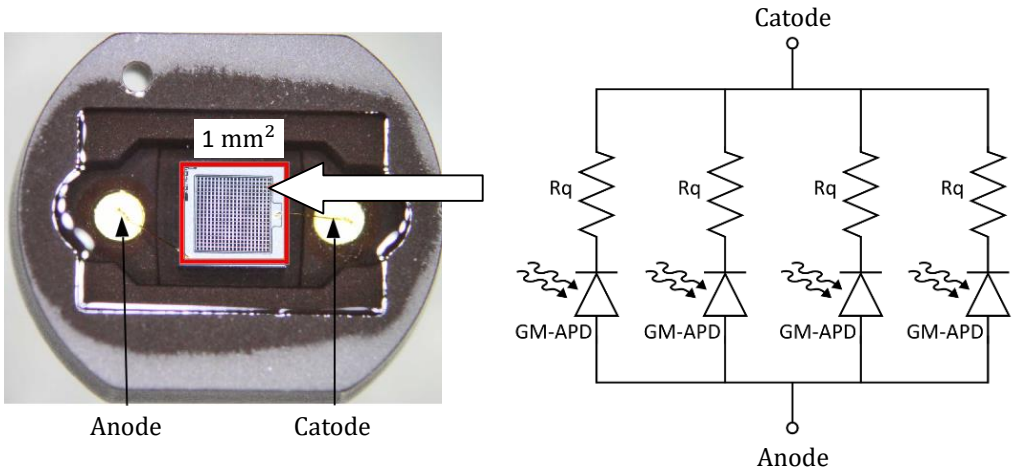

Figure 3.1: Picture of Hamamatsu S12571-100P SiPM (left) and the equivalent circuit schematics (right). The micro-cells can be identified in the highlighted region of the picture.

schematic representation of a typical APD layout can be seen in figure 3.2, while charge distribution and electrical field for uniformly doped layers can be found in figure 3.3. On top of the device an anti-reflective coating is applied to prevent photon backscattering. When a particle or a photon enters the detector it has a certain probability to generate an electron-hole pair through impact ionization close to the $p^+ - n^+$ junction (multiplication region). The multiplication region is very thin ($\sim$ 0.1µm) and the chance for a photon to convert in such a small volume is low. To solve the problem the epitaxial p^- layer is added, creating a wider fully depleted area. Pairs produced in that area (drift region) move toward the avalanche area and then generate the signal. In such way the active volume depth is enhanced to few micrometers. The side guard-rings help forming a uniform field in the multiplication region. This structure is called *"n on p"* and the amplification region is located near the cathode. A specular device can be created by inverting the dopant concentrations (the *"p on n"* structure), with the multiplication region located near the anode.

In the multiplication region the electric field accelerates both electrons and holes which, depending on the bias voltage V_b applied, have a chance to generate secondary ionization. At low voltages no secondary ionization take place and the device behaves like a simple photo-diode. As V_b increases the electrons start to generate secondary pairs. However, as the bias voltage remains below the junction breakdown voltage V_{break} (usually few tens of volts) the holes do not participate to the

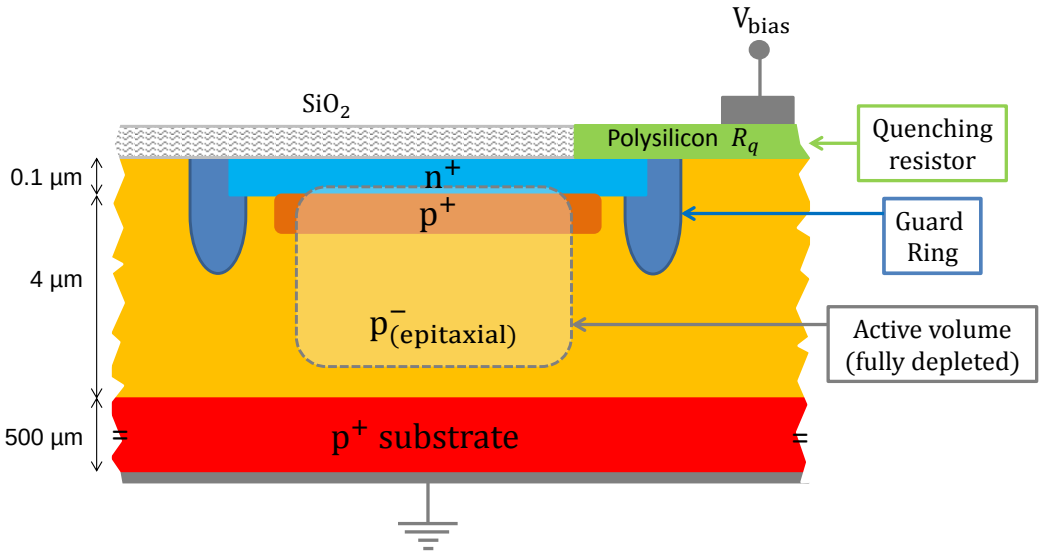

Figure 3.2: Example of an APDs internal structure. The layer widths are not in scale, The anti-reflective coating is often used also as photo-converter.

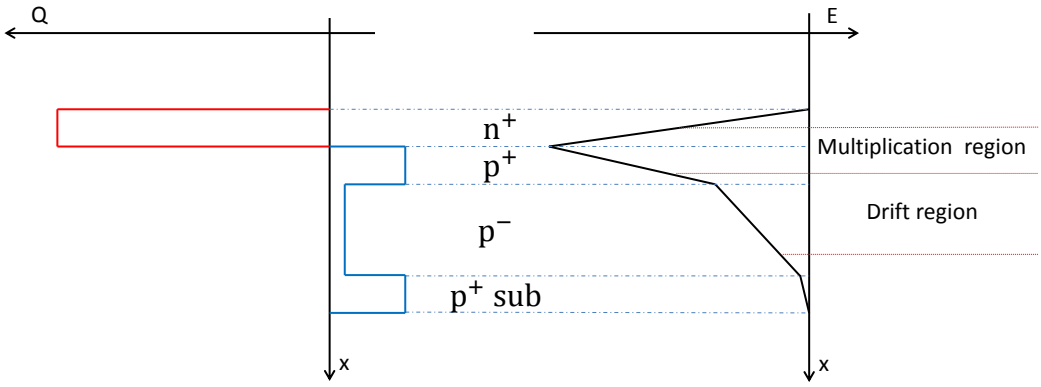

Figure 3.3: APD charge distribution (left) and electric field (right).

process and the signal is proportional to the initial ionization. We talk about GM-APD when $V_b > V_{break}$: both electrons and holes perform secondary ionization and a self propagating avalanche starts meaning that, without quenching, a steady current

flows indefinitely in the device. Simultaneously the rising current in the GM-APD generates an increasing voltage drop through the quenching resistor, reducing the effective V_b seen by the device. When the voltage is reduced to V_{break} the avalanche is quenched, and after the operating voltage is slowly restored trough R_q. The value of R_q has to be high to prevent V_b to rise again before the avalanche is completely dumped: typical value are 100-400 kΩ. Due to this behaviour the output signal of a GM-APD does not depend on the amount of primary ionization and in this sense it behaves like a digital sensor. The bias voltage is typically of 1-2 V above the V_{break} of the device. The voltage exceeding V_{break} is often referred as the *over voltage* V_{ov} and many parameters of the sensor critically depend on its value.

The output shape of a GM-APD can be inferred looking at the cell modelization of figure 3.4, where we can find the equivalent circuit of a GM-APD[95] together with a waveform acquired during the tests described later. The resistor R_s in the schematics represents the bulk resistance. In order to have a working device the condition $R_s << R_q$ must be satisfied. When the device is in ready mode the switch

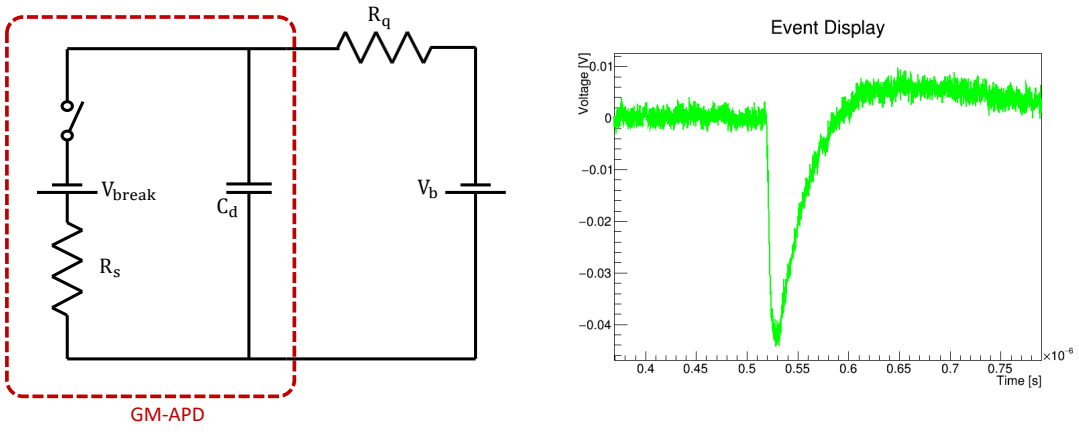

Figure 3.4: GM-APD equivalent circuit (left) and example of an output signal (right). The signal as been acquired with the oscilloscope during the measurement campaign. The event display is provided offline with the software that I developed.

is open and the voltage across the APD equals V_b. The primary ionization triggers the switch closure and the capacitance discharge through R_s until the voltage reaches V_{break}. Later the initial condition is slowly restored through R_q. This recovery time introduces a dead time in the APD, during which it is insensitive to further radiation.

The cell signal will show a fast leading edge, with a time constant $\tau_l = R_s C_d$, and much slower trailing edge, with $\tau_t = R_q C_d$. For the detector used in this work we got a leading time of ~ 1 ns and a trailing time of ~ 40 ns. The time for a complete pixel recovery can be considered around ~ 100 ns. The output signal amplitude depends mainly on the detector capacitance C_d (proportional to the cell area) and the voltage applied: the cell gain, defined as the number of charges collected from a fired cells is usually $10^5 - 10^6$. To operate the device properly and obtain the best performance is necessary to collect the signal from the electrode closer to the avalanche region.

3.1.1 SiPM output characteristics

When multiple cells are connected in parallel to form a SiPM the resulting output is the sum of all the internal cell signals: the information about light intensity or particle flux is recovered. If the *Signal to Noise Ratio*[1] ($SNR^{(1)}$) of a single fired cell, defined as the ratio between the mean amplitude of the signal from one cell ($V_{amp}^{(1)}$) and the noise RMS (N_{RMS}), is above 2 is possible to count the number n of cells simultaneously fired. The signal is quantized with an amplitude $V_{amp}^{(n)} = n \cdot V_{amp}^{(1)}$ as show in figure 3.5.

The separation between the peaks, clearly visible for low counting, became lower when the number of fired cells is high. This is mainly due to fluctuations in the cell gains, that mainly depend on small differences in the V_b effectively seen by the cell. Still, the uncertainty on n remains always of few counts. The resolution in the number of cell as well as the SNR have a strong dependence from the applied V_{bias}, being related to the gain of the single cell.

When the application requires a precise measurement of the incident flux there is another parameter that must be considered, the *Photon Detection Efficiency* (PDE). Indeed when a particle/photon impacts in the sensor there is a certain probability that at least an avalanche is triggered: while for a particle this probability is close to 1 the same is not true for a photon. The PDE is the probability that a an incident photon of wavelength λ will produce an avalanche. The PDE is a function of wavelength λ and V_b and can be expressed as

$$PDE(\lambda, V) = \eta(\lambda)\epsilon(V_b) \cdot F, \tag{3.1}$$

[1] In this chapter I will refer to the quantities which depend from the number of simultaneously fired cells by adding a superscript which indicates the number of cells involved. Hence the SNR of a signal with n active cells will be $SNR^{(n)}$, similarly for the signal amplitude and, later, for the time resolution.

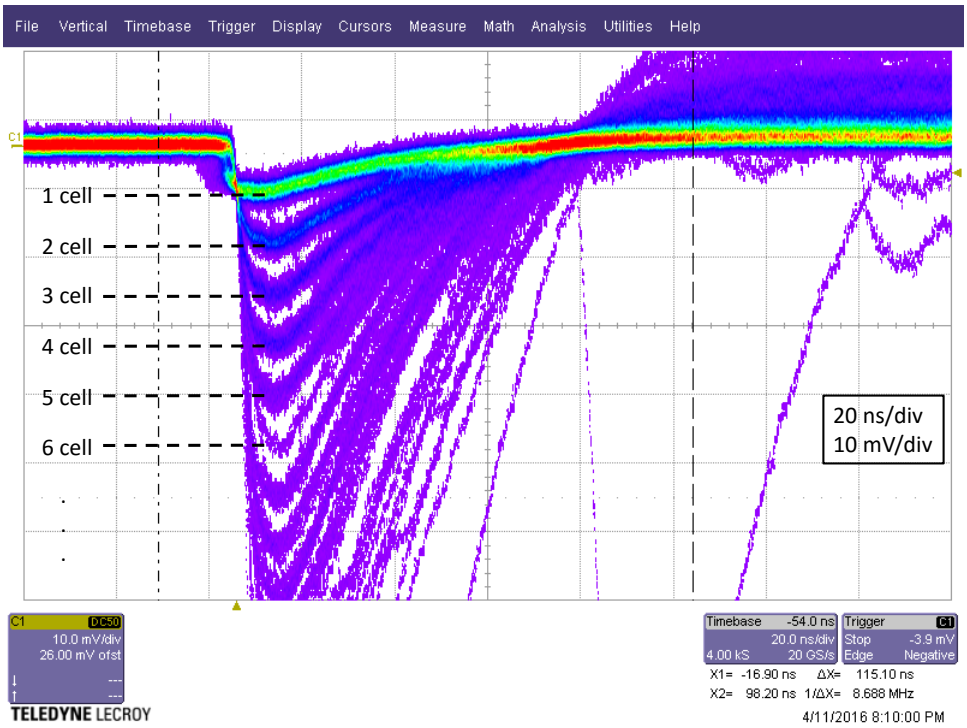

Figure 3.5: Oscilloscope shot showing multiple superimposed waveforms. The discrete nature of the SiPM output is clearly visible.

where $\eta(\lambda)$ is the quantum efficiency of silicon and $\epsilon(V_b)$ is the probability that an electron reaches the multiplication region and starts the avalanche. The *Fill factor* F determines the ratio between the SiPM area and the sensitive area, resulting from the gaps between adjacent cells.

The waveform acquired in figure 3.5 has been collected in few seconds without exposing the SiPM to any source (and the rate of cosmic rays in an area of 1 mm^2 is negligible). This open the discussion about the *dark counts* (DC) in SiPM devices. DCs are signals generated by thermally excited electrons either in the drift or in the multiplication regions of the cell. Such electrons can trigger the avalanche in the cell as if they were induced by a photon or by particle ionization. The response of the cell to a thermal electron is thus indistinguishable and take the name of dark count. The frequency of dark counts depends on the biasing voltage, that determines the probability of the thermal electron to trigger the avalanche, and of course on the temperature of the device. At room temperature and standard operating bias voltage (1-2 V above V_{break}) the dark count rate is in the range $0.1 - 1$ MHz. The effect of the temperature can be found in [96], where a dark count rate of ~ 40 Hz has been obtained operating the SiPM at -196 C°. Operatively we can assume that

the DC rate halves for each reduction of 10 C° in the temperature.

The DCs does not explain the presence in figure 3.5 of signals generated by more than one micro-cell. The presence of such signals is indeed related to the cell *optical crosstalk*, an additional component of SiPM noise. During the avalanche formation the carriers near the multiplication region can emit a photon during the acceleration. This photons are generated in the infrared region and can reach a neighbour cell, triggering a new avalanche. The process can be considered instantaneous, in the timescale of the signal formation, and multiple cells can be interested. Due to this effect one thermal electron can generate signals equivalent to an event involving multiple micro-cells. The crosstalk not only affects the DC events, but also the signal generated by the incident light/particles, reducing the detector resolution on the flux. On the other hand, when used for timing, crosstalk can be somehow useful, providing an additional (but not constant) amplification factor. The probability to have at least one cell fired with this mechanism is called the *crosstalk probability* and it is a function of the V_{ov} and the distance between neighboring micro-cells. For a precise statistics of the phenomenum multiple considerations must be done, which take into account the geometrical distribution of the cells, the possibility for a cell fired by crosstalk to propagate the effect to other cells and the saturation effect.

There is one last source of noise, the *afterpulses*, which are pulses correlated with a previous signal peak. Even if the mechanism is not completely understood and multiple sources may contribute, afterpulses are believed to be generated from electrons produced during an avalanche and trapped. After a delay that can be long from nanoseconds to microseconds they are released generating a new avalanche. In contrast to DC and crosstalk, the amplitude of the signal is not constant, but it depends on the recovery status of the cell and is not synchronous with the primary pulse. As for the previous noise source a strong dependence w.r.t the over-voltage is found.

The effect of the temperature on the SiPM behaviour is not limited to the noise but an effect on V_{break} is also present. As the temperature increase the V_{break} get lower, rising the gain of the cell and affecting all the parameters that depend on it. This effect can be however canceled if the measurements are performed w.r.t. V_{ov} instead of V_b. The breakdown voltage can be measured at different temperatures and the V_b adjusted to maintain the same V_{ov}. It must be noted that the temperature dependence of V_{break} is much lower than the DC dependence. Drift values of the order of 20 mV/°C are commonly reported in literature[96, 97].

The noise source of the SiPM, particularly the DCs, put serious limitation in the

usage of the SiPM as a direct MIP detector. The passage of a charged particles, either MIP or not, will release an huge amount of charge compared to the single couple produced by a photon, but the charge will be localized in one or two pixels. This will cause a signal indistinguishable from the DC, unless an external trigger is not used. When the external trigger is not available (or when the SiPM has to be used as a trigger) is possible to use multiple planes of SiPMs and trigger on their coincidence or use a light radiator. The radiator, either a cherenkov or a scintillator, will convert the energy released by the particle in multiple photons, that will hit multiple cells on the sensor. If the amount of generated light is enough it will be possible to distinguish the particle signal from the DC. Another solution is possible, that foreseen to operate the detector at cryogenic temperature, so that DC are greatly suppressed.

Obviously the most practical choice is to couple the SiPM to a scintillator, the strategy followed to build the trigger detectors. When a radiator is used is important to ensure that the light generated from a MIP is enough to have a signal above the dark count threshold. Is thus important to investigate the characteristics of the device that will be employed, with particular attention to the DC rate and to the crosstalk probability, which together determine the frequency of a DC above a given threshold. In the next section I will present the characterization of the devices employed in my work. The characterization will be extended also to other parameters (gain, SNR, counting resolution), providing important information to operate the device.

3.2 Sensors characterization

3.2.1 Sensor and electronics

The first step of my work consisted in the choice of the SiPM model to employ and in the definition of the polarization circuit. With this goal I designed a prototype board (fig. 3.6, top) conceived to host different types of SiPMs (also in terms of package/footprint) with different connection schemes. My final choice on the SiPM model fell on the S12571-100C from Hamamatsu[98]. The device has a surface of 1 mm^2, divided in 100 micro-cells of $\sim 100 \cdot 100$ μm^2, with a fill factor F=0.78. The sensor has a *"p on n"* structure which is suitable for the coupling with a plastic scintillator, having its PDE maximum located in the near ultraviolet region. Moreover the ceramic package ensures a great mechanical resistance and electrical isolation,

which proved useful for the building of the trigger detectors. Concerning the polarization scheme I choose the one reported in figure 3.6. Since the device is a *"p on*

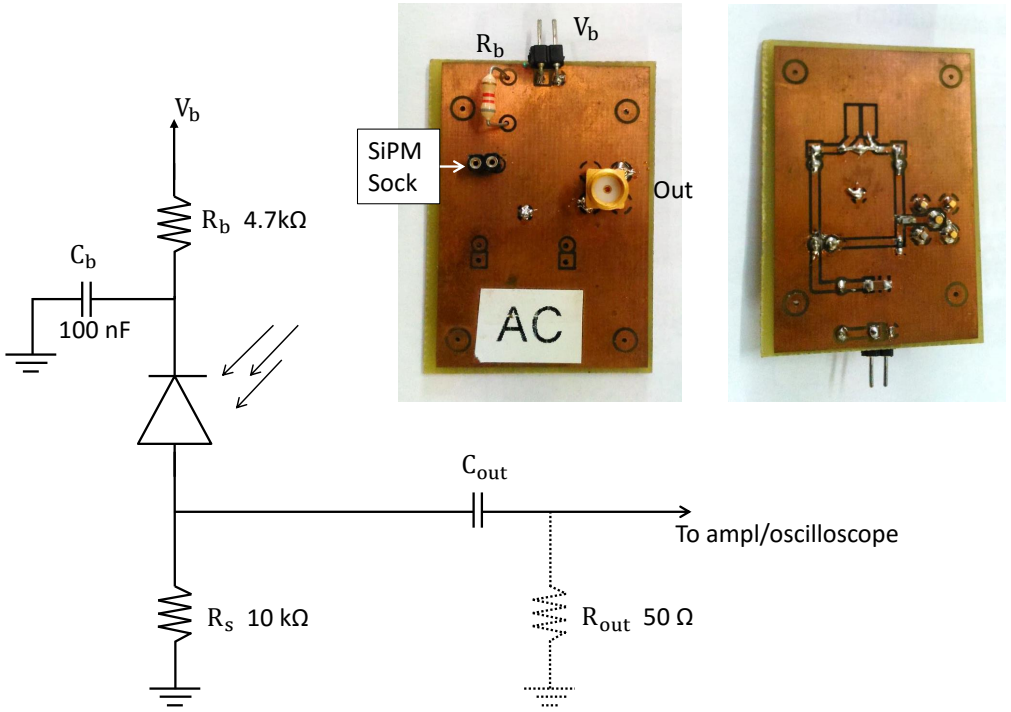

Figure 3.6: Picture of the SiPM prototype board (both sides). The final polarization scheme is also reported.

n" SiPM the charge has to be collected from the anode. The configuration which I adopted has multiple advantages, leading to a good flexibility:

- the output signal is referenced to the ground.
- there is no need to decouple the output from V_b.
- no negative voltages are employed.

The output capacitor C_{out} can be used to filter the signal or by-passed to allow a direct connection between the SiPM and the amplifier/oscilloscope. The output signal is generated by the current flow in a 50 Ω resistor. If a direct measure of the signal close to the anode with the probe is necessary the R_{out} resistor can be added. Instead, when the signal is readout through the SMA connector (see picture in fig. 3.6) the coaxial cable termination will grant the load resistance. The R_s will play an relevant role only when C_{out} is used, granting the device DC polarization.

The prototype board has been later redesigned (fig. 3.7.a) following the scheme just described. The new version can be mounted on top of a general purpose single

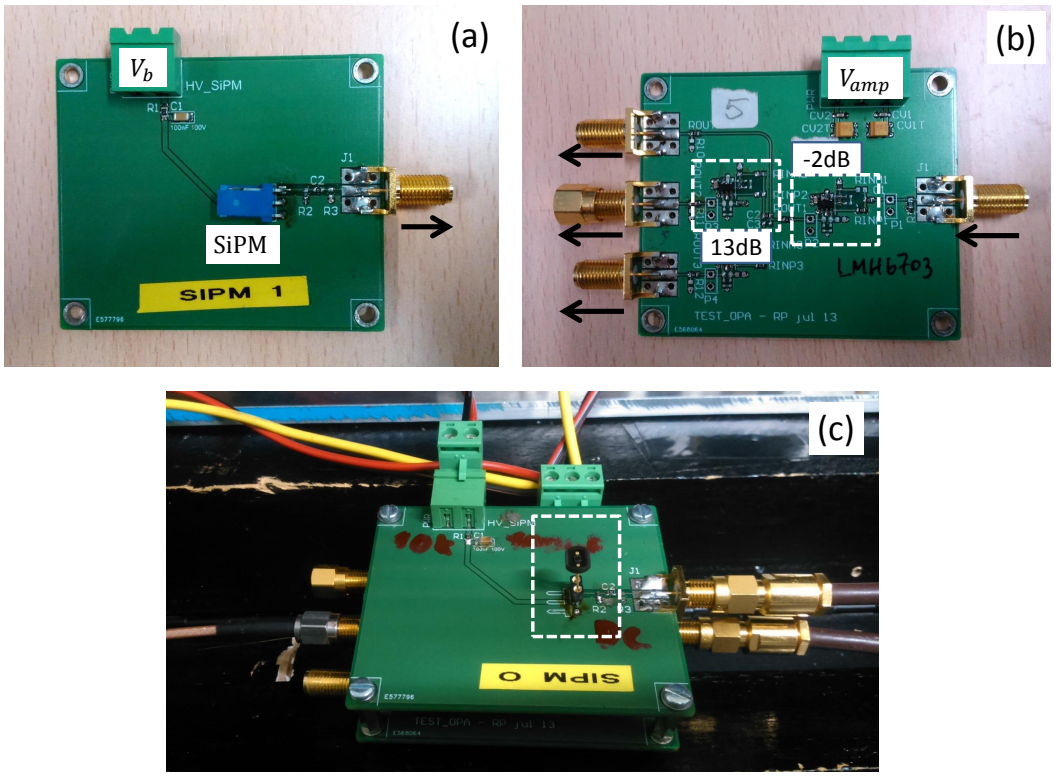

Figure 3.7: Electronic boards for SiPM operation. On top the polarization board (a) and the amplification board (b) are showed. On the bottom the mounted setup is presented, with the SiPM mounted on top. The same electronics is used in the trigger detector by substituting the SiPM socket in picture *c* with the connector in figure *a*.

channel amplifier board (fig. 3.7.*b*), developed in INFN-PISA. The amplification board is based on a two-stage amplification (with the LMH6703 operational amplifier), which gain can be adjusted by changing the resistors mounted on the board. The configuration of each stage (inverting or non inverting) can also be changed. Three different single-ended outputs are available, with different gains. After some tests I decided to set the first stage in inverting configuration, with a gain of 6 dB. The second stage was instead a non-inverting configuration with 14 dB gain (overall $G = 20$ dB). This value was the one which granted the best SNR and the polarity inversion allows to operate the SiPM with NIM electronics. After the amplifier I put a decoupling capacitor of 10 nF so that, together with 50 Ω termination, an

high pass filter is formed. In this way I can cut the long tails of the signal without reducing significantly the amplitude, so that a reduction of pile-upped signal is possible. The final setup used for the device configuration is showed in figure 3.7.*c*, with the SiPM under test mounted on top. The same electronics will be used later in the trigger detector. The amplified output signal was finally readout with a LeCroy SDO3010 oscilloscope (3 GHz bandwidth, 20 GS/s).

3.2.2 Breakdown voltage

As mentioned before is always good practice when working with SiPM to refer all the measurements w.r.t. the over voltage V_{ov}. Therefore a determination of the V_{break} must be done. To reduce the temperature effect all the data have been collected in few hours, in a closed box with an almost constant temperature of 21 ± 1°C. To measure the V_{break} I studied the I-V curve of the device. A scan of V_{bias} has been performed measuring the current drown from the device with a picoammeter. The results reported in figure 3.8 are obtained from two twin devices ($S_{\#0}$ and $S_{\#1}$), both showing a similar behaviour. In the figure we can appreciate the linear behaviour for $V_b < 64V$, while at higher voltage a step current increase is found, as expected. For a good measurement of V_{break} I collected multiple measurements in the range $64 - 65$ V with $S_{\#1}$(magnified in the figure). I performed a linear fit with the point collected at $V_b < 63V$ and then I extrapolated to higher values. I defined the V_{break} as the point where the measurements deviate from the linear regression. The final value was $V_{break} = 64.15 \pm 0.05$ V.

3.2.3 Sensor performances

The SiPM and the electronics were put inside a black box and the oscilloscope was used to acquire dark signals. Indeed, for our previous discussion, such signals are indistinguishable from the photon induced signals and can therefore be used to study the SiPM performance without providing external stimuli. I collected 20 samples of 30K events at different V_{ov} in the range $0.85 - 2.85$ V, equally spaced. Moreover bigger samples of $\sim$ 100K events were collected at V_{ov} =1.85, 2.15 and 2.45 V for a more precise determination of the afterpulsing and DC. All the events were acquired in self-trigger with threshold of 3.5 mV that, as will shortly see, corresponds to ~ 0.5 $V^{(1)}_{amp}$. On each trigger a window of 5 µs is recorded, with the triggering edge centered at 500 ns.

Looking at the waveform examples reported in figure 3.9 is clear that a multi-

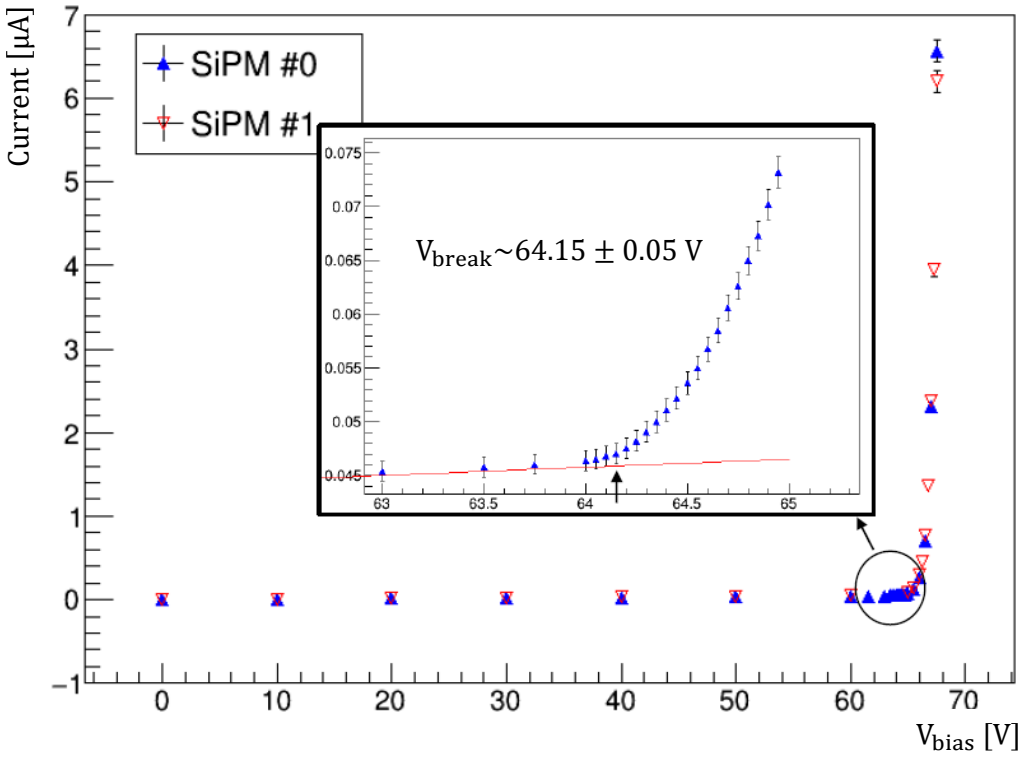

Figure 3.8: I-V curves for two Hamamatsu S12571-100C SiPM. For the device #0 the area around the V_{break} has been magnified to show the deviation from the linear response.

peak identification algorithm is needed, since simple algorithms based on multi-thresholds (Schmitt trigger like) or the functions found in the ROOT framework does not give good results. I developed an analysis suite (C++) with multiple built-in function designed to be used with oscilloscope data (fit algorithms, time resolution calculation, DSP, signal parametrization). I used the same suite also for the diamond sensors study. The flexibility of the code allows to perform precise measurements on a large signal varieties (SiPM, diamond, digital pulses) by changing few lines of code and multi-channel analysis is also available to extract timing information.

To identify all the peaks in the waveform a threshold V_{th} is first decided on the base of a very raw study on the waveform sample. Than the waveform measured voltage W_v is scanned. If at a certain time T_{th} the condition $W_v > V_{th}$ is met[2] a *Region of interest* (ROI) of 1 μs is defined, starting at T_{th}. A series of linear

[2]All the amplitude values are provided with positive sign. Negative signals are inverted by the analysis code prior the analysis steps.

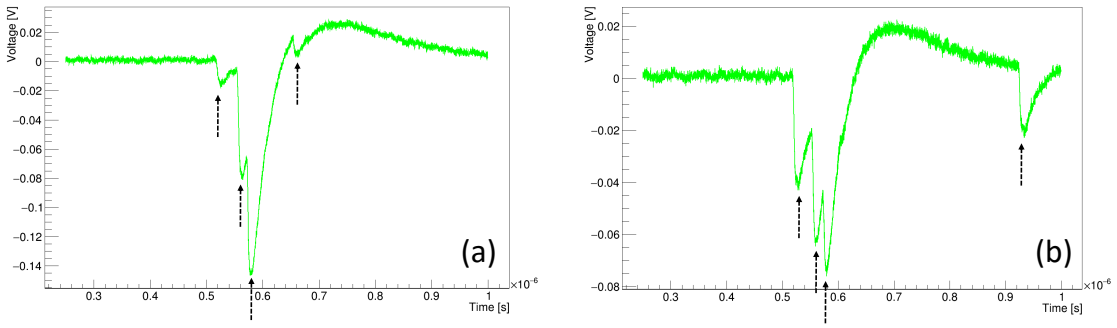

Figure 3.9: Examples of SiPM waveform with multiple peaks. Multiple peaks, coming from afterpulse and DC can be found in a short interval. The identification can not rely a multi-threshold methods.

interpolations is than performed, with the $n-$th fit covering the range $T_{th} + 5 * n < t < T_{th} + 5 * n + 30$ ns, so that a large overlap is provided. The slope of the fit is than used to identify the rising (falling) edge of the signal, defined from the fitting intervals where the fit slope is above (below) a given threshold. The length of the fitting interval and the overlap region, as well as the slope thresholds, have been carefully optimized to maximize the discrimination between the noise and signal. A peak is defined when both rising and falling edges are found within 20 ns (4 fit intervals). For each peak the local maximum is computed and the corresponding time extracted. If multiple peak are found the ROI is redefined starting from the last one. When the ROI region is exited the scan of the waveform is continued until a new ROI is found or the end of the data sample is reached.

Many sensor parameters can be extracted by the study of the signal amplitude distribution and the measurements of their leading time t_l^{20-80} (defined as the time that the signal takes to go from 20% to 80% of its maximum amplitude) and the noise RMS. The analysis procedure which I followed to extract such parameters from the recorded waveforms is described in section 4.3.2. The only remarkable difference arise from the need to exclude the signals which are summed to some previous signal, since they can degrade my measurements. To exclude this signals I first locate all the peak in the waveform with the procedure described above, and then I performed the analysis only on the first signal for which a region of 500 ns (before its maximum) without other peaks was found. The noise RMS and the signal leading time have been found independent from the V_{ov}, with value of $N_{RMS} = 0.83 \pm 0.03$ mV and $t_l^{20-80} = 2.5 \pm 0.1$ ns respectively. While a constant behaviour was expected for N_{RMS}, the same was not obvious for the leading time. An example of the amplitude

distributions obtained can be found in figure 3.10. The distribution peaks appear

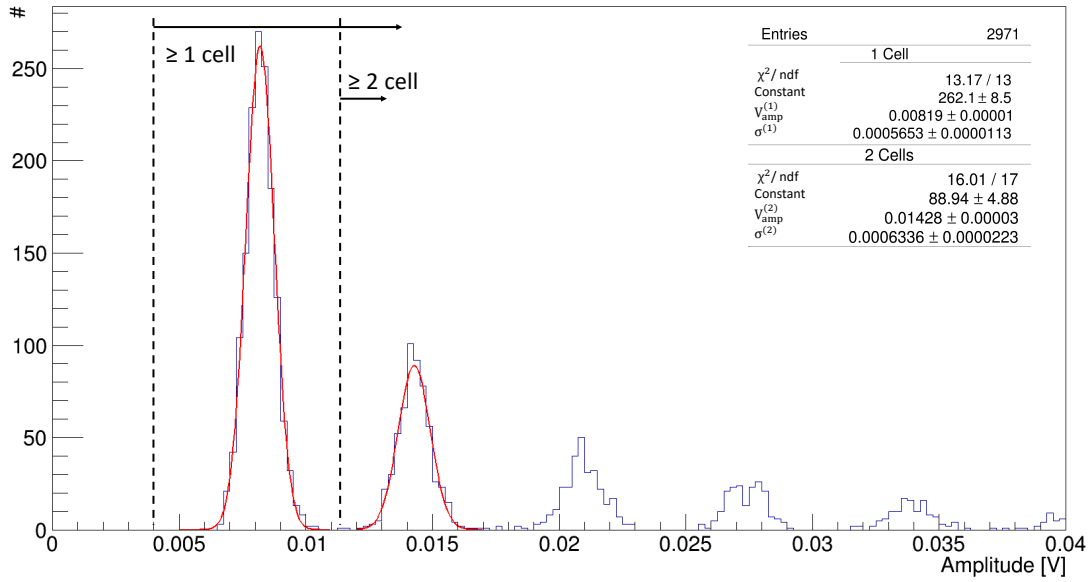

Figure 3.10: Amplitude distribution for DC signal with $V_{ov} = 1.85$ V. The fit on the single and double cell polpulations are reported.

well separated and a gaussian fit can be performed on the first two peaks of the distribution obtaining the $V_{amp}^{(1,2)}$ of the two populations.

With such measurements I could extrapolate some of the sensor parameters already introduced: cell gain, $\mathrm{SNR}^{(1)}$ and crosstalk probability. To such parameters I also added the resolution power RP, defined as

$$RP = \frac{V_{amp}^{(2)} - V_{amp}^{(1)}}{\sigma^{(2)} + \sigma^{(1)}} \tag{3.2}$$

where $\sigma^{(n)}$ is the standard deviation of the gaussian fit on the $n-$th distribution amplitude peak. This parameter give a feeling of the effective capability of the instrument to count the number of photons received and is directly linked to the energy resolution when coupled to a light radiator. The gain of the cell in terms of signal amplitude can be defined with the difference $V_{amp}^{(2)} - V_{amp}^{(1)}$. This methods leads to a better measurement respect to the comparison between $V_{amp}^{(1)}$ and the noise pedestal. The same values of $V_{amp}^{(1)}$ can be used to compute the $\mathrm{SNR}^{(1)}$. The determination of the crosstalk probability can indeed be done computing the ratio between the number of events with ≥ 2 active cells $N_{\geq 2}$ and the number of events with ≥ 1 active cell $N_{\geq 1}$:

$$CP = \frac{N_{\geq 2}}{N_{\geq 1}}. \tag{3.3}$$

The results of this analysis is reported in figure 3.11, where some additional details are provided.

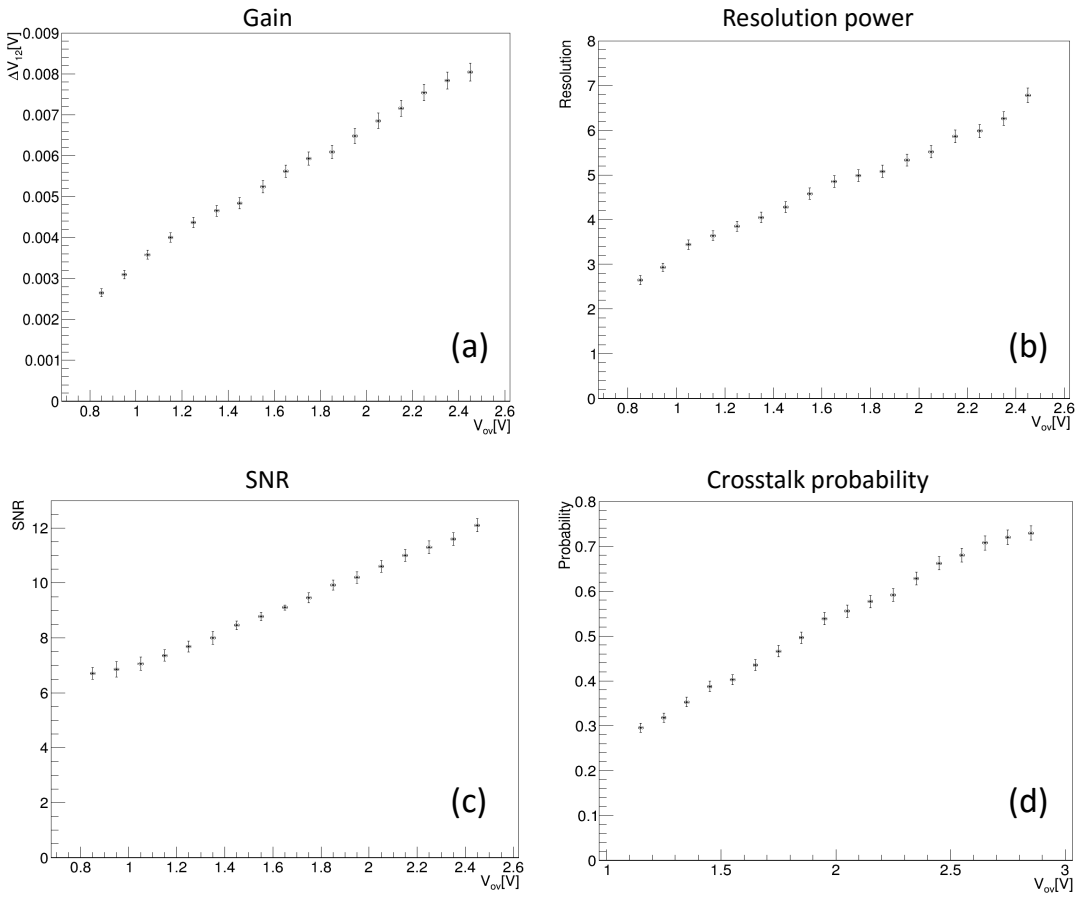

Figure 3.11: Gain(a), resolution power(b), SNR(c) and crosstalk probability(d) as a function of V_{ov}. In a, b, c the points with $V_{ov} > 2.45$ has not been computed because the change in the oscilloscope resolution (needed for the intensity of the signal) leads to a bigger noise RMS, dominated by the oscilloscope resolution. In d points with $V_{ov} < 1.15$ are not measured because the poor SNR reduce the efficiency in the identification of single cell signal, with a subsequent overestimation of the crosstalk probability.

With the exception of the crosstalk probability, all the other measurements depend from the electronics employed. Since the electronics is the same that will be used for the final detector, such values are of great interest for the system characterization.

3.2.4 Afterpulsing and dark counts

The study on the DCs and on the afterpulses has been performed on the larger data samples collected at V_{ov} =1.85, 2.15 and 2.45 V. For each waveform I run the peak finder algorithm and than I compute all the time differences ΔT_{12} between consecutive maxima. The distribution of $\Delta T_{12} < 1.7$ µs is reported in figure 3.12 for V_{ov} =2.15 V. Two exponential contributions are present. The one with the shorter

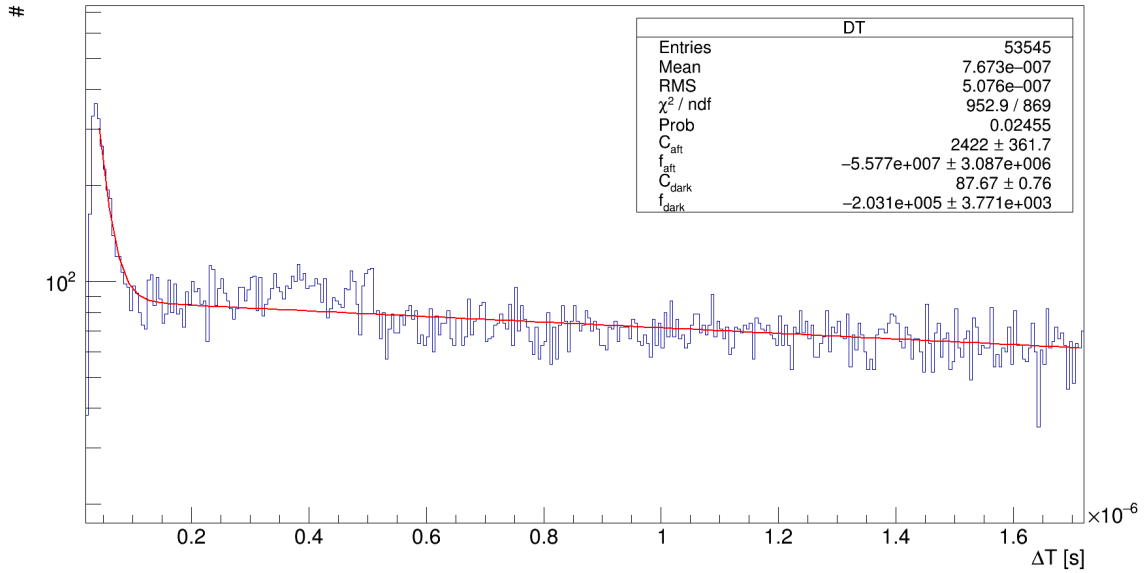

Figure 3.12: Time difference distribution between consecutive peaks. The fit with the function (3.4) has been performed on the range $0.035 < \Delta T_{12} < 4.5$ µs but here I report only the region close to 0 to better show the two exponential contribution.

time constant is related to the aftrepulse, while the other is related to the DC. I performed a double exponential fit on the data in the interval $0.035 < \Delta T_{12} < 4.5$ µs with a the function

$$f(x) = C_{aft} e^{-x \cdot f_{aft}} + C_{dark} e^{-x \cdot f_{dark}}. \tag{3.4}$$

The lower limit in the fit range is set because the identification of peaks closer than 30 ns has lower efficiency, depending on the signal relative magnitude.

The afterpulse probability has been computed by integrating the two contributions in the range $0 - \infty$ and taking the ratio between the two values. The errors in the probability computation has been obtained by varying the fit parameters in their confidence intervals. In table 3.1 the results on the three data samples are reported. For the afterpulse I reported the parameter $\tau_{aft} = 1/f_{aft}$, being the characteristics time of the afterpulse more interesting than the frequency. The results

V_{ov} [V]	C_{aft}	τ_{aft} [ns]	C_{dark}	f_{dark} [KHz]	P_{aft} [%]
1.85 ± 0.05	$2.72 \cdot 10^3 \pm 2.3 \cdot 10^2$	21.8 ± 0.8	92.3 ± 0.8	210 ± 4	13.5 ± 2
2.15 ± 0.05	$2.42 \cdot 10^3 \pm 3.6 \cdot 10^2$	17.9 ± 1	87.7 ± 0.7	203 ± 4	10.0 ± 2
2.45 ± 0.05	$4.46 \cdot 10^2 \pm 1.4 \cdot 10^2$	21.5 ± 2.9	61.2 ± 0.6	162 ± 4	2.5 ± 1

Table 3.1: Summary of the afterpulse and DC measurements.

show an afterpulse probability of the order of $\sim 10\%$ also for high value of V_{ov}, well below the typical values ($\sim 30 - 40\%$), as expected from the sensor manufacturer declaration[98]. The DC rates, as the afterpulse probability, increases with the bias from ~ 160 KHz up to ~ 210 KHz.

Based on this measurements I decided to set the nominal operating voltage at $V_{ov} = 2$ V (the maximum value recommended by the manufacturer), and this value has been used in the timing measurements reported hereafter. This value can grant the best gain, PDE and time resolution achievable without risk of sensor damage. This value can be sustained since the trigger system uses at least two sensors, triggering on their coincidence, and because the presence of a scintillator generates a signal with multiple cells involved, allowing an high discrimination threshold (several times $V^{(1)}_{amp}$). If instead the detector had to be used without radiator, exposed directly to the beam, this V_{ov} would have been too high. Indeed when triggering on the coincidence the rate of accidental coincidences f_{ac} can be predicted[121] as

$$f_{ac} = W \cdot f^2_{dark}, \tag{3.5}$$

where W is the time that the signal stay above the discrimination threshold for each DC. For the discussion in section 3.1.1 the signal from a particle will usually involve only one cell, justifying the usage of f_{dark} in equation 3.5 (the discrimination threshold must be below $V^{(1)}_{amp}$). Considering $W \sim 10$ ns we get $f_{ac} \sim 400$ Hz.

3.2.5 Laser test

The time resolution of the system was tested before the final detector assembly. The expected time resolution can be computed as a combination of the previous measurements. The order of magnitude of the time resolution σ_t of a detector can be indeed theoretically computed[121] as

$$\sigma_t = \frac{t_l^{10-90}}{SNR} = \frac{1.6 \cdot t_l^{20-80}}{SNR}. \tag{3.6}$$

With the previous measurements is thus possible to predict the timing performance of the sensor at different V_{ov} and for different mean number of photons. As an

example the resolution expected with $V_{ov} = 2$ V on a single photon will be ~ 360 ps. It must be kept in mind that this is just a very raw estimation since it does not take into account the internal processes of the SiPM. For example different wavelengths will convert at different depth in the sensor and hence the avalanche will start with a certain jitter. The time for the photo-electron to reach the multiplication region depends moreover on the bias voltage, which modifies the mobility of the charge carriers. The time resolution estimation become even more difficult when we try to analyze event with $n > 1$ (even if fixed) cells involved. In this case not all the cells will be triggered by a photon, but some of them are caused by crosstalk or by a fast afterpulse event, so that different processes are overlapped.

To perform the timing measurements I used a laser driver from Picoquant (model PDL 800-B) coupled to a near ultra-violet picosecond laser to stimulate the sensor (fig. 3.13). The laser emission wavelength has been chosen to be similar to the

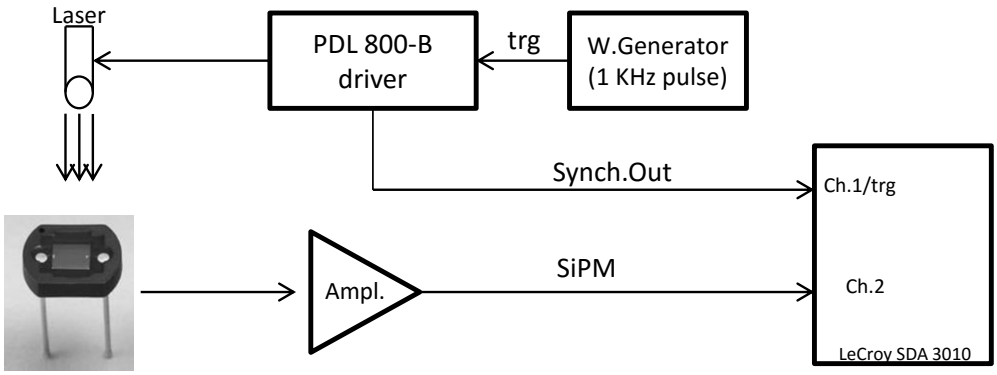

Figure 3.13: Setup used for the timing resolution measurements.

emission peak wavelength of the scintillator that I used in the detector final assembly. The driver pulse was triggered with a waveform generator at 1 KHz rate. To trigger the oscilloscope acquisition I used the driver synchronization output. Being the jitter of the synchronization output < 20 ps, the same signal can be set as timing reference. The laser was adjusted so that only few photons were collected in the SiPM for each pulse. Considering that the emission time of the laser at low intensity is ~ 40 ps, the total jitter of the reference system can be considered < 50 ps. On each trigger both the synchronization signal and the SiPM output were collected. To extrapolate the single photon time resolution (SPTR) I selected the events where the SiPM signal amplitude was in the range $5 < V_{ampl} < 11$ mV. Looking back at

figure 3.10 this corresponds to the events with only one active cell (almost the same for $V_{ov} = 2$ V). For each event surviving the amplitude cut a time difference ΔT_{12} is computed between the two signals. The resolution of the system is computed by measuring the standard deviation of the ΔT_{12} distribution. The extrapolation of ΔT_{12} has been done has described in the analysis algorithm #4 (with 30% threshold level) in section 4.3.2. The SiPM bias was kept at the nominal voltage of $V_{ov} = 2$ V, since I wanted to investigate the performance in the operational condition. Of curse better performances can be obtained raising the bias or changing the laser wavelength. The SPTR was found $\sigma_t = 293 \pm 10$ ps. The error reported in the resolution take into account the different values obtained when slightly varying the analysis parameters.

The same analysis as been performed by selecting the events with 2 active cells ($11 < V_{ampl} < 18$ mV). In this case we can not say that those events are generated by two photons. The signal can indeed be generated by a single photon event, followed by a cell crosstalk or by an afterpulse. The increase in the time resolution is however significant, with a value of $\sigma_t^{(2)} = 240 \pm 10$ ps.

In literature value of SPTR in the range 100-200 ps are usually reported[99, 100] for SiPMs, with strong dependence from the bias voltage and the wavelength of the incident light. I check if a better time resolution was achievable with a different amplification stage. To check if the time resolution critically depends on the amplification stage I first replaced on the amplifier board the LHM6703 with the OPA694 operational amplifier. The performances in terms of gain, SNR and the others parameters were almost the same but the time resolution get worse, due to the lower rise time of 3.3 ± 0.1 ns. The SPTR was found $\sigma_t = 396 \pm 11$ ps, while the resolution on double cell signals was $\sigma_t^{(2)} = 311 \pm 11$ ps.

Looking for a better amplifier I got an high-end broadband amplifier from CAEN (model A1423) with 1.5 GhZ bandwidth and selectable gain. I set the amplification gain to 21 dB, the closest value to 20 dB available, to perform a direct comparison. The leading time of the SiPM signal was reduced to $t_l^{20-80} \sim 0.8$ ns with a $\mathrm{SNR}^{(1)} \sim 18$. The timing resolution resulted greatly improved, as reported in table 3.2, with an SPTR $\sigma_t = 172 \pm 5$ ps and a double count resolution $\sigma_t^{(2)} = 137 \pm 5$ ps . In the same table other characteristics for all the three amplification stages are reported. We can see that, even if showing an overall superior performance, the RP with the A1423 amplifier is lower.

As a final test I measured the resolution of the SiPM without any amplifier, reading the signal output of the polarization board directly in the oscilloscope. In

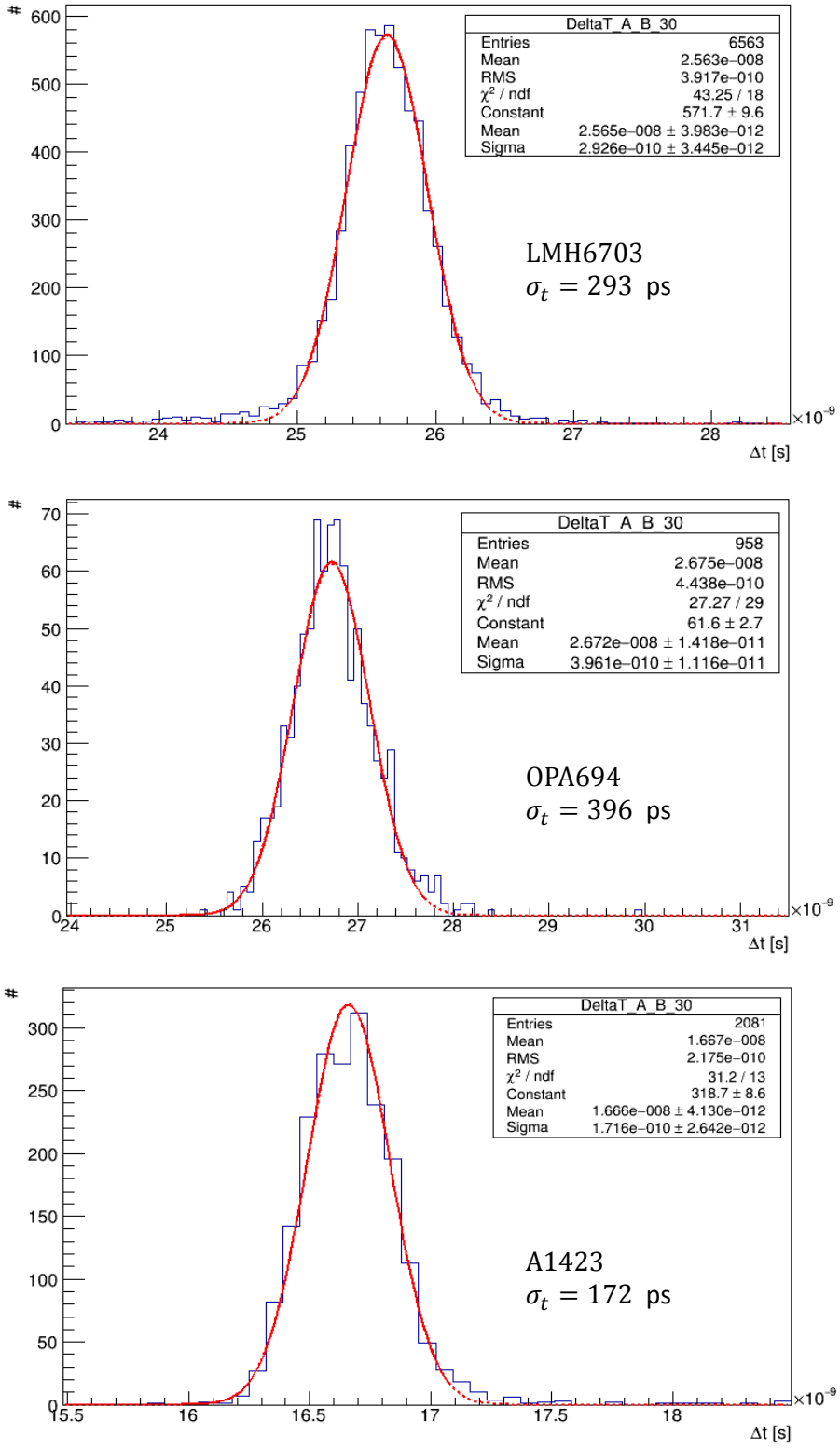

Figure 3.14: Single photon timing resolutions with three different amplifiers.

Ampl	Gain [mV]	RP	t_l^{20-80} [ns]	$SNR^{(1)}$	$\sigma_t^{(1)}$ [ps]	$\sigma_t^{(2)}$ [ps]
LMH6703	7.19 ± 0.01	5.41 ± 0.01	2.5 ± 0.1	11.1 ± 0.2	293 ± 10	240 ± 10
OPA694	6.85 ± 0.03	5.25 ± 0.1	3.3 ± 0.1	10.7 ± 0.2	396 ± 12	311 ± 10
A1423	7.60 ± 0.03	3.4 ± 0.1	0.86 ± 0.03	18.3 ± 0.1	172 ± 5	137 ± 5

Table 3.2: Parameter comparison with different amplifiers. The superscript in the resolution indicates the number of active cells in the events analyzed.

this case it was not possible to perform cell counting or to detect a single photon signal. Although this I tuned the laser power so that signals with mean $V_{amp} = 6.48 \pm 0.04$ were measured in the analysis. Considering the previous amplification of 20 dB we can assume that a mean number of $\sim$ 10 cells were fired (mix of photon, crosstalk and afterpulse induced signals). The timing analysis shows a time resolution of $\sim 93 \pm 2$ ps. The leading time was found the same as with the A1423 amplifier, meaning that no edge distortion was introduced by such amplifier, and the timing resolution with the A1423 can be considered close to the best achievable with this setup.

3.3 Detector assembly

The final detectors must operate as a trigger for the diamond sensor under test. As already discussed the use of a radiator is mandatory and the scintillator is the most practical choice. Diamond sensors have typical area of $4.5 \cdot 4.5$ mm^2, well below the typical test beam spot size. Using large pad scintillator leads to a large inefficiency in the acquisition, being many of the events collected empty. This can represent a problem if the acquisition rate is limited, as in the case of an oscilloscope. Hence the dimension of the scintillator must be as small as possible, but at the same time it must be able to generate enough photons from a MIP passage so that the detector efficiency remains high. Not only the scintillator but also the SiPM package and readout electronics must be compact, since it has to fit in a small RF shielded box and must be put as close as possible to the diamonds to reduce alignment difficulties. As a last requirements a time resolution below 1 ns on MIP was set as goal, useful for TOF discrimination at trigger level.

The scintillator manufacturing was made starting from a large tile of scintillator recovered from the upgrade of the CDF pre-shower detector. The characteristics were proved to be the same[101, 102], in terms of light yield and signal rise time, as

the Bicron-408 from Saint-Gobain[103]. I cut from the pad small fingers of dimensions $4 \cdot 4 \cdot 45$ mm^3. From this pieces I realize the smaller fingers reported in 3.15.*a*. The final pieces have a main body of $3 \cdot 3 \cdot 30$ mm^3 and the final part (1 cm long) is tapered with a maximum angle of $\sim 30°$ so that the light produced in the main body can be collected in a the final SiPM active spot of ~ 1 mm^2. Since any machine working was damaging the scintillator (except the initial cut) all the procedure is handmade, with a long series of final polishing steps (fig. 3.15.b). The fingers was then enveloped in an aluminium foils to enhance the light collection capability and an outer layer of black tape was added (fig. 3.15.*c*).

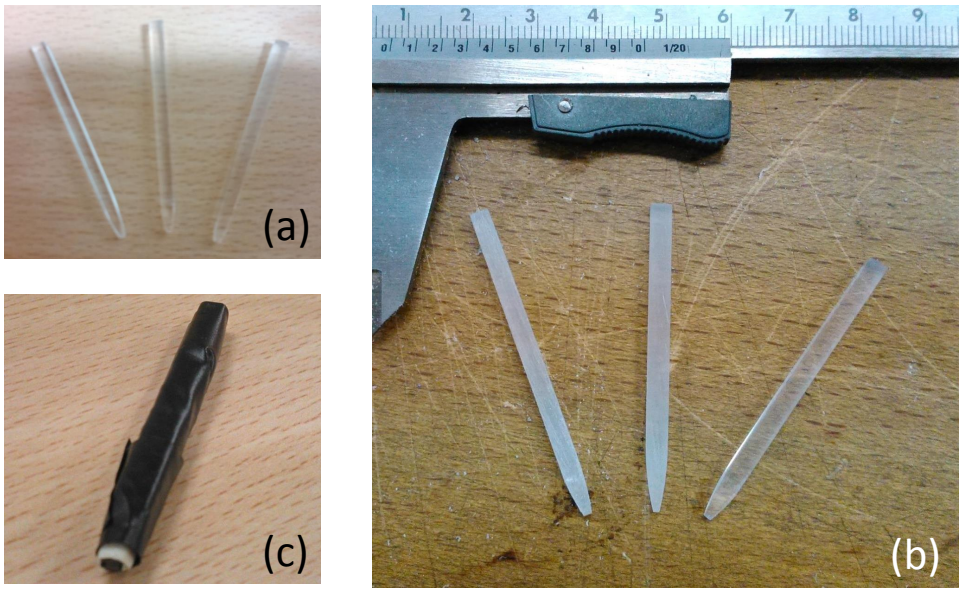

Figure 3.15: Picture of the scintillators manufacturing. In *a* three polished fingers are showed. After a first raw modeling the polishing has been made by hand, first with coarse-grained sandpaper, than with fine-grained and finally with abrasive paste. The three polishing steps are visible in picture *b* (left to right). The scintillator envelop is indeed reported in *c*.

The second fabrication step is the insertion of the SiPM into the special support of figure 3.16.*a*, *b*. External additional cable shield is added, even if it was reduced in the later assembly. The support provides mechanical strength to the device and allows for a better centering of the sensor spot. Finally I connected the scintillator finger and the SiPM with the aluminium structure visible in figure 3.16.*d*. While the SiPM position is already centered, the scintillator can be aligned by means of small screws. The connection between the SiPM and the scintillator is done with optical grease, that is also used to check the scintillator print on the center of the

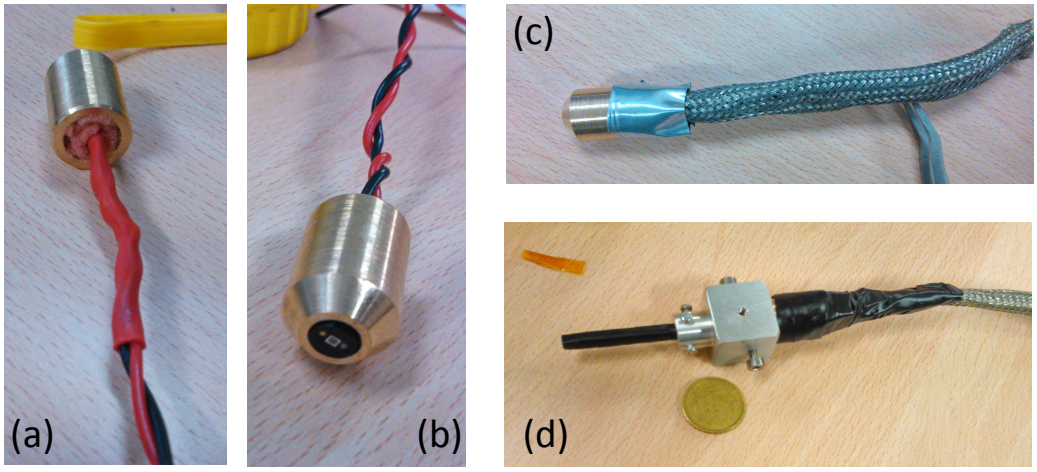

Figure 3.16: Trigger detector assembly picture. In a, b the mechanical support for the SiPM is showed. The SiPM is put inside a socket with a small hole (smaller than the SiPM size) in the center. Plastic material is added to provide mechanical resistance. After the shield is placed (c) and the final assembly can took place (d).

SiPM. Once aligned the SiPM can be removed and eventually substituted without the need for a new alignment. This can be useful in case of a damaging of the sensor, especially since it will operate in the beam spot. In figure 3.17 is possible to see a picture of the three detectors which I manufactured and a picture of one of the setup in which they have been involved. When put in cross configuration as in figure they can provide a trigger spot of ~ 3 mm^2, suitable for the diamonds.

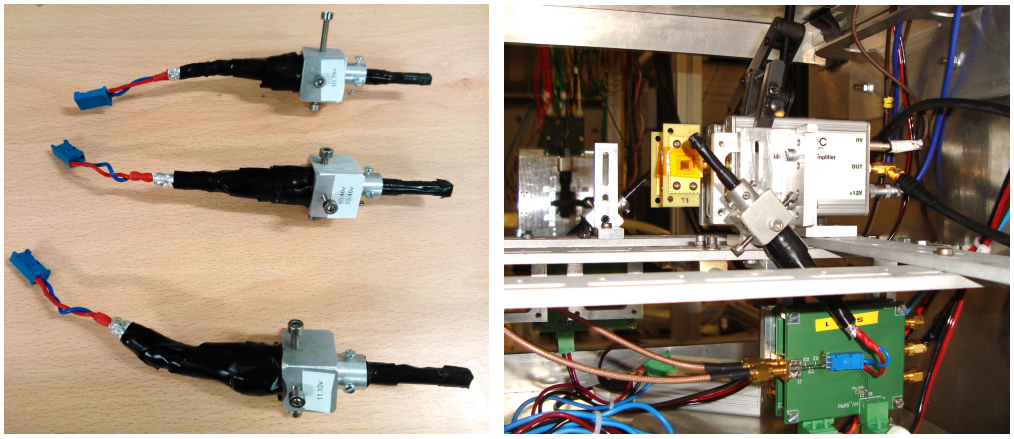

Figure 3.17: Picture of the three trigger detectors completed (left) and an example of one setup in which they have been used (right). The numbers written on the side of each module report their nominal operating voltage (50 V to be added).

With this design at least 10 photons are expected to be collected from a MIP particle, so that the overall time resolution of the sensor and the electronics, based on the measurements performed in the previous section, is well inside the specification. There was thus no need for the development of a new amplifier or to employ the A1423, and the one I used for the sensor characterization results as a time saving and cost effective (at least one order of magnitude) solution. When the SiPM is coupled to the scintillator the time resolution will thus be dominated by the decay time of the scintillator which, for the Bicron-408, is ~ 1 ns. When multiple photons are collected this time further reduces. Moreover the small size and the shape of the scintillator greatly reduce the time degradation due to internal light scattering, and the final detector can respect the specifications.

The detectors were used in a long series of test beams always performing without problems. They were usually operated triggering on their coincidence, after a discrimination with a threshold of ~ -50 mV. Almost zero noise was found on their coincidence, while their trigger rate with the beam was well above our DAQ storage capability. Unfortunately no efficiency studies have been performed on them. The timing performance was indirectly checked in the test beam described in the next chapter, where they were succesfully employed to measure the particle time of flight.

Chapter 4

Diamond Detectors

After the work on the SiPM detectors I moved on with the investigation of another detector technology for the TOTEM upgrade: diamonds, or more precisely synthetic Chemical Vapour Deposition (CVD) diamonds. Employment of CVD diamonds as a particle detector is already widely used, for example in [105, 106], but development of a diamond detector able to measure a single MIP particle with exceptional time resolution is a real challenge. To better understand strengths and weaknesses of this technology I will first describe in section 4.1 the diamond structure and characteristics, focusing only to the aspects involved in the present work. Later (sec. 4.2) I will describe how the diamond can act as a detector and what signal is expected from a MIP particle. Finally in section 4.3 I will present the results obtained with commercial detectors and electronics during test beams. Such results are the subject of [104].

4.1 Introduction to diamond detectors

4.1.1 The Diamond structure

An ideal crystal is constructed by an infinite repetition of identical, non-overlapping, groups of atoms, called *basis*. The set of mathematical points to which the basis are attached is called the *Bravais lattice*. All the points forming the lattice are connected by translation vectors

$$\mathbf{r}_n = n_1\mathbf{a}_1 + n_2\mathbf{a}_2 + n_3\mathbf{a}_3 \tag{4.1}$$

where n_1, n_2, n_3 are any tern of integer numbers. The non-coplanar vectors $\mathbf{a}_1, \mathbf{a}_2, \mathbf{a}_3$ are called *primitive translation vectors*.

The parallelepiped defined by the three primitive vectors is called *primitive unit cell* and its volume is $V = \mathbf{a}_1 \cdot (\mathbf{a}_2 \times \mathbf{a}_3)$. The choice of the primitive translation vectors and so the shape of the primitive cell is not unique. It is therefore useful to select the primitive cell with the highest possible symmetry. Moreover from the definition of Bravais lattices follows that it is possible to describe lattice using non-primitive cells, (called *conventional unit cells*), containing an integer number of primitive cells (fig. 4.1). An important and very useful choice for the primitive

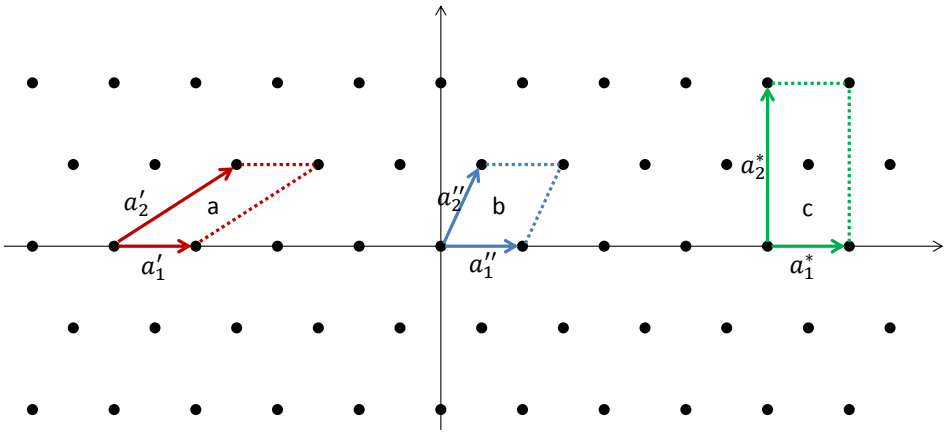

Figure 4.1: Example of unit cell for a bidimensional lattice. Three different choices for the unit cell are presented. **a)** and **b)** are both primitive cell while **c)** is a conventional cell used to better exploit the rotational symmetry of the crystal.

cell has been suggested by Wigner and Seitz. The cell can be obtained by bisecting with perpendicular planes the vectors joining one atom with the nearest neighbors, second nearest neighbors, and so on, and considering the smallest volume enclosed.

The complete geometrical description of a crystal can thus be done specifying the primitive translation vectors of the underlying Bravais lattice and a set of basis vectors, which individuate the equilibrium position of the nuclei of all the atoms in the primitive cell. If a conventional cell is used both set of vectors are defined using the conventional cell reference system. In three dimensions symmetry consideration lead to 14 different bravais lattices. One of the Bravais lattices is the *face centered cubic* (fcc), a lattice well described by a cubic cell with a lattice point at all its corners and in the middle of all the six faces. The diamond lattice, represented in figure 4.2, is indeed a fcc lattice with side $a = 3.57$ Å with a basis formed by two

carbon atoms in position

$$\mathbf{d}_1 = (0,0,0), \qquad \mathbf{d}_2 = \frac{a}{4}(1,1,1) \tag{4.2}$$

The three primitive vectors are:

$$\mathbf{a}_1 = \frac{a}{2}(0,1,1), \qquad \mathbf{a}_2 = \frac{a}{2}(1,0,1), \qquad \mathbf{a}_3 = \frac{a}{3}(1,1,0) \tag{4.3}$$

Each atom is thus surrounded by 4 atoms at a distance $(a/4)\sqrt{3}$ and 12 second neighbors at $(a/2)\sqrt{2}$, resulting in an atomic concentration of $1.76 \times 10^{23}\text{cm}^{-3}$ and a density of 3.52 gcm^{-3}.

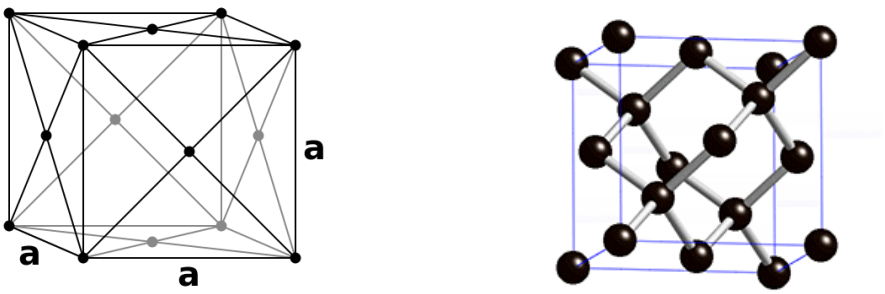

Figure 4.2: fcc diamond lattice conventional cell (left) and diamond structure (right).

To understand diamond properties is also very useful to define the *reciprocal lattice*, that is the description of the lattice in the reciprocal space. Given the three primitive translation vectors $\mathbf{a}_1, \mathbf{a}_2, \mathbf{a}_3$ we can define three vectors in the reciprocal space

$$\mathbf{k}_1 = \frac{2\pi}{V}\mathbf{a}_2 \times \mathbf{a}_3, \qquad \mathbf{k}_2 = \frac{2\pi}{V}\mathbf{a}_3 \times \mathbf{a}_1, \qquad \mathbf{k}_3 = \frac{2\pi}{V}\mathbf{a}_1 \times \mathbf{a}_2 \tag{4.4}$$

where V is the volume of the primitive cell in direct space. All points defined by vector of the type

$$\mathbf{k}_m = m_1\mathbf{k}_1 + m_2\mathbf{k}_2 + m_3\mathbf{k}_3, \tag{4.5}$$

with n_1, n_2, n_3 integer numbers, belongs to the reciprocal lattice. From the definition (4.1) and (4.5) and using relation (4.4) we can derive that the relation

$$\mathbf{k}_m \cdot \mathbf{r}_n = i \cdot 2\pi \tag{4.6}$$

holds for every $\mathbf{k}_m$ ($\mathbf{r}_n$) vector of the reciprocal (direct) lattice. From the definition of the lattice is also possible to prove[107] that a plane wave $exp(i\mathbf{k}\cdot\mathbf{r})$ has the lattice periodicity if and only if the wavevector $\mathbf{k}$ is a reciprocal lattice vector.

The Wigner-Seitz cell can be constructed also in the reciprocal space, and is reported in figure 4.3 for the diamond. The volume enclosed in the cell is referred to as the *first Brillouin zone*.

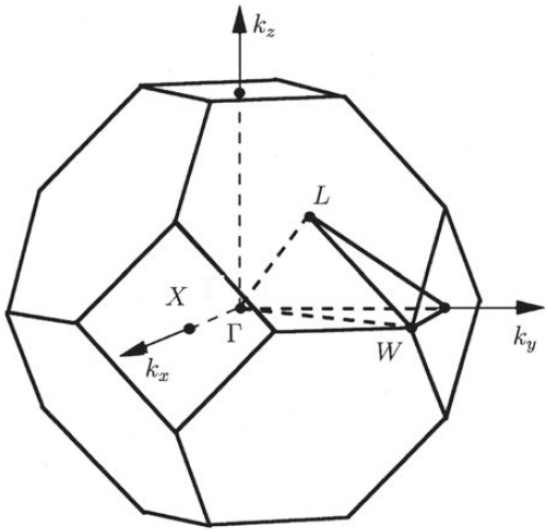

Figure 4.3: First brillouin zone for fcc lattice (truncated octahedron). Some high symmetry points are highlighted.

The diamond structure is an example of *covalent bond* common to elements in column IV of the periodic table, where the atom valence band is half filled ($[s^2p^2]$ for Carbon). When carbon atoms are close enough the s- and p- states of each atom hybridized in four tetrahedral club-shaped functions, leading to the covalent bond. Silicon, Germanium and grey tin can crystallize in the diamond structure, with different lattice constant a. This explains why almost all properties of diamond can be described with the same physics of semi-conductors.

4.1.2 Energy band structure

One of the elementary results of quantum mechanics is that a particle in a single quantum well can assume only discrete energy levels. Is possible to extend such result to model the crystal potential seen by a moving particle as a periodically repeated quantum wells: the model is known as Kronig-Pennay model[108]. If

the crystal dimension is much grater than the lattice constant a we obtain the formation of continuous energy band accessible to particle moving inside the crystal potential. The energy bands are actually regions of many discrete levels which are so closely spaced that can be considered as a continuum, while the *forbidden energy gap* are area with no available energy level. More precise band structure calculations are performed with different and more precise models, but certain assumptions are always done to facilitate the calculation. In figure 4.4 we report the band structure of the diamond obtained with the *linearized augmented plane wave method*: details on the derivation can be found in [107]. The energy levels are usually reported with respect to the momentum $\mathbf{k}$, but the projection on the energy axes can show better the band structure.

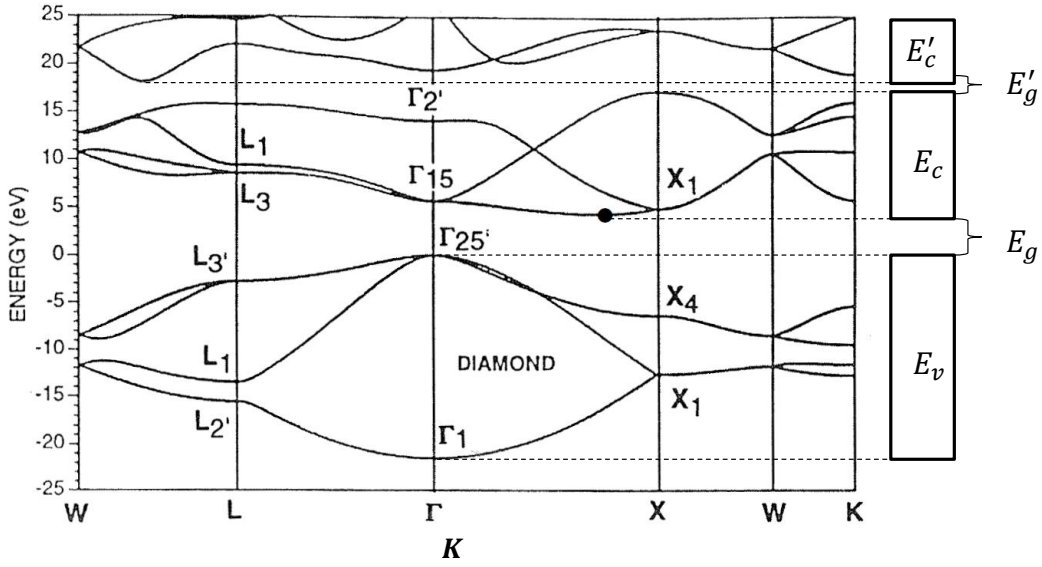

Figure 4.4: Band structure of diamond. The projection on the energy axes is also shown on the left.

If we compare the band structure with the reciprocal lattice reported in figure 4.3 we notice that the energy bands are reported only for the first brillouin zone: it is a direct consequence of the periodicity of the crystal. Indeed in *single electron approximation* the electron wave in a periodic potential

$$U(\mathbf{r}) = U(\mathbf{r} + \mathbf{r_n}) \tag{4.7}$$

with $\mathbf{r}_n$ vector of direct lattice will be the solution of the Schrodinger's equation

$$\Big(-\frac{\hbar^2}{2m}\partial_{\mathbf{r}}^2 + U(\mathbf{r})\Big)\Psi(\mathbf{r}) = E\Psi(\mathbf{r}) \tag{4.8}$$

Is proved (*Block theorem*[107]) that the solutions are plane waves modulated by an appropriate function with the lattice periodicity

$$\Psi_n(\mathbf{r}) = u_n(\mathbf{r})e^{i\mathbf{k}\cdot\mathbf{r}}, \qquad \text{whith } u_n(\mathbf{r}) = u_n(\mathbf{r}+\mathbf{r_n}); \tag{4.9}$$

From this result we can directly derive that

$$\Psi_n(\mathbf{r}+\mathbf{r_n}) = e^{i\mathbf{k}\cdot\mathbf{r_n}}\Psi_n(\mathbf{r}); \tag{4.10}$$

Using equation (4.6) we see that the wavefunction does not change under translation in the reciprocal space $\mathbf{k'} = \mathbf{k} + \mathbf{k_n}$ if $\mathbf{k_n}$ is a vector of the reciprocal lattice defined by (4.5). This implies that knowing the band structure in the first Brillouin zone is enough to describe the band structure in all the reciprocal space.

Observing figure 4.4 we see that the maximum energy available in the *valence band* E_v (higher energy band for electron free states) is the point marked as Γ'_{25} while the minimum of the *conduction band* E_c (minimum energy band for electron unbound states) is marked with the black circles. At 0 °K and without external perturbation all electrons reside in the valence band, which is fully occupied, and none is free to move in the lattice. In order to participate to the current, becoming a *carrier*, an electron must jump to the conduction band; an electron promoted to the conduction band leaves an *hole* in the valence band which also contribute to the total current in the system. The band gap E_g between conduction and valence band is usually used to define conductors (no gap), semi-conductors (small gap) and insulators (big gap). For the diamond the gap is 5.47 eV, big enough to be usually considered as an insulator from the conductivity point of view. Electron-hole pairs are indeed continuously generated by thermal energy, but at same time recombination may occurs. Under stable condition an equilibrium is reached. The concentration of carrier for a crystal free of defects is:

$$n_i = \sqrt{n_c n_v} exp\Big(-\frac{E_g}{2k_B T}\Big) \tag{4.11}$$

where n_c and n_v are the density of states in the conduction band and valence band respectively, k_B the Boltzman constant and T the temperature. For diamond we have $n_c \sim 10^{20}\text{cm}^{-3}$ and $n_v \sim 10^{19}\text{cm}^{-3}$, giving at room temperature a carrier density of $\sim 10^{-27}\text{cm}^{-3}$, almost zero.

Looking at the band structure we must also notice that the conduction band and valence band extremal occur at different points of the Brillouin zone: the transition is not "vertical" and the semi-conductor is called *indirect*. Non-vertical transitions near the energy gap may occur but some source must supplies the momentum needed

for total crystal momentum conservation; an internal source can be phonons, that can accommodate any appropriate momentum and thus indirect transitions assisted by phonons become possible.

Finally, when dealing with particles in a crystal is very useful to define an *effective mass* as

$$\frac{1}{m^*} = \frac{1}{\hbar^2}\frac{d^2E(k)}{dk^2}. \tag{4.12}$$

The effective mass is thus correlated with the local curvature of the dispersion relation. Electrons and holes will have different m^* because they belongs to different energy bands. Effective mass can be very usefull in many calculation, since it can be proved[107] that carriers moving inside the crystal can be treated as free particles with $m = m^*$.

4.1.3 Crystal defects

When dealing with crystals we must always take into account the presence of defects, that lead to a distortion of the crystal periodicity and so of the potential. Ad example during diamond synthesization (see section 4.1.4) the presence of foreign atoms in the process can never be completely avoided, and different specimen will thus be present in the crystals. Another way of creating defects is the exposure of the crystal to ionizing radiation: this will be treated later. A large variety of defects is summarized in figure 4.5 and described hereafter.

Planar defects often arise during the crystal growing when different crystal merge together, generating a perturbation on the contact surface if the two crystals do not have exactly the same alignment. Actually the external surface of a crystal is also a surface defect because the atoms on the surface adjust their positions to accommodate for the absence of neighbouring atoms outside the surface.

Line defects, or dislocations, are lines along which whole rows of atoms in a solid are arranged anomalously. For example we can have an extra half-plane of atoms in a lattice. The dislocation is called a line defect because the perturbation produced in the lattice lies along a line along the top of the extra half-plane. The inter-atomic bonds are significantly distorted only in the immediate vicinity of the dislocation line.

Point defects usually involves only one or two atoms in the lattice. We call *vacancy* a defect when a lattice site is not occupied so that the nearest neighbour move closer toward the vacancy. In the opposite we talk of *interstitial* defect when we have an additional atom in the cell: in such case we can have *self-interstitial*

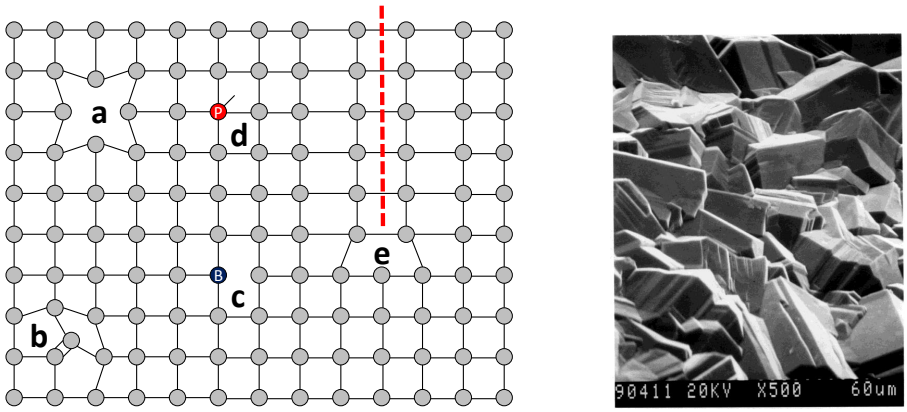

Figure 4.5: Example of crystal defects. On the right point and line defects: vacancy (a), self-interstitial (b), sostitutional (c,d) and half-plane (e, the dotted line indicates the line defect axis). On the right a microscopic scansion of a poly-crystalline diamond, showing multiple surface defects.

where the atom is a carbon, or *foreign-interstitial* where the atom is any other element. *Sostitutional* defects occur when a C atom of the ideal crystal is replaced by another atom. Particularly interesting for us are the *Frenkel* defects, where an atom leaves its place in the lattice, creating a vacancy, and becomes an interstitial by lodging in a nearby location. The concentration of Frenkel defects is usually much lower than the others for a new crystal, but they increase when the diamond is irradiated. When non-carbon atoms are involved in the defect we also talk of *impurities*.

Finally *grain defects* are volume of crystal characterized by an high concentration of defects or, even worse, were inclusion of a non-diamond material (usually graphite) is present.

Many electronic and optical properties of diamond depend on the concentration of defects. An electron in the conduction band may recombine with an hole in the valence band with the emission of a photon. The process is the opposite of the e-h pair creation and is called *radiative* recombination. However in the process both energy and momentum must be conserved, making the probability of recombination very rare for indirect semi-conductors. However, if we compare the expected lifetime of carriers[111] w.r.t the experimental results a big discrepancy is found, since the

experimental lifetime is much shorter than the expected. Other process like the *Auger* recombination, where a free electron recombines with a hole transferring its momentum to another free electron, show an even less probability, involving three particles in the process. The most important source of recombination are indeed crystal defects, which perturb the energy band structure by adding additional levels in the energy gap. For example in the case of substitutional defect with elements of group III an additional state near the valence band (*acceptor*) is created, since one nearest C atom will be left without one covalent bond. In the same way a foreign element of group V will crate a state near the conduction band (*donor*), since one electron of the atom is not bonded to any C atom (fig. 4.6). This states,

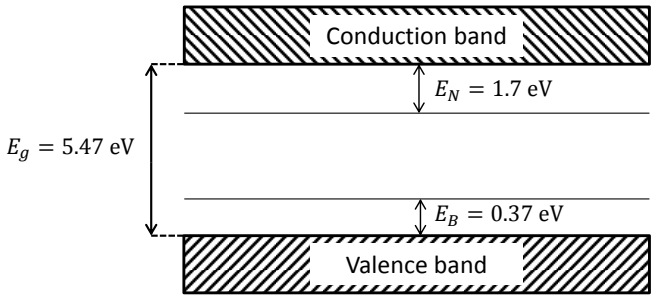

Figure 4.6: Energy levels crated by Boron and Lithium in diamond crystal. The band structure is projected on the vertical axis.

spatially localized in the area of the defect, may act as a *trapping* center, capturing an electron in the conduction band or a hole from the valence band. If both hole and electron are trapped recombination occurs, otherwise the carrier will be release after a characteristic time which spans from ns to μs or even more, depending on the defect and on the temperature of the crystal. Such additional level not only reduce carrier lifetime but also assists the creation of e-h pairs reducing the band gap. The overall result is a greater number of carriers with shorter lifetime.

4.1.4 CVD Diamond

Natural diamonds are not suitable for applications as particle detector for their high concentration of impurities. Synthetic diamonds can be grown with two techniques. The first use an high temperature (900-1300 °C) high pressure (45-60 kBar) process,

reproducing the condition for natural diamond formation. The latter, the CVD techniques, use lower temperature (<1000 °C) and low pressure (∼0.1 bar), producing the highest quality diamond to date. Without going into details, that can be found in [109], we will describe the process, even if each diamond manufacturer have its own secret "receipt".

A gas mixture of methane (CH_4), molecular hydrogen(H_2) and optionally an oxygen compound is introduced in a low-pressure reactor cavity, and a plasma is crated with a microwave generator or an hot filament. After the breakup of molecular hydrogen in atomic hydrogen carbon atoms are produced by stripping hydrogen atoms from the methane through the reaction

$$CH_x + H \rightarrow CH_{x-1} + H_2. \tag{4.13}$$

A substrate (molybdenum, silicon nitride, tungsten carbide or diamond itself) is placed under the plasma center and the free carbon atom can settle on it, starting the nucleation phase. Nucleation process, which leads to the formation of a new crystal, is still not completely understood and represent an active field of study. The description of the process is out of the scope of the present work, but the reader can find a model of nucleation in [110]. The process is very critical since graphite inclusion may arise in this stage. Many studies are indeed performed in methods for removing graphite or preventing its formation. One important role is again played by atomic hydrogen that etches non-diamond bonded materials from the surface of the crystal, particularly graphite. Atomic hydrogen play another important function in the last stage of the process, the crystals grown, removing hydrogen atoms residual bonded to the surface carbon atoms, leaving a diamond surface free of impurities and ready to receive other carbon atoms.

Diamond crated with such process are poly-crystalline (pCVD) diamond, since multiple nucleation area will lead to multiple crystals, with a columnar structure of grain (see figure 4.5), and consequently a large number of planar defects. The column size typically increase during the process so that some crystals are naturally selected in the process, eventually giving rise to a single crystal (sCVD) diamond. The use of sCVD diamond as substrate increase the efficiency of the process. The resulting crystal have better electronic quality than a pCVD diamond, but the time of grown are much longer, an so the costs. Moreover having a large area sCVD crystal is not easy and the usual dimension on market does not exceed $5 \cdot 5$ mm^2 area with 500 μm thickness.

Before being ready to be used as detector a diamond must be *metalized*. The surface has to be coated with a metal, that will than be wire-bonded or put in

direct contact with a pad. The contact must be stable, non-volatile and resists to mechanical stress. Moreover the contact must unsure a constant electric field when a bias voltage is applied and the contact surface between the diamond and the coating must be *ohmic*, that is the current across the junction must be linear with the applied voltage. This process is usually performed by a third party and also in this case the procedure is often not public. During this stage the detector can be divided in pixels of the desired geometry and size, simply making a pad metallization. With this procedure is thus possible to easily create the segmentations desired for the TOTEM upgrade (sec. 2.5-2.6).

4.2 Diamond for MIP detection

4.2.1 Principle and signal shape

Diamond properties discussed above make of it an excellent candidate for charged particle detection. The absence of free carriers ensure that under an external electric field no current will flow across the device. Although in real life leakage current will rise due to the presence of impurities, for diamond described in this works it remains of the order of few pA, and so there is no need to create a depleted area as in the silicon detectors.

The detector scheme proposed in figure 4.7 is a simple scheme for a detector as used in section 4.3; in chapter 5.1.2 we will introduce another solution. When a MIP pass through the crystal part of its energy is released to the crystal, generating phonons and electron-hole pairs[13]. If an external potential V_b is applied to the

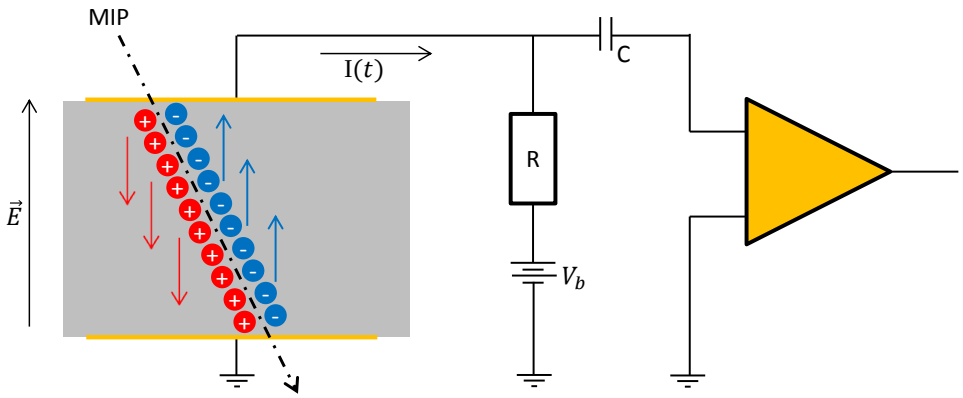

Figure 4.7: Detector scheme for diamond detector.

crystal an electric field **E** is created; the electrons and holes start to drift with a velocity $v_{d,e}(E)$ and $v_{d,h}(E)$ respectively toward the electrodes and a current $I(t)$ is thus induced on them. Such current can be amplified and then read. The decoupling capacitor in figure 4.7 is used to decouple the amplifier input from V_b.

The intrinsic signal shape from the diamond can be derived using the Shockley-Ramo theorem [121], describing the induced current on an electrode by means of a *weighting potential* Φ_w

$$I(t) = q\nabla\Phi_w \frac{d}{dt}\mathbf{r}(t) = -q\mathbf{E}_w v(t) \tag{4.14}$$

For a parallel plate configuration placed at distance d the weighting fields is $E_w = -\frac{d\Phi_w}{dx} = -1/d$. Since the charge will drift along the field axes we have the current $i(t)$ induced from a single carrier

$$i(t) = q v_d(x,t)/d \tag{4.15}$$

Assuming a time and position independent V_d, which means a constant uniform electric field in the crystal, the total current in the diamond will be

$$I(t) = q\Big((N_e(t)v_{d,e}) + (N_h(t)v_{d,h})\Big)/d \tag{4.16}$$

where $N_e(t)(N_h(t))$ are the number of electrons (holes) generated from the MIP but still not collected at the electrode. The passage of a particle is almost instantaneous and all the charges are generated at the same time, after their number will linearly decrease. After a transit time

$$t_{t,e} = \frac{d}{v_{d,e}} \qquad (t_{t,h} = \frac{d}{v_{d,h}}) \tag{4.17}$$

all the electrons (holes) are collected and their induced current become zero: the total charge induced will be $N(0)/2$. The signal generated from the diamond is reported in figure 4.8. If $t_{t,e}$ and $t_{t,h}$ are close the signal has a triangular shape. The almost zero rise time of the signal is excellent for timing measurements (from eq. 3.6).

Due to recombination is possible that not all carrier will be collected, reducing the signal. We can define a *Charge Collection Efficiency* as the ratio between the generated charge N(0) and the total induced charge N_i

$$CCE = \frac{N_i}{N(0)} \tag{4.18}$$

and the *Charge Collection Distance* as

$$CCD = \frac{N_i}{N(0)} \cdot d = CCE \cdot d \tag{4.19}$$

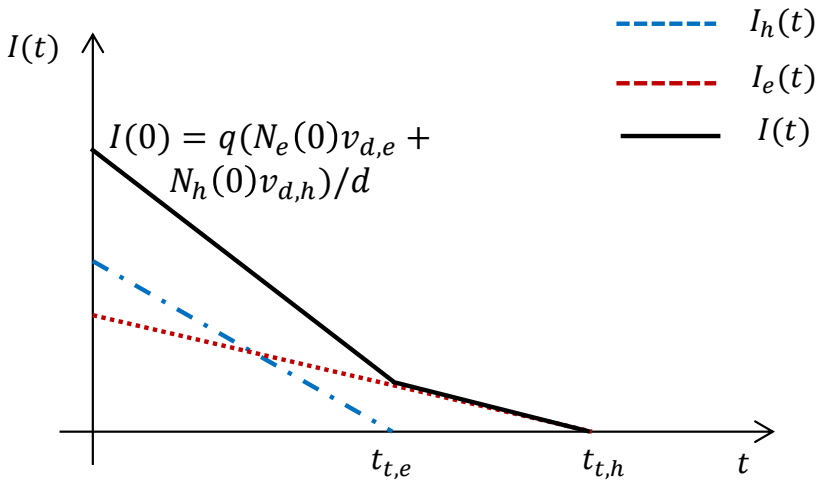

Figure 4.8: Current generated from MIP particle passing through a diamond detector assuming a constant electric field.

Thanks to the low impurity concentration and the absence of planar defects CCE for sCVD crystals is close to 1 (for a 500 µm crystal). For pCVD the value is much lower and the CCD are usually in the range 200-300 µm, giving a CCE∼50%. As we will see later, signal amplitude is critical for diamond sensors, and the choice of sCVD crystal is therefore obliged.

The signal from an ideal detector can be thus fully described from the knowledge of the amount of carriers generated from a MIP and the drift velocity.

4.2.2 Expected output

To estimate the amount of charge collected to the electrode we must first compute the number of e-h pairs generated from a particle passing through a diamond detector. A more precise value for the mean energy release of a MIP on diamond is given in [13]: taking into account density effect correction we get $dE/d\xi \sim 1.7$ MeVg^{-1}cm^2.

As seen before diamond is an indirect semi-conductor, that implies that the energy needed for e-h generation is greater than the energy band gap of 5.47 eV, since some additional energy will be used to excite phonon. This additional energy for many material has been measured by [113] and values are reported in figure 4.9.

For diamonds we have a mean excitation energy $E_{eh} \sim 16$ eV: the mean total

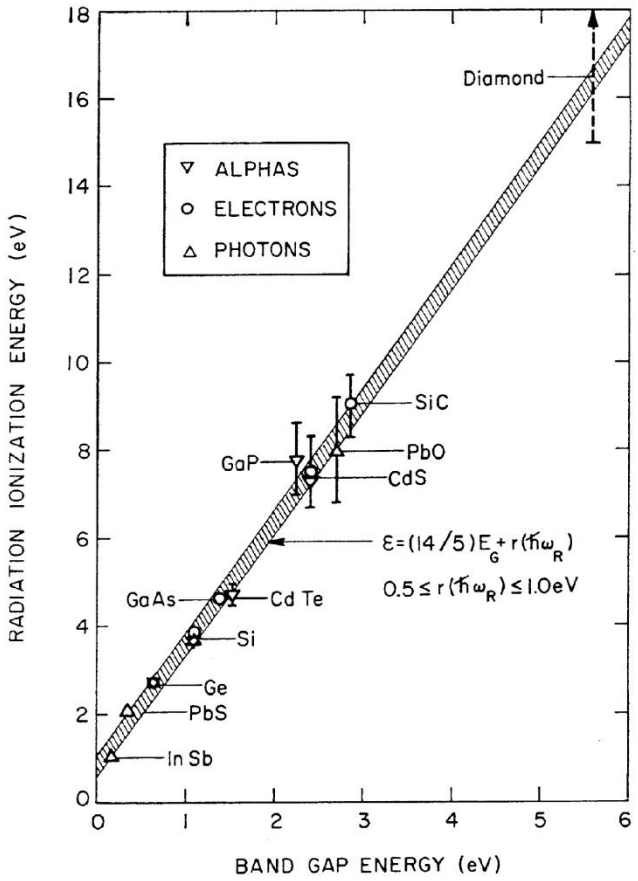

Figure 4.9: Energy needed to generate an e-h pair for different material[113].

amount of e-h pairs generated is thus

$$N_{eh} = \frac{dE}{d\xi} \cdot \frac{D \cdot W}{E_{eh}}, \tag{4.20}$$

where D is the density of the diamond and W the detector thickness seen by the particle. In the present work we always used diamond of $W = 500$ µm with almost perpendicular beams, giving N_{eh} ∼18500, that is a total collected charge of ∼1 fC.

The drift velocity dependence from the applied electric field can be estimated with the classical Drude model[114]. As described in section 4.1.2 the electron is treated as free particles with mass m_e^* accelerated by an electric field. After a relaxation time $\tau_{R,e}(T)$, which strongly depends on temperature and defect concentration, the electron collides with an atom or with a phonon gathering a random momentum

(zero on average). Under this assumption we have a v_d linearly dependent from $\mathbf{E}$

$$v_{d,e} = \frac{e\tau_{R,e}(T)}{m^*}\mathbf{E} = \mu_e \mathbf{E} \tag{4.21}$$

where μ_e is called electron *mobility*. In the same way is possible to define $v_{d,h} = \mu_h \mathbf{E}$. This equation can be considered valid only in the *low field* approximation ($E < 10^3$ V/cm).

At higher fields the value of the mobility is no longer independent from E and shows a dependence $\propto E^{-1/2}$; at very high electric fields ($E > 10^4$ V/cm) became $\propto 1/E$, and the v_d became asymptotically equal to the saturation velocity

$$v_{sat} = \sqrt{\frac{8E_{opt}}{3\pi m^*} tanh\Big(\frac{E_{opt}}{2k_B T}\Big)} \tag{4.22}$$

where E_{opt} is the optical phonon energy (163 meV in diamond). Physically, saturation occurs because a proportional fraction of the kinetic energies of carriers is lost in the crystal by atomic collisions and phonons generation.

We can try to merge low and high field behaviour using the simple model reported in [115], where v_d over a large field range can be described with

$$\mathbf{v}_d(\mathbf{E}) = \frac{\mu \mathbf{E}}{1 + \frac{\mu \mathbf{E}}{v_{sat}}} \tag{4.23}$$

which reduces to the Drude model at low field and take into account the saturation velocity at high fields.

Reaching the saturation velocity can have many advantages: the fastest signal is achieved, which means bigger currents, and any perturbation on the drift potential does not change the signal shape. In the present work we always use field in the range 1.5-2 V/µm (that for 500 µm crystal means 0.75-1 kV) , since the design of a PCB which can tolerate higher voltages in the vacuum is not trivial (see sec. 5.3). Moreover we did not measure any important difference in the time resolution of our detector in the tested range, indicating that higher fields are not really mandatory.

In [116] *Pernegger et al.* reported carrier mobility values for sCVD crystals and confirmed the relation (4.23). The low field mobility dependence w.r.t. temperature was found to be $T^{-3/2}$ for T range 300-400 °K, and $T^{-3.7}$ for T range 400-540 °K. Low field mobility of μ_e =1714 cm^{2}V^{-1}s^{-1} and μ_h =2064 cm^{2}V^{-1}s^{-1} and saturation velocities of 9.6×10^6 cm/s and 14.1×10^6 cm/s for electron and holes respectively has been observed. Such values depend on the concentration of defects: for example mobilities of 4500 cm^{2}V^{-1}s^{-1} and 3800 cm^{2}V^{-1}s^{-1} for electron and holes respectively have been measured in a special sample of *ulta-pure* sCVD diamond at

room temperature[117] and they represent the best values obtained so far. Diamond characteristics at $T = 300$ °K, compared with silicon, are summarized in table 4.1.

Element	Density [gcm^{-3}]	Intr. carrier conc. [cm^{-3}]	e-h energy [eV]	μ_e $\left[\frac{\text{cm}^2}{\text{V·s}}\right]$	μ_h $\left[\frac{\text{cm}^2}{\text{V·s}}\right]$	$v_{s,e}$ [cm/s]	$v_{s,h}$ [cm/s]
C	3.52	10^{-27}	∼16	1714	2064	$8 \cdot 10^6$	10^7
Si	2.33	10^{10}	3.62	1350	480	$9.6 \cdot 10^6$	$1.4 \cdot 10^7$

Table 4.1: Comparison chart between carbon and silicon properties. Silicon data are from [121][118].

With such values the characterization of the signal in figure 4.8 can be completed, assuming an external field of 1.6 V/µm. Using the conservative values [116] for the mobilities and equation (4.23) we get high field drift velocities of $7.11 \cdot 10^6$ cm/s and $9.8 \cdot 10^6$ for electrons and holes respectively. From equation (4.17) we can derive the transit times $t_{t,e} = 7$ ns and $t_{t,h} = 5.1$ ns. The expected currents at t=0 are $I_e(0) = 0.42$ µA and $I_h(0) = 0.58$ µA.

I performed some simulations using *Weightfield 2*, a freeware 2D simulator for silicon and diamond detectors[119]. The simulation in figure 4.10 was performed with 500 µm detector with an applied external potential of 800 V (1.6 V/µm) metalized with a single pad. The particle trajectory is perpendicular to the device surface with an energy release computed every 5 µm using GEANT4[120], a toolkit for the simulation of the passage of particles through matter.

In figure 4.11 the currents in the detector are plotted. Total current shape as well electron-hole relative magnitude are the one expected from our calculation. The slightly different values are due to the mobility and saturation velocity employed by the simulator. In the plot we also reported the input current and voltage seen by an amplifier with an input resistance of 50 Ω. Detector capacitance was set to 10 pF.

One of the main problem of diamond as MIP detector arise from this results: the input signal in the amplifier is very low, with a total collected charge of ∼1 fC and a peak current of ~ 1 µA. If indeed the intrinsic SNR of the detectors is $\sim 10^5$, things change when we add the amplifier. Modern commercial low-noise current amplifier have input noise of few nV/$\sqrt{Hz}$; since we have to preserve the signal rise time we need at least a band of 2 GHz, meaning an input noise similar or even grater

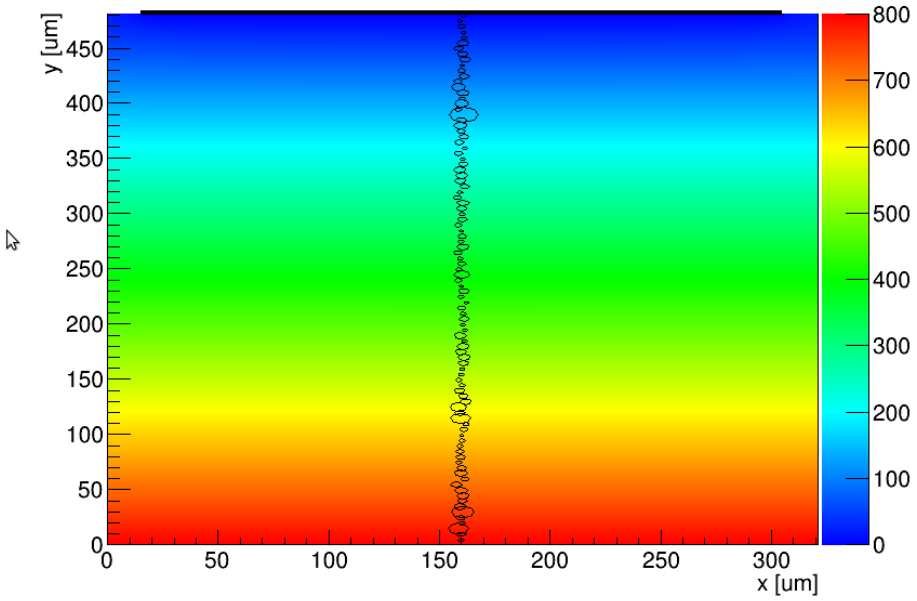

Figure 4.10: Charge release for MIP particle (Landau distribution) in a diamond detector. The applied field is also shown.

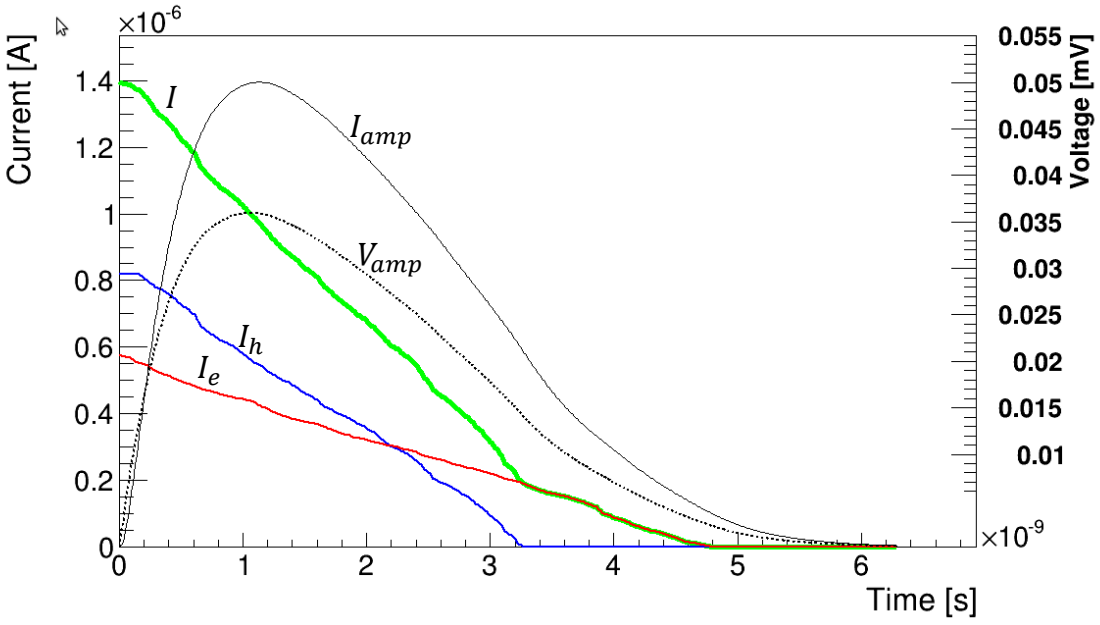

Figure 4.11: Current generated from MIP particle passing through a 10 pF diamond detector with 500 µm thickness and a bias voltage of 800 V.

than the detector signal, that is a final SNR∼1 in the best case. Charge sensitive amplifier can behave better having typical input noise charge of ~ 0.1 fC, but larger signal rise time. In both cases the final rise time will depend also on the detector capacitance, that should be kept as low as possible. We will see in next section that the measurements performed with commercial detector/amplifier will confirm our supposition leading to the solution described in chapter 5.

One of the main requirements of our application is the radiation hardness. The work of the RD42 collaboration[122] shows that the sCVD diamonds can operate also after receiving $5 \cdot 10^{13}$ protons/mm^2. Still the radiation has a negative impact on the sensor CCD, which is exponentially reduced. The sCVD became equals, in terms of collected charge, to a pCVD after $\sim 3.8 \cdot 10^{13}$ p/mm^2. This value is far from the foreseen irradiation in the vertical RP ($5 \cdot 10^{10}$ p/mm^2 for 100 pb^{-1}) and can be thus safely used. They can moreover be used for the CT-PPs project, where the integrated dose for 20 fb^{-1} ($\sim$ 1 year) is $\sim 10^{13}$ p/mm^2.

4.3 Tests with commercial diamond detectors

Commercial devices were extensively tested at PSI [1] in June 2014, and later at CERN. Small changes on setup and detector was introduced between the two tests. To allow direct data comparison special care was put in collecting data only from MIP particles.

4.3.1 Beam lines and experimental setup

PSI

During PSI test beam our setup was hosted on the πM1 secondary beam line[123]. πM1 is an high resolution pion beam line with momentum range between 100 and 500 MeV/c, which characteristics can be found on table 4.2.

Primary beam impacts in a production target displaced $\sim$ 21 m from the center of the experimental area, generating $e^{\pm}$, $\pi^{\pm}$ and $\mu^{\pm}$. Electrons and pions relative abundances with respect to selected particle momentum are reported in figure 4.12. To avoid contribute also from primary protons negative particles were selected, even if the resulting flux was lower.

[1] Paul Sherrer Institute, Villigen, CH

Total path length	21 m
Momentum range	100-500 MeV/c
Solid angle	6 msr
Momentum acceptance (FWHM)	2.9 %
Momentum resolution	0.1 %
Dispersion at focal plane	7 cm/%
Spot size on target (FWHM)	15 mm horizontal 10 mm vertical
Angular Divergence on target(FWHM)	35 mrad horizontal 75 mrad vertical

Table 4.2: πM1 beam line characteristics.

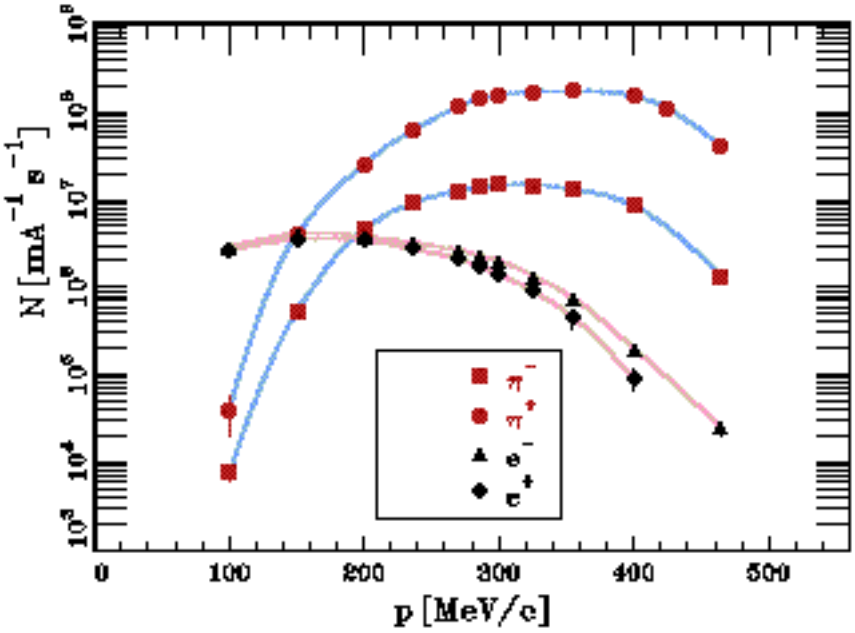

Figure 4.12: Pion and electron fluxes wrt selected momentum at PSI

The setup consists of an RF-shielded box ($30 \cdot 30 \cdot 60$ cm^3) housing both the detectors under test and the trigger system (fig. 4.13). The devices under study were two identical diamond detectors from CIVIDEC (D1 and D2), coupled to front-end electronics from the same company. The diamond detectors were ultra pure

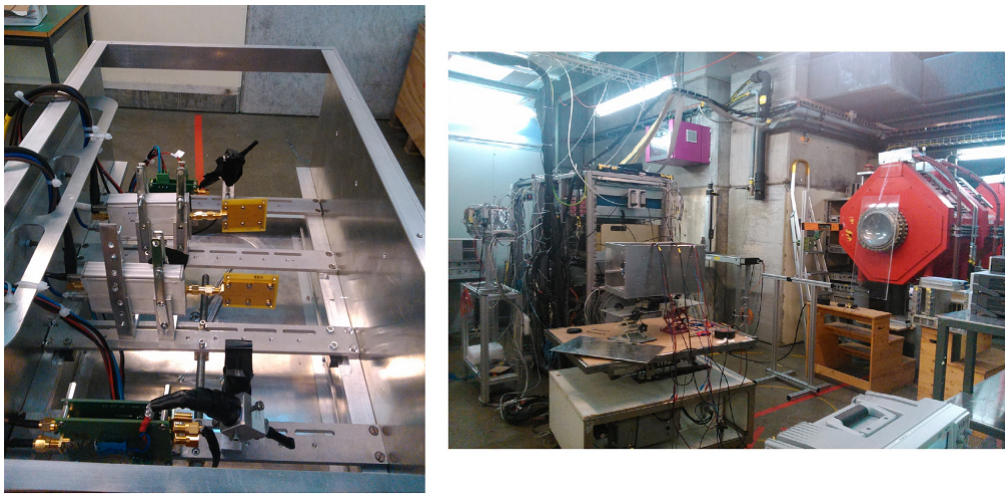

Figure 4.13: Picture of the detector setup at PSI. The open RF box with the two diamond detector in the middle (left) and the experimental hall (right).

sCVD crystals with an area of $4.5 \cdot 4.5$ mm^2 and a thickness of 500 μm, metalized with a single pixel of $4.2 \cdot 4.2$ mm^2. Each diamond was directly connected with an SMA junction to the front end electronics providing HV and signal readout. To perform signal amplification both CIVIDEC Broadband Amplifier (BA) and Fast Charge Sensitive Amplifier (CSA) were tested. However the SNR with broadband amplifiers was very poor (~ 1, as expected from previous calculation), and no deeper tests with them were performed.

Waveforms from both diamonds were acquired through an Agilent Infiniium DSO9254A oscilloscope (2.5 GHz; 20 GSa/s). Using an high sampling rate oscilloscope allowed us to perform advanced offline timing analysis with different algorithms, described later. The drawback was a low acquisition rate, and thus the need to have an high *trigger efficiency* (TE), defined as the ratio between triggered events and events with signal from at least one of the diamond detectors

$$TE = \frac{N_{trg}}{N_{Det1+Det2}} \tag{4.24}$$

We used 2 of the scintillator detectors described in section 3.3, that together with high spatial resolution can provide also a precise time reference. The two scintillators were put in cross configuration, one upstream and the other downstream the diamonds, so that the resulting intersection area was comparable with the diamond size: a scheme of the setup is given in figure 4.14. TE was found in average $\sim$40%, depending on the alignment of the devices with respect to the beam. Intrinsic efficiency of the diamond can be instead considered around unity. To check this we try

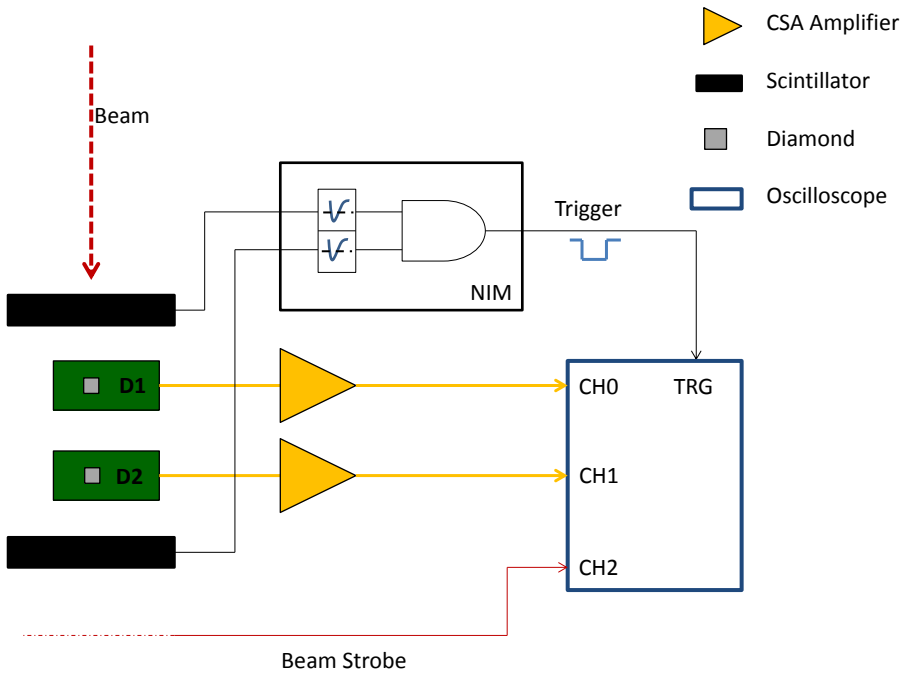

Figure 4.14: Scheme of the detector setup at PSI

to repeat the alignment until we reach a trigger efficiency of almost 100% during one data taking run. Since this fine alignment was time consuming we can not do it for each tested setup.

Particle momentum was kept at the nominal working point of 250 MeV/c in almost every data taking. At that momentum only π^- and μ^- can be assumed as MIP ($\beta\gamma_\pi = 1.79$, $\beta\gamma_\mu = 2.36$), while e^- energy release is much bigger due to radiation loss: particle discrimination was thus needed. It was done using the particle TOF from the target to the detector. We first measured the time difference between the beam strobe signal, which gives the time reference of the primary beam on the production target, and the coincidence signal from the scintillators. We make this measure for different beam momenta obtaining the results displayed in figure 4.15.

In the picture peaks generated from the same collision are indicated; since TOF difference between different particles type is bigger than the collision period (20 ns) multiple beams are overlapped. As expected the e^- time of flight does not vary with beam energy. Moreover at 250 MeV/c π^- tof distribution are clearly resolved with our trigger time resolution. Muon contribution at 250 MeV/c is negligible. To acquire data only from π^- we used the beam strobe to generate a narrow gate for

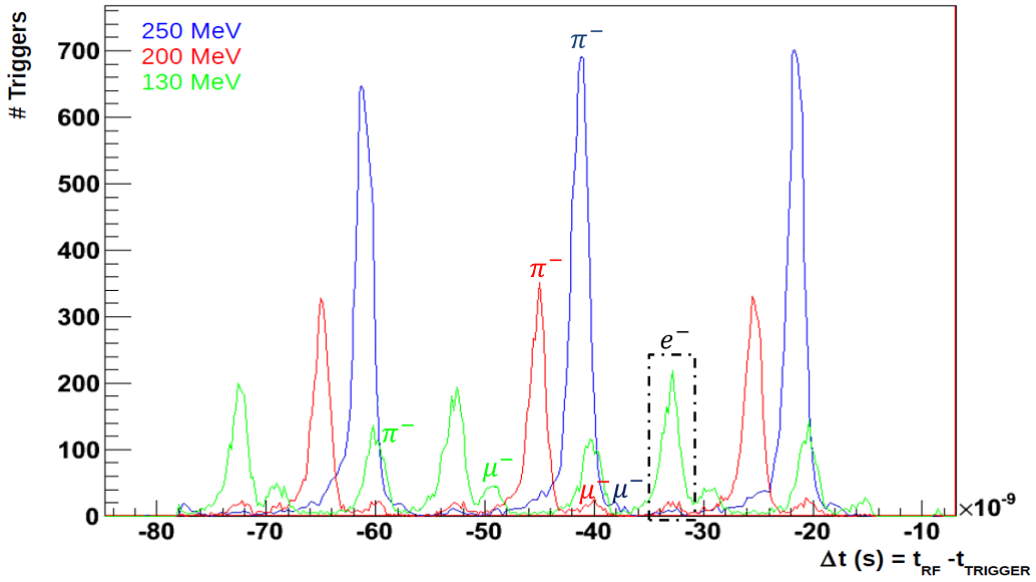

Figure 4.15: $T_{strobe} - T_{trigger}$ for different particle momenta. Detector distance from the production target was estimated to be ∼18 m.

the trigger centered on their expected arrival time. Particle flow was regulated to have ∼ 1kHz trigger rate, to kept at minimum pile-up events.

PS

Almost the same setup was used during the data taking at T9 beam line at CERN[124], served by the Proton Synchrotron (PS) accelerator. The T9 beam line is able to provide charged particles with momentum up to up to 12 GeV/c, mainly $\pi^{\pm}$ and protons, randomly distributed in slots of ∼400 ms.

For our purpose we selected negative particles with momentum of 10 GeV/c. Again selecting particle with negative sign is possible to get rid of the proton component, leaving an almost pure π^- beam. To check electron contamination we made use of a gaseous cherenkov counter placed upstream the detector (fig. 4.16). Cherenkov gas pressure was tuned to detect 10 GeV/c particles lighter than π and put in coincidence with the trigger system. A contamination below 1‰ was detected.

The selection of negative particles had as side effect a very low luminosity beam ad thus forced us to enhance trigger efficiency by placing another detector in front of the box. Such detector was composed of $10 \cdot 10$ cm^2 tale of plastic scintillator with

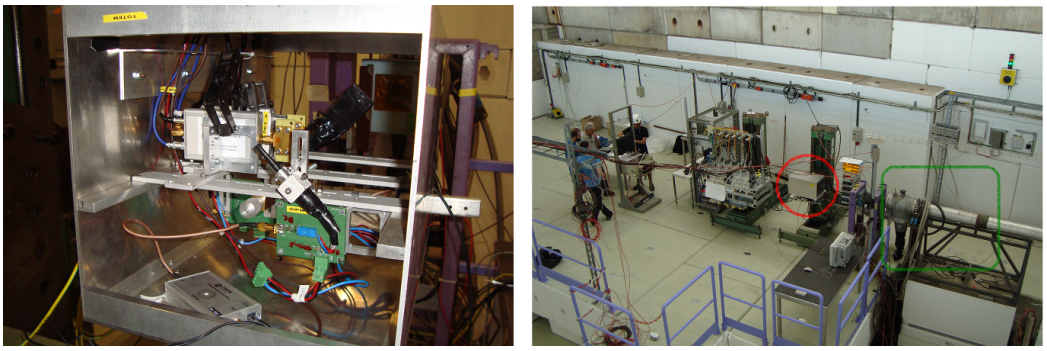

Figure 4.16: On the left a picture of the box with an anticoincidence scintillator on the back. On the right a picture of the T9 experimental area

a round hall of 1 mm^2 aligned with the beam coupled to a PMT. Signals from it were used to generate a veto signal on the trigger. With such we reach a maximum TE of 60% with fast alignment procedure. The setup scheme is in figure 4.17.

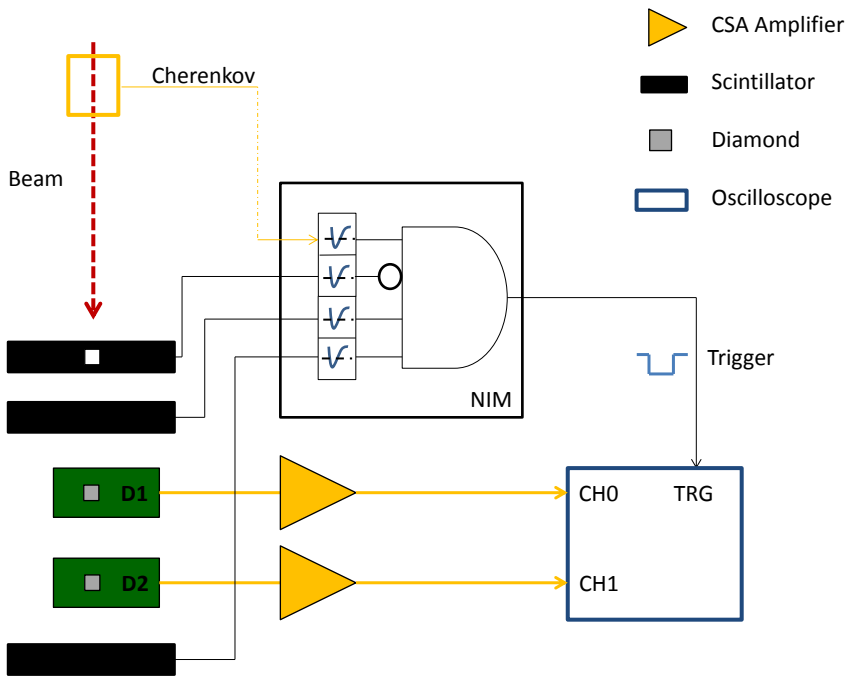

Figure 4.17: Scheme of the detector setup at PS

The devices under test were the same diamonds of the previous test beam, but the PCB had been cut and the transmission line length reduced by CIVIDEC. The standard version of the detector have a capacitance of $\sim$ 15 pF, that was reduced

to ~ 5 pF with the rework (fig. 4.18). That was done to understand how detector capacitance affect timing performance. AT PS we also performed some tests for signal digitization using the NINO chip. We will discuss it in section 6.2.1.

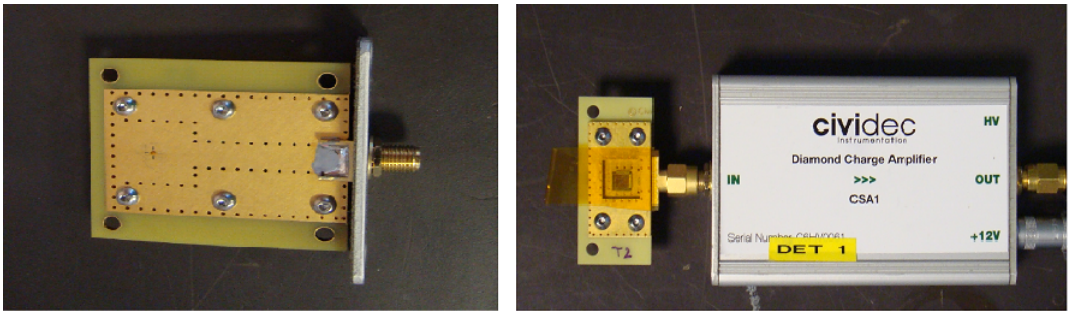

Figure 4.18: Picture of the reduced capacitance detector. The detector with standard PCB (left) and reduced capacitance PCB attached to the CSA (right).

4.3.2 Results

The analysis can take big advantage from the use of an oscilloscope with large bandwidth and high sampling rate to determine detector resolution σ_t.

For each event acquired we have two waveforms as in figure 4.19: we can split them in two segments, the left one, were we have nothing else than noise, and the right one, were the particle signal can be found. First step is the selection of the events to be included in the analysis. Indeed not all events contains particle signals in both D1 and D2 and an offline trigger must be used.

From the left side we can extract the noise RMS (N_{RMS}) and the waveform offset (V_{os}) with a constant fit. For each waveform we compute the waveform amplitude (V_{am}) as the difference between the maximum (V_{max}) and the V_{os}. The V_{os} is used in all the analysis step redefining the waveform measured voltage V_v as $V_{v'} = V_v - V_{os}$ Based on the V_{am} distributions obtained (fig. 4.20) we can put a threshold on each detector, selecting only the events in which both are over threshold.

For each selected event we identify two points on the waveforms (T_{det1}, T_{det2}) and we compute the time difference ΔT_{12}. The time resolution σ_t is obtained as $\sigma_{12}/\sqrt{2}$, where σ_{12} is the standard deviation of the ΔT_{12} distribution. We are assuming that the two diamond detectors have the same resolution, using a worst case estimation. We must indeed take into account that even if we use the same CSA model in both devices, the tolerance given by CIVIDEC results in small differences in the behaviour of the amplifiers that may lead to a different time resolution.

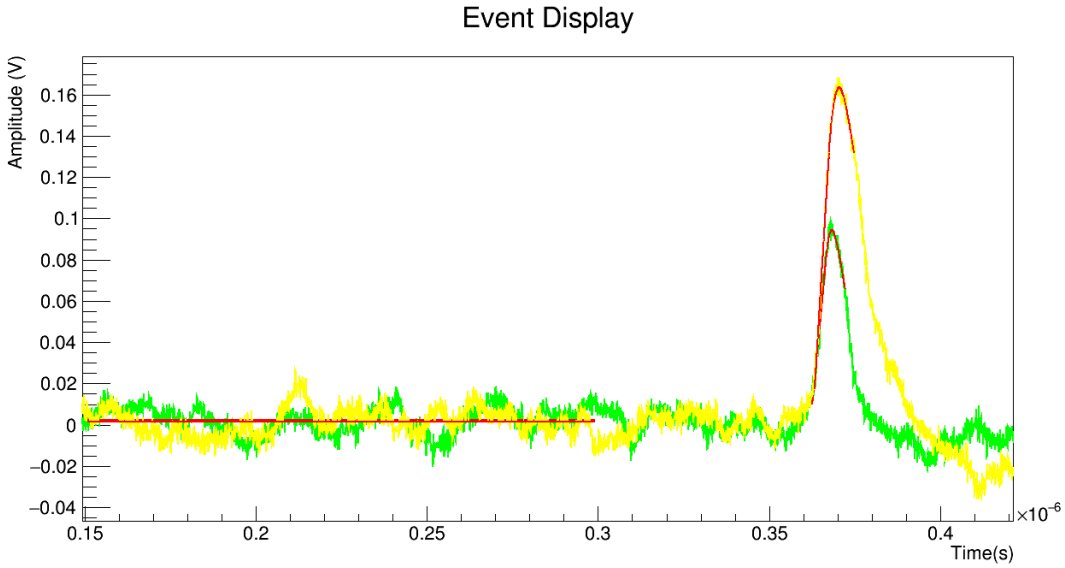

Figure 4.19: Event display. We see the noise analysis on the left side and the application of the timing analysis method #4 (described later) on the right side.

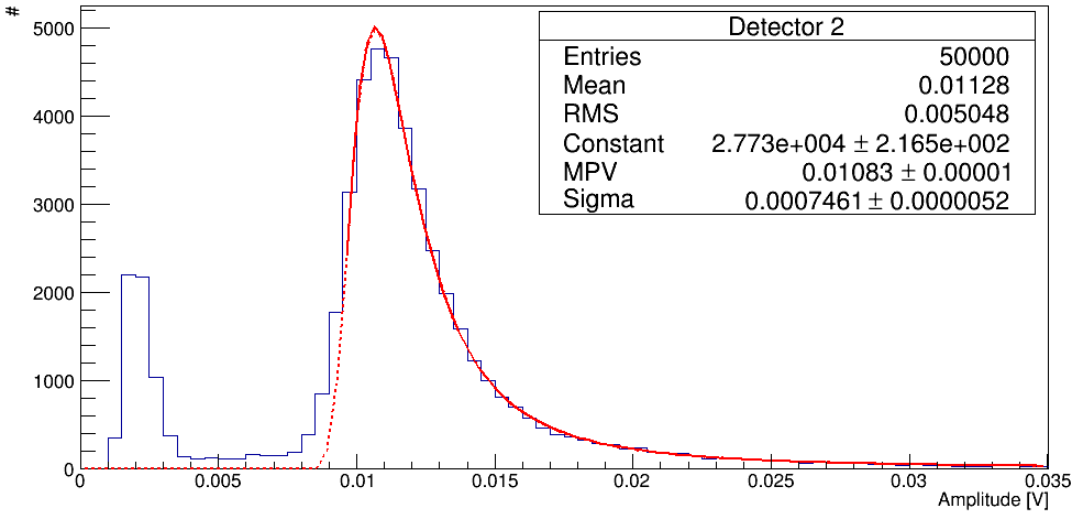

Figure 4.20: Example of V_{am} distribution for detector 2 during PS test beam. We can see that noise pedestal and signal are clearly resolved. A landau fit is performed on the signal, as expected from energy release distribution.

The way T_{det1} and T_{det2} are computed make great difference in the final result. As mentioned before we tried different algorithms to compute them:

1. the *Fixed Threshold* uses a fixed value Th_F for both waveform and $T_{det1,2}$ are

defined as the time when $V_{v'1,2} > Th_F$.

2. in the *Normalized Threshold* we proceed as before but we now select two independent threshold $Th_{N1,2}$ defined as the X% of the $V_{am1,2}$. A scan on X is needed to understand the best value.

3. the *Maximum position* simply assign to $T_{det1,2}$ the time at which the waveform reach the maximum value.

4. in the *Fitted Normalized Threshold* (FNT) we first perform a fit with a second order polynomial on the maximum of the signal to enhance the precision on the computation of the V_{am}, than we identify on the rising edge of the signal the point were the amplitude reach the 20% and 80% of V_{am}. A first order polynomial fit is then performed between those point. Finally we proceed as in point 2 but $T_{det1,2}$ are computed on the fitted function.

5. the *Offline Constant Fraction Discriminator* (CFD) emulates the standard technique widely used in the electronic circuits to reduce the time walk effects. In particular each waveform is inverted, attenuated, delayed and finally added to the original one. The time for which the resulting function has a null amplitude is taken as an estimate of $T_{det1,2}$. The value of the attenuation factor and of the time shift used in this method is respectively 0.45 and 7 ns.

6. Finally in the *extrapolation* we proceed with a 6th degree polynomial fit on rising edge the signal. From the fit we extract two time values at 25% and 60% of V_{am} and finally we perform a linear extrapolation to $V_{v'=0}$.

Method #1 is actually the only one which does not provide any correction to the signal *time walk*. The time walk is an effect introduced when two signals have different amplitudes. By measuring the time difference ΔT_{12} with a fixed threshold the signal with higher V_{am} will reach the threshold before the other, even if simultaneous, adding a large smearing to the measure. All the others methods can instead provide a correction based on the signals relative amplitude. Method #6 usually gives the best results but the implementation is not straightforward, since for many waveform the fit must be guided to reach the convergence. Method #4 is the most reliable and, if the threshold is carefully chosen, the results are the same of the CFD. Moreover they can be compared with #6 when the signal rise time t_r^{20-80} is below 2 ns. It has been therefore the most used during my work.

The best results have been obtained at PS, using the low capacitance PCB. In figure 4.21 we can see the fitted ΔT_{12} distribution obtained with method 6, with

a resulting $\sigma_t = 196$ ps. We report in table 4.3 the results obtained with the

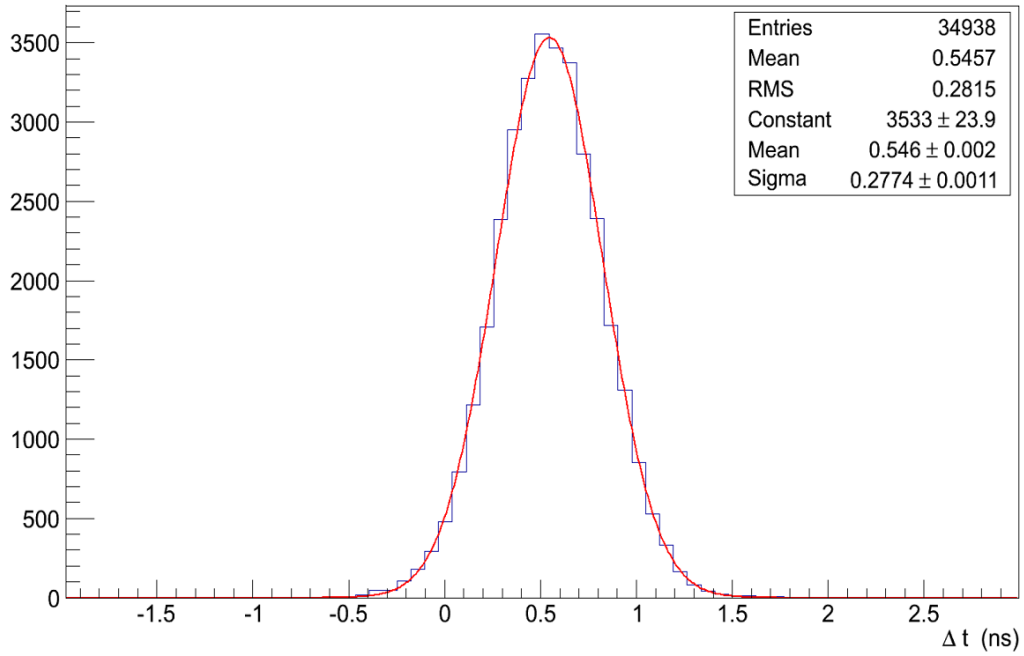

Figure 4.21: ΔT_{12} with method 6 on the data collected at PS, best result with commercial detectors

different algorithms. All the diamond time resolutions quoted in this work can be considered with a precision within 5%. This value take in account also the sensor to sensor variations that are present also in twins detectors (i.e. for the diamond or metalization quality).

Offline algorithm	ΔT_{12} RMS [ps]	$\sigma_{12}(\sigma_T)$ [ps]
Fixed Threshold (12 mV)	1490	1450 (1025)
Maximum Position	754	719 (508)
Fitted Normalized Threshold 80%	417	389 (275)
Fitted Normalized Threshold 30%	340	336 (237)
Fitted Normalized Threshold 50%	322	313 (221)
CFD	298	306 (210)
Extrapolation	281	277 (196)

Table 4.3: Analysis methods comparison. Not all the algorithms are reported

In figure 4.22 the main parameter for both diamond sensor are reported for comparison. The t_r^{20-80} is computed in the first part of analysis algorithm #4, while

the SNR is computed as $SNR = V_{am}/N_{RMS}$. The offline trigger thresholds used were T_{D1}= 8 mV and T_{D2}= 10 mV. The analysis have been repeated by reducing the minimum value of $T_{D1,2}$ of the analyzed waveforms to 4.5 mV. The fit results are stable at 1% level while outliers appears in the ΔT_{12} distribution so that the RMS get worse by about 10%. In general, by selecting the signal where higher amount of charge is released the time resolution improves. As an example, by not including in the analysis the 20% of the diamond signals having with the smallest V_{am} above threshold the time resolution is about 5-10% better, depending on the method.

As mentioned before the two detectors are not identical, mainly due to small differences in the CSA. D1 have bigger gain (bigger V_{am}, almost same SNR) but show a worse rise time, $\sim$ 20% more than D2. Since in this setup a direct measurement of the time resolution is not possible we can only use relation 3.6 to extrapolate a resolution (best case) of $\sim$165 and $\sim$206 ps respectively for D1 and D2. Even if this was the case the results are still not sufficient for our purpose.

To understand the effect of the reduction of the capacitance is useful to compare the PS result with the PSI test beam. In table 4.4 are reported the values obtained for different dataset (DS) at PSI together with the PS values.

	PS	PSI DS1	PSI DS2	PSI DS3	PSI DS4
Particle	π^-	π^-	π^-	All	All
Momentum [MeV]	10k	250	130	250	250
Angle to Beam	90°	90°	90°	90°	45°
SNR_1	20.7	15.6	16	17.3	22.3
SNR_2	19.3	17.1	19.8	18.1	19.5
t_{r1} [ns]	2.7	3.3	3.2	3.2	3.2
t_{r2} [ns]	3.4	3.7	3.7	3.6	3.7
$\sigma_{12}(\sigma_T)$ [ps]	313 (221)	401 (283)	415 (293)	423 (299)	325 (230)

Table 4.4: Results summary. The SNR value are computed as the mean of the distributions removing noise pedestal. Time resolution is obtained with analysis method 4 (50% level threshold).

DS1 (π^-,250 MeV) is the one to be used for comparison. We can appreciate the differences introduced by the capacitance reduction in figure 4.23, were both SNR and rise time have an improvement around 20%, giving a $\sim$ 22% better time resolution.

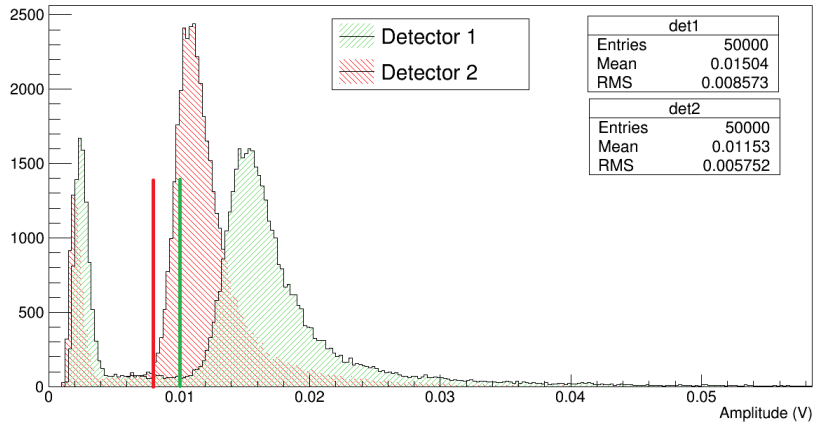

(a) Waveform Amplitude

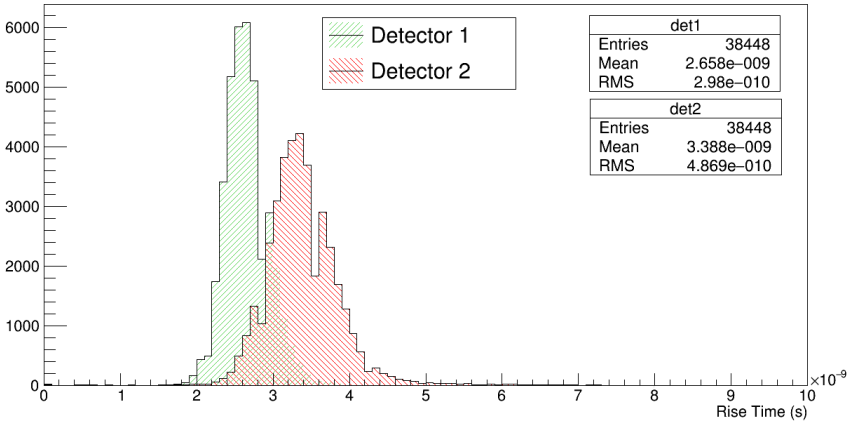

(b) Rise Time 20%-80%

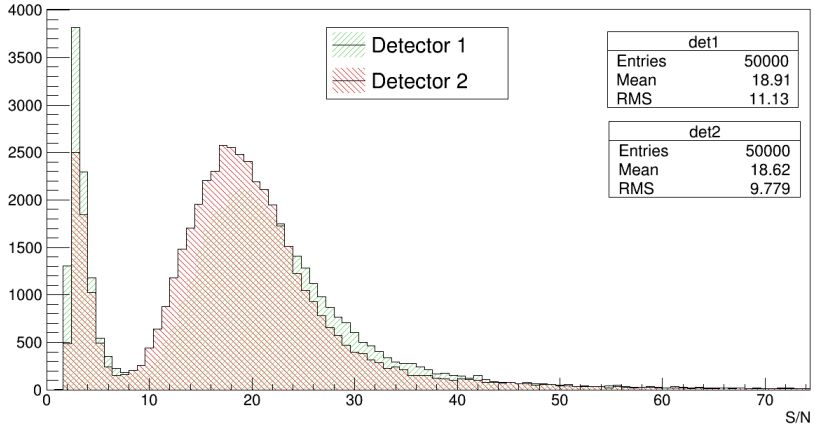

(c) Signal to Noise Ratio

Figure 4.22: Comparison between detectors parameters with low capacitance. The thresholds used for the analysis are highlighted (T_{D1}= 8mV, T_{D2}= 10mV) in (a).

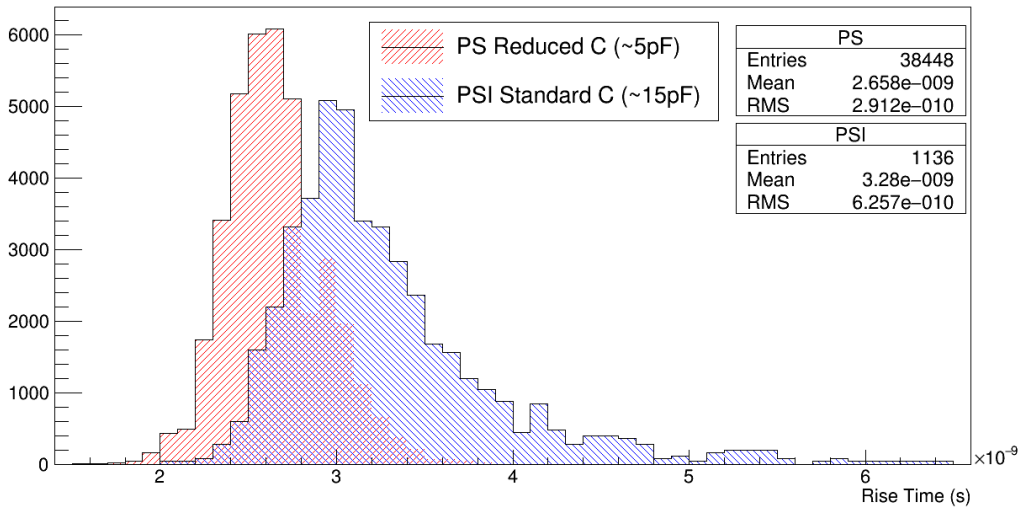

(a) Rise Time 20%-80%

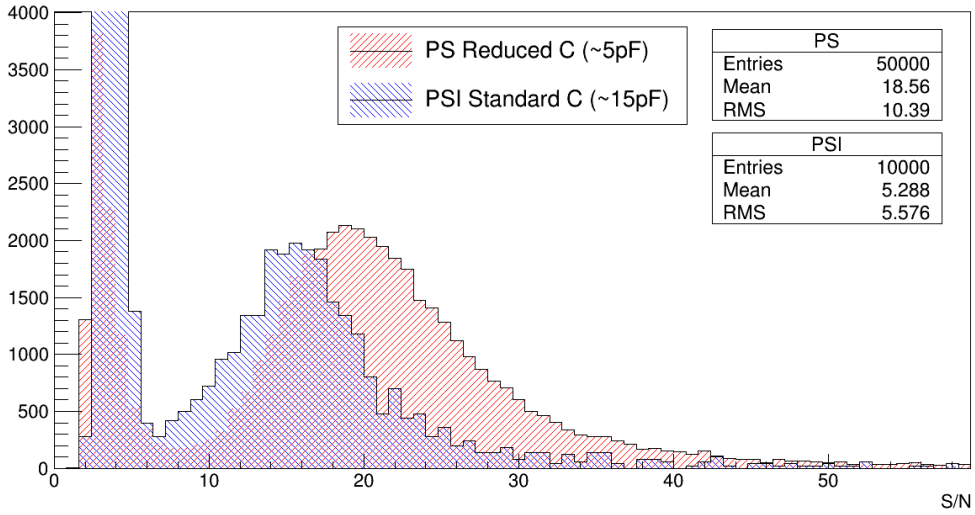

(b) Signal to Noise Ratio

Figure 4.23: Comparison between standard and reduced capacitance detector. Distributions have been rescaled for better comparison

DS2(π^-,130 MeV) has been analyzed to check if the results have some critical dependence from the pion momentum. No clue of that was found. In DS3 we removed the TOF selection. The slightly worse results can be explained taking into account that different particles lead to different signals from the detector and the analysis algorithms show different performances, reducing the overall resolution. Finally in DS4 D1 was tilted to 45° with respect to the beam axis, resulting in a detector thickness (seen by the particles) of $500 \cdot \sqrt{2} \approx 707 \mu$m. The expected increase in the SNR ratio has been verified and the resulting time resolution improved by ∼23% wrt DS3.

Such results, with a best performance of $\sigma_t = 196$ ps with the 5 pF sensor, were not satisfactory for our purpose, but the technology seemed very promising as it matched all the requests for the upgrade. We were convinced that a custom low-capacitance detector design with an integrated amplifier could get the goal and we moved on with its realization.

Chapter 5

The TOTEM TOF detector: development and performances

In this chapter I will describe the development of the TOTEM detector. The sensor and front-end integration procedure will be described and the performances of the TOF system presented. In section 5.1 the steps that brought us to choose the amplification scheme will be reported together with the first time resolution below 100 ps obtained with a TOTEM sensor. In section 5.2 I will present the hybrid board prototype integrating both the sensor and the complete amplification electronics. The study of the performance dependence from the pixel area and the sensor efficiency will be also presented. The results obtained confirmed our strategy and the final detector (sec. 5.3) has been built and successfully tested. I had a main role in all the work here reported, which has been recently published [125, 126].

5.1 Detector development

The results obtained in the previous chapter make clear that a development of an hybrid board, hosting both the sensors and the front-end electronics is the only way to achieve the 100 ps resolution needed. The reduction of the parasitic capacitance seen by the first amplification stage was not the only objective that we pursued. Indeed, even in the hypothesis that the connection between the sensor and the electronics introduces no additional capacitance, the intrinsic capacitance of a pixel with an area of $4.2 \cdot 4.2$ mm^2 (the bigger foreseen) and 500 µm thickness is ~ 2 pF. Considering that in our previous measurements a reduction of the capacitance of a factor 3 brought to a gain of $\sim 30\%$, is clear that we cannot rely exclusively on the integration to reach the goal. We indeed decided to develop a new multi-stage

amplification chain, designed and optimized for the diamond special needs.

The development of the chain was performed at the CERN SPS test beam facility, where the TOTEM experiment has its test area (H8C). Protons accelerated at an energy of 450 GeV are extracted from the SPS and a secondary beam made of protons, pions and muons is generated by interaction of the primary protons with a fixed target. The secondary particle momentum used during our tests was of 180 GeV/c and therefore no particle identification was necessary, since they can all be treated as MIP. Since the SPS serves multiple test beam lines and experiments, in addition to the LHC, the beam is not continuously delivered. Particles are debunched[1] and sent to the beam line every ~ 30 s for a time of ~ 5 s. This values are only approximate, since beam periodicity and duty cycle can vary at any moment depending on the beam request. During our test beams we could "play" with the magnet settings of the transmission line, optimizing the beam in terms of intensity and spot size. We worked with a spot of ~ 2 cm, in order to reduce the problem of alignment, adjusting the beam intensity with the collimators to achieve an optimal trigger rates. With the oscilloscope we controlled that the probability to have particles hitting the same sensor in the same acquisition window was negligible.

5.1.1 The HADES telescope

Our work moved from the results of the HADES[2] collaboration[130], which had already developed a diamond timing detector, and that kindly borrowed us one of their prototype. We hence started by measuring its performances.

The detector is a telescope composed of two planes of detection. In the middle of each plane a diamond is glued ($4.2 \cdot 4.2$ mm^2 area, 500 μm thickness). During the metallization the diamond surface has been divided in 8 pixels. Each pixel has a capacitance of ~ 0.25 pF and is readout by a dual stage amplification chain, formed by a pre-amplifier and a booster. The first stage is based on a RF amplifier with low input capacitance. The peculiarity of the pre-amplifier is its high input impedance of 2 KΩ, necessary to obtain a low bias current and a reduced input noise. The booster is a dual stage amplifier ($G = 50$ dB) which provides a signal shaping with a rise time of $t_r^{20-80} \sim 1.4$ ns. The pre-amplifier is located as close as possible to the diamonds, while the booster is not integrated in the telescope. Two booster modules were provided by the HADES collaboration, each one with 6 channels.

[1] In the SPS they are collected in bunch, like in the LHC. This packet are destroyed before the injection in the test beam lines.

[2] *High Acceptance Di-Electron Spectrometer*, Darmstadt,Germany (GSI laboratory)

In figure 5.1 a picture of the detector during our tests is proposed, together with an image of the segmented diamond surrounded by the pre-amplifiers made by HADES. The trigger was generated, as for the previous test beams, with two SiPM

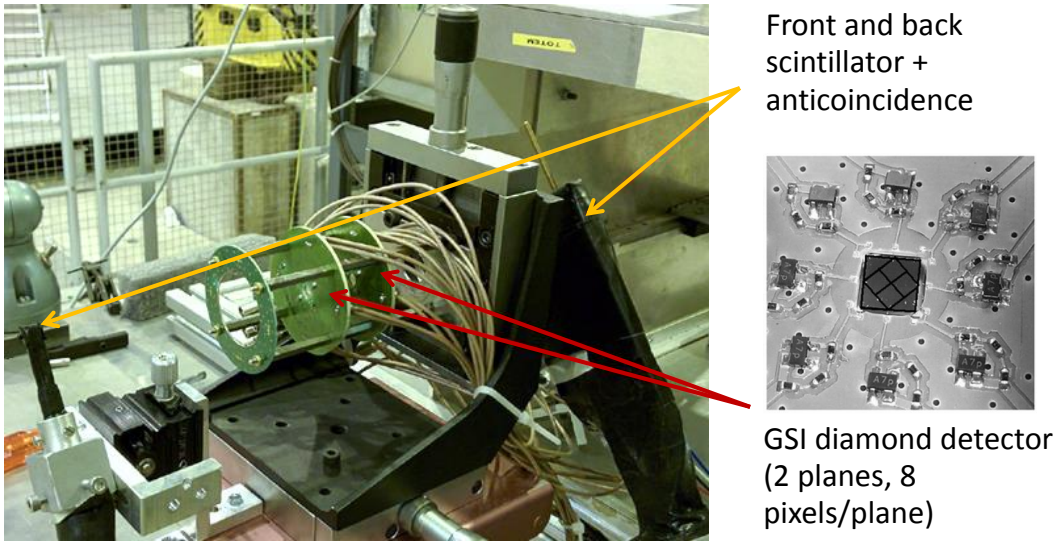

Figure 5.1: Picture of the HADES telescope during the test. On the left the experimental setup used to measure its performance. On the right the segmented diamond surrounded by the pre-amplifiers (picture from [131]).

detectors in cross configuration, one upstream and one downstream the HADES telescope, reinforced with anti-coincidence scintillator. The scheme of the setup is the same of the PSI (fig. 4.14), where the CIVIDEC diamonds are replaced by the HADES sensor and the CSA with the booster. Before performing the measurements we first checked with a source which pair of pixels (two aligned pixels on the two planes) provided the bigger signal and the lower noise.

The distribution of the time difference between the two sensors is reported in figure 5.2.

The analysis was performed with the FNT method (#4) described in the previous chapter, but an offline low pass filter (cut frequency of 1 GHz) was applied to the waveforms. The result shows a standard deviation $\sigma_{12} = 126$ ps for the time difference ΔT_{12} measured between the two planes of the detector. The threshold applied on the waveform amplitude was set to 0.2 V. Again moving this threshold gives negligible effects. Since the parameters of the sensors were found identical (for one of the pixel they are reported in figure 5.3) the resolution of each plane can be estimated as $\sigma_t = \sigma_{12}/\sqrt{2} = 89$ ps. This is a good result, well below the

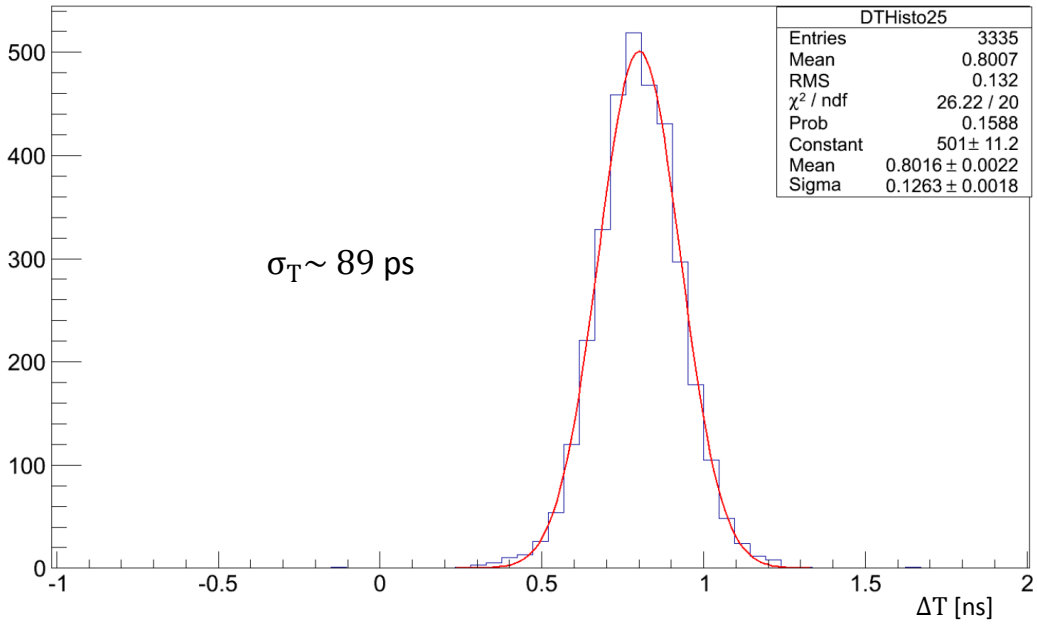

Figure 5.2: Distribution of the time difference ΔT_{12} between the two HADES sensors.

desired 100 ps required. Removing the filter the resolution is $\sim$ 10 ps worse. Must be however taken into account that the sensor capacitance is $\sim$ 8 times smaller than the one foreseen for our bigger pixels (2 pF). The expected time resolution using this amplification electronics with the large pixel is therefore not satisfactory. Nevertheless the work of the HADES collaboration was a golden starting point to build our own hybrid.

5.1.2 TOTEM amplification chain

We decided to build a first hybrid prototype, integrating the sensor and, as close as possible to it, the pre-amplifier. The design of the pre-amplifier was taken from the HADES detector and the board was designed from the University of West Bohemia (Pilsen, Czech Republic). The same university developed the later versions of the board and the amplifiers here discussed, following our results and indications. The connection of the diamond to the pre-amplifier is different from the one used in chapter 4, being the signals readout from the negative electrode (fig. 5.4). This configuration does not need a decoupling capacitor, removing a possible additional source of noise. The pre-amplifier is based on the BFP840 transistor, an hetero-junction (SiGe) bipolar transistor, designed for low noise RF applications. The

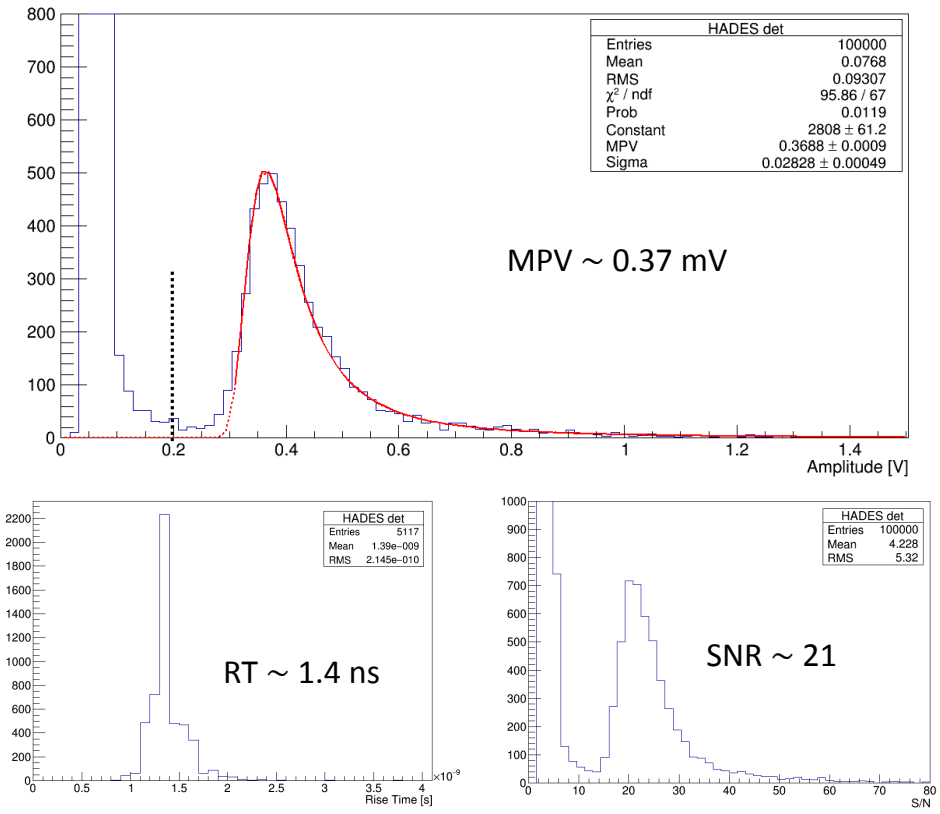

Figure 5.3: Distribution of the HADES signal amplitude, t_r^{20-80} and SNR. The distributions are the same for both pixel (front and rear).

feedback is designed and implemented to keep the parasitic capacitance at minimum. The bias current is indeed provided through 3 resistors in series in order to reduce their capacitive coupling. The input resistance is $\sim$ 2 KΩ, providing a low bias current and a better SNR[3]. High input resistance and high performance amplifier are almost never found in commercial amplifiers, usually designed to match with 50 Ω transmission lines, but become mandatory for a diamond sensor. The values of the feedback and collector resistances has been optimized in order to keep a good time resolution also for the large capacitance pixels, with a nominal gain of the pre-amplifier of 31 dB[4]. On the hybrid we glued and bonded the diamond from CIVIDEC used in the previous chapter. The possibility to re-bond a diamond without damaging the sensor or the metalization has been a pleasant discovery, allowing us to use the same sensor in multiple boards, enhancing the quality of the

[3]The SNR increases with the input resistance of the amplifier, until a saturation limit, depending on the diamond capacitance, is reached.

[4]The gain of the amplifier is determined by the voltage applied to the transistor collector.

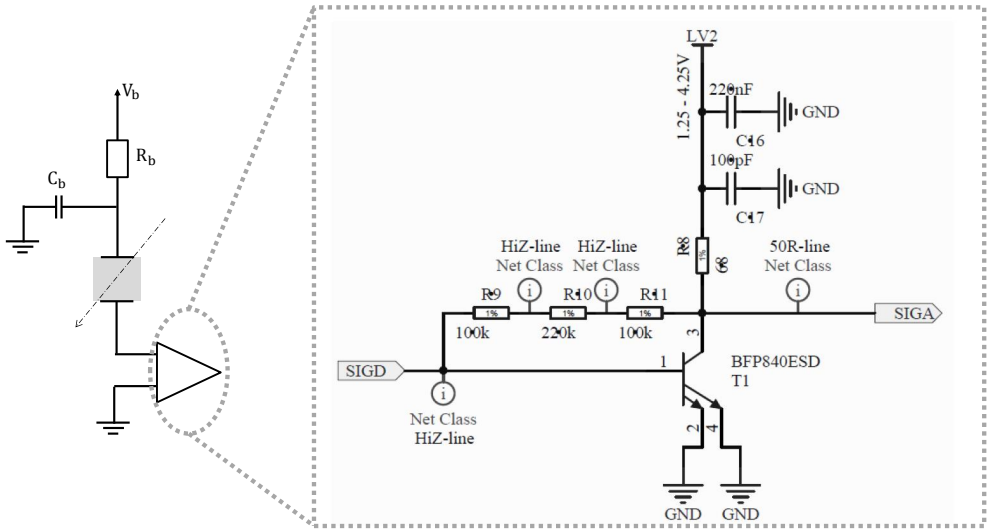

Figure 5.4: Scheme of the first TOTEM hybrid prototype. The diamond connection to the pre-amplifier is showed on the left, while the pre-amplifier scheme is on the right. Optionally the transistor can be substituted with a BFP720 or BFG310 (the one employed by HADES).

performance comparison.

The next amplification stage was developed by using one of the pixel of the HADES telescope studied in the previous measurements as reference, with the setup showed in figure 5.5.

The same booster of HADES was at first used to provide the final amplification, but the result was not satisfactory with a sensor resolution of the order of ~ 150 ps. Not a surprise, bearing in mind that a diamond with full pad metallization has a much larger area than the HADES pixels. Later we tested multiple solutions based on two different MMIC (*Monolithic Microwave Integrated Circuit*) amplifiers: the ABA-51563 and the MGA-71543, both GaAs low-noise high-frequency amplifiers. Particular effort was put to obtain a linear phase and a nearly constant group delay in the operational bandwidth, in order to avoid signal distortions. The ABA was identified as the most promising solution and deeper studies were performed in different configurations. Without going into the details we tested different solutions differing on:

- number of stages.
- presence and value of a filter between the pre-amplifier and the amplifier.
- signal decoupling.

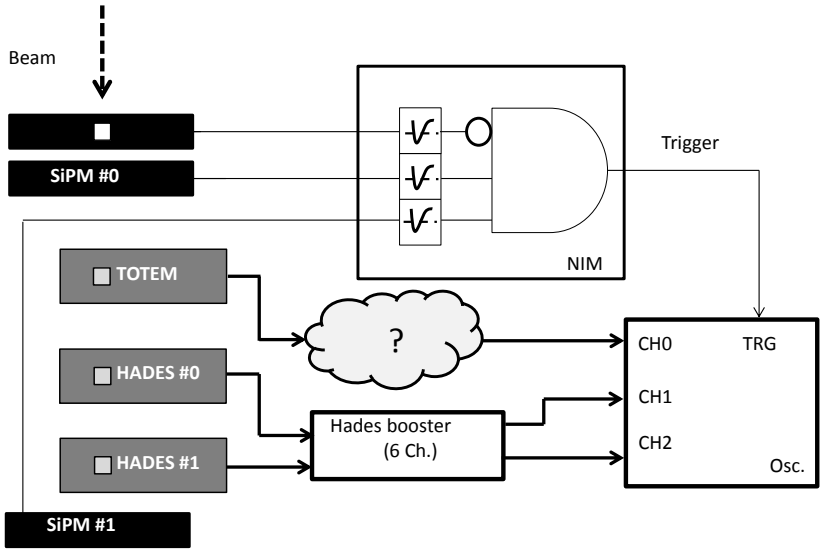

Figure 5.5: Scheme of the setup used for the TOF electronics test at SPS. The grey cloud in the figure represents all the solutions that we tested. The pre-amplifers are integrated in the hybrid board for all the devices.

- voltage provided to the pre-amplifier.

The results obtained with the better configurations are visible in figure 5.6. The quoted resolution has been obtained by deconvolving from the standard deviation σ_{12} of the time distribution ΔT_{12} the resolution of the HADES sensor measured in the previous section (again the FNT method is used to measure ΔT_{12}). Looking at the results we see that the single stage has much better performances than the dual stage. The same for the filtering, that has to be avoided. On the other hand the applied voltage seems to have a minor impact on the resolution, but with slightly better results at lower voltages. No difference is found removing the decoupling capacitor. The performance with the best configuration (1 stage, 3 V, no filtering) gives a results of $\sim$ 150 ps, comparable with the one obtained with the HADES booster. However this results can be improved by adding an offline low pass filter with cut-off frequency of 700 MHz. The best resolution with this filter is 130 ps. The gain of this second stage (to which I will refer as amplifier stage or ABA-stage) is $G = 22$ dB. More information on the electronic configuration will be provided in the next section, where the amplifier scheme will be reported.

The best value of 130 ps is already a big step forward, especially from the $\sim$ 220 ps achieved in chapter 4, but it is still not enough and we needed to go forward.

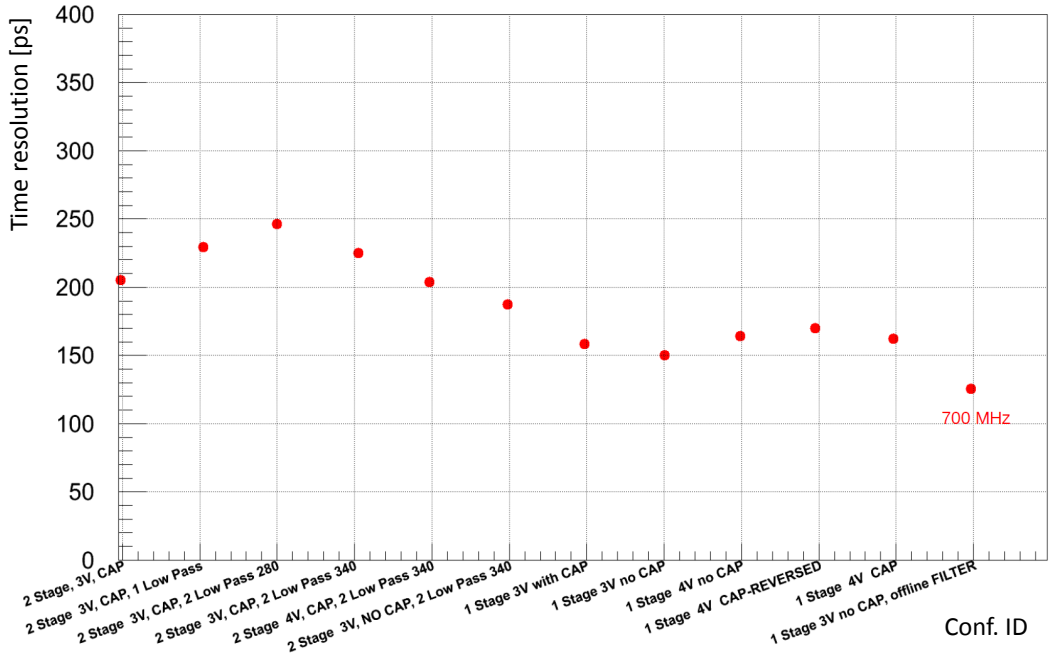

Figure 5.6: Resolution of the TOTEM sensor with different second amplification stages. The main differences in the configuration are reported in the x axis.

Looking at the waveforms we convince ourselves that the problem was now related to the reproducibility of the signal. The amplifier was fast, with ~ 600 ps rise time, but the shape of the output signals were not similar, and all the timing algorithms suffer from this. A shaper was needed and we try to add the booster of HADES after the ABA (trivia fact, the test was made with the last beam before Christmas 2014). Since the booster was saturating but we did not want to change the parameters of the amplifier we added a 10 dB attenuator in between the two stages (fig. 5.7). The overall gain of the system was $G = 93$ dB.

The result was excellent (fig 5.8), with a resolution (after the deconvolution of the HADES resolution) of $\sigma_t \sim 90$ ps, the same of the HADES detector but with a pixel capacitance 8 times larger. In this case we make use of the algorithm #6 (polynomial fit) that can give the best results. Using the FNT still the timing resolution of ~ 100 ps is achieved. Unfortunately few statistics was collected due to the beam Christmas shutdown. In this case the usage of an offline filter gives negligible benefits. The comparison between the two sensor parameters can be found in figure 5.9.

The scheme of figure 5.7 was hence considered the golden one, and the next generation of hybrids had to be based on this scheme, with all the three stages of

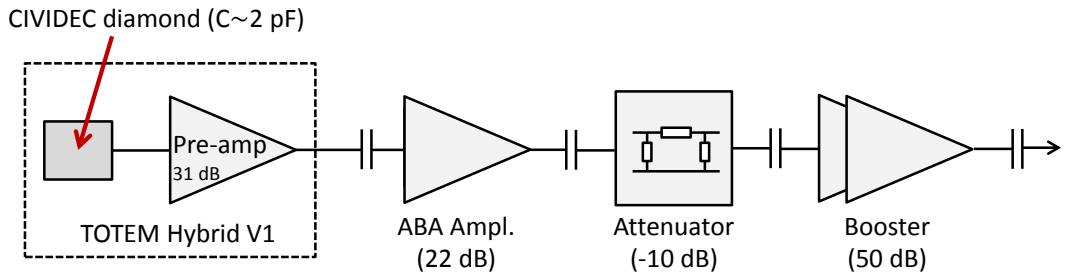

Figure 5.7: The amplification chain developed at SPS. The double symbol for the booster represents that it is internally formed by two stages.

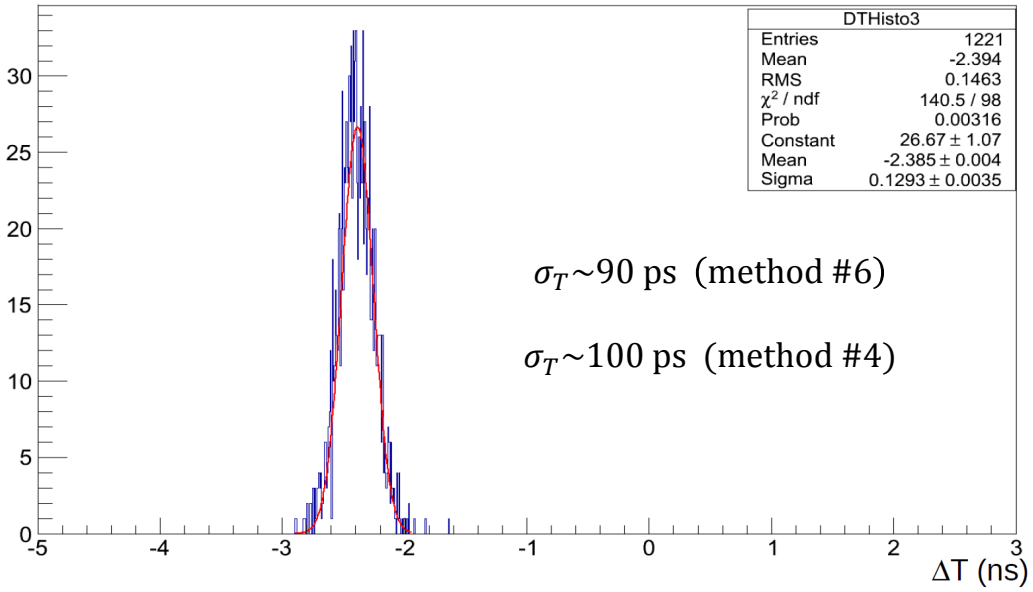

Figure 5.8: Best timing result obtained with the TOTEM hybrid at SPS. The Distribution of the time difference is done with the HADES sensor and best TOTEM amplification chain configuration. The data have been analyzed with algorithm #6 (polynomial fit). Resolution with FNT method is also quoted.

amplification integrated.

5.2 Prototype validation

A second prototype of the hybrid board (fig. 5.10) was developed following the result of the SPS test beam. This revision has four channels with all the electronics (pre-amp, amplifier and booster) fully integrated. The inner part (magnified in the

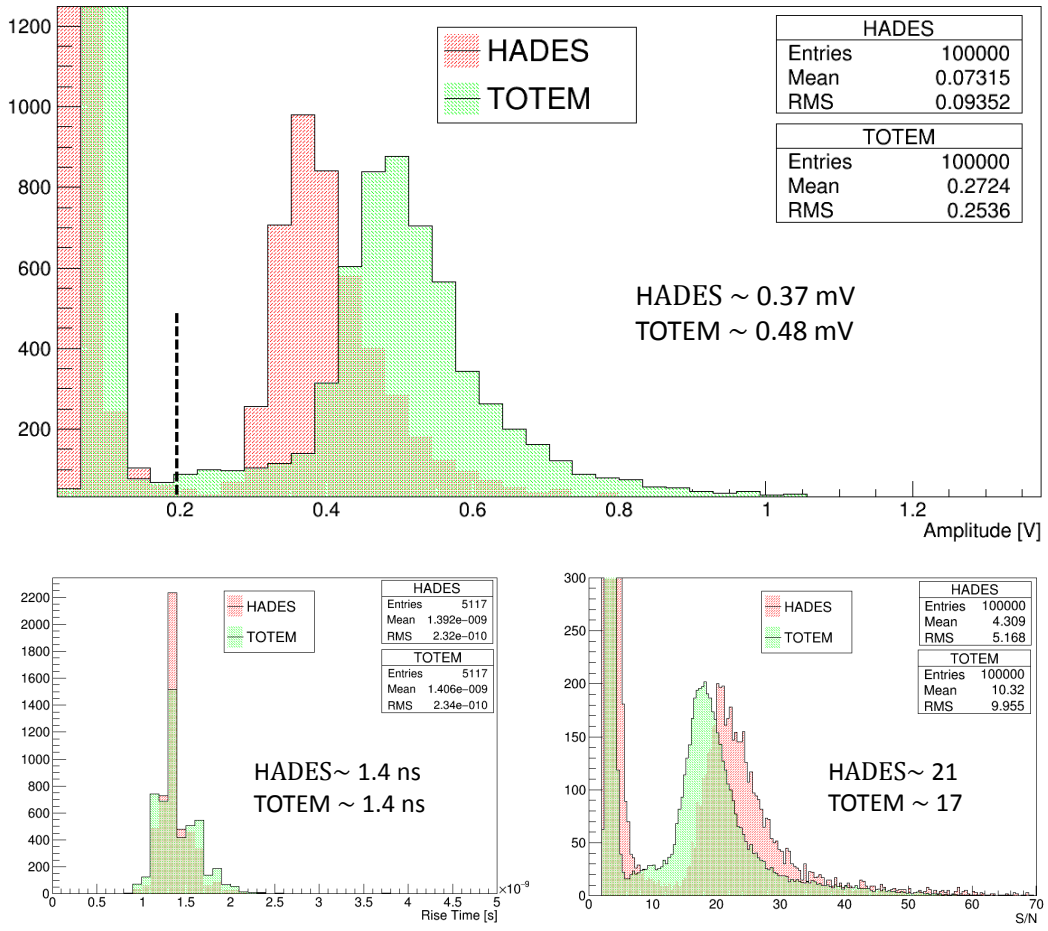

Figure 5.9: Comparison between HADES and TOTEM sensor parameters at SPS: signal amplitude, t_r^{20-80} and SNR are provided. Amplitude and SNR are rescaled for better comparison.

figure) contains the sensors and the four pre-amplifier. The area can be covered with an RF shield that is fixed to the board. Outside the shield the ABA stage and the booster are placed. To provide different low voltages to each stage on board regulators have been added. The sensor in the figure is the one with the strip metallization, discussed later.

The scheme of the TOTEM amplifier and the booster, re-adapted from the HADES one, are reported in figure 5.11. For our booster we used two stages with the wideband NPN transistor BFG425W. The first booster stage is the one which define the shaping time of the signal, through the RLC circuit located between the collector and the feedback of the transistor. Between the amplifier and the booster the attenuator is placed, used to tune the circuit during the tests.

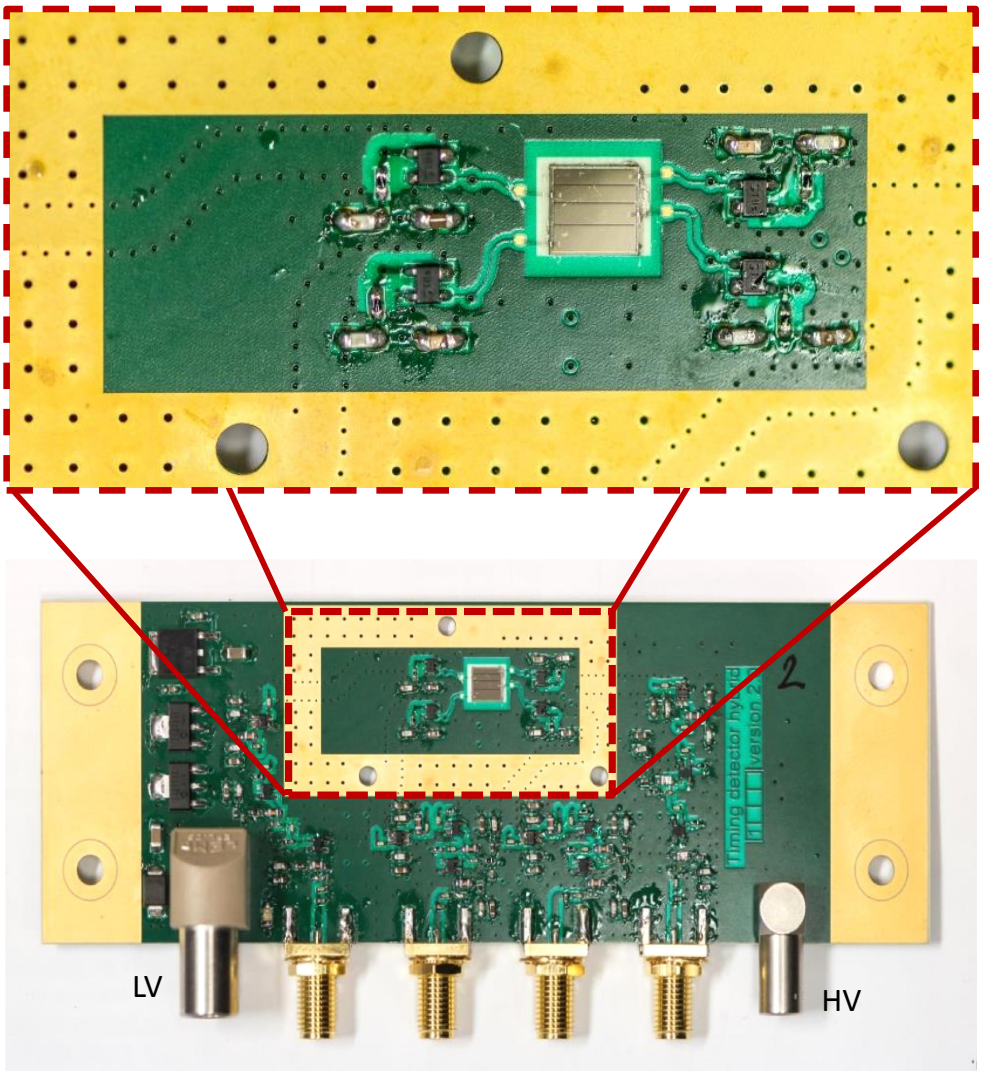

Figure 5.10: Picture of the second version of the hybrid board prototype. The low voltage regulators are placed on the left side. Diamond and pre-amplifiers are shown in the magnified area.

The hybrid was extensively tested at the DESY[5] laboratory (beam line T21) with four main goals:

- optimize the new hybrid board and confirm the SPS result.
- provide a final validation of the amplification chain.
- study the dependence of the performances from the sensor capacitance.
- measure the detector efficiency.

[5] *Deutsches Elektronen-Synchrotron*, Hamburg, Germany.

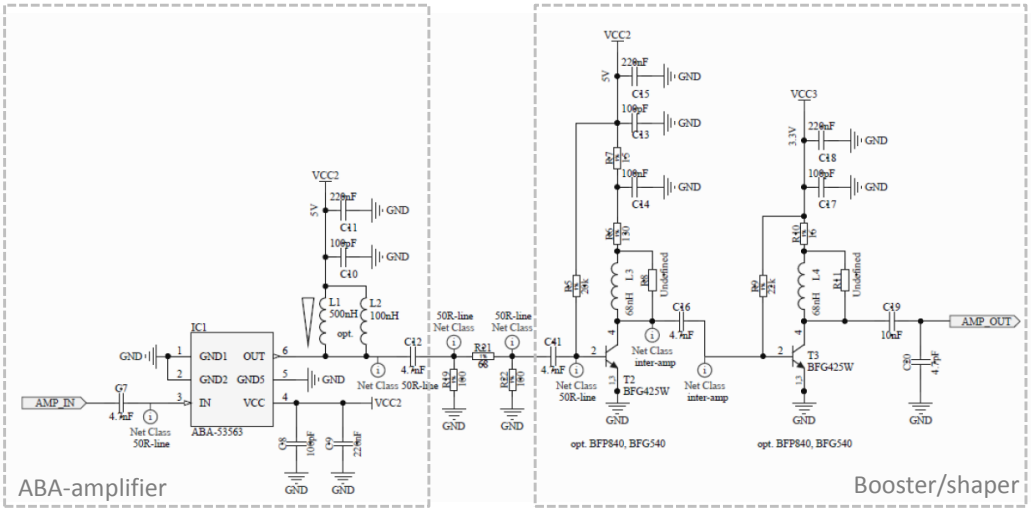

Figure 5.11: Scheme of the amplifier and shaper integrated by TOTEM. Compent values may differ from the final one.

The tests were performed in two separate test beam weeks at the begin of 2015. The first was mainly focused to the hybrid optimization and validation, while the last one was oriented to the efficiency studies. The choice to perform such test in DESY instead that at SPS was done for the availability of a tracking detector on the T21 beam line, put at disposal of the users. The use of a tracking detector was indeed mandatory to perform the efficiency measurement program.

5.2.1 Experimental setup

The Desy T21 beam line provides high energy electrons in the range 1-6 GeV, with an energy resolution of 5% and angular divergence of 5 mrad[127]. Electrons are accelerated in the DESY II synchrotron up to 7 GeV. A bremsstrahlung photon beam is created by the interaction of the electrons with a carbon fiber inside the ring. The photons interact outside the ring with a secondary target, used to generate electron/positron pairs. A magnetic dipole is then used as a spectrometer to select electrons or positrons with the desired energy. The current and the polarity of the magnet can be controlled from the test beam control room. The particle flux depends on the desired energy, with its peak located at $\sim$ 2.2 GeV, and rapidly decreasing as the energy rise.

In the experimental hall the DATURA[6] telescope[128] is installed and available

[6] *DESY Advanced Telescope Using Readout Acceleration.*

for the users. The DATURA telescope is one of the detectors born from the EUDET\AIDA project. The tracker is formed by six detection planes, three upstream the *Device Under Test* (DUT) and three downstream (fig. 5.12). The offline re-

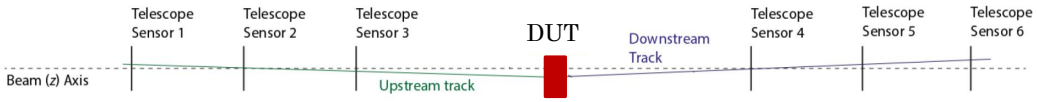

Figure 5.12: Setup of the DATURA telescope. Tracks are independently reconstructed on each arm.

construction algorithm can reconstruct the tracks in the two arms of the detector independently, thus taking into account the possible multiple scattering that the particles may have in the DUT. This feature is particularly usefully with the electrons. Each plane integrates the MIMOSA-26 sensor[129]. The sensor is a CMOS pixel sensor with active area of $21.2 \cdot 10.6$ mm^2 and only 50 µm thickness, divided into 1152 columns of 576 pixels each. This segmentation provides a pitch of ~ 18.4 µm, with a final resolution of ~ 5 µm on each plane. The installed CMOS sensors work in accumulation mode, with an integration time of 112 µs, meaning that information of all particles detected during one integration time are piled-up. The maximum frame rate is ~ 1 Kf/s. The frames are continuously readout, after a zero suppression, but are recorded only on trigger.

The large integration time puts some problems when the device under study is not a tracker but, as in our case, a detector with a coarse segmentation, since it is not possible to disentangle multiple tracks. To overcame this limitation we had to collect data in two different configurations. When the tracker was not needed (timing measurements) we collect data with 4 GeV electrons, which granted a good rate ($\sim$1 KHz) to reduce statistical uncertainties. In this configuration we measured a mean multiplicity of ~ 4 tracks in the detector. When indeed the tracker information has to be integrated we use 5.6 GeV electrons, obtaining a mean track multiplicity of ~ 2.5, but with a drop in the trigger rate to $50-100$ Hz. We checked in our detector if the energy release of the electrons was different at the two energies but, as seen in figure 5.13, no difference is found.

Almost all the measurements were performed using three hybrid boards, two equipped with diamonds with full pad metallization and one with a segmented diamond[7]. The full pad diamonds were the "old" sensor from CIVIDEC and a brand

[7]The segmentation is done during the metalization of the diamond pad. One side, which is

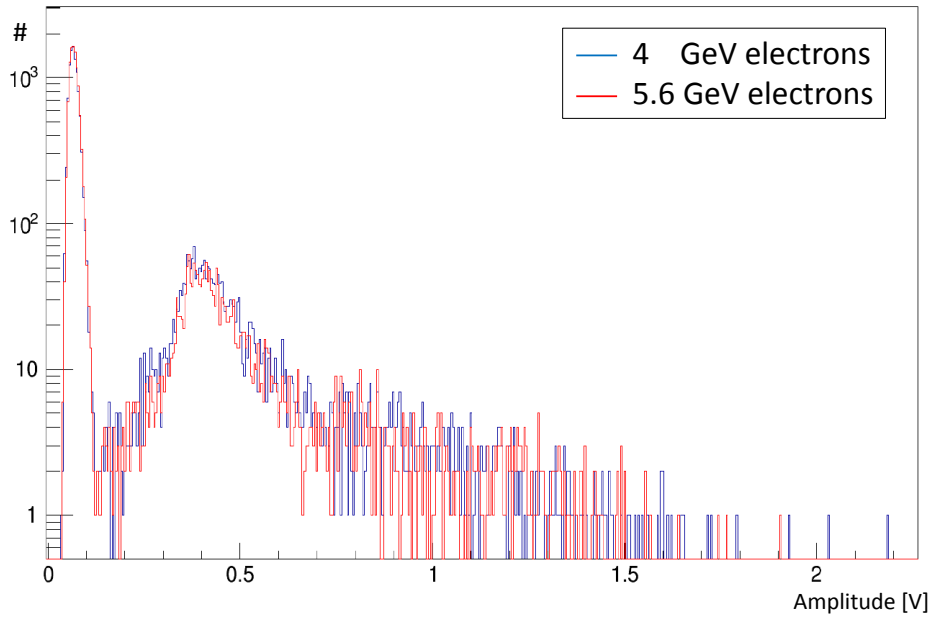

Figure 5.13: Signal amplitude distributions from electrons with 4 and 5.6 GeV energy. The distributions perfectly overlap.

new diamond from Element6, metalized by the Princeton university (New Jersey, U.S.A). The segmented diamond had the four strip segmentation foreseen for the vertical upgrade inner diamond (fig. 2.22, channels 1-4), and was metalized from the GSI laboratory (Darmstadt, Germany). Between two strips a spacing of 0.1 mm is present: the efficiency in this area will be later discussed. We also had the GSI telescope as in the SPS test beam, but the channels used in the previous analysis was giving worse results and were therefore not used. In table 5.1 a summary of the sensors is reported, together with their area and capacitance.

Sensor ID	CIV	Strip A	Strip B	Strip C	Strip D	PRN
Metallized by	CIVIDEC	GSI	GSI	GSI	GSI	Princeton
Area [mm^2]	$4.2 \cdot 4.2$	$0.7 \cdot 4.2$	$0.83 \cdot 4.2$	$1.02 \cdot 4.2$	$1.35 \cdot 4.2$	$4.2 \cdot 4.2$
Cap. [pF]	2	0.29	0.34	0.42	0.56	2

Table 5.1: Summary of the diamond sensors employed at DESY. The sensor ID will be used through all this section.

At the beginning of the first test beam all our detectors were placed in between

connected to the HV has all the surface metalized, while in the other the pixel pattern is applied

the DATURA arms, but we later decide to reduce the material budget, which effect will be visible in section 5.2.3. In the final configuration we use the hybrid with the strips as DUT while the other two hybrids were placed downstream the tracker (fig. 5.14).

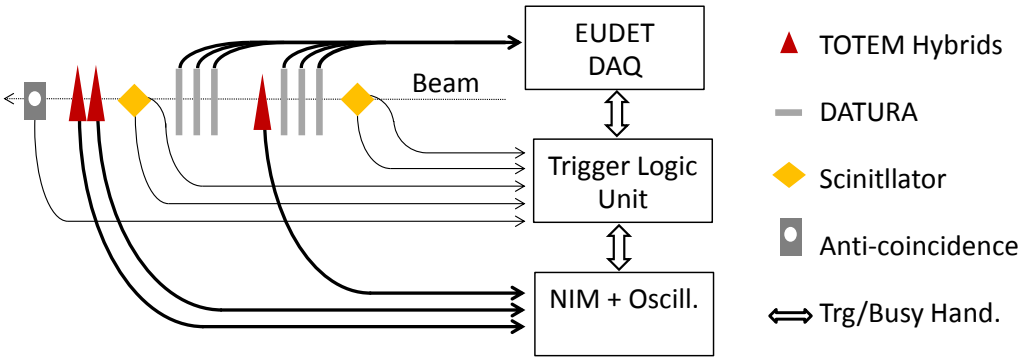

Figure 5.14: Scheme of DESY test beam setup.

The trigger system is provided by the facility and is composed by two set of scintillators in cross configuration upstream and downstream the tracker, very similar to our standard setup but tuned to trigger on particles hitting in the wider DATURA sensors. To reduce the alignment inefficiency generated with this configuration (many triggers on particles outside the diamond area) we had to reinforce the trigger requirements changing the signal of one of the local scintillators with the anti-coincidence scintillator used at SPS, placed downstream all the others detectors. All the trigger signals were sent to the *Trigger Logic Unit* (TLU), which propagates the final trigger signal both to the tracker DAQ (EUDAQ) and to our oscilloscope (same as the previous test beams). Some pictures of the setup can be seen in 5.15.

The synchronization between the telescope and the oscilloscope is possible through a busy signal which the DUT must send to the TLU in order to block additional triggers. To remove the trigger veto the busy signal must be asserted and released. The same procedure is followed by the tracker. In our setup the busy signal was generated with the *trg_out* signal of the oscilloscope, which acknowledges the event acquisition.

The busy handshake was however complicated by our decision to acquire with the oscilloscope in the so called *segmented mode*. This acquisition mode permits to acquire data at higher rate (up to $\sim$ 1 KHz, with very low dead-time), storing the

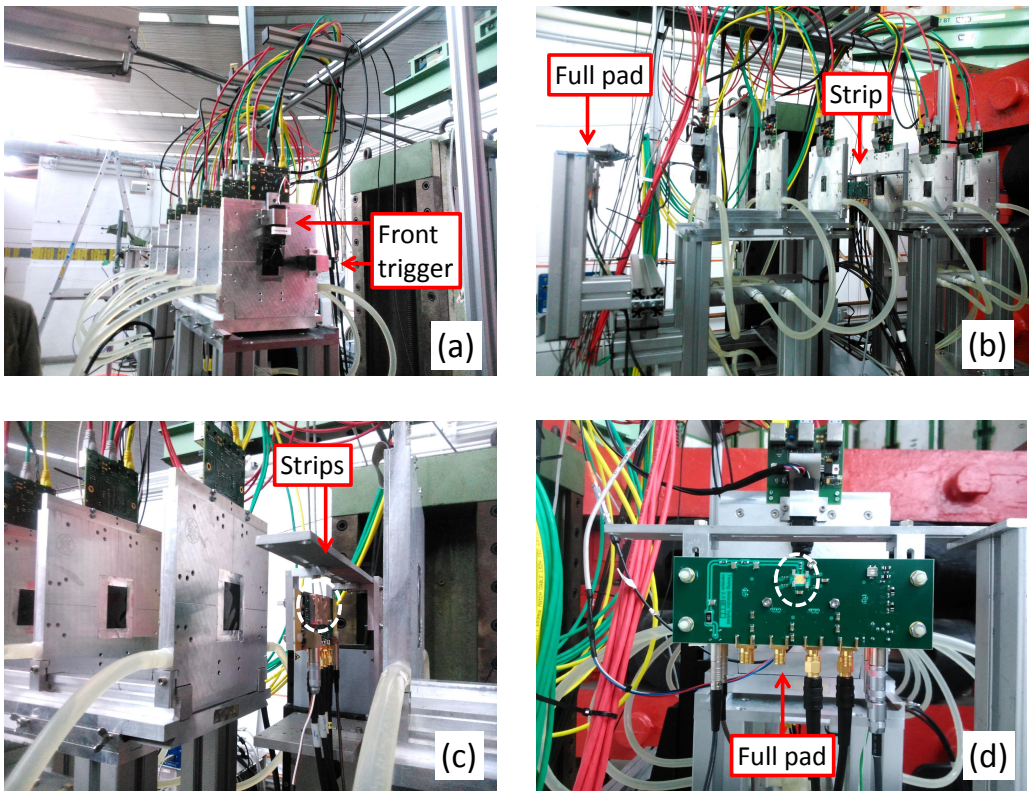

Figure 5.15: Pictures of the DESY setup. In a, b a panoramic of the detector system is visible. In c the strip diamond, with the RF shield placed (reduced to a small copper foil). In d the full pad diamonds (back side). Notice the presence of the capacitors near the sensor in d, which effect (in terms of material) will be clearly visible in the later efficiency studies.

data in the RAM of the oscilloscope. When a programmable number of waveforms (segments) have been acquired, they can be manually saved by the user on the disk and another acquisition can be started. The data saving can take several seconds, but the increase in the mean DAQ rate is however considerable (especially when the beam line provides burst of particles like in DESY) and it was necessary to collect all the data wee needed.

Two issues arise from this modality. First the process is not automatic, since the data saving and the DAQ restart commands must be manually provided. This problem has been solved by developing a python code (of which I wrote the core and the main functionality) that communicates with the oscilloscope through TCP/IP. The code open a communication with a socket on the oscilloscope machine and send ASCII strings that are interpreted as command from the device. After the

connection check the software manage the acquisition, data saving and re-arming the oscilloscope, automatizing the data taking. The program can run on any machine (usually we make it run directly in the oscilloscope, which is remotely controlled by remote desktop) without additional software, apart from the python interpreter.

The second problem is generated in the handshake procedure with the TLU. When the segmented acquisition is completed the next trigger generated by the TLU will never get the busy back from the oscilloscope (is not possible to generate a fake *trg_out* signal). The system will get stack. We make a work-around with the help of a dual timer and few additional NIM modules (fig. 5.16). While the segmented

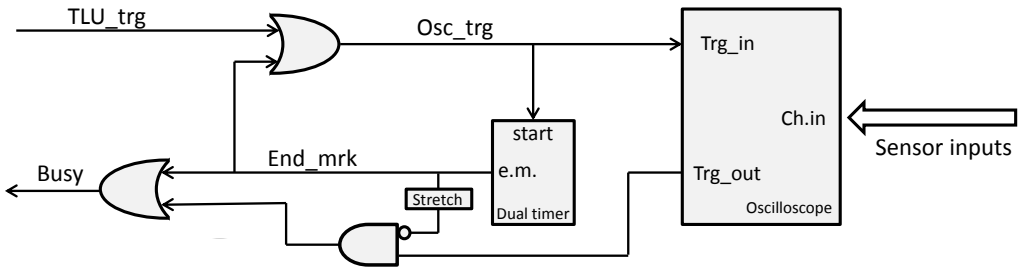

Figure 5.16: Scheme of the TLU/oscilloscope trigger handshake. Additional delay units have been used but not reported. TTL to NIM voltage translators have been used when needed.

acquisition is ongoing the dual timer will continuously restart its countdown and no *end_marker* signal is generated. When the oscilloscope stops to accept triggers and the TLU is waiting the *end_marker* will be generated from the dual timer, re-arming the system. The dual timer is set to wait a sufficient amount of time to ensure the oscilloscope data saving and acquisition restarting operations are accomplished. The *end_marker* is back propagated to the oscilloscope to maintain the event number alinement, even if the first event of each segmented acquisition has to be discarded in the analysis. For this first event the *trg_out* of oscilloscope is vetoed. The data taking was smoothly with this arrangement and no data desynchronization was found.

5.2.2 Optimization and performances

We performed the optimization of the hybrid by testing the system performances varying three parameters:

- the attenuation between the amplifier and the booster stage.

- the capacitor value on booster first stage collector.
- the voltage provided to the first stage of the booster collector.

The modifications were made in the hybrid with the CIV sensor, while the larger strip (Strip D) was kept with a fixed configuration and used as reference. This results are the first time resolution obtained between two TOTEM hybrid, and could be considered the first real test of the resolution of the final TOF system. In figure 5.17 the best configurations tested are reported. Again the same FNT algorithm has been used. Since at this stage we did not have any estimation of the resolution, it was not possible to deconvolve the Strip D resolution from the ΔT_{12} distribution standard deviation. This is not a problem since we were interested only on the difference between the configurations. Although this I will report the value divided by $\sqrt{2}$. The quoted values are not exactly the resolution of each sensor, since the different area give slightly different timing performances, but can still be considered a hint of the final resolution. For the low voltage we identified a plateau where no

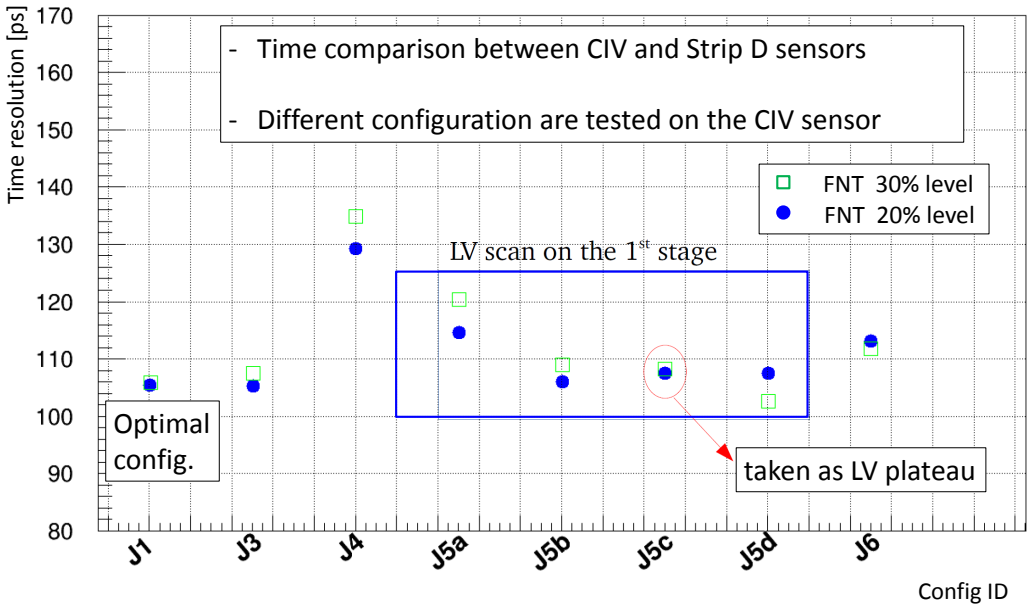

Figure 5.17: Timing resolutions with different electronics configurations. The J5X differs only for the LV applied (step of 0.2 V, 2.0 V in J5c). Configuration J1 as been taken as the optimal one. Results with 20% and 30% threshold level are reported (analysis algorithm #4). J1 is not the original configuration, which gave worse results.

differences were found, and we set the final value in the middle of it.

The independence of the resolution from the LV is extremely important and must not be underestimated. In the previous section also the LV of the pre-amplifier was found to have a minor impact on the resolution. This means that the gain of this stages (that depends on the low voltage) can be adjusted without signal degradation. This allow to set the amplification at the maximum without incurring in the saturation of the next stage. In this way each plane of the detector can be optimized and better performances can be achieved.

After the optimization the best configuration has been implemented in all the four channels of the segmented diamond and in the PRN sensor. The resolution has a function of the sensor capacitance has been investigated (fig. 5.18), first by measuring the time difference distribution of the different strips against the CIV sensor and later by the CIV and the PRN diamonds. Since the PRN and CIV sensors

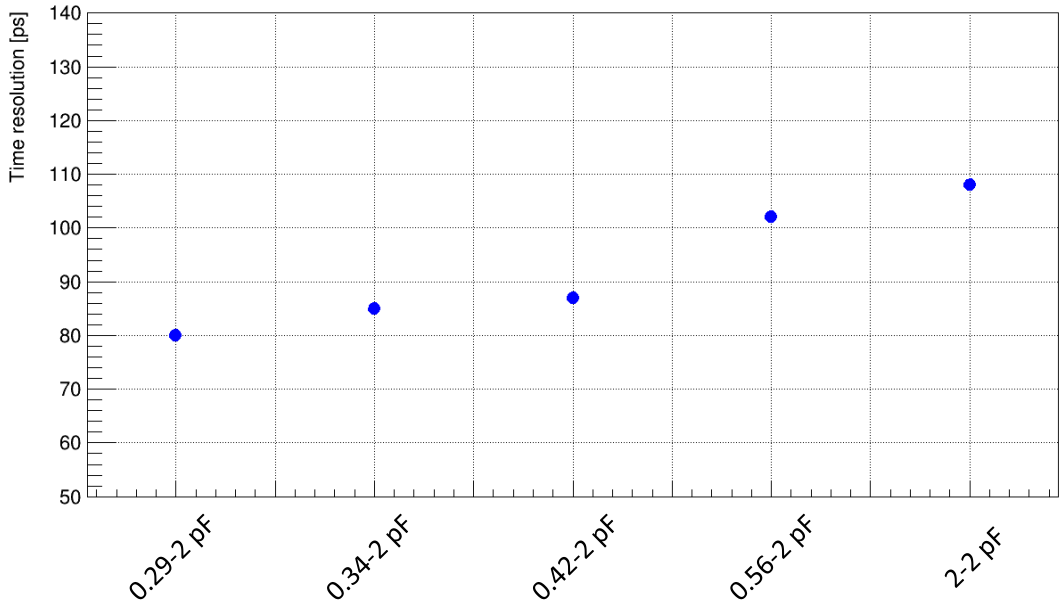

Figure 5.18: Time resolution as a function of the detector area. All the channels work with the optimized electronics.

were identical (same electronics configuration and pixel size), we extrapolated their resolution from their time difference distribution ΔT_{12} as $\sigma_t = \sigma_{12}/\sqrt{2} = 108$ ps. This value represents the worst case scenario, being related to the larger area pixels. The result is worse than the one obtained at SPS with the non-integrated chain, but still acceptable. Moreover this was the first measurements involving only TOTEM sensors. The time resolution for the strips has been obtained by deconvolving the CIV resolution from the measurements. The results are extremely good, with the

smaller strip reaching a resolution of ~ 80 ps, better then our expectations.

In figure 5.19 the analysis result for the time difference distribution obtained between the smaller strip and the full pad sensor is reported, while in figure 5.20 the distributions of the main parameters for both sensors are given for comparison. The results span in the range $80 - 108$ ps. This was a milestone for our project

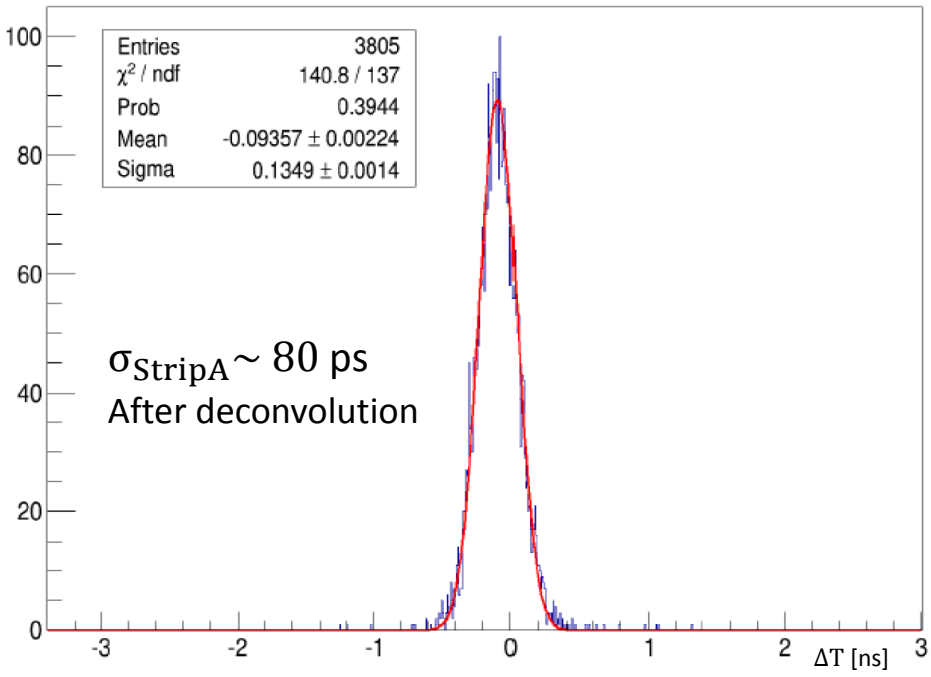

Figure 5.19: Distribution of the time difference between Strip A (0.29 pF) and CIV (2 pF) sensors.

because it demonstrated that we could achieve the ~ 100 ps resolution as required. Here no external reference is employed but only our hybrids, with all the channels equipped with final electronics. In table 5.2 a summary of the results is reported.

5.2.3 Efficiency

The efficiency measurements has been done in the strip detector, using the DESY tracker to determine the passage of the particle through one of the strips, using the strip detector as DUT. The data have been offline merged thanks to the synchronization procedure already described and the track reconstruction has been performed through the software suite available for the tracker users. First events with tracks on both arms of the detector pointing to same coordinate (within the telescope resolution) in the diamond detector plane have been selected. Then to locate the

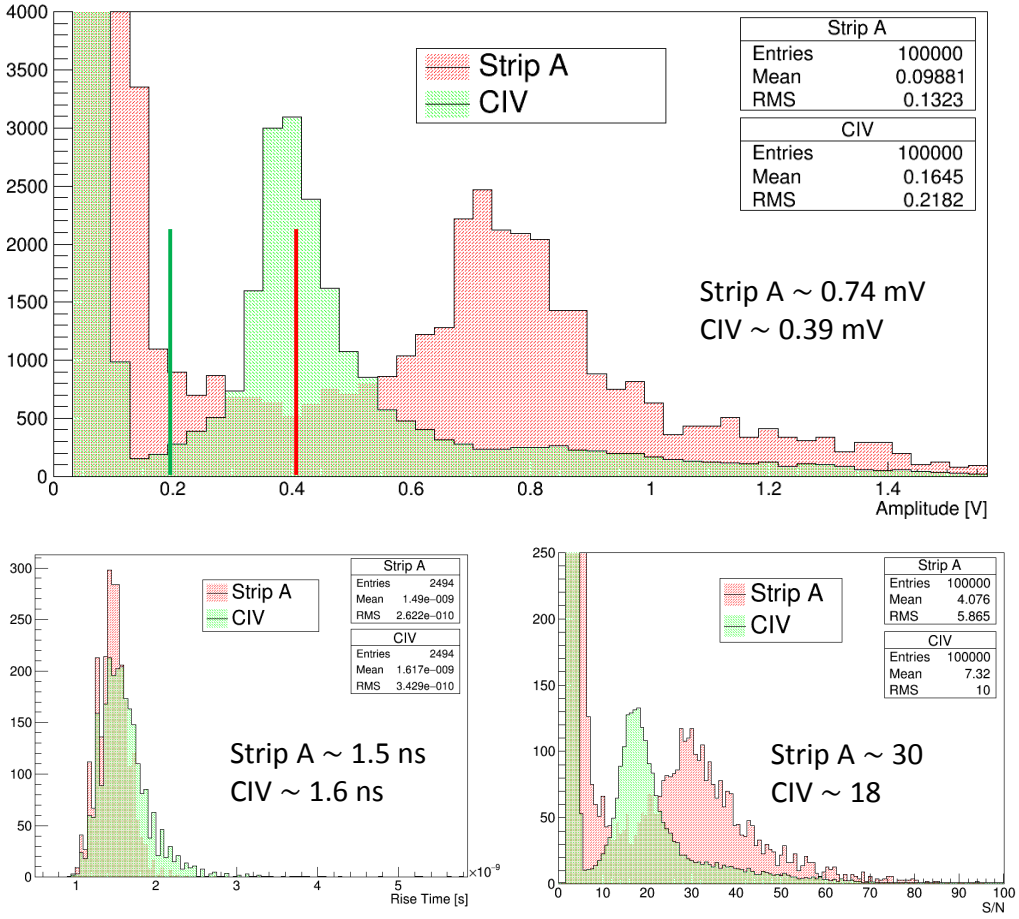

Figure 5.20: Comparison between Strip A (0.29 pF) and CIV (2 pF) parameters: signal amplitude, t_r^{20-80} and SNR are provided. Analysis thresholds were set to 0.2 and 0.4 V for CIV and Strip A respectively. Amplitude and SNR are rescaled for better comparison.

Sensor	Pad area [mm^2]	σ_t	Ampl. [V]	Rise Time [ns]	SNR
StripA	$0.7 \cdot 4.2$	80	0.74	1.48	30
StripB	$0.83 \cdot 4.2$	85	0.70	1.51	31
StripC	$1.02 \cdot 4.2$	87	0.70	1.48	30
StripD	$1.34 \cdot 4.2$	102	0.62	1.49	28
PRN	$4.2 \cdot 4.2$	108	0.39	1.56	18

Table 5.2: Summary of the results obtained with different area sensors. All the timing measurements are obtained against the CIV sensor. An error of ± 1 can be considered on the last digit of amplitude, rise time and SNR.

position of one strip we selected the events without signal in the strip and we observe the resulting track distribution in the DUT plane perpendicular to the beam. The threshold to determine if a signal was present or not has been determined from the amplitude distribution of the strip. Examples of hit distributions obtained with the tracker are provided in figure 5.21. We can now appreciate the effect of the

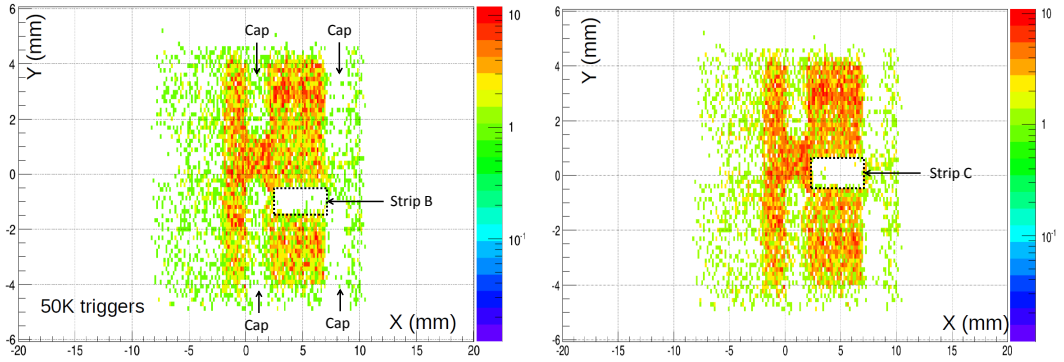

Figure 5.21: Distributions of the track hits in the DUT plane, when requiring one strip without signal. The effect of the material on the electrons can be appreciated in the distributions. The shadows of the capacitors are clearly visible.

material on the electron beam: in the figure the shadows of the four capacitors near the diamond (see picture 5.15.*d*) is evident.

The efficiency has later been measured by checking if a signal was given from one strip when a track pointing to that strip was found. Thanks to the high resolution of the tracker it has been possible to perform a bi-dimensional scan of the diamond. A uniform efficiency, above 98%, has been measured in the bulk area of the diamond (fig. 5.22). From the plot we see that the areas between the strips (without metalization) does not have any drop in the efficiency. To better investigate the inter-strip area in figure 5.23 the projection of the efficiency in the Y axis is shown for the measurements performed on strips B and C. The efficiency of the detector remains high also in the interstitial area, with a minimum of $\sim 80\%$. However in the dip area we have two strips which are able to detected the particle, with an overall efficiency of $\sim 96\%$. Still for the particles hitting in the low efficiency area a worse time resolution is expected, since the amount of charge collected from the strip is lower. Corrections based on the collected charge in both strips can still be performed to reach the nominal resolution.

With the DESY measurements the amplification chain and the hybrid structure could be considered validated, both in terms of timing and efficiency, and the final

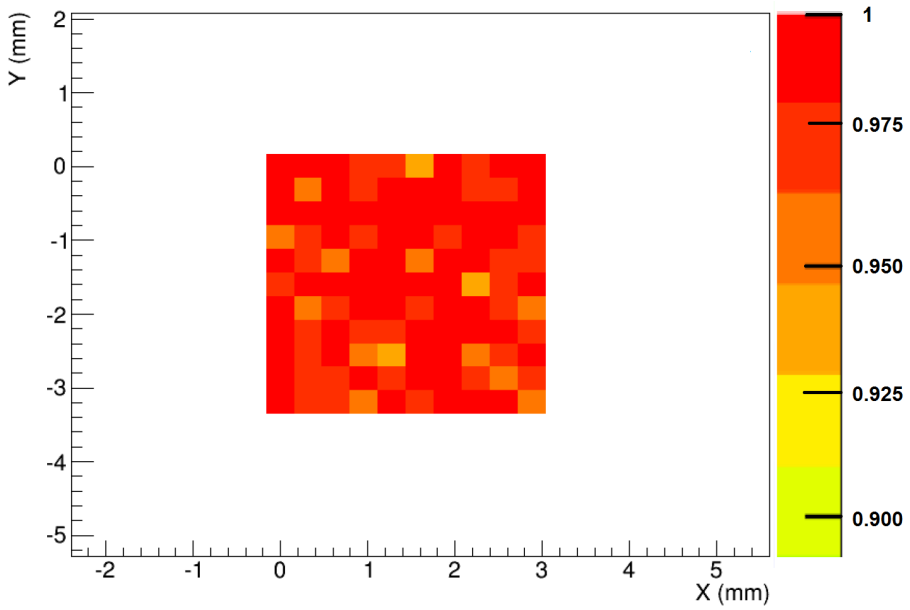

Figure 5.22: Efficiency scan in the diamond bulk area. Overall efficiency is measured above 98%. On each bin a statistical error $\sim 10\%$ is present.

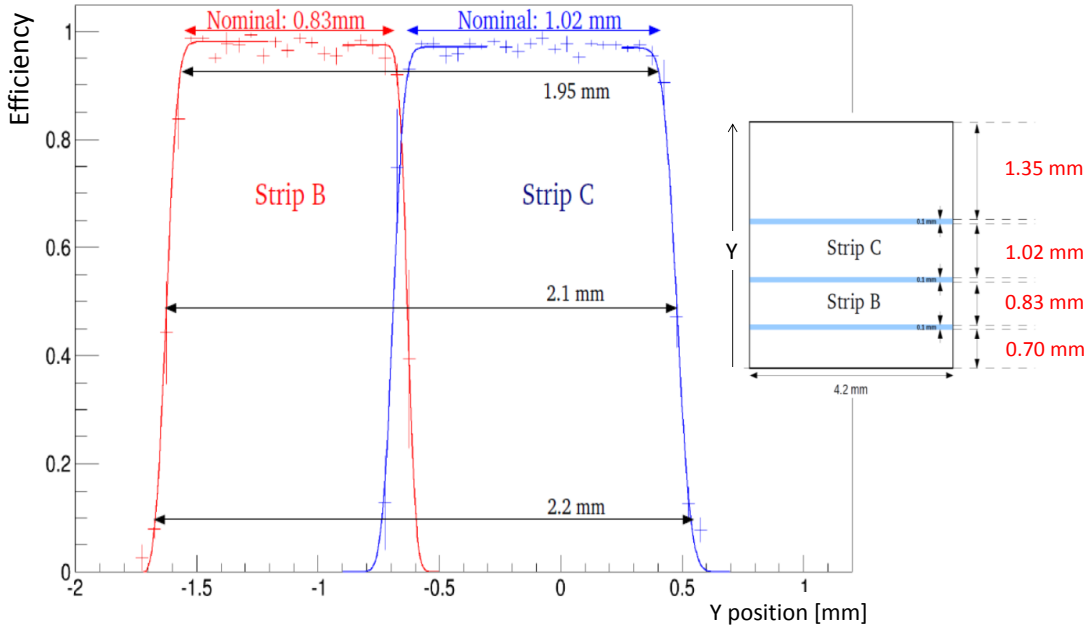

Figure 5.23: Efficiency measure in the inter-strip area. Strip B and C have been used. Data from both strips were simultaneously collected.

board production took place.

5.3 The TOTEM TOF detector

The final version of the detector has been completed, produced and tested. The board hosting the 12 channels as described in chapter 2.5 can be seen in figure 5.24. The three stages has been integrated into three separate sections. To each section

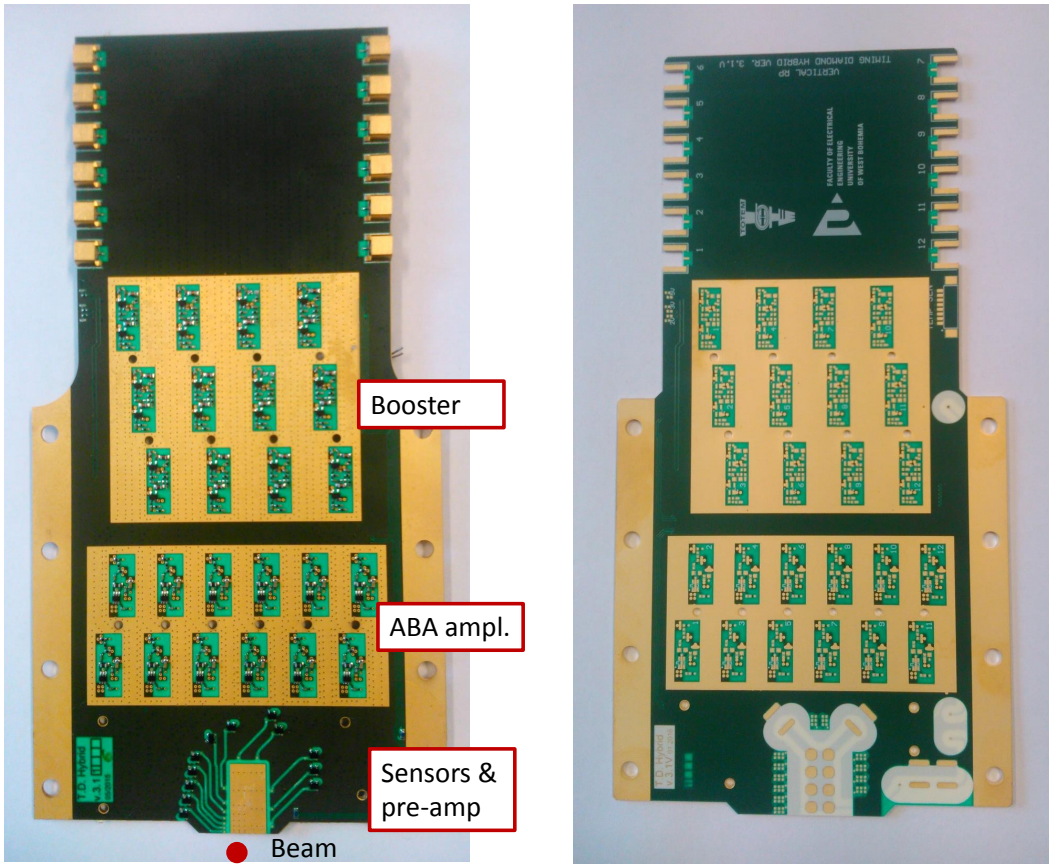

Figure 5.24: Pictures of the Totem TOF hybrid boards. Both revisions are showed. The left one is the one used for the measures here described, while on the right the revised version is present. Identical except for the HV isolation.

RF shield can be added. The output signal is readout through MCX connectors.

It should be noted that the LV regulators have been removed. The LV regulation and distribution is indeed performed outside the RP. For each plane of detection hosted in the RP (4 in total) a different LV for the pre-amplifier can be remotely controlled, while the booster LV will be the same for all the boards, but still con-

trolled. In this way the voltage optimization will be done also after the detector enclosure in the RP.

In the figure two versions of the board are reported. On the left the board used to perform the final test hereafter described, while on the right an upgraded version, which solves the issue of the high voltage identified on the first revision. The second version is indeed identical to the first, except for a redesigned HV distribution and isolation. The new version has been produced after the vacuum tests performed on the original one, that showed the presence of sparks at high voltage (above 450 V) at the nominal vacuum ($\sim$ 40 mbar) that will be created in the RP. An additional coating is also applied on the diamond after the bonding to prevent sparks from the diamond top surface.

The detector was tested at the SPS test beam line, in the same beam condition described in section 5.1. Two boards were employed (TB1 and TB2), populated with four diamonds (fig. 5.25). Referring to figure 2.21 we had 8 available channels, from 1 to 7 plus channel 12, so that all the different pixel areas were available. The detector were moreover installed in RP station, even if no vacuum was still provided.

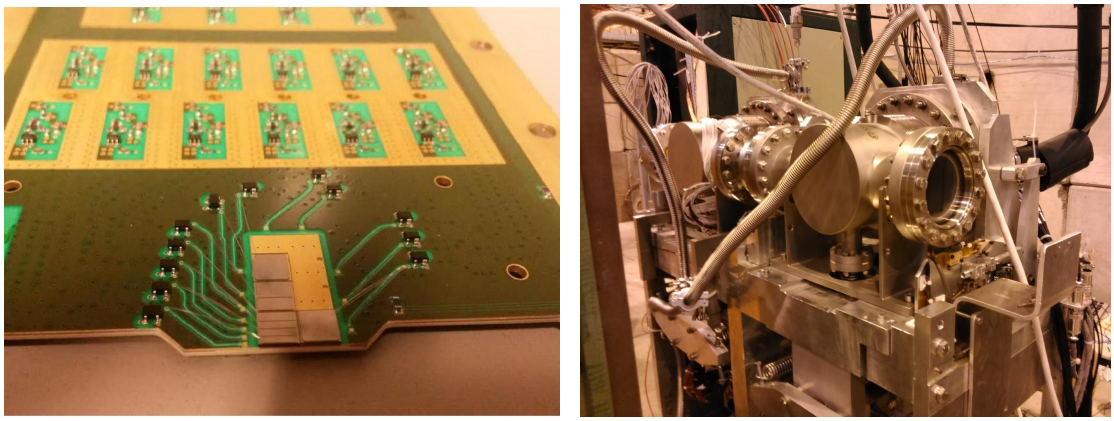

Figure 5.25: The totem TOF during the final tests. The bonded diamonds are visible on the left image. On the right the RP system equipped with two of our detectors.

The setup was completed by the three hybrids used during the DESY test beam (all equipped with full pad diamond), a tracker from the RD51 collaboration (CERN) and a *Micro Channel Plate* (MCP) detector. Two of the hybrid were attached to the RP system (upstream and downstream), while the third one was in a stand-alone movable table and was used as a beam position monitor (BPM). The two

fixed to the RP were used to center the RP system by maximizing the number of coincidences with the BPM. The trigger was provided by a set of scintillators, placed downstream the tracker, before the BPM and the RP. The readout of the TOTEM RP was again performed with the same oscilloscope. The tracker detector was made of three planes of triple GEM, very similar to the one described in section 2.3.2, with a spatial resolution of ~ 70 µm on each plane. This tracker, even if less precise than the DATURA, does not suffer of pile-up issue and high particle flux can be sustained. The synchronization with the oscilloscope was performed with the same handshake procedure introduced in the previous section. Finally the MCP was used as an additional timing reference. MCP are indeed detector with exceptional time resolution (20-30 ps), but unfortunately have a low radiation resistance and are not suitable for the LHC near-beam environment.

The time resolution of the pixels was tested with the standard procedure. The time provided from the two boards were compared with the MCP , which adds a negligible smearing of the resolution (hence assumed $\sigma_t \sim 0$). As an additional check the time resolution among same channels of the two boards has been carried out. The results are displayed in figure 5.26.

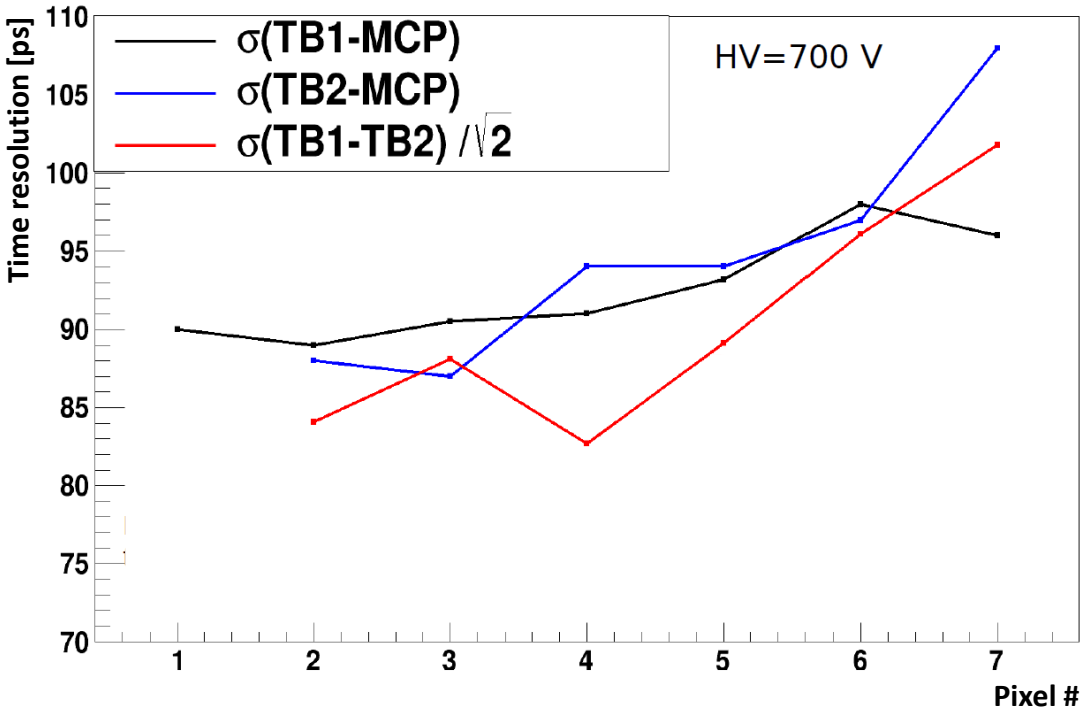

Figure 5.26: Time resolution of the TOTEM TOF detector for the different pixels. All the pixel sizes involved in the final configuration have been tested.

This results once again confirm that our detector has the desired time resolution even for the large area pixels. Moreover on TB1 the LV optimization make possible to have a resolution below 100 ps also for pixel 7 (big capacitance). A check on the efficiency has also been performed, confirming the result of DESY, with an overall value of $\sim$ 99%. The detector can be therefore considered ready for the final production and installation. With this results our detector is, at the time I'm writing, the diamond detector with the best timing resolution ever built.

Actually we are testing the RP which will be used in CT-PPS (chapter 2.6), hosting the diamond detector that I have just described, with the only difference in the diamond arrangement (refer to fig. 2.24). The installation is foreseen in few weeks and the data collected will be extremely valuable to investigate the hint of new physics at CERN. The detector for the vertical upgrade TOF system will instead be completely assembled, tested and optimized during the next months (we expect some additional performance enhancement from the LV optimization) and installed at the beginning of September. Others improvements and amplification schemes will be tested in the meanwhile, to reach an even better result and being finally compatible also with the CT-PPS timing requirements.

Chapter 6

Signal digitization

The results obtained in the previous chapter fully satisfy our requirements, but a detector is not made by sensors and front-end electronics only, and care must be hence put to develop a readout system that will not degrade the detector performances. Until now we always made use of the oscilloscope, which allows sophisticate offline algorithms. Two solutions have been investigated by the TOTEM collaboration, and will be here reported. The first solution foreseen the use of a fast sampler (6.4 GSa/s), the SAMPIC chip. The possibility to reconstruct the signal waveform offline makes possible to use the same algorithms presented in this work, preserving the performances. The SAMPIC will be described in section 6.1, where I will also report some results which confirms the whole system performance. The second possible readout investigated is performed though a discriminator (NINO) designed for TOF systems coupled to a TDC, and will be analyzed in section 6.2. The development of a TOTEM board to integrate the NINO, where I had a important role, and the performance results which I obtained will be presented. The SAMPIC will result as the best choice for the TOF system, since the second solution introduced a degradation on the timing. However the NINO+TDC scheme found its employment in the CT-PPS project, due to the SAMPIC rate limitation.

6.1 The fast sampler

The solution adopted by the TOTEM collaboration for the signal digitization in the vertical RPs is based on the SAMPIC (*SAMpler for PICosecond time pick-off*) chip[87, 88]. A picture of a commercial module developed at LAL (Orsay), hosting the SAMPIC is reported in figure 6.1. The module is based on a motherboard on which a mezzanine with the chip and an FPGA (which is used as a bridge) is

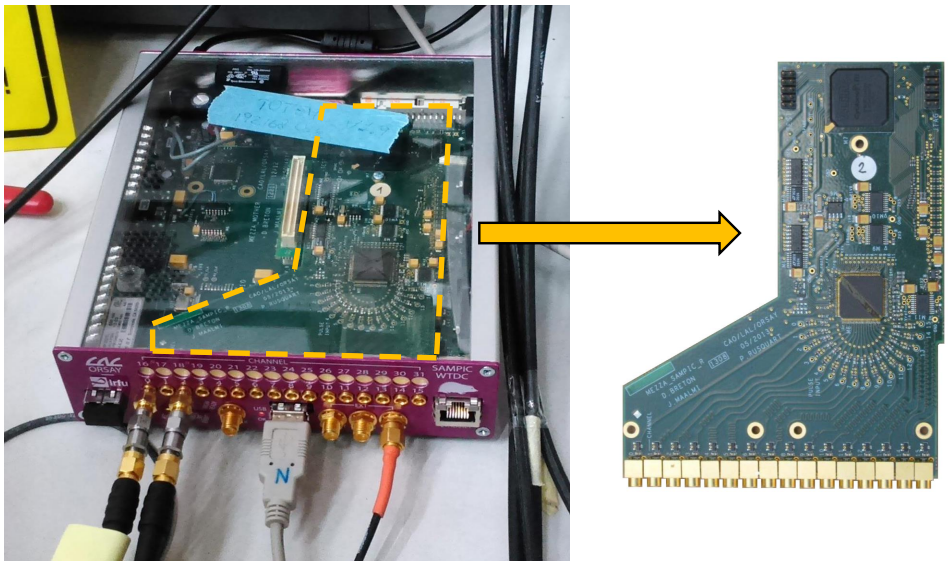

Figure 6.1: Picture of the SAMPIC module. The SAMPIC mezzanine, hosting the chip and the bridge FPGA, is highlighted on the motherboard and then shown on the right. The same module can host two mezzanines, providing a total of 32 channels.

plugged. This mezzanine is compatible with the TOTEM readout board and will be implemented "as it is". A custom revision is later foreseen. The FPGA will simply act as a bridge between the Microsemi FPGA in the TOTEM readout board and the SAMPIC (more on that in chap. 7).

The SAMPIC is a 16 channel ASIC, which works as a waveform and time to digital converter (WTDC), able to provide a fast sampling of the analog input signals, similar to an oscilloscope. The sampling frequency can be adjusted in the range $1 - 10$ GSa/s, even if at 10 GSa/s the available channel number is reduced to 8. In the TOTEM application we use the chip at 6.4 GSa/s, which grant good stability and performance. The signal input range is ~ 1 V (single-ended) with a 1.6 GHz bandwidth, and thus suitable for the diamond sensors (eventually attenuators can be added).

The chip core (fig. 6.2) is composed by a coarse counter (few ns step), a *Delay Line Loops* (DLL) and an analog memory. A DLL is basically formed by a series of analogical delay buffers (64 in the SAMPIC) which transmit the input clock, with an active feedback which ensure that the input clock phase is the same of the output. The status of the internal cells in the DLL can provide a virtual multiplication of the base clock frequency. When a channel is triggered the coarse counter value and

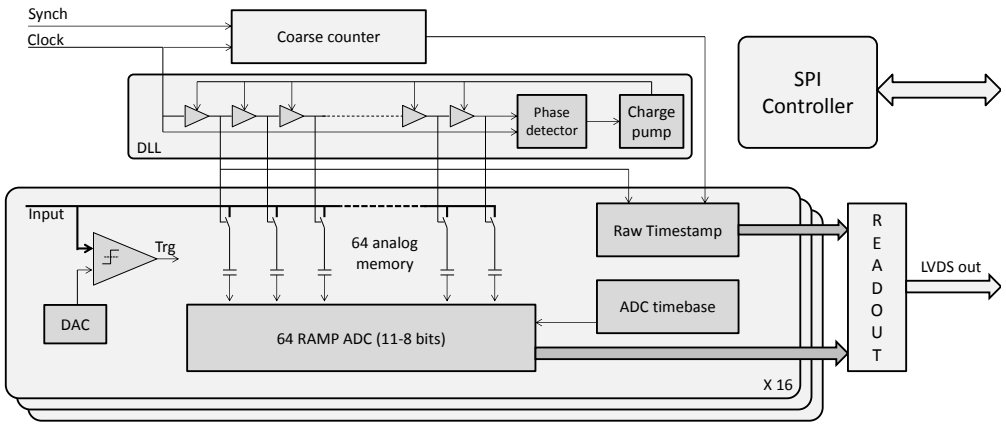

Figure 6.2: Scheme of the SAMPIC chip. In the scheme the trigger is generated with the self-trigger mode and distributed to all the sub-units. The chip control is done through the *Serial Peripheral Interface* (SPI) interface.

the DLL status are sampled and stored for subsequent readout. This information can be used as a raw timestamp of the hit with the precision of the DLL, which in the SAMPIC can be set to a minimum of 100 ps. The analog memory is made of 64 analog-switched capacitors, each one controlled by the status of one of the DLL cells, which continuously sample the waveform, acting like a circular buffer. Each cell is hence overwritten every clock cycle until the trigger arrives. With the analog memory is thus possible to collect up to 64 samples of the signal. After the trigger each element of the memory cell is converted into a digital value with an analog ramp ADC and the result of the conversion is stored in the output buffer. The resolution of the ADC can be selected in the range 8-11 bits. During the conversion no other hits are accepted and the resulting dead time of the channel (not of the chip) vary in the range $0.2 - 1.6$ µs, depending on the desired resolution.

The rate limitation of the chip is caused by its triggering capability. The actual chip revision allows for two trigger modalities: external trigger or self-trigger. The external trigger is almost useless for our project, since the maximum latency that can be handled is 2 ns (we deal with latencies of the order of microseconds). In self-trigger mode, the one that we use, each channel is self-triggered by an internal discriminator on the input and digitized independently from the others. In this modality the channel readout order is random, without time sorting, and the event building must be done elsewhere, which for the TOTEM experiment means in the

FPGA of the readout board (see chap. 7). As a consequence all the hits have to be readout from the chip, and only later a selection based on the central trigger can be performed. The readout of one event requires more than 400 ns (25 ns+6.2 ns/sample), provided that the full chip LVDS I/O speed (160 MHz) can be sustained. In principle it is possible to reduce the number of samples to be acquired, defining a region of interest, but this feature is not usable by TOTEM since it will lead to the loss of important information on the signal shape. This time estimation is even optimistic for our application (but also in general), since the communication between the FPGA on the SAMPIC mezzanine and the motherboard, which represents the first layer where all the information for the hit selection are available, is performed with the CMOS standard, that hardly can sustain a communication speed above $100 - 120$ MHz. However, even in the best case, we have to face a limit of ~ 2 MHz on the maximum hit rate that can be readout from the chip. The hit rate on the diamond sensors foreseen in the high luminosity run will be ~ 2 MHz/channel, which means a global hit rate on the chip of ~ 16 MHz. This make the chip not usable to digitize the diamond detector signals in the CT-PPS project. On the other hand, it can be used for the vertical upgrade, where the mean hit rate is ~ 10 KHz/channel.

6.1.1 SAMPIC performance

In principle the SAMPIC characteristics grant that all the algorithms introduced in this work can be applied also to the LHC data, so that no degradation in the measurements will be introduced during the signal digitization. The 64 samples acquired with the chip grant, at 6.4 GSa/s, an acquisition window of 10 ns. Since our signal have a rise time below 2 ns, the window is sufficiently large to sample not only the rise time and the peak of the signal, but also the noise pedestal, which is useful for the timing algorithms. Only the signal tail will be eventually cutted (when the amplitude is high), but its knowledge gives a negligible contribution to the system timing.

The chip has been extensively tested, using the module provided by the LAL (fig. 6.1). The module is indeed quite easy to use and it requires only a 5 V voltage supply to operate. Communication and readout are performed through USB or Ethernet connection, so that both local or remote (i.e. from the control room) operations are possible. The module can be controlled by a *Graphical User Interface* (GUI) distributed with the module. The interface, where calibration and advanced timing analysis are available, provides also an online monitor, somehow

similar to an oscilloscope. In figure 6.3 a screen capture performed during the data acquisition hereafter described is showed. Data from multiple channels and events

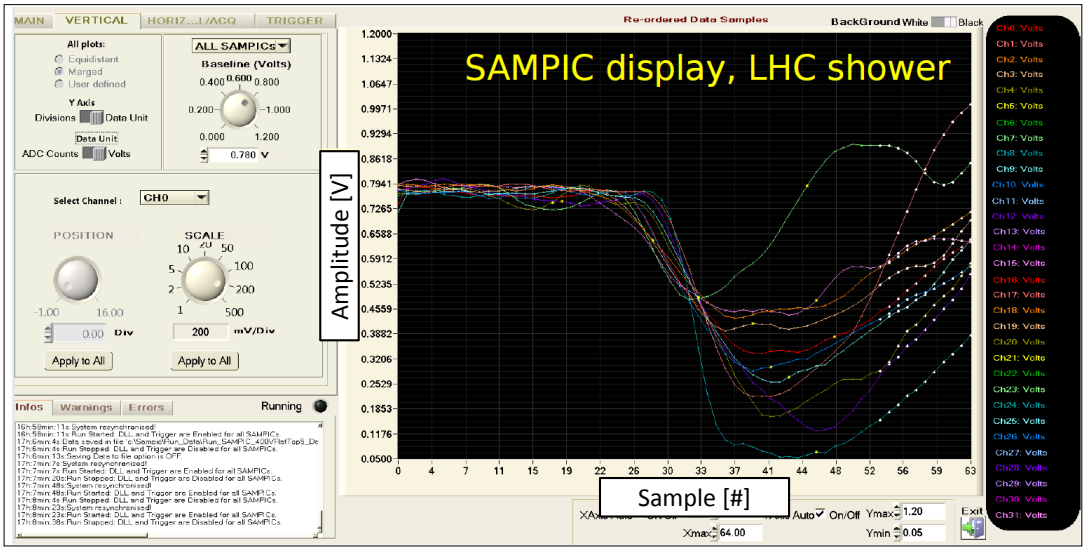

Figure 6.3: Screenshot of the SAMPIC GUI during data taking. On the left one of the configuration tabs. On the right signals from multiple diamond pads collected in the LHC tunnel are superimposed. Each sample is spaced of $\sim$ 160 ps.

are superimposed (persistence option). All the important parts of the signal are collected, but, as told before, we can not use any ROI to reduce the data payload.

The SAMPIC has been tested multiple times during the detector development. The results obtained always confirmed that no differences in the time resolution with the oscilloscope or with the SAMPIC are present, as expected. The SAMPIC performed as foreseen in all our tests, justifying our choice to use it for our detector readout.

In particular a key test has been performed during the end of 2015. Two detector planes were installed in the LHC tunnel (only one detector arm) and data were collected with the SAMPIC module. The hybrids, installed in the RP, were kept at a temperature of $\sim$ 30° and at a pressure of $\sim$ 200 mbar. The pressure was above the 45 mbar that will be present in the nominal operational condition, but still sufficient to operate the RP in garage position. Lower pressure can not be used since the hybrids under test were the first version of the final board, where the HV isolation was still not optimal. The detector was operated at a lower voltage of 500 V, to avoid discharge that can cause the channels damaging. For this test a PC was placed in the tunnel, remotely controlled through remote desktop. The

acquisition rate, being in garage position, was low (< 10 Hz), but still we were able to collect sufficient statistics to perform timing analysis. The results were extremely positive, with the full system (detector+digitizer) detecting LHC particle showers and showing the expected time resolution. The distribution ΔT_{12} of the time difference between the two installed planes is reported in figure 6.4 for pixel #3 of figure 2.22, which was found the best aligned within the two boards and hence the one with larger statistics. The resolution $\sigma_t = \sigma_{12}/\sqrt{2} = 91$ ps is perfectly

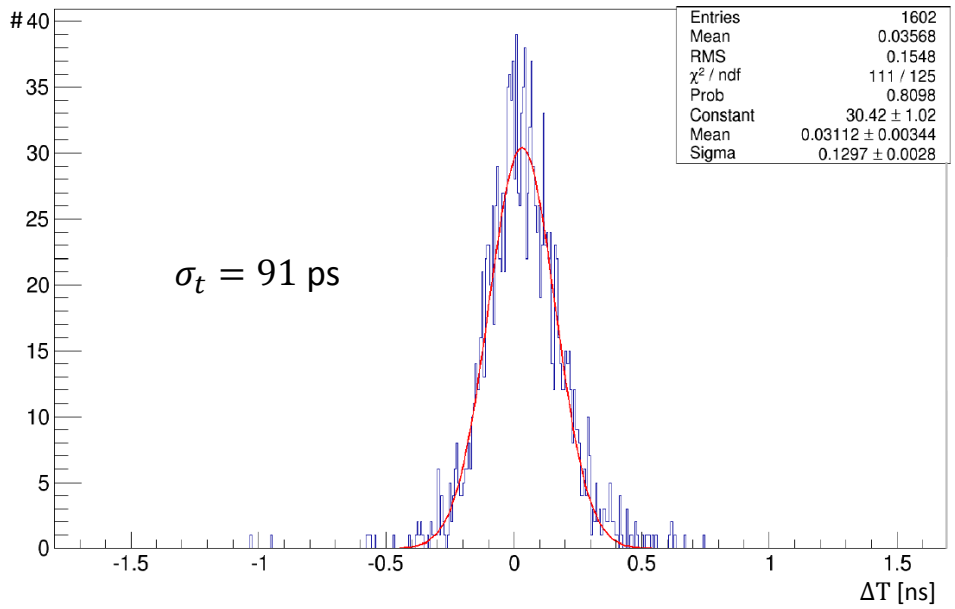

Figure 6.4: ΔT_{12} distribution for pixel #3 with LHC showers. This data are collected using the SAMPIC readout module.

in line with all our previous measurements. This was a key test because it shows that the tunnel environment does not introduce any degradation (induced by the environmental noise) in our system. This can be considered the final check on our work. Production of the SAMPIC mezzanine is actually ongoing, in parallel with the work described in the next chapter. The installation and the first LHC real data are expected in few months for the commissioning of the vertical TOF system.

6.2 Discriminator and Time to Digital Converter

The second readout that I analyzed in my work is the more "classic" discriminator coupled to an high precision TDC. The discriminator is needed because TDCs usually accept only digital signals, and therefore the digitization must be done by

another unit, the discriminator. In this case large part of the signal information is lost, and is not possible to perform the timing algorithms used with the oscilloscope or with the SAMPIC, resulting in a negative impact on the performances.

The TDC employed by the CT-PPS collaboration, and widely used at CERN, is the HPTDC[90]. The HPTDC can be set to different resolutions, with a maximum of 32 channels available which can simultaneously detect both leading and trailing edges of the input signals. When the maximum resolution is required, as in our case, the number of channels is reduced to 8. In this modality the bin of the TDC is 25 ps, which leads to a nominal resolution $\sim$ 7 ps. This value is well below our characteristic timing performance and we can therefore consider that the TDC does not add any additional resolution detriment to the system. In this section I will thus analyze the effect on our detector introduced by the discriminator. The output will be registered with the oscilloscope, but the result will not change if the HPTDC is used instead.

For the discrimination we selected the NINO chip[89], an 8 channel ultra-fast low-power differential amplifier and fixed threshold discriminator, designed for the TOF system of the ALICE (CERN) experiment[132]. A schematic block of one channel of the chip is provided in figure 6.5. The input stage, which also act as

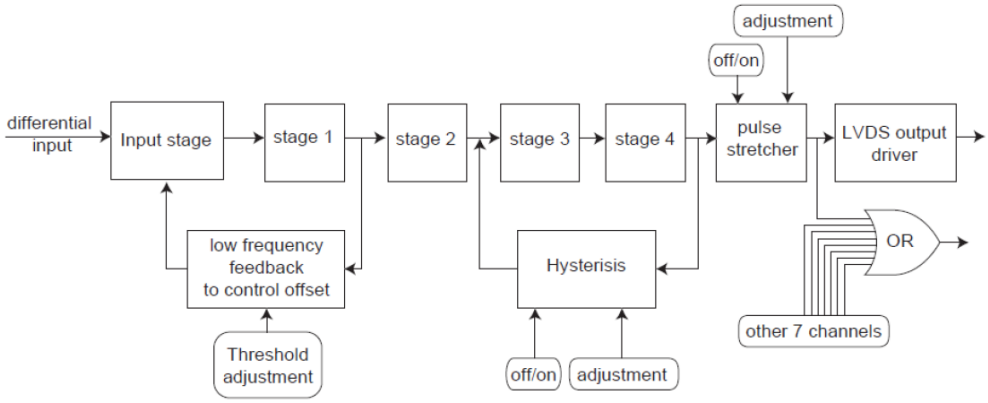

Figure 6.5: Block scheme of the NINO chip[89].

discrimination stage, is a common gate differential circuit, sensible to the charge injected from the detector, with an input range $0.01 - 2$ pC. The discrimination threshold can be adjusted in the range $10 - 100$ fC through the differential voltage applied to dedicated pins of the chip. The signal is then amplified by four identical amplification stages. It is possible to add an hysteresis to the discriminator so that a better noise rejection is provided. The differential output can be regulated through

external resistors so that it can be made compliant with the LVDS digital standard. The quoted resolution of the device is ~ 25 ps. This resolution is however measured with a generator or with detectors characterized by a large SNR: for the diamond sensor it will be later investigated.

In addition to its intrinsic time resolution the chip can encode the input charge from the detector in the output width W, as schematized in figure 6.6. This charac-

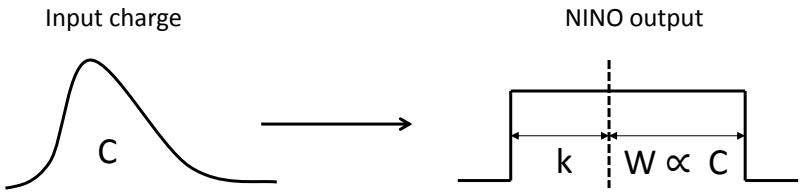

Figure 6.6: Concept of the input charge encoded in the NINO output width. The width is found to scale not linearly with the input charge.

teristics make of it an optimal candidate for TOF systems. This information, called *Time Over Threshold* (TOT), is indeed extremely useful since it allows for a precise correction of the signal time walk caused by the fixed threshold discrimination. The TOT is computed has the time that the integrated charge stay above the selected threshold. By default W varies in the range $2 - 8$ ns. This widths are too short for many TDC (included the HPTDC), that are unable to measure both edges of a signal if not enough spaced. A work-around as been introduced by adding a stretcher circuit, which sums a constant time k to the width of the signal, making the chip compatible with the rest of the readout chain. As for the hysteresis the stretcher circuit can be enabled and adjusted through the bias voltage provided to dedicated input pins.

One important feature of the chip is the generation of a global trigger signal, formed by the logic "OR" of all the outputs. Even if no trigger from the diamond detector is actually foreseen, a future upgrade can make use of this signal. In our implementation we hence took care to preserve this possibility.

6.2.1 Development of TOTEM NINO board

The use of the NINO with our detector suffers of a major issue, due the differential input of the chip, since the diamond sensors have a single-ended output. Moreover the signal is a voltage signal and not a charge signal. Fortunately the chip input

stage can work also with single-ended inputs. I hence decided to test the chip in this modality and I try to connect the sensor to the NINO with the scheme reported in figure 6.7. The input signal is first (optionally) attenuated and then terminated

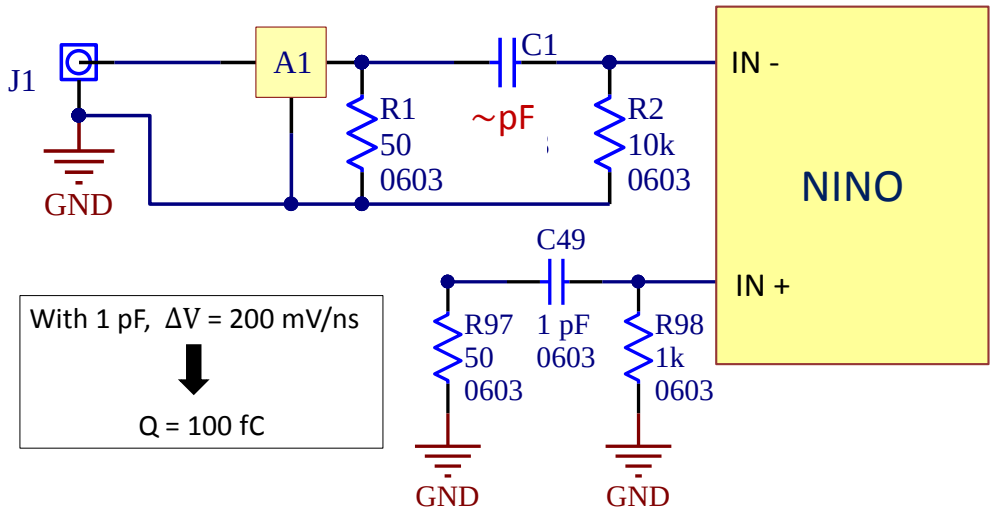

Figure 6.7: Connection of a single-ended signal to a NINO input channel. This scheme has been used for the final TOTEM NINO board. The block $A1$ is the input attenuator.

with a 50 Ω resistor (the signals are extracted from the RP with coaxial cables). The signal is than decoupled from the negative input stage of the NINO with a capacitor . The value of the capacitor C is critical since it will convert the voltage into a charge that will flow in the negative input of the NINO channel. Its value must be properly tuned, since it defines the input effectively seen by the chip. The measured charge Q can indeed be estimated as

$$Q = C \cdot \frac{\Delta V}{\Delta t} \cdot \tau, \tag{6.1}$$

where τ is the characteristic input time of the circuit, which is $\sim$ 550 ps. The system is thus sensible to the edge of the signal. The other channel input is grounded by a similar circuit. This scheme is used for negative polarity signals, but it can be reverted for positive inputs. Is to be noted that the capacitance on the grounded pin must have a value of few picofarad at most, otherwise eventual noise in the ground will generate large charge injection in the chip. The attenuator is used to reduce the input signal amplitude, and it is often necessary since otherwise the needed value of the capacitor can be below 1 pF. In this case the parasitic capacitance of the input

circuit may dominate and the resulting "amplification" of the input will undergoes large variations from channel to channel. On the other side a large attenuation factor can make the input signals so small that the noise pickup in the passive components may degrade the signal SNR. However it must be noted that within this limits, the tuning of the input will depend on the ratio between the attenuation and the capacitor values, and not on their absolute values.

I started to test the NINO chip as a possible solution for the diamond readout at PS, while we were still testing the sensors from CIVIDEC (sec. 4.3). To test the circuit I used the board developed by ALICE[132], after having modified one of the inputs as discussed. The input signal was provided by one of the CIVIDEC diamond, connected to the CSA amplifier. The value of the capacitor was set to 10 pF. The signal from the diamond was first sent to the oscilloscope (1 MΩ terminated) and then to the NINO. The NINO output was connected to another input of the oscilloscope. The test was successful, demonstrating not only that the NINO chip works in this configuration but also that the TOT correction was available for the diamond signals. The study of the NINO was however put aside for the much more promising SAMPIC readout and to focus on the detector development.

The NINO R&D was again conducted, given the impossibility to use the SAMPIC, and we found that the NINO/HPTDC are the best candidates for the integration of our detectors in CT-PPS. Based on the circuit which I validated with the PS measurements and on the scheme of the ALICE card we developed a TOTEM board, hosting four discriminator chips (fig. 6.8). The board, as described in section 2.6 host 4 NINO chips, making available 32 channels. On each board an I^2C interface is present so that the chip thresholds can be remotely controlled, through four on board 8-bit DACs. For test purpose the thresholds can be also adjusted by means of potentiometers. Two boards can be connected together, so that only one I^2C and voltage cable can be used for both.

The chip input scheme is exactly the one of figure 6.7. During the measurements here described I used 18 dB attenuation and a capacitor value of 4.7 pF. The final value chosen for the board production has almost the same attenuator/capacitor ratio, with 6 dB attenuation and $C = 1$ pF. The thresholds are always set almost at maximum (100 fC), since lower levels result in large noise. The 4 trigger signals coming from the NINO chips are already connected to the readout board, and enters in the main FPGA. In this way a future use of the trigger will be possible without any hardware redesign.

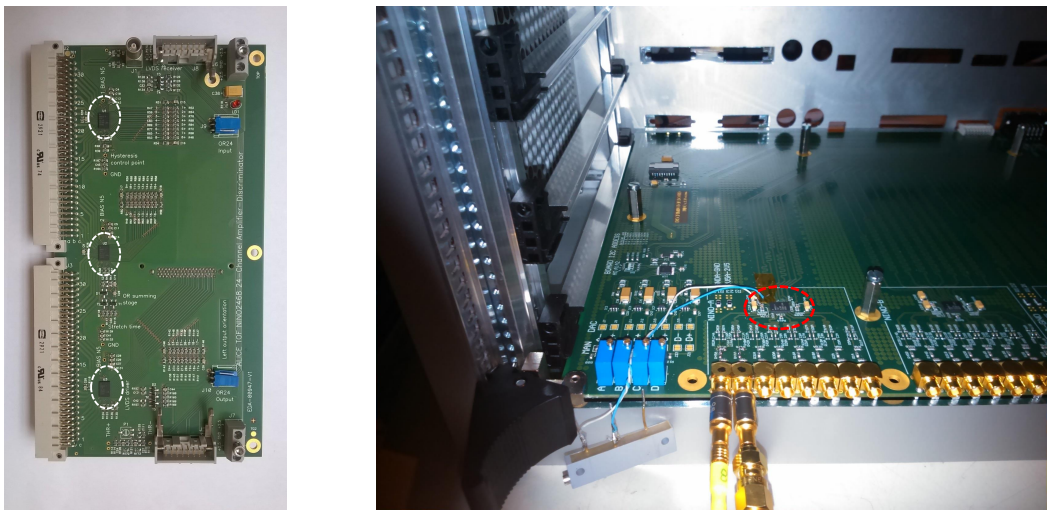

Figure 6.8: Picture of the ALICE (left) and TOTEM (right) boards with the NINO chips (highlighted). On the left side of the TOTEM board the threshold control circuit is visible, while on the right a NINO chip with the eight inputs. Other three NINOs, with the same identical placement and routing, are present on the board. The board is over-sized to fit the existing cabinet (in the picture) that will also hosts the readout boards.

6.2.2 Tests with waveform generator

To check the behaviour of the board, we first performed some measurements with a waveform generator. The connection scheme was exactly the same used at PS with the ALICE board, with the oscilloscope reading the generator signal and the NINO output (with a differential high-bandwidth probe). The signal from the generator has a rise time $\sim$ 4 ns, stable w.r.t. the signal amplitude V_{ampl}. We performed a scan varying the input amplitude (and hence its charge) and measuring:

- the relation between the input charge and the output width W.
- the time resolution of the output leading edge w.r.t the input signal.
- the resolution on the W measure.

The measurements were performed directly with the oscilloscope (always the same AGILENT) built-in functions. The rising and falling edge times of the output, as well the time of the input signal leading edge were automatically computed by measuring the time at which the signal cross the 50% of its maximum amplitude. No interpolation is provided. The resolution is computed as the standard deviation

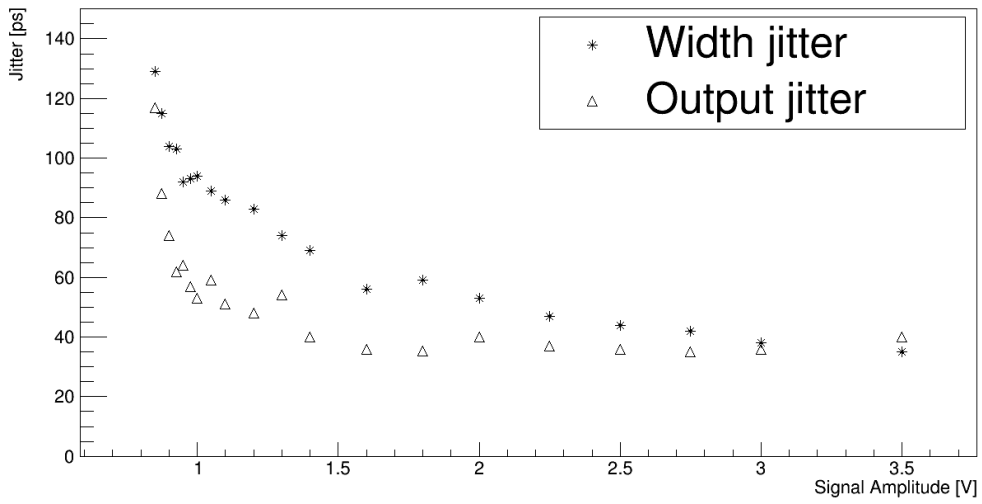

Figure 6.9: Output leading edge and width resolution w.r.t. input signal V_{ampl}.

of the measured distributions. The results are provided in figure 6.9. Before looking at the chart its interesting that the NINO starts to trigger on signals with amplitude $V_{ampl} \sim 0.85$ V. This is in accordance with equation 6.1, which raw estimation gives a resulting charge (keep in mind the factor eight of attenuation) of ~ 70 fC, close to the threshold value. The resolution, for both measurements, get better as the input signal increase. The timing resolution settles around twice the minimum V_{ampl}, which correspond to ~ 200 fC. For bigger signal the value stay in the range $30 - 40$ ps. This is in agreement with the resolution (<25 ps) quoted for the chip[89]. Indeed a smearing factor on the measurements is introduced by the oscilloscope used at 10 Gs/s (1 point every 100 ps), resulting in a intrinsic resolution $100/\sqrt{12} \sim 28$ ps.

From this results it seems reasonable that the input circuit should be tuned to have input charges well above 200 fC. However before taking any decision, we must look to the relation between the input charge and W, which will be used for the TOT correction. This measurements were performed also on the ALICE board, equipped with 2.2 pF capacitor and without attenuator. Both curves are reported in figure 6.10. As expected the ALICE board get active with an input amplitude a factor 4 lower than the TOTEM one. The plot indicates an identical behaviour, highly non linear, with a step dependence at lower charge. Comparing all this measurements we decided that the input must be tuned so that the diamond signal will generate a charge in the in the region around 200 fC, where the time resolution of the leading edge settle to minimum and the output width still shows a good dependence from the input charge. Indeed having a good time resolution in the leading edge has the

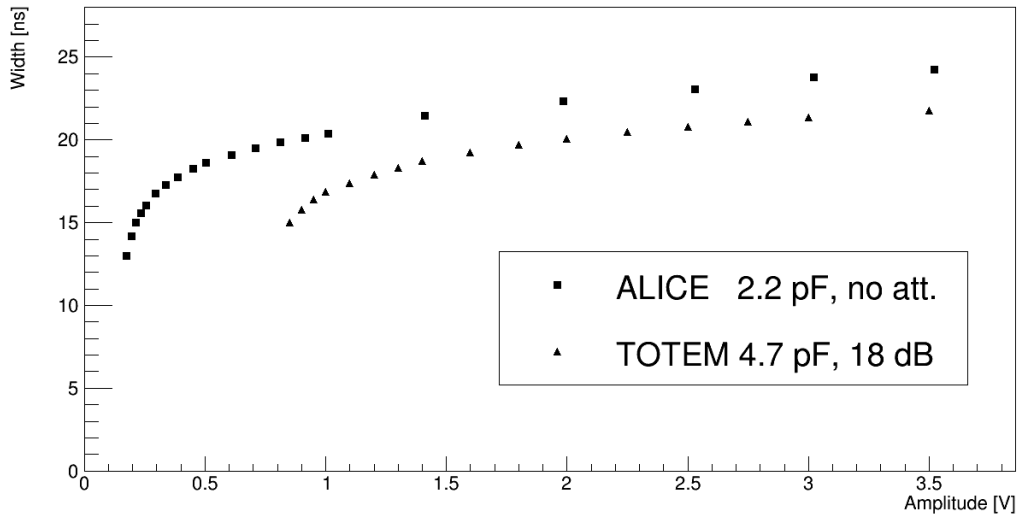

Figure 6.10: NINO W as a function of signal V_{ampl}. The measure has been reported for both ALICE and TOTEM boards.

priority, being the other parameters used only to apply the correction.

Before going on with MIP tests I decided to perform a better test on the time resolution of the chip pulsing again with the generator, which does not require the TOT correction, setting $V_{ampl} = 2$ V. The timing resolution between the generator input and the NINO output was obtained with the same algorithm of the previous chapters (FNT), treating the NINO as a diamond sensor. The resolution in this case is directly the standard deviation σ_{12} of the time difference distribution ΔT_{12}. The resolution was found $\sigma_t = \sigma_{12} = 28$ ps (fig. 6.11), recovering part of the smearing introduced by the oscilloscope sampling frequency. The board developed by TOTEM is thus working as expected and we hence moved to test it with our detector on test beam.

6.2.3 NINO performances with the TOTEM diamond detector

We used two diamond hybrid boards (the one with full amplification chain integrated, see section 5.2) equipped with the full pad diamond sensors. The tests were performed again at the SPS, which beam setup and characteristics have already been discussed in the previous chapter. The two hybrids (named D1 and D2) were put on the beam line and their signals were sent to the oscilloscope (1 MΩ terminated) and to the input channels of the NINO board. The outputs of the chip, named N1

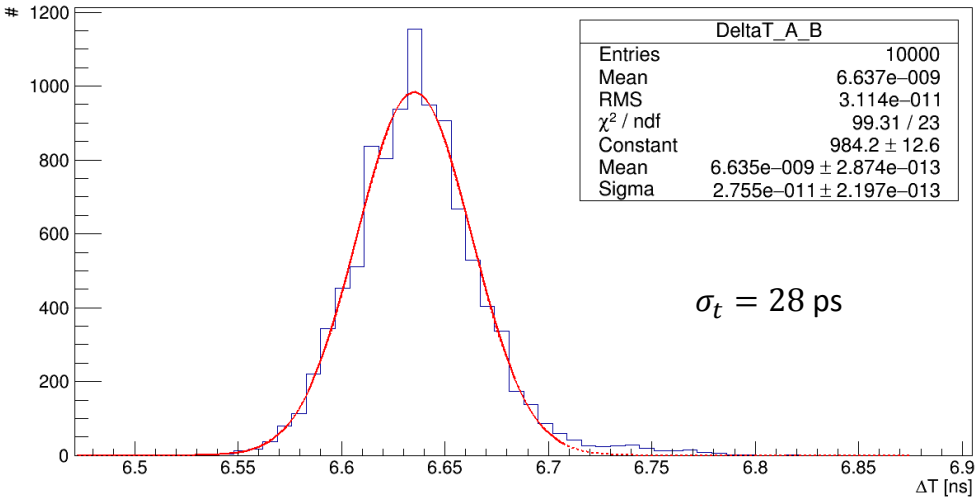

Figure 6.11: Distribution of the time difference between the generator and the NINO output. The channel resolution is given by the standard deviation.

and N2 (generated by D1 and D2 respectively), were readout by two differential probes (fig. 6.12). The segmented mode acquisition was triggered by D1, with a

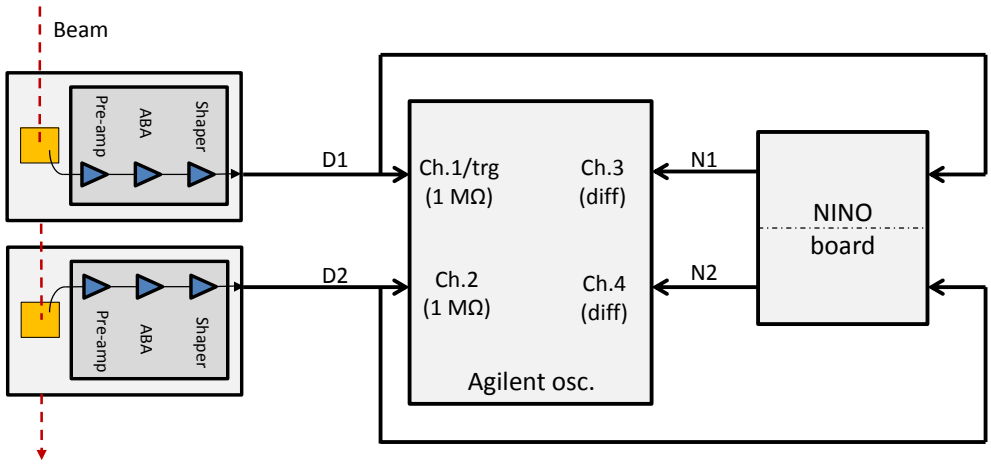

Figure 6.12: Scheme used to test the TOTEM NINO board. Notice that the connection of the hybrid signal with the oscilloscope is done as short as possible (using a "T" on the oscilloscope input) to avoid signal reflection.

threshold of 0.2 V. Such threshold was the same used in the previous analysis on the performance of the hybrid and grants that almost no MIP signals are missed. Since the MPV value of the hybrid signal amplitude, which were mounting new diamonds, was located around 0.5 V and the rise time of the signal was $\sim$ 1.7 ns, we decided

to reduce the attenuation to 12 dB so that the charge generated by the signal was $\sim$ 190 pC. This was indeed the condition that we were looking for.

To extract timing information from the data I used the usual strategy followed in this work. All the time differences are extrapolated with FNT algorithm (30% threshold). The width of the NINO is computed by fitting both edges of the signal and making the time difference between the two point where the signal cross the 30% of its V_{ampl}.

In figure 6.13 the bi-dimensional histogram of V_{ampl} vs W is reported. For low

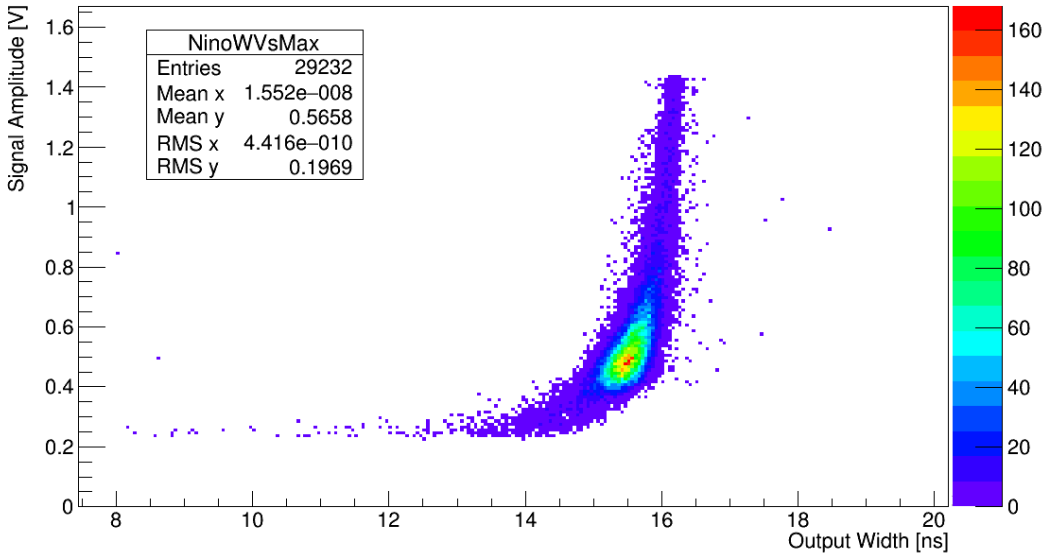

Figure 6.13: Scatter plot of input signal amplitude and NINO output width. At low V_{ampl} the width can take almost any value $<$ 15 ns.

V_{ampl} the width range of the output became larger, being totaly unreliable for signals close to the threshold of the chip. This plot has been done using the data from D2 and N2, so that no amplitude cuts are introduced from the triggering condition. However the plot for the other sensor is exactly the same. Also a measure of the efficiency has been extrapolated from the data by making the ratio between the number of signals above 0.1 V in D2 and the number of registered outputs from N2. The efficiency with this test configuration was $\sim$ 98%.

To understand the real performance of the system we have now to forget the input signal and use only the information that will be available during the real data analysis. First I measured the raw distribution of the time difference ΔT_{12} between the two signals coming from the NINO (fig. 6.14). The effect of the fixed threshold discrimination gives a very poor resolution. Being the two sensors and readout

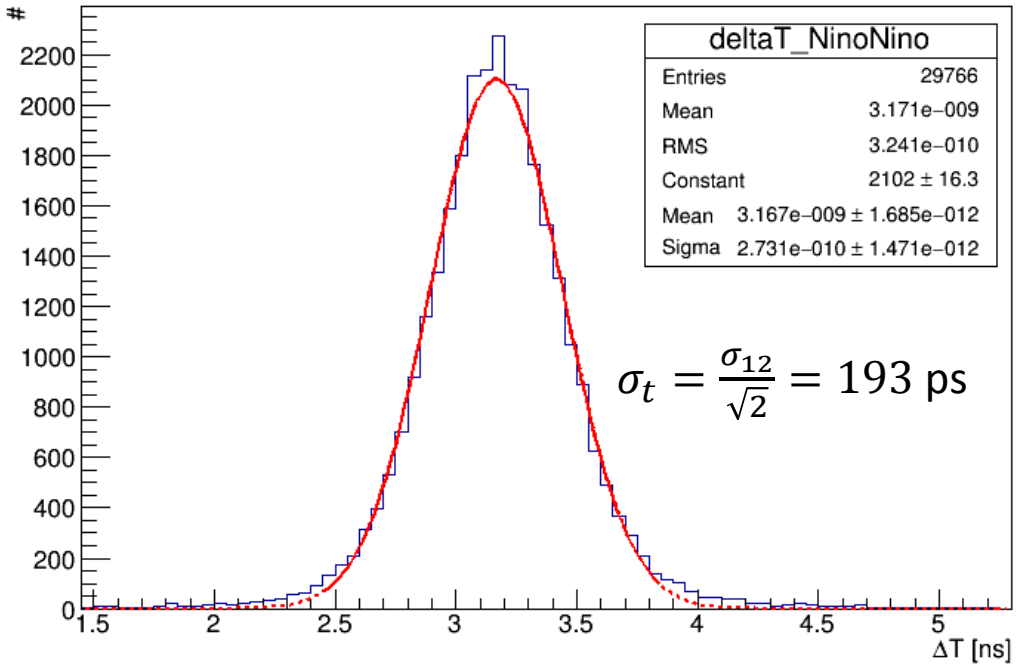

Figure 6.14: Raw ΔT_{12} distribution between the two NINO output.

channels identical, it is possible to estimate $\sigma_t = \sigma_{12}/\sqrt{2} = 193$ ps, ~ 85 ps worse than the intrinsic detector resolution.

To implement the TOT correction I studied the correlation between the raw time difference ΔT_{12} and the difference $\Delta W = W_1 - W_2$, where $W_{1,2}$ are the measured widths of $N_{1,2}$. The scatter plot is reported in figure 6.15. The correlation between the two variable is present as expected and the correction can be applied. Outside the central region some isolated points are present, characterized by a large absolute value of ΔW. Such measures are generated from events where one of the signal is at the threshold: for them the correction can not be applied due to the chip bad behaviour. Such events, representing the 1% of the sample has been excluded from the correction. The parameters useful for the TOT correction can be extrapolated by performing a linear fit on the profile histogram generated from the scatter plot (figure 6.16). The fit is restricted to the central area, where almost all the events are grouped. The correction can be applied to the ΔT_{12} distribution by redefining the time difference as

$$\Delta T_{corr} = \Delta T_{12} - p_1 * \Delta W + p_0, \tag{6.2}$$

where p_0, p_1 are the coefficients of the linear fit. The resulting corrected distribution, from which a much better time resolution $\sigma_t = 127$ ps is obtained, is reported in

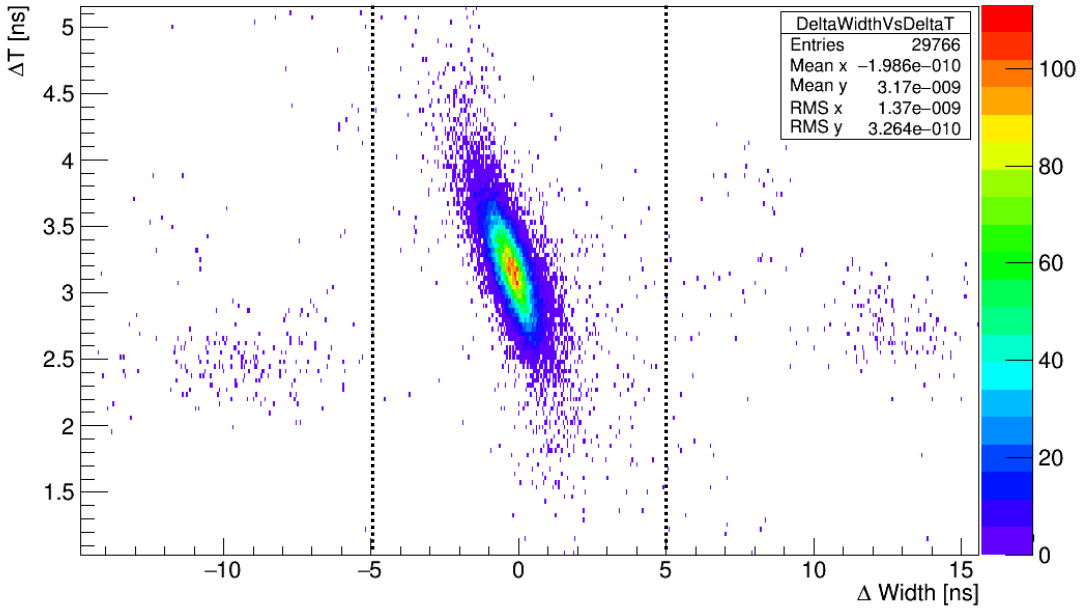

Figure 6.15: Scatter plot of ΔW Vs raw ΔT_{12}. The cut region ($|\Delta W| < 5$) is highlighted.

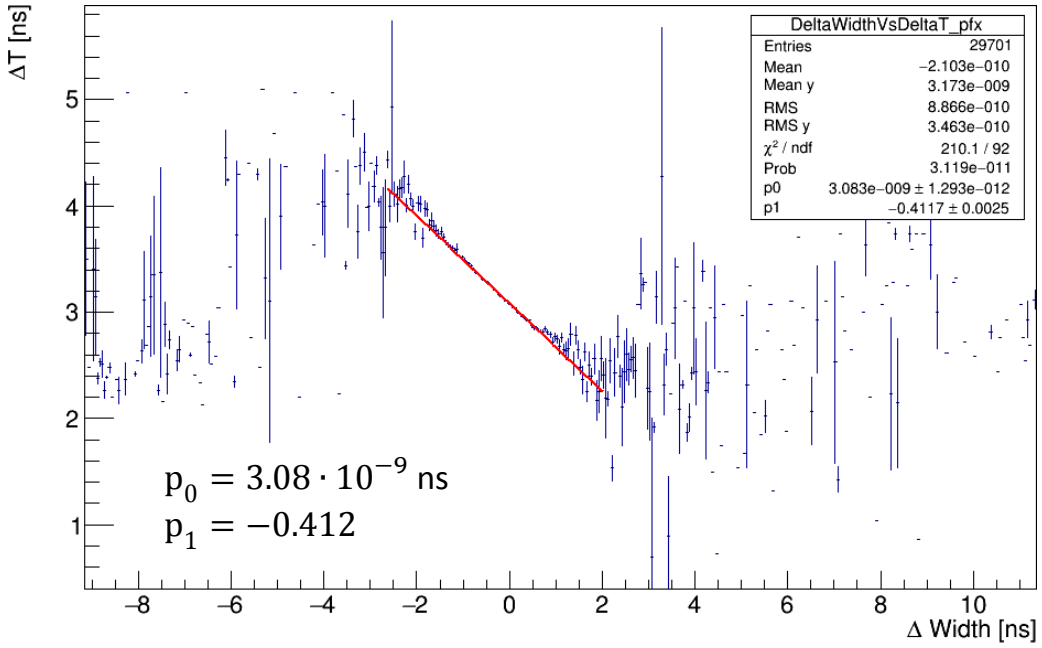

Figure 6.16: Profile distribution for the $\Delta W - \Delta T_{12}$ scatter plot.

figure 6.17. With this result we can conclude that the introduction of the NINO in the readout chain bring an absolute performance degradation of $\sim$ 20 ps (w.r.t

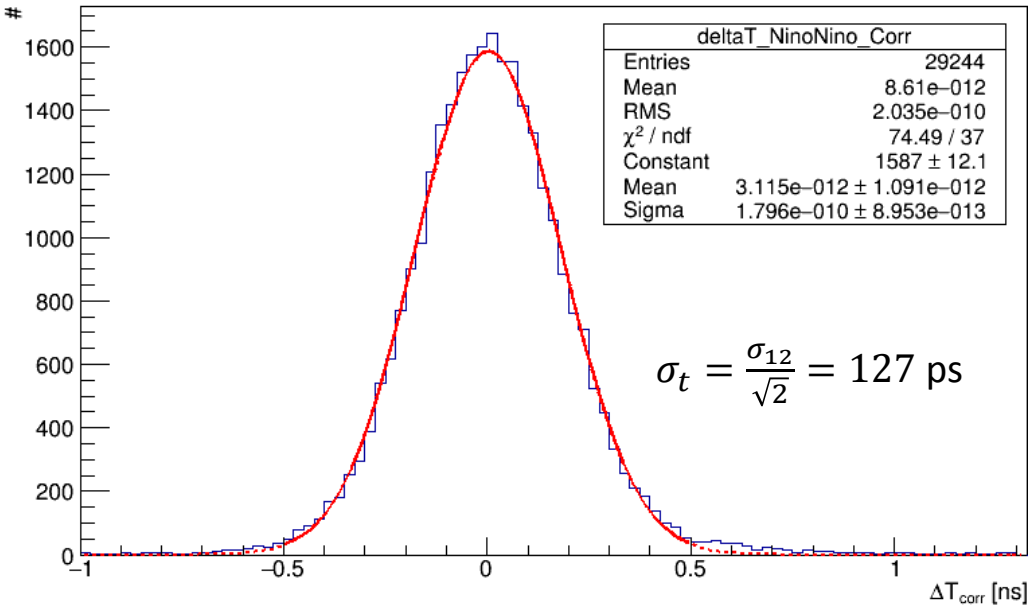

Figure 6.17: Corrected ΔT_{12} distribution between the two NINO outputs.

the time resolution of the two hybrids, which had been measured of $\sim$ 108 ps in the previous chapter). The performance loose is not negligible and not tolerable for the TOTEM vertical upgrade. Still can be used for the first stage of the CT-PPS project.

The effect of the NINO seems much larger than the one measured with the waveform generator. If indeed the time resolution of the output w.r.t. the input would have been of the same order of the one measured with the generator ($\sim$ 30 ps) we will not have noticed any timing detriment. This has been cross checked by comparing the timing of D2 with the corresponding NINO output (N2). The same analysis as the one just described has been performed, replacing the variable ΔW with W_2. The correlation plot and the profile are reported in figure 6.18, while the time distribution ΔT_{12}, before and after the TOT correction, is reported in figure 6.19.

The effect of the correction is here visible also in the shape of the two distributions. Fitting the corrected distribution with a gaussian function does not give a good result. This is a consequence of the fact that the resolution of the chip is not constant but varies as a function of the input charge. I performed a double gaussian fit, which give two contribution with standard deviation of 142 and 90 ps respectively. The timing uncertainties is in the order of 100 ps, as inferred from the

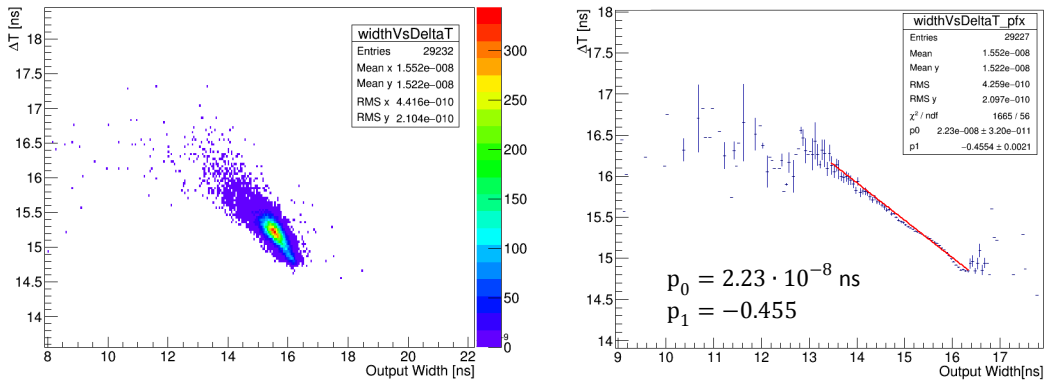

Figure 6.18: Scatter plot (left) and profile distribution (right) of W_2 vs raw ΔT_{12}. No cuts have been applied.

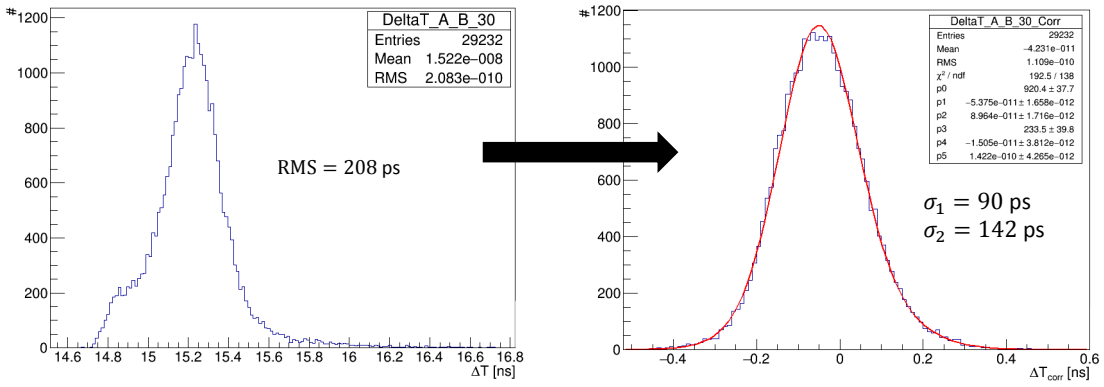

Figure 6.19: Raw (left) and corrected (right) ΔT_{12} distribution between the N_2 and D_2 signals. No meaningful fit can be done on the raw distribution. The double gaussian fit well approximates the corrected distribution.

previous measurements, much greater than the 28 ps measured with the generator. This is due to the lower SNR of our detector, which inject a larger noise charge in the NINO input. Tuning the input to work with a larger charge does not help since the the noise comes from the detector and the SNR will remain the same. Moreover this is not possible since the chip starts to trigger on the noise.

The result here described is the best obtained with our diamond detectors so far with this setup. At the moment the optimization of the board for the CT-PPS installation is ongoing, with the complete system foreseen operational before summer

2016. The resolution of the system with the discriminator can be estimated in the range $100 - 130$ ps, depending on the pixel size.

Chapter 7

Detector readout and control

In this chapter I will provide a description of the detector readout and control system. In section 7.1 I will describe the motherboard used to interface the detector with the DAQ and control infrastructures. The motherboard is designed to work both in the LHC tunnel, where the TOTEM DAQ and control systems are available, and in test beam, with a stand alone configuration based on a USB interface. The system rely on a high-end FPGA, which firmware I am currently designing. The main firmware functionalities and features will be reported in section 7.2.

7.1 The readout board

Independently from the digitization adopted the data will be finally collected in the readout motherboard (RMB) which, as introduced in section 2.5, can host either a mezzanine with 4 HPTDCs or two SAMPIC mezzanines. A scheme of the system can be seen in figure 7.1, configured for the SAMPIC readout. The same RMB is used to access the slow control of the system.

The heart of the RMB is the SmartFusion2[133] (SF2) SoC FPGA from Microsemi, an high-end FPGA designed for security/military applications where SEU (*Single Event Upset*) events must be tolerated. A SEU is a change of state caused by the passage of one single ionizing particle in a sensitive area of the FPGA. The state change is a result of the free charge created by the ionization. Even if the readout electronics will be located few meters away from the beam pipe, the radiation will still be quite high, and the chance to have a SEU is not negligible. A SEU can not only result in an event data corruption, but can also require to reprogram the device, an operation that is always better to avoid during data taking.

SAMPIC control, local event building and timing synchronization will be per-

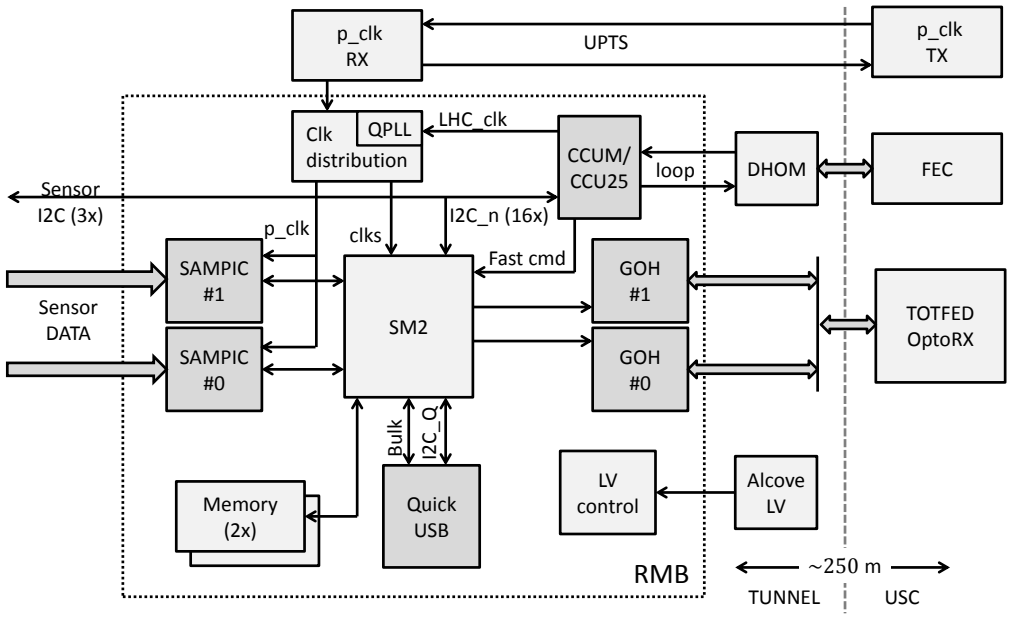

Figure 7.1: Scheme of the diamond sensors readout and control. On the RMB the mezzanines are represented with a square filled with dark grey. All signals to/from USC are provided through optical connections.

formed inside the device, as described in section 7.2. The SF2 is coupled to two SRAM modules (Cypress CY7C1041B) with 256K x 16 bit memory available on each. The memory will be used if the internal FPGA resources will not be sufficient to retain all the data while waiting for the trigger decision. Since the memories are not SEU tolerant a CRC control must be eventually implemented in order to detect data corruption.

Other than the SF2 on the RMB is possible to find multiple mezzanines, with different goals:

- the QuickUSB module for test beam stand-alone readout/control operations.
- the GOH mezzanines for data optical transmission.
- the CCUM mezzanine for slow control and fast command delivery.

The QuickUSB[134] (QUSB) is a versatile module which hosts a Cypress EZ-USB FX2LP microcontroller. The module communicates with a PC through high-speed USB 2.0 and is able to perform data transfer at the maximum rate available (54 MB/s). The on-board microcontroller is capable to perform communication with a target device on the motherboard through a large series of standard protocols among

which the I^2C, used for the TOTEM slow control. For fast data readout it exhibits a fast parallel 16-bit protocol (with 8-bit addressing), disciplined with an 50 MHz clock (that can be distributed to the target). The parallel interface can be used with different levels of handshake and it is an optimal candidate to interface with FIFOs inside FPGA. This characteristics make of the QUSB an optimal choice to test and develop the board and the firmware. Moreover using the module is possible to operate the full board in test beams, without the need to have the full readout and control systems of the experiment in place.

The GOH[83] (*Gigabit Opto-Hybrid*) is used to serialize and send the sensor data to the USC (*Underground Service Cavern*), where the DAQ receivers are placed, through optical link. Actually two GOHs can be mounted on the board, so that each one will transmit the data coming from one SAMPIC chip. The chip has a 16-bit input bus. When the *data_valid* signal is asserted on each clock cycle (40 MHz) the data on the input bus are serialized and sent as a continuous bit stream through an optical fiber at 800 Mb/s. The fiber is pulsed with a 1310 nm laser, which power can be controlled. Data reach the OptoRX module in the USC, where are converted back to electrical. Up to 12 fibers can be readout with an OptoRX and data from multiple fiber/OptoRX are collected in the TOTFED boards (developed by TOTEM), which contain the *Front-End Drivers*[135] (FED) used for event building. Data are then finally delivered to DAQ. The full TOF system requires 6 RMBs (see sec. 2.5), with a total of 12 transmitting GOHs. In principle is thus possible to readout the full system with only one OptoRX and one TOTFED.

System slow control is possible from the *Front End Controller* (FEC) boards in the USC. Slow control instructions and fast commands (trigger and synchronization signals) are transmitted onto a token ring via the FEC modules. The token ring starts with 40 Mb/s optical link transmission from the FEC to the detector location. There optical signals are converted to electrical signals by a module called *Digital Opto Hybrid Module*[136] (DOHM). The *control loop* is formed by multiple *Communication and Control Units* (CCU, hosted in the CCUM). Each CCU can detect and send the LHC clock and the fast commands through LVDS lines to the target. In our case we will have only one CCU in the ring. Fast commands are sent to the main FPGA, while the LHC clock is routed to the clock distribution circuit of the RMB.

The clock distribution is a critical component, since it has to receive the precise clock (*p_clk*) from the UPTS timing system and redistribute to the SF2 and the SAMPIC mezzanines. A selection can also be done between the *p_clk* or the LHC

clock. The distribution make use of the QPLL chip, a PLL (*Phase Locked Loop*) which can generate a local clock also without an input reference. This feature is particularly useful in test beam and during the system debug, since we do not need the control loop or the UPTS system to be active on order to have a local clock.

The slow control is done with the I^2C protocol. I^2C is a serial transmission protocol, with a *Serial DAta* (SDA) and *Serial CLock* (SCL) lines. The protocol can handle multi-master multi-slave communication, with an internal 7-bit addressing scheme. Up to 12 I^2C control lines are generated from each CCU. All the I^2C line are connected to the FPGA, providing a large number of internal registers that can be read/write with direct addressing. Moreover three lines can be extracted from the RMB through a 9-pin D-sub connector and used to control the sensors LV. In the CT-PPS project they are also connected to the NINO board for thresholds adjustment.

7.2 The firmware

Two firmware are being currently developed, one for the HPTDC and the other for the SAMPIC. Here I will focused on the SAMPIC configuration, which I'm developing, and which is the one used for the TOF system. The firmware can be ideally divided in two paths: the control path, used for the slow control of the SAMPIC, and the readout path, which collects the incoming data packets from the mezzanine, performs the event building for the events accepted by the DAQ, and sends the output data frame to the DAQ.

The control path scheme is reported in figure 7.2. Three I^2C lines from the CCUM are employed, two dedicated to read/write the two SAMPIC mezzanine configurations and the third for the internal FPGA registers. A forth I^2C line, not generated from the CCU, but from the QUSB module allows to bypass the CCU lines and access to the I^2C registers through a system of multiplexers. For each line a dedicated I^2C slave module is present. The module handles the bus communication and decodes the internal address and the data to be written or read. Such modules are not completely standard since they have to handle communication speed up to 1 MHz, not foreseen I^2C standard, and which requires some timing adjustments.

At startup the QUSB module will be disabled and accessing to internal registers will be possible only through the control loop. There is no possibility to interfere with the QUSB module. To switch in debug mode is sufficient to write the code

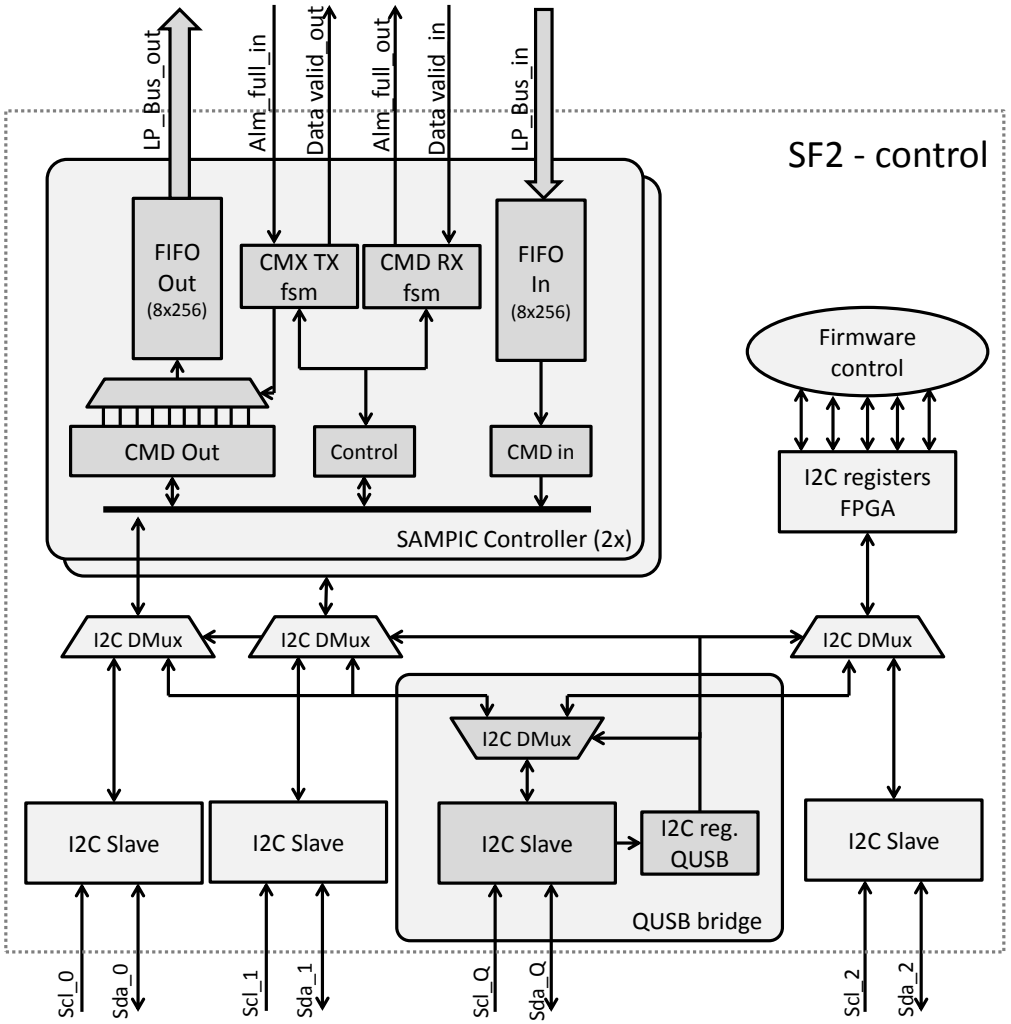

Figure 7.2: Scheme of the firmware control path.

of the line (internal, SAMPIC #0, SAMPIC #1) in the QUSB I^2C register and perform the desired read/write operations. The address of the QUSB register is therefore reserved to avoid conflicts with the other registers. The QUSB can use also other protocols, even much faster and less complicated, to perform access to internal 8/16-bit registers. However with this scheme is possible to enhance the system debugging. Indeed, except for the I^2C slave modules (which are however identical), all the upstream system can be tested and debugged without the control loop.

Each line dedicated to the SAMPIC grants the access to the registers placed in the *SAMPIC controller units*. Commands can be sent to the SAMPIC in packet of 8-bit words. To send a command to the SAMPIC is first necessary to build the com-

mand packet. This can be done by loading all the bytes in the *CMD out* registers. The loaded values can also be readback, to ensure that the bits have been correctly delivered. With the *control registers* is then possible to load the byte sequence in the TX FIFO and start the data sending. The data transfer is performed through a dedicated unidirectional 8-bit bus (LP_Bus), with an handshake provided with an *almost_full* (AF) and a *data_valid* (DV) signals. The DV is used to signal to the receiver that the data on the bus are valid, while the AF is used from the receiver to stop the data transmission because its internal RX FIFO is full. In this sense the AF acts as a negate read acknowledge. The response, if the command sent foreseen a response, will arrive with the same procedure in the RX FIFO. The RX FIFO is connected to a single register: every read access to the register activate the transfer of the next word in the RX FIFO to that register. All the controller status information (like fifo occupancy, fsm status) will be available on the control registers.

The firmware for the data readout path (fig. 7.3) is composed of three main blocks:

- synchronization unit (SU).
- data selection & sorting (DSS).
- event builder (EB).

The synchronization unit is the module which provides the synchronization of the SAMPIC data with the experiment DAQ. Fast commands arrive from the CCU encoded in a 3-bit LVDS transmission. The bits are decoded in the *decoder* unit and 5 signals are extracted:

- *Event Accepted* (EA), which means that the event has been accepted from the DAQ and a data frame is expected in the FED.
- *Event Counter reset* (EC0), which reset the number of EA elapsed.
- *Bunch Cross zero* (BC0), which signal that the bunch #0 are colliding (and that the beams have completed one LHC orbit).
- *Orbit Counter reset* (OC0), which reset the number of BC0 elapsed.
- *Resynch* (RES), used for synchronize all the sub-systems (no special actions are foreseen for us).

We already discussed the importance of such signals, part of the data frame output, to provide the offline data synchronization between TOTEM and CMS DAQs in

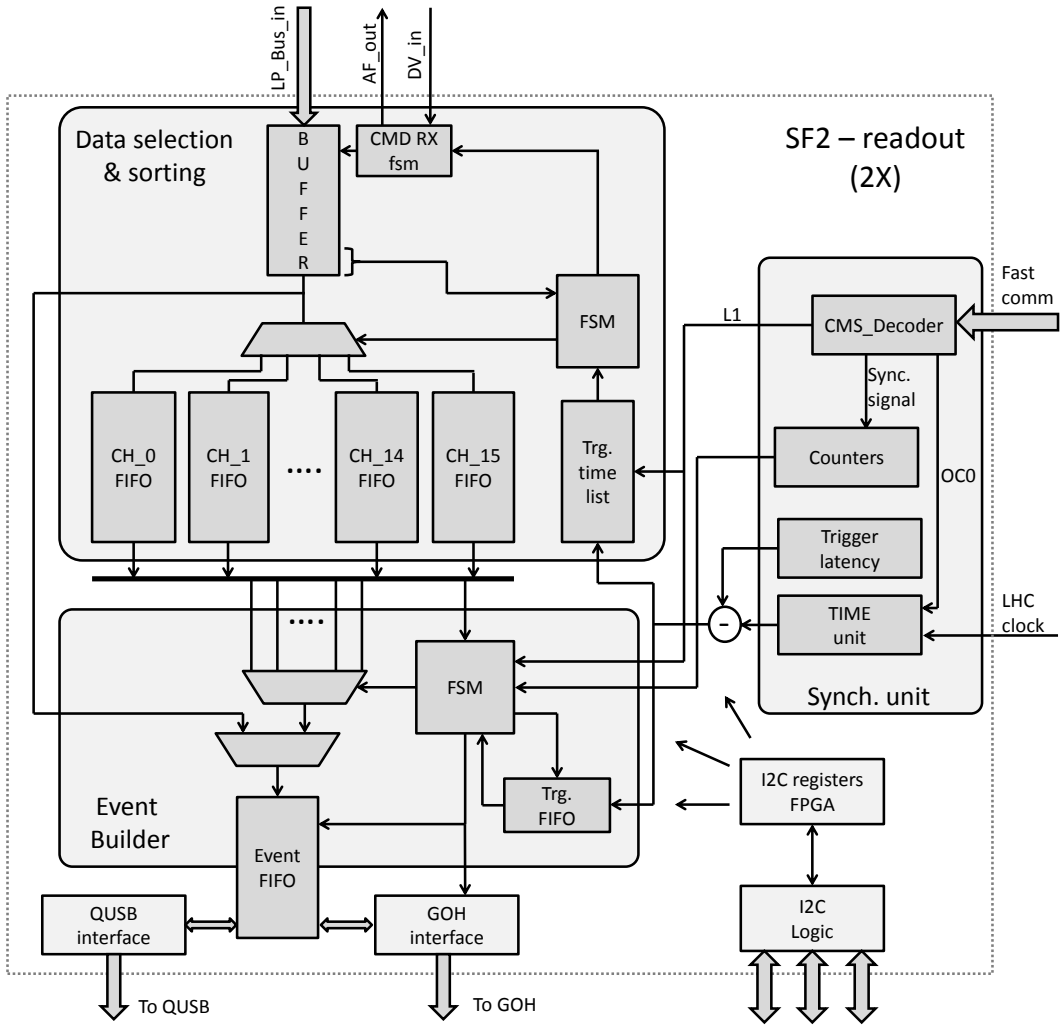

Figure 7.3: Scheme of the firmware readout path. The I^{2}C registers are controlled through the control path.

section 2.4. In this case they are also used to generate on each EA a time tag, called *Trigger Time Tag* (TTT), by subtracting the trigger latency (remotely controlled) from the actual timestamp. The actual timestamp is a simple counter running with the LHC clock and cleared by the OC0. The resulting TTT is registered both on a list in the DSS unit and in a FIFO in the EB units.

When an event is generated in a SAMPIC the relative data will be encapsulated into a data packet, which contains the event channel number and the event timestamp. When switched in run mode the firmware re-route the incoming data packets from the SAMPIC in the readout path. Since each packet from the mezzanine will contains the data from only one channel an event building must be locally performed. Moreover as pointed out in section 6.1 not all the packets will be related

to triggered events and no time ordering is provided. The first stage of the readout scheme, the DSS, is hence devoted to perform a data selection and a sorting of the collected packets.

Data are collected in the same way as in the control path but instead of a FIFO they enter in a pipeline. The pipeline can be adjusted to introduce a delay greater than the trigger latency (~ 5 µs). When the packet arrives toward the end of the pipeline a dedicated FSM checks the event packet timestamp against the TTTs in the list of the accepted events. If a correspondence is found, the SAMPIC channel number is extracted and the packet is sent to the FIFO dedicated to that channel. If instead the timestamp is not present, the data are discarded. The latency introduced by the pipeline ensures that the eventual EA signal related to that packet is already arrived and the TTT is present in the list. In this way is possible to achieve a significant data reduction. Moreover since the packets coming from the same channel are time ordered each channel FIFO will contains time ordered data packets.

Next the event is built. The final frame, without going into annoying details, must follow the CMS specifications, with an header, the data payload and finally a defined footer. The FSM of the EB reads the first TTT in the timestamp FIFO (which means the older one), which we will call TS. Then it fills the *Event FIFO* (EF) with the output frame header. After that it starts to retrieve from all the channel FIFOs the packet with the timestamp equal to TS. It keeps going until all the channel FIFOs have data packet with timestamp greater than TS or when a time $TS + 100$ µs (this number is again remotely controlled) is elapsed. Waiting this time ensures that all packets related to TS are already arrived. Finally the frame footer is added and the event can be sent to the DAQ.

The final readout can be done with the QUSB, with the fast parallel protocol, or through the GOH. The presence of a frame ready for transmission is signaled to the GOH controller by the EB FSM, while for the QUSB a flag is issued on one of the module generic IOs. For test purpose is possible to skip the event building and the data reduction so that all packets are received. It must be noted that once again the data paths used for the QUSB and for the GOH readout coincide until the very end, enhancing the testability of the system. As a final remark I want to mention that also another readout is possible, using the control path. The readout will be slow and no event building is possible, but still can be useful for debugging in the tunnel, where the QUSB will not be used.

Currently I'm writing and testing the firmware here described, with the goal to be ready for the installation in September.

Conclusions

Totem is an experiment focused to elastic scattering and diffractive physics. It's double arm proton reconstruction in the Roman Pots has been proved very effective and can give a fundamental contribution to the understanding of the Pomeron nature and to deeply investigate the proton structure. Moreover many QCD phenomena, like the gap survival probability, can be deeply investigated.

The TOTEM experiment has developed a new important physics program, to be carried out in collaboration with the CMS experiment, to deeply study low mass spectroscopy, glueballs, diffractive charmonium state production and central diffractive Jet production. The feasibility of the project has been first demonstrated with a common data taking during 2012, which has been possible thanks to the TOTEM trigger upgrade. The measurements will be performed in two complementary running scenarios. In both an advanced TOF detector has to be developed and installed in the RP stations in order to survive to the large pile-up probability. In the high-$\beta^\star$ scenario the upgrade is carried on the vertical RPs and developed entirely by the TOTEM collaboration. For standard optics the CMS-TOTEM Precise Proton Spectrometer project will be available, with both timing and tracking detectors to be installed in the horizontal RPs. The TOF system for the vertical upgrade must have a resolution below 50 ps, an efficiency close to 1 and high radiation hardness. Moreover low material budget and the possibility to have different pixel sizes is required.

In this work two detector technologies has been presented and investigated: diamond and SiPM. I reported my preliminary studies on the SiPM technology. The SiPM resulted in a detector easy to handle and operate, but its drawback (DC counts, needs of a radiator) convince us to adopt the other solution. The SiPMs have been used to build the trigger detectors for the later diamond test beams. A device characterization has been done to understand how to properly operate the devices. The polarization scheme and the electronics have been developed and tested. The intrinsic time performance of the device has been proved by stimulating the

sensor with a laser. Using an high-end amplifier an SPTR of 172 ps has been found, stimulating the device with a near ultraviolet laser and operating it with $V_{ov} = 2$ V. The trigger detectors have been built by coupling the SiPM to a plastic scintillator. Such devices always operated within the specifications, and their compactness and reliability greatly helped during the diamond detector development.

The diamond shows instead all the desired characteristics. Moreover up to four detection planes can fit in a RP, reducing the required resolution to $\sim$ 100 ps. During the first test (at PS and PSI test beam facilities) on commercial diamonds and related electronics we confirmed, as theoretically expected, that the main issue with such technology arise from the very low output signal ($\sim$ 1 fC/MIP), that is of the same order of magnitude of the input stage noise of high-end amplifiers found on the market: even with the algorithms here described, we can not achieved a time resolution better then $\sim$ 221 ps. However we learnt that reducing the capacitance of the sensor (and the parasitic one of the amplifier input stage) we could greatly improve the resolution. As an example with a reduction of the overall capacitance from 15 pF to 5 pF an increase of $\sim$ 30% in the performance is found.

We hence started to develop the hybrid board which, integrating both sensor and front-end as close as possible, could reach the desired performances. The work at SPS proved effective and for the first time we could achieve a resolution below the 100 ps with a TOTEM sensor. The final amplification chain was made of three stages: a pre-amplifier based on an RF SiGe transistor, an amplifier based on a MMIC amplifier and a final dual stage booster used for signal shaping. The first prototype (with 4 channels), integrating all the three amplification stages, was optimized and validated at DESY. One of the prototypes tested was mounting a segmented diamond, with the metallization pattern foreseen for the final installation, so that all pad dimensions could be tested. We performed a detailed study of the performance w.r.t. the pixel size (and hence the pixel capacitance). The results were extremely positive, with all the pixels showing a time resolution in the range $80 - 108$ ps, depending on the size. The final board, with the 12 channels foreseen in the project, has been produced and tested, not only confirming the results of DESY, but also achieving a resolution of 100 ps even for the larger pixel. Also the efficiency of the sensor has been studied, resulting in a bulk efficiency of 99%. The inter strip area has also been carefully controlled, detecting a minimum efficiency of 96%. The detector was not only validated for the final production but its advanced status of development and its performances made of it a suitable choice also for a first stage of the CT-PPS project, aiming to study some recent hints for BSM physics.

To achieve the detector resolution measured with the oscilloscope with the final system the digitization of the signal has to be performed carefully. The best solution is to use the SAMPIC chip to sample the full waveform and then perform the same offline reconstruction algorithms used with the oscilloscope data. The SAMPIC readout has been tested with a commercial module implementing the same chip mezzanine that we will use in the TOF system. A final test with the hybrid installed in the LHC tunnel and the SAMPIC readout has been done, confirming the whole system performance also in the tunnel environment. For the CT-PPS things are made complicated from the rate limitation of the SAMPIC and an alternative readout has been proposed and realized. Based on some studies which I performed on the NINO chip at PS we developed a TOTEM NINO board, so that a digitization through the NINO discriminator and the HPTDC is possible. The board has been tested, optimized and proved fully working. The discriminator introduce a degradation of the performances, even after the TOT correction. Still I proved that a final system resolution in the range $100 - 130$ ps, again depending on the pixel size, can be achieved. This resolution is acceptable for the CT-PPS employment, where the sensors will be mainly used, at this stage, for tracking.

The interface of the TOF detector with the TOTEM readout and control infrastructure has been presented, focusing on the description of the firmware for the SF2 FPGA. The firmware will have to interface the TOTEM I^2C control loop with the SAMPIC configuration protocol. Moreover it will have to perform the event selection and building, providing the data frame for the DAQ. Both the RMB and the firmware are designed to operate in the tunnel or in test beam, providing a strong testability of the system.

The TOTEM TOF system for the vertical upgrade will be installed in September, so that we will be able to collect data for the detector commissioning before the dedicated high-$\beta^\star$ run scheduled in 2017. The installation for CT-PPS is indeed ongoing, with the first data collected in few weeks from now. The work on the diamonds will move on to investigate alternative detector schemes and electronics solutions in order to use our detector also for the final TOF system of CT-PPS.

Acknowledgments

I would like to thank my supervisor Dr. Nicola Turini for guiding me throughout my PhD, always ready to help me. If I have grown as a researcher it's thank to you.

I'm also grateful to the whole TOTEM collaboration, in particular to the Spokeperson Dr. Simone Giani, for the support to our work. A special thanks to Prof. Angelo Scribano who introduced me to TOTEM. I would like to thank also the rest of the PISA-TOTEM group (both actual or past), for the good time spent together: Mirko, good friend and colleague, Liliana, Giuseppe and Eraldo. Many thanks also to the other TOTEM colleagues, especially the ones with whom I have worked more closely in these years.

Tornando ad una lingua con la quale mi sento più a mio agio, vorrei ringraziare la sezione INFN di PISA, il dipartimento di Fisica di Siena ed il Centro Fermi, che mi hanno permesso di portare avanti il mio lavoro in questi anni. Un ringraziamento davvero speciale al Prof. Riccardo Paoletti, che ha sopportato le mie continue richieste di supporto e consigli. Un gran ringraziamento anche al Prof. Giovanni Batignani, al Dr. Federico Pilo e al Dr. Luca Baldini, nonché al resto delle persone con cui ho lavorato in stretto contatto: Aldo, Carlo, Fabio, Giuseppe.

Vorrei ringraziare anche tutti i miei amici, uno ad uno, ma siete troppi e dover fare un taglio sarebbe troppo doloroso. Vi abbraccio tutti e vi ringrazio di cuore. Un ringraziamento unico va invece alla persona che ogni giorno tifa per me, mi sopporta e mi sprona ad andare avanti con i miei progetti e al cui sorriso non posso negare nulla. Grazie Chiara. Infine un grazie ai miei genitori e alla mia famiglia, per tutto quello che hanno fatto e fanno per me.

Grazie.

Bibliography

[1] M.L.Good and W.D.Walker. *"Diffractive Dissociation of Beam Particles"*, Physical Review, volume 120, 1857 (1960).

[2] P.D.Collins *"An introduction to Regge Theory And High-Energy Physics"*, Cambridge University Press, 1977.

[3] A.Martin *"Unitarity and High-Energy Behavior of Scattering Amplitudes"*, Phys. Rev. 129, 1432 (1963).

[4] I.I.Pomeranchuk *"Equality of the Nucleon and Antinucleon Total Interaction Cross Section at High Energies"*, Sov. Phys. JETP, Vol.7, No.3, p.499 (1958).

[5] L.B.Okun', I.I.Pomeranchuk *"The Conservation of Isotopic Spin and the Cross Section of the Interaction of High-Energy π-Mesons and Nucleons with Nucleons "*, Sov. Phys. JETP, Vol.3, No.2, p.307 (1956).

[6] TOTEM Collaboration (G.Antchev et al.) *"Measurement of proton-proton elastic scattering and total cross-section at $\sqrt{s}$=7 TeV"*, Europhisics Letters, 101 (2013) 21002.

[7] TOTEM Collaboration (G.Antchev et al.) *"Proton-proton elastic scattering at the LHC energy of $\sqrt{s}$=7 TeV"*, Europhisics Letters, 95 (2011) 41001.

[8] TOTEM Collaboration (G.Antchev et al.) *"First measurement of the total proton-proton cross-section at the LHC energy of $\sqrt{s}$=7 TeV"*, Europhisics Letters, 96 (2011) 21002.

[9] TOTEM Collaboration (G.Antchev et al.) *"Measurement of proton-proton inelastic scattering cross-section at $\sqrt{s}$=7 TeV"*, Europhisics Letters, 101 (2013) 21003.

[10] ISR - CR Collaboration, Phys. Lett. B, 62 (1976) 460; ISR - ACHGT Collaboration, Phys. Lett. B, 39 (1972) 663; ISR - R-211, Nucl. Phys. B, 262 (1985) 689;

ISR - R-210, Phys. Lett. B, 115 (1982) 495; UA1, Phys. Lett. B, 147 (1984) 385; UA4, Phys. Lett. B, 127 (1983) 472; 198 (1987) 583; UA4/2, Phys. Lett. B, 316 (1993) 448; CDF, Phys. Rev. D, 50 (1994) 5518; E710, Phys. Rev. Lett., 68 (1992) 2433; Nuovo Cimento A, 106 (1992) 123; D0, D0 Note 6056-CONF; pp2pp, Phys. Lett. B, 579 (2004) 245.

[11] COMPETE Collaboration (J.R.Cudell et al.) *"Benchmarks for the Forward Observables at RHIC, the Tevatron-Run II, and the LHC"*, Phys. Rev. Lett., 89 (2002) 201801.

[12] TOTEM Collaboration (G.Antchev et al.) *"Measurement of Elastic pp Scattering at $\sqrt{s} = 8$ TeV in the Coulomb-Nuclear Interference Region – Determination of the ρ-Parameter and the Total Cross-Section"*, CERN-PH-EP-2015-325.

[13] K.A. Olive et al. (Particle Data Group), Chin. Phys. C, 38, 090001 (2014).

[14] TOTEM Collaboration (G.Antchev et al.) *"Luminosity-Independent Measurement of the Proton-Proton Total Cross Section at $\sqrt{s}$=8 TeV"*, Physical Review Letters, 111, 012001 (2013).

[15] A.Donnachie, P.V.Landshoff *"Total cross sections"*, Physics Letters B, Volume 296 (1992), pp.227-232

[16] G.A.Jaroszkiewicz, P.V.Landshoff *"Model for Diffraction Excitation"*, Physics Review D, Volume 10, 891 (1974)

[17] J.Chen et Al. *"Glueball spectrum and matrix elements on anisotropic lattices"*, Int. J. Mod. Phys. E, 18 (2009) 1

[18] V.Matheiu, N.Kochelev and V.Vento *"The physics of glueballs"*, Int. J. Mod. Phys. E, 18 (2009) 1

[19] F.J.Llanes-Estrada et Al. *"QCD glueball Regge trajectory and the pomeron"*, Nuclear Physics A, Volume 710 (2002), pp. 45–54

[20] M.N.Sergeenko *"Glueballs and the pomeron"*, Europhisics Letters, 89 (2010) 11001.

[21] WA91 Collaboration (S.Abatzis et Al.) *"Observation of a narrow scalar meson at 1450 MeV in the reaction $pp \to p_f(\pi^+\pi^-\pi^+\pi^-)$ at 450 GeV/c using the CERN Omega Spectrometer"*, Physics Review B, Volume 324, 509-514 (1994)

[22] L.N.Lipatov *"Reggeization of the Vector Meson and the Vacuum Singularity in Non-abelian Gauge Theories"*, Sov. J. Nucl. Phys. 23 (1976) 338.

[23] E.A.Kuraev, L.N.Lipatov, and V.S.Fadin, *"The Pomeranchuk Singularity in Non-abelian Gauge Theories"*, Sov. Phys. JETP 45 (1977) 199.

[24] I.I.Balitsky and L N.Lipatov, *"The Pomeranchuk Singularity In Quantum Chromo-dynamics"*, Sov. J. Nucl. Phys. 28 (1978) 822.

[25] G.Ingelman and P.E.Schlein, *"Jet structure in high mass diffractive scattering"*, Phys. Lett. B152 (1985) 256.

[26] UA8 Collaboration (R.Bonino et al.), *"Evidence for Transverse Jets in High Mass Diffraction"*, Phys. Lett. B211 (1988) 239.

[27] J.A.Crittenden , *"Results on Diffractive Processes from the HERA Collider Experiments"*, Contributed to the proceedings of the EPIC'99 Workshop on Physics with an Electron/Polarized-Ion Collider, Indiana University Cyclotron Facility, 8-11 April 1999, Bloomington, arXiv:hep-ex/9908023

[28] R.D.Field, *"Application of pertubative QCD"*, Addison-Wesley, Reading, MA (1989).

[29] R.G.Roberts, *"The structure of the Proton"*, Cambridge University Press, Cambridge, UK (1990).

[30] J.C.Collins, D.E.Soper and G.Sterman, *"Factorization of Hard Processes in QCD"*, arXiv:hep-ph/0409313, Adv.Ser.Direct.High Energy Phys.5:1-91 (1988)

[31] R.P.Feynman, *"Photon-Hadron Interactions"*, Addison-Wesley, Reading, MA (1998).

[32] G.Altarelli and G.Parisi, *"Asymptotic Freedom in Parton Language"*, Nucl. Phys. B, 126 (1977), 298.

[33] Yu.L.Dokshitzer, *"Calculation of the Structure Functions for Deep Inelastic Scattering and e^+e^- Annihilation by Perturbation Theory in Quantum Chromodynamics"*, Sov. Phys. JETP 46 (1977) 641-653, Zh. Eksp. Teor. Fiz. 73 (1977) 1216-1240.

[34] [40] V.N.Gribov and L.N.Lipatov, *"Deep inelastic ep scattering in perturbation theory"*, Sov. J. Nucl. Phys. 15 (1972) 438.

[35] J.D.Bjorken, *"Rapidity gaps and jets as a new physics signature in very high-energy hadron hadron collisions"*, Phys. Rev. D47 (1993) 101–113.

[36] A.B.Kaidalov et Al. *"Probabilities of rapidity gaps in high energy interactions"*, Eur. Phys. J. C21 (2001) 521–529, arXiv:hep-ph/0105145.

[37] S.Erhan and P.E.Schlein, *"Inelastic diffraction data and the Pomeron trajectory"*, Phys. Lett. B481 (2000) 177–186.

[38] UA8 Collaboration (A.Brandt et al.), *"Measurements of single diffraction at* $\sqrt{s} = 630$ *GeV: Evidence for a non-linear* $\alpha(t)$ *of the pomeron"*, Nucl. Phys. B514 (1998) 3–44.

[39] K.Goulianos, *"Twenty years of diffraction at the Tevatron"*, arXiv:hep-ph/0510035. Presented at EDS-2005, XIth International Conference on Elastic and Diffractive Scattering, Chateau de Blois, France, 15-20 May 2005

[40] TOTEM Collaboration (G.Antchev et al.) *"Timing Measurements in the Vertical Roman Pots of the TOTEM Experiment"*, CERN Technical Disign Report, CERN-LHCC-2014-020, TOTEM-TDR-002.

[41] CMA and TOTEM collaborations *"CMS-TOTEM Precision Proton Spectrometer"*, CERN Technical Disign Report, CERN-LHCC-2014-021, TOTEM-TDR-003, CMS-TDR-13

[42] W.Ochs, *"The status of glueballs"*, J. Phys. G, 40 (2013) 043001

[43] A. Kirk, *"Resonance production in central pp collisions at the CERN Omega Spectrometer"*, Phys. Lett B, 489 (2000) 2

[44] Ames-Bologna-CERN-Dortmund-Heidelberg-Warsaw Collaboration (Breakstone et al.), *"Production of the* f_0 *meson in Double Pomeron Exchange reaction* $pp \to pp\pi^+\pi^-$ *at* $\sqrt{s} = 62$ *GeV"*, Z. Phys. C, 31 (1986) 185

[45] J.Turnau on behalf of STAR collaboration, *"Measurement of the Central Exclusive Production of pion pairs using tagged forward protons at the STAR detector at RHIC"*, PoS DIS2014 (2014) 098

[46] Axial Field Spectrometer Collaboration (T.Akeson et al.), *"A Search for Glueballs and a Study of Double Pomeron Exchange at the CERN Interacting Storage Rings"*, Nucl. Phys. B, 264(1986) 154

[47] M.G.Albrow, T.D.Coughlin and J.R.Forshaw, *"Central exclusive particle production at high energy hadron colliders"*, Prog. Part. Nucl. Phys., 65 (2010) 149, arXiv:1006.1289.

[48] L.A.Harland-Lang, V.A.Khoze, M.G.Ryskin and W.J.Stirling, *"Standard candle central exclusive processes at the Tevatron and LHC"* Eur. Phys. J. C, 69 (2010) 179.

[49] CDF Collaboration (T. Aaltonen et al.), *"Observation of Exclusive Charmonium Production and $\gamma\gamma \to \mu*+\mu^-$ in $p\bar{p}$ Collisions at $\sqrt{s} = 1.96$ TeV"*, Phys. Rev. Lett., 102 (2009) 242001.

[50] LHCb Collaboration (R. Aaij et al.), *"Central Exclusive Dimuon Production at $\sqrt{s} = 7$ TeV"*, LHCb-CONF-2011-022 (2011).

[51] LHCb Collaboration (R. Aaij et al.), *"Updated measurements of exclusive J/Ψ and $\Psi(2s)$ production cross-sections in pp collisions at $\sqrt{s} = 7$ TeV"*, J. Phys. G, 41 (2014) 055002.

[52] Alice Collboration (B.B.Abelev et al.), *"Exclusive J/Ψ photoproduction off protons in ultra-peripheral $p - Pb$ collisions at $\sqrt{s_{NN}} = 5.02$ TeV"*, CERN-PH-EP-2014-149 (2014), arXiv:1406.7819.

[53] L.Motyka, *"Searching for odderon in exclusive vector meson hadroproduction"*, Proceedings of DIS2008 (2008), arXiv:0808.2216.

[54] R.S.Pasechnik, A.Szczurek and O.V.Teryaev, *"Diffractive production of $\chi_c(+^+; 1^+; 2^+)$ mesons at LHC, Tevatron and RHIC"*, PoS EPS-HEP2009, (2009) 335, arXiv:0909.4498.

[55] Yu.L.Dokshitzer, *"Calculation of the Structure Functions for Deep Inelastic Scattering and e^+e^- Annihilation by Perturbation Theory in Quantum Chromodynamics"*, Sov. Phys. JETP 46 (1977) 641-653, Zh. Eksp. Teor. Fiz. 73 (1977) 1216-1240

[56] J.D.Bjorken, *"Rapidity gaps and jets as a new physics signature in very high-energy hadron hadron collisions"*, Phys. Rev. D47 (1993) 101-113.

[57] A.B.Kaidalov et Al., *"Probabilities of rapidity gaps in high energy interactions"*,Eur. Phys. J. C21 (2001) 521-529, arXiv:hep-ph/0105145.

[58] The CMS Collaboration, *"Search for new physics in high mass diphoton events in proton-proton collisions at $\sqrt{s} = 13$ TeV"*, Tech. Rep. CMS-PAS-EXO-15-004 (CERN, Geneva, 2015).

[59] The ATLAS Collaboration, *"Search for resonances decaying to photon pairs in 3.2 fb^{-1} of pp collisions at $\sqrt{s} = 13$ TeV with the ATLAS detector"*, Tech. Rep. ATLAS-CONF-2015-081 (CERN, Geneva, 2015).

[60] SFichet, G.von Gersdorff, C.Royon, *"Measuring the diphoton coupling of a 750 GeV resonance"*, http://arxiv.org/pdf/1601.01712.pdf

[61] Csaba Csaki, Jay Hubisz, John Terning, *"The Minimal Model of a Diphoton Resonance: Production without Gluon Couplings"*, arXiv:1601.07187

[62] O.S.Bruning et Al., *"LHC Design Report*, CERN design report, 10.5170/CERN-2004-003-V-1

[63] R.Schmidt, *"Accelerator Physics and Technology of the LHC"*, CERN Yellow Report 99-01, 1998

[64] V.Avati et Al.,, *"TOTEM Technical Design Report"*, CERN Technical Design Report, CERN-LHCC-2004-002

[65] TOTEM experiment web site: http://totem.web.cern.ch/Totem/

[66] U.Amaldi et Al., *"The energy dependence of the proton-proton total cross-section for centre-of-mass energies between 23 and 53 GeV"*, Phys. Lett. 44B (1973) 112.

[67] P.Aspell et al., *"VFAT2 : A front-end system on chip providing fast trigger information, digitized data storage and formatting for the charge sensitive readout of multi-channel silicon and gas particle detectors"*, Proceedings of TWEPP-07, Topical Workshop on Electronics for Particle Physics, Prague, Czech Republic 3-7 September 2007.

[68] H.Niewiadomsky, *"Recontruction of Protons in the TOTEM Roman Pot Detectors at the LHC"*, Ph.D. Thesis, University of Manchester (2008), CERN-THESIS-2008-080.

[69] R. Engel, Z. Phys. C, 66 (1995) 203; R. Engel and J. Ranft, Phys. Rev. D54 (1996) 4244.

[70] E.Oliveri, *"The forward inelastic telescope T2 for the TOTEM experiment at the LHC"*, Ph.D. Thesis, University of Siena (2010), CERN-THESIS-2010-178.

[71] TOTEM Collaboration (G.Antchev et al.), *"Measurement of the forward charged particle pseudorapidity density in pp collisions at* $\sqrt{s} = 7$ *TeV with the TOTEM experiment"*, Europhys.Lett. 98 (2012) 31002.

[72] CMS and TOTEM Collaboration *"Measurement of pseudorapidity distributions of charged particles in proton-proton collisions at* $\sqrt{s} = 8$ *TeV by the CMS and TOTEM experiments"*, Eur.Phys.J. C74 (2014) 10, 3053.

[73] The CMS Collaboration, *"CMS The Muon Project"*, CERN-LHCC 97-32, 1997.

[74] The CMS Collaboration, *"CMS Physics TDR: Volume I (PTDR1), Detector Performace and Software "*, CERN technical design report, CERN-LHCC-2006-001, 2 February 2006.

[75] The CMS Collaboration, *"Description and performance of track and primary-vertex reconstruction with the CMS tracker"*, JINST 9 (2014) P10009.

[76] The CMS Collaboration, *"Energy calibration and resolution of the CMS electromagnetic calorimeter in pp collisions at* $\sqrt{s} = 7$ *TeV"*, JINST 8 (2013) P09009.

[77] The CMS Collaboration, *"Performance of CMS muon reconstruction in pp collision events at* $\sqrt{s} = 7$ *TeV"*, JINST 7 (2012) P10002.

[78] F.Siklèr (for the CMS Collaboration), *"Low* p_T *Hadronic Physics with CMS"*, Int. J. Mod. Phys. E16 (2007) 1819-1825.

[79] The CMS Collaboration, *"Study of the inclusive production of charged pions, kaons, and protons in pp collisions at* $\sqrt{s} = 0.9$*, 2.76, and 7 TeV"*, Eur. Phys. J. C 72 (2012) 2164.

[80] N.Turini et Al., *"The trigger system of the TOTEM experiment at LHC"*, Proceeding of the 13th ICATPP Conference, Villa Olmo, 2011

[81] J.Kopal (for the TOTEM Collaboration), *"Totem Trigger system"*, Proceeding of International Conference on Applied Electronics , 2013

[82] P.Chalmet and W.Snoeys, *" TOTEM Coincidence Chip Specification"*, Web page: http://totem.web.cern.ch/Totem/work_dir/electronics/RPMB/CCSPECv2.pdf

[83] J.F.Grahl, *"Optical Da ta Links in CMS ECAL"*, 10th Workshop on electronics for LHC experiments (LECC2004), Boston, USA.

[84] CMS and TOTEM Collaborations, *"Measurement of pseudorapidity distributions of charged particles in proton-proton collisions at $\sqrt{s} = 8$ TeV by the CMS and TOTEM experiments"*, Eur.Phys.J. C74 (2014) 10, 3053

[85] M.Bousonville and J.Rausch, *"Universal picosecond timing system for the Facility for Antiproton and Ion Research"*, Phys. Rev. ST Accel. Beams 12 (2009) 042801.

[86] M.Berretti, *"Performance studies of the Roman Pot timing detectors in the forward region of the IP5 at LHC"*, CERN-TOTEM-NOTE-2014-001 (2014).

[87] E.Delagnes et al., *"The SAMPIC Waveform and Time to Digital Converter"*, IEEE Nuclear Science Symposium and Medical Imaging Conference (2014 NSS/MIC), and 21st Symposium on Room-Temperature Semiconductor X- Ray and Gamma-Ray Detectors, Nov 2014, Seattle, United States.

[88] H.Grabras., *"Developing Picosencond Time Of Flight detectors"*, Ph.D. Thesis, Universitè Paris Sud (2013).

[89] F.Anghinolfi et Al., *"NINO: an ultra-fast and low-power front-end amplifier/discriminator ASIC designed for the multigap resistive plate chamber"*, Nuclear Instruments & Methods In Physics Research A, 533 (2004) pp.183-187.

[90] J.Christiansen, *"HPTDC High Performance Time to Digital Converter for HPTDC version 1.3"*, CERN/EP, March 2014.

[91] M.Albrow et al., *"Quartz Cherenkov counters for fast timing: QUARTIC"*, Journal of Instrumentation 7 (2012) P10027.

[92] W.Sadrozinski et al., *"Ultra-fast silicon detectors"*, Volume 730, pp. 226–231, 2013.

[93] N.Cartiglia et al., *"Performance of Ultra-Fast Silicon Detectors"*, arXiv:1312.1080 (2013).

[94] E.Bossini and R.Paoletti, *"A Modular, Versatile, Low Cost Readout System for Cosmic Ray Telescope of Multi-Gap Resistive Chambers"*, Nuclear Science Symposium and Medical Imaging Conference (NSS/MIC), 2013 , DOI: 10.1109/NSS-MIC.2013.6829723.

[95] Advancid application note. *"Introduction to SiPMs"*. web page: https://advansid.com/attachment/get/up_89_1411030571.pdf

[96] P.K.Lightfoot et Al, *"Characterisation of a silicon photomultiplier device for applications in liquid argon based neutrino physics and dark matter searches"*, JINST 3, P10001 (2008), arXiv:0807.3220.

[97] N.Dinu et al, *"Temperature and Bias Voltage Dependence of the MPPC Detectors"*. 2010 IEEE Nuclear Science Symposium, Medical Imaging Conference, 2010, pp.215-219.

[98] S12571 Hamamatsu datasheet, web page: https://www.hamamatsu.com/resources/pdf/ssd/s12571-025_etc_kapd1042e.pdf

[99] V.Puill et al, *"Single photoelectron timing resolution of SiPM as a function of the bias voltage, the wavelength and the temperature"*. Nuclear Instruments & Methods In Physics Research A, 695, 2012, pp. 354–358

[100] F.Acerbi et al, *"Characterization of Single-Photon Time Resolution: From Single SPAD to Silicon Photomultiplier"*. IEEE Transactions on Nuclear Science, 61, (2014), issue 5

[101] M.Gallinaro, *"A New Scintillator Tile/Fiber Preshower Detector for the CDF Central Calorimeter "*. IEEE Transactions on Nuclear Science, 52, (2005), pp.879-883.

[102] A.Artikov et al, *"CDF Central Preshower and Crack Detector Upgrade"*. CDF internal note. FNAL-PUB-07-023-E

[103] *"Bicron 408 spec."*. Web page: http://ajbell.web.cern.ch/ajbell/Documents/Optical_Fibres/BICRON%20BC408.pdf, http://www.phys.ufl.edu/courses/phy4803L/group_I/muon/bicron_bc400-416.pdf

[104] M.Berretti, E.Bossini and N.Minafra, *"Timing performances of diamond detectors with Charge Sensitive Ampliier readout"*. CERN-TOTEM-NOTE-2015-003 (2015).

[105] B.Dehning et Al. *"Diamond detectors as beam monitors"*, Proceedings of BIW10, Santa Fee, New Mexico, US, p. 49-52, 2010.

[106] H.Frais-Kölbl et Al. *"Medical diamond beam monitor – pre-clinical evaluation and future applications"*, NIM A, Vol. 581, p. 103–106, 2007

[107] G.Grosso, G.Pastori Parravicini, *"Solid State Physics"*, 2nd edition, 2000.

[108] R. de L. Kronig and W. G. Penney. *"Quantum Mechanics of Electrons in Crystal Lattices"*. Proc. Roy. Soc.; A130 499 (1930).

[109] M. Schwander, K. Partes *"A review of diamond synthesis by CVD processes"*. Diamond and Related Materials Volume 20, Issue 9, October 2011, Pages 1287–1301.

[110] M. Sunkara et Al. *"Nucleation of diamond crystals"*. Carbon 28 (6) (1990) 745 – 746.

[111] G.Restelli. *"Semiconductors properties of Silicum and Germanium"* in *Semiconductor detectors*. Ed. by G.Bertolini and A.Coche. p.27-52

[112] K.A. Olive et al. *"Particle Data Group"*, Chin. Phys. C, 38, 090001 (2014).

[113] C.A.Klein. *"Bandgap Dependence and Related Features of Radiation Ionization Energies in Semiconductors"*. J. of Applied Physics, Volume 39, Issue 4, p.2029-2038

[114] N.W. Ashcroft,N.D. Mermin. *"Solid State Physics"*. Edited by Cengage Learning Emea, 2000, p. 6-7, Carbon 28 (6) (1990) 745 – 746.

[115] Zheng Li, H.W. Kraner . *"Modeling and simulation of charge collection properties for neutron irradiated silicon detectors"*. Nuclear Physics B - Proceedings Supplements, Volume 32, May 1993, Pages 398-409

[116] H. Pernegger et al. *"Charge-carrier properties in synthetic single-crystal diamond measured with the transient-current technique"*. J. Appl. Phys. 97, 073704 (2005);

[117] J. Isberg et al. *"High Carrier Mobility in Single-Crystal Plasma-Deposited Diamond"*. Science (2002) 297, 1670.

[118] C. Jacoboni et Al., *"A review of some charge transport properties of silicon"*. Solid-State Electronics, 1977, Vol. 20, p. 77-89.

[119] Weightfield 2 home page: http://personalpages.to.infn.it/~cartigli/Weightfield2/Main.html

[120] GEANT 4 home page: https://geant4.web.cern.ch/geant4/

[121] W.R.Leo. *"Techniques for Nuclear and Particle Physics Experiments"* 2nd edition Ed. by Springer-Verlag. 1994

[122] W. Trischuk (for the RD42 collaboration), *"Recent Advances in Diamond Detectors"*. Proceedings for IHCEP08. arXiv:0810.3429

[123] http://aea.web.psi.ch/beam2lines/beam_pim1.html

[124] L. Durieu, A. Mueller, and M. Martini. *"Optics Studies for the T9 Beam Line in the CERN PS East Area Secondary Beam Facility"*. Conf.Proc., C0106181:1547–1549, 2001.

[125] E.Bossini (for the TOTEM Collaboration), *"Results on diamond timing detector for the TOTEM experiment"*. Nuclear Instruments and Methods in Physics Research Section A, Volume 824 (2016), Pages 87-88.

[126] M.Berretti (for the TOTEM Collaboration), *"The diamond time of flight detector of the TOTEM experiment"*. Nuclear Instruments and Methods in Physics Research Section A, in press, doi:10.1016/j.nima.2016.04.068.

[127] *"Desy beam page."* Web page: http://particle-physics.desy.de/e252106/

[128] *"MIMOSA telescope twiki"* Web page: https://twiki.cern.ch/twiki/bin/view/MimosaTelescope/WebHome

[129] J. Baudot, *"First test results of MIMOSA-26: A fast CMOS sensor with integrated zero suppression and digitized output"* 2009 IEEE Nuclear Science Symposium Conference Record (NSS/MIC), DOI:10.1109/NSSMIC.2009.5402399

[130] J.Pietraszko et al., *"Diamonds as timing detectors for minimum-ionizing particles: The HADES proton-beam monitor and START signal detectors for time of flight measurements"*. Nuclear Instruments & Methods In Physics Research A, Volume 618, Issues 1–3 (2010), Pages 121–123.

[131] J.Pietraszko, 3rd CARAT Workshop, GSI Dec. 11-13, 2011.

[132] *"The ALICE Time Of Flight Detector"*.ALICE TOF web page: http://aliceinfo.cern.ch/Public/en/Chapter2/Chap2_TOF.html

[133] *"SmartFusion2 SoC FPGA family"*. Web page: http://www.microsemi.com/products/fpga-soc/soc-fpga/smartfusion2#overview

[134] *"QuickUSB User Guide"*. Web page:http://www.bitwisesys.com/v/public/media/quickusb_user_guide_v2.11.41.pdf

[135] J.Troska et al., *"Implementation of the timing, trigger and control system of the CMS experiment"*. IEEE Trans. Nucl. Sci. 53 (2006), 834

[136] F.Drouhin et al., *"The control system for the CMS tracker front-end"*. IEEE Trans. Nucl. Sci. 49 (2002), 846